University of
Nottingham
UK | CHINA | MALAYSIA

**Manufacturing Metrology Team**
Advanced Manufacturing Technology Research Group
Department of Mechanical, Materials and Manufacturing Engineering
Faculty of Engineering
University of Nottingham

# Improving coherence scanning interferometry signal modelling and topography measurement for complex surfaces

by

**Matthew Thomas**

Thesis submitted to the University of Nottingham for the degree of
*Doctor of Philosophy*

First submission: 24 May 2022
Final submission: 25 Oct 2022

Supervisors: Professor Richard Leach, Dr Rong Su

*To my parents, who have always supported me.*

*That I have got this far is thanks to you*

*In memory of Grandpa David and Grandpa Jeremy*

# Abstract

This thesis presents work on advanced optical surface metrology methods that enable extending the range of surface slopes that can be reliably measured by optical surface topography measurement instruments, and on investigating the reliability of the current capability. Optical instruments can only capture a limited portion of light scattered from an object's surface, determined by the instrument's numerical aperture. As the surface measured becomes steeper, less scatter is captured until all specular scatter is lost, referred to as the specular reflection limit (SRL). While surface measurement of slopes beyond the SRL by modern instruments is possible via the capture and detection of non-specular scatter, the instrument response to these slopes is not well understood. In addition, as the non-specular scatter has a low signal-to-noise ratio, data dropout can occur. Topography measurement of steep and complex surfaces using optical methods can therefore be challenging and have an unknown reliability, and can have significant errors when multiple scattering is present.

The instrument modelling and experimental work focussed on coherence scanning interferometry (CSI). Through use of an approximate linear model the instrument response of a CSI instrument to various slope angles and spatial frequencies was described by a three-dimensional (3D) surface transfer function (STF). This theory was experimentally verified by demonstrating that an experimental 3D STF obtained from measurement of microspheres can be used to generate a filter that can compensate for the effect of lens aberration at a fundamental level and consequently reduce errors in the topographies obtained, especially from surface slopes just below the SRL. Second, a rigorous two-dimensional boundary element method (BEM) model of electromagnetic surface scatter was verified through multiple comparisons including an exact analytical Mie scatter solution and through experimental comparison to measurement data from a laser scatterometer, providing evidence of the BEM model's capability to accurately predict scatter from complex surfaces, including those that linear models cannot accurately model. A CSI model based on this BEM scattering model was then developed and verified, demonstrating the model's capability to accurately model the CSI signal for complex surfaces which contain steep surfaces, including those that produce multiple scattering. Using this BEM-CSI model and experimental measurement, the capability of optical surface topography measurement methods for measurement of steep surfaces was investigated, illustrated for the first time with both fringe data and the resulting height estimates for a series of surfaces at slopes steeper than the SRL. At high tilt angles it was found that sharp edges with undercuts still provide strong signals which appear as plateaus in the topography data, with a width corresponding to the width of the point spread function of the instrument. While phase information was lost, part of the topography could still be obtained from the non-specular scatter. The BEM-CSI model's results were accurate even for challenging surfaces beyond the capabilities of linear models, providing a tool for future investigation of other complex surfaces and providing progress towards evaluating the measurement uncertainty of complex surface measurements by optical instruments.

*"In science, if you know what you are doing, you should not be doing it. In engineering, if you do not know what you are doing, you should not be doing it. Of course, you seldom, if ever, see either pure state."*

— Richard Hamming, The Art of Doing Science and Engineering (1997)

Mac: *"Let's magnify, and see if we can get a reflection off her eye"*
Stella: *"Magnification times 100, for starters"*

— CSI: NY - S1.E10 "Night, Mother" (2004)

# Table of Contents

**Cover**

**Dedications** ........ iii

**Abstract** ........ v

**Epigraph** ........ vii

**Table of Contents** ........ ix

**List of Figures** ........ xiii

**List of Tables** ........ xix

**List of Abbreviations** ........ xxi

**Declaration** ........ xxiii

**Acknowledgements** ........ xxv

**Chapter 1 : Introduction** ........ 1

1.1 Background ........ 1

1.2 Aims and objectives ........ 6

1.3 Novelty ........ 7

1.4 Thesis structure ........ 8

**Chapter 2 : Background & State of the art** ........ 11

2.1 Metrology ........ 11

2.2 Surface metrology ........ 12

2.3 Coherence scanning interferometry ........ 17

2.3.1 Principles of CSI ........ 18

2.3.2 Instrument design ........ 22

2.3.3 Fringe acquisition ........ 25

2.3.4 Surface reconstruction methods ........ 27

2.3.5 Current capability ........ 31

2.4 Overview of CSI models ........ 37

2.4.1 A simple linear cosine intensity CSI model ........ 38

2.4.2 More advanced linear models ....................42
2.4.3 Non-linear models ....................46
2.5 Scalar scattering and imaging theory ....................50
2.5.1 Scalar scattering theory ....................50
2.5.2 Imaging theory by back-propagation of far-field scatter ....................56
2.6 Outside-NA measurement ....................61
2.6.1 State of the art for outside-NA measurement ....................62
2.7 Summary ....................66

**Chapter 3 : Lens aberration compensation of CSI using the foil model....................69**
3.1 Introduction ....................70
3.2 Theory ....................72
3.2.1 Scattering under the KA ....................72
3.2.2 Scalar theory imaging ....................75
3.2.3 Interferometric imaging ....................78
3.2.4 3D transfer function ....................80
3.2.5 3D STF measurement and correction ....................82
3.3 Materials and methods ....................84
3.3.1 Precision microspheres ....................85
3.3.2 Surface measurement ....................86
3.4 Result and analysis ....................89
3.4.1 Characterisation of 3D STF ....................89
3.4.2 Inverse filtering of 3D PSF ....................92
3.4.3 Improved surface measurement ....................93
3.5 Conclusion and discussion ....................99
3.6 Summary ....................101

**Chapter 4 : Verification of a BEM optical scattering model ....................103**
4.1 Introduction ....................103
4.2 Theory ....................104
4.3 Methodology ....................109
4.3.1 Scatterometer measurement method ....................109

4.3.2 Comparison with BEM modelling ........ 112
4.3.3 Model comparison for a range of sinusoids ........ 115
4.4 Results & Discussion ........ 116
4.4.1 Comparison to Mie scattering ........ 116
4.4.2 Comparison to scatterometer ........ 117
4.4.3 Survey of agreement with KA method ........ 121
4.5 Conclusion and discussion ........ 125
4.6 Summary ........ 127

**Chapter 5 : Modelling of CSI beyond the linear regime ........ 129**
5.1 Introduction ........ 129
5.2 CSI modelling theory ........ 131
5.2.1 CSI signal synthesis ........ 131
5.3 Implementation ........ 135
5.3.1 Choice of inputs ........ 136
5.3.2 BEM for surface scattering ........ 137
5.3.3 CSI signal synthesis in $\boldsymbol{\xi}$-space ........ 137
5.3.4 Discrete sampling considerations ........ 141
5.3.5 Coordinate grid interpolation ........ 144
5.4 Methods and materials ........ 152
5.5 Results ........ 154
5.5.1 Optical flat ........ 154
5.5.2 Sinusoidal gratings ........ 155
5.5.3 Step height ........ 158
5.5.4 Vee-groove ........ 160
5.6 Conclusion and discussion ........ 161
5.7 Summary ........ 163

**Chapter 6 : Measurement beyond the specular reflection limit with CSI ........ 165**
6.1 Introduction ........ 165
6.2 Materials and methods ........ 167
6.2.1 CSI instrument ........ 167

6.2.2 Test samples ..... 167
6.2.3 Experimental methods ..... 169
6.2.4 Modelling methods ..... 170
6.3 Results and analysis ..... 173
6.3.1 Roughened flat topography ..... 173
6.3.2 Blazed grating topography ..... 174
6.3.3 Fringe generation ..... 176
6.3.4 Fringe analysis ..... 181
6.4 Conclusion and discussion ..... 184
6.5 Summary ..... 187

**Chapter 7 : Conclusions and future work ..... 189**
7.1 Thesis summary ..... 189
7.1.1 Aims and objectives ..... 189
7.1.2 Contribution to the field ..... 190
7.2 Areas for future work ..... 193
7.2.1 Specific improvements ..... 193
7.2.2 Novel future work ..... 195

**References ..... 199**

**List of Publications ..... 219**

**Appendix A : Foil model inverse filtering graphical user interface ..... 221**

**Appendix B : Summation identities for complex numbers ..... 225**

# List of Figures

**Figure 1.1.** (a) A milling cutter tool, (b) exploded-view of aspherical microlens arrays found in smart phone cameras, and (c) total knee replacement part mounted in a wear simulator from [17]. .......... 1

**Figure 1.2.** Diagram of the measurement of a mirror-like surface which only specularly reflects, shown (a) untilted (surface normal parallel to the optical axis) and (b) tilted at angle $\theta$. .......... 3

**Figure 1.3.** Diagram of the measurement of a rough surface which produces some specular and diffuse scatter .......... 3

**Figure 2.1**. Modelled interferogram using a simple model .......... 22

**Figure 2.2**. Schema of a vertical scanning style CSI instrument, equipped here with a Mirau-type interferometric microscope objective. .......... 23

**Figure 2.3**. A subset of the images captured by a CSI instrument during a scan of a sinusoidal grating. .......... 26

**Figure 2.4**. Slices of the 3D fringe data obtained from measurement of a sinusoidal grating. .......... 26

**Figure 2.5**. A diagram to present how the fringe data can be considered as columns of adjacent interferograms, each of which encode the surface height at a particular position. .......... 27

**Figure 2.6**. Axial cross section of fringe data from measurement of a microsphere. .. 28

**Figure 2.7.** Schematic illustrating the concept of a maximum collection angle for a microscope system (repeated from Figure 1.2). .......... 33

**Figure 2.8**. Modelled interference signal (interferogram) for CSI (right) using a Gaussian optical distribution with FWHM of 100 nm and mean of 500 nm (left), where a point source is considered at the centre of the pupil plane. .......... 40

**Figure 2.9**. Modelled interferogram for CSI (right) using a Gaussian optical distribution with FWHM of 20 nm and mean of 500 nm (left). .......... 41

**Figure 2.10**. Modelled interferogram for CSI using a Gaussian optical distribution with a mean wavelength of 500 nm, where: (a) the FWHM is 100 nm and the NA is 0.2, and (b) the FWHM is 20 nm and the NA is 0.6. .......... 42

**Figure 2.11**. Modelled CSI fringes using a rigorous method for a vee-groove surface .......... 47

**Figure 2.12.** Geometry used for the derivation of Eq. (2-24) ....................................52
**Figure 2.13.** Geometry used for the derivation of Eq. (2-27) ....................................54
**Figure 2.14.** Geometry used for the derivation of Eq. (2-33). ...................................58
**Figure 2.15**. Diagrams illustrating the concept of collection angle for a microscope system for a tilted surface tilted beyond the acceptance angle ...................................62
**Figure 3.1.** Visualisation in $k$-space of a $k_x$-$k_z$ slice of a) the ideal 3D transfer function given by Eq. (3-19) and b) the NA limited 3D transfer function for a NA of 0.6, given by Eq. (3-20). ..........................................................................................................78
**Figure 3.2.** A lateral-axial 2D slice of a) the real part of the PSF $HK\mathbf{r}$ and b) the magnitude of the associated 3D STF $HK\mathbf{K}$ given by Eq. (3-30), for NA=0.6 and $k0 = 2\pi\lambda$, $\lambda = 0.5$ µm. ..........................................................................................81
**Figure 3.3.** A lateral-axial 2D slice of a) the real part of the PSF $HK\mathbf{r}$ and b) the magnitude of the associated 3D STF $HK\mathbf{K}$ given by Eq. (3-32), for NA=0.6 and a Gaussian spectrum illumination. ......................................................................82
**Figure 3.4.** SEM images showing the micro textures in surfaces R521, R525 and R527. ...........................................................................................................................88
**Figure 3.5.** Experimentally characterised 3D STF of the CSI system. .......................90
**Figure 3.6.** Experimentally characterised 3D PSF of the CSI system. .......................93
**Figure 3.7.** Measurements of surface R521. .............................................................94
**Figure 3.8.** Measurements of surface R527. .............................................................95
**Figure 3.9.** Measurements of surface R525. .............................................................96
**Figure 3.10.** CSI measurements of the Ti-6Al-4V AM surface. ................................99
**Figure 4.1.** Geometry of the object considered for the scattering problem ..............105
**Figure 4.2.** Illustration of the surface geometry of the measured sinusoidal grating. .........................................................................................................................110
**Figure 4.3.** Overall block diagram for the CASI scatterometer. ..............................111
**Figure 4.4.** Geometry of BRDF measurement. ........................................................111
**Figure 4.5.** Simulated far-field scattered intensity due to illumination of a sinusoidal grating .........................................................................................................113
**Figure 4.6.** Convolution function (black line) obtained by convolution of a rectangular function of width 0.9° (blue dashed line) with a Gaussian function with standard deviation of 0.2° (red dashed line). .........................................................................114
**Figure 4.7.** Result of convolution of the ASD calculated using BEM.....................115

**Figure 4.8.** Magnitude of the scattered field and total field for the BEM model and the Mie solution for a homogenous cylinder. ....................116
**Figure 4.9.** Measurement of the BRDF (in units of inverse steradians) produced by the CASI scatterometer at UNCC. ....................117
**Figure 4.10.** Comparison of BEM scatter data (after convolution with an aperture kernel function) against CASI measurement data, under the assumed measurement configuration. ....................119
**Figure 4.11.** The cosine corrected BRDF as measured by CASI, compared to the ASD obtained from our BEM computational model (after convolution with an aperture function). ....................120
**Figure 4.12.** ASD produced using (top) the KA-based method, (middle) using the BEM model, and (bottom) the difference between these results. ....................122
**Figure 4.13.** Geometrical optics reflections from a sinusoidal grating ....................123
**Figure 4.14.** ASD for a perfect sinewave for surface wavelength of 90 μm and amplitude of 9.5 μm, (top) using a KA-based method, (middle) using the BEM model, and (bottom) the difference between these results. ....................124
**Figure 4.15.** ASD for a perfect sinewave for surface wavelength of 65 μm and amplitude of 9.5 μm ....................124
**Figure 4.16.** ASD for a perfect sinewave for surface wavelength of 45 μm and amplitude of 9.5 μm ....................125
**Figure 4.17.** Differences between the KA-based linear model and the BEM rigorous model for a sinusoidal grating with amplitude 9.5 μm and 0.633 μm wavelength illumination for a range of different surface wavelengths (left). ....................125
**Figure 5.1.** Flowchart describing the operation of the CSI model. ....................136
**Figure 5.2.** Diagram of construction of signal in $\boldsymbol{\xi}$-space at $\mathbf{k}s - \mathbf{k}i$ using $\mathbf{k}s$ and $\mathbf{k}i$. ....................139
**Figure 5.3.** Spectral density $Sk0$ and weighting factor $Sk0k0$ for a Gaussian distributed $Sk0$ with a mean of 1.786 μm$^{-1}$ and FWHM of 0.351 μm$^{-1}$ ....................140
**Figure 5.4.** Intensity of angular scatter from monochromatic (λ=0.57 μm) normal incidence illumination of a flat surface with length a) 25 μm, and b) 50 μm. ....................142
**Figure 5.5.** Modelled Gaussian spectral density with a mean wavenumber of 1.754 μm$^{-1}$ and FWHM of 0.246 μm$^{-1}$ ....................144

**Figure 5.6.** Discrete 2D rectangular grid in a) real space and b) **ξ**-space, with constant spacing a) d$x$ and d$z$, and b) d$\xi x$ and d$\xi z$. ............................................................ 145

**Figure 5.7.** Locations of demodulated scatter in **ξ**-space at $\boldsymbol{\xi} = \mathbf{k}\mathrm{s} - \mathbf{k}\mathrm{i}$ given by red cross marks for 141 equally spaced observation wavevectors **k**s (for a NA of 0.40), for monochromatic (λ=0.50 μm) normal incidence illumination ($\mathbf{k}\mathrm{i} = -k0\xi z$). ........... 146

**Figure 5.8.** Diagram displaying a 1D simplification of the 2D blurring method...... 147

**Figure 5.9.** Locations of demodulated scatter in **ξ**-space at $\boldsymbol{\xi} = \mathbf{k}\mathrm{s} - \mathbf{k}\mathrm{i}$ given by coloured dots, for monochromatic illumination (λ=0.50 μm) over a range of incident angles limited by a NA of 0.40 ...................................................................... 148

**Figure 5.10.** Locations of demodulated scatter in **ξ**-space at $\boldsymbol{\xi} = \mathbf{k}\mathrm{s} - \mathbf{k}\mathrm{i}$ given by coloured dots, for polychromatic illumination (from λ=0.415 μm to λ=0.628 μm) over a range of incident angles limited by a NA of 0.40 ................................................ 150

**Figure 5.11.** Magnitude of the CSI fringe spectrum for a sinusoidal surface (PV of 1.4 μm, surface wavelength of 14.8 μm) tilted at 30°.............................................. 151

**Figure 5.12.** Cross-sectional CSI signal of an optical flat, a) experimental result after BPF filtering, c) corresponding simulation of fringe............................................... 155

**Figure 5.13.** Cross section of the magnitude of the *k*-space CSI signal from measurement of an optical flat, a) experimental result and b) corresponding simulation. ................................................................................................................... 155

**Figure 5.14.** Cross-sectional CSI signal of a sinusoidal grating Rubert 543E, a) experimental result and b) corresponding simulation............................................. 156

**Figure 5.15.** Cross section of the magnitude of the *k*-space CSI signal from a sinusoidal grating Rubert 543E, a) experimental result and b) corresponding simulation. ........ 157

**Figure 5.16.** Cross-sectional CSI signal of a sinusoidal grating Rubert 528E, a) experimental result and b) corresponding simulation............................................. 157

**Figure 5.17.** Cross section of the magnitude of the *k*-space CSI signal from a sinusoidal grating Rubert 528E, a) experimental result and b) corresponding simulation. ........ 158

**Figure 5.18.** Cross-sectional CSI signal of a step height obtained from cross grating sample NPL ACG-2.1 XP01, a) experimental result, b) corresponding simulation for a step height, assuming a step inclination of 90°, and c) experimental result after removal of the out-of-plane *k*-space signal. ......................................................................... 159

**Figure 5.19.** Cross section of the magnitude of the *k*-space CSI signal from a step height found on the cross grating sample, a) experimental result, b) corresponding simulation for a step height. ........ 160

**Figure 5.20.** a) Simulated CSI signal in real space for a vee-groove as described in Table 3.1. ........ 161

**Figure 6.1.** The profile of the GR13-0305 blazed grating as measured by an AFM instrument. ........ 168

**Figure 6.2.** Diagram presenting the two measurement cases used for measurement of the blazed grating while tilted at angle $\phi$ ........ 170

**Figure 6.3.** CSI fringe generation based on a BEM scattering model. ........ 172

**Figure 6.4.** Geometry of the profile used for modelling, where the central region of each longer facet has had surface texture added digitally ........ 173

**Figure 6.5.** Topography results from a 20× lens of the roughened flat (a,b,d,e) when tilted at 30°, and (c, f) when untilted. ........ 174

**Figure 6.6.** Topography results after plane form removal from a CSI measurement of a GR13-0305 blazed grating with tilting arrangements of (a) L0, (b) L45, and (c) R45, using a 50× lens ........ 174

**Figure 6.7.** Modelling results for scattered intensity from the blazed grating shown in Figure 6.6, for the mean intensity obtained from both s- and p-polarised monochromatic illumination ........ 176

**Figure 6.8.** Modelled (left and middle column) and experimental (right column) fringes of the L case blazed grating at different tilts ........ 178

**Figure 6.9.** Modelled (left and middle column) and experimental (right column) fringes of the R case blazed grating at different tilts ........ 179

**Figure 6.10.** Visual comparison of (a) the PSF obtained from the Foil model associated with an ideal CSI instrument, and (b) modelled fringes from the BEM-CSI model near to the shorter facet for the L case blazed grating tilted at 50° ........ 180

**Figure 6.11.** Modelled fringes from the modelled blazed grating profile tilted at 50° under s-polarisation illumination in the (a-c) L case, and (d-f) the R case. ........ 182

**Figure 6.12.** Experimental fringes from the blazed grating tilted at 50° in the (a-c) L case, and (d-f) the R case. ........ 182

**Figure 6.13.** Topography estimate (coherence profile) obtained from the experimental measurement of the blazed grating tilted at 50° in (a,b) the L case, and (c,d) the R case. ........ 183

**Figure 6.14.** Diagram of the relative sizes of the blazed grating shorter facet and the instrument sampling spacing for different measurement conditions, alongside a PSF of the instrument to scale. ........................................................................................ 186

**Figure A.1**. Flow chart for the method to produce the surface transfer function (STF) and associated inverse filter ........................................................................................ 221

**Figure A.2**. Screenshot of the GUI for the loading, filtering and analysing of fringe data, to obtain STFs via method displayed in Figure A.1. ........................................ 223

**Figure A.3.** Fringe data of a measurement of a microsphere, after Gaussian spatial filtering ........................................................................................ 224

**Figure A.4.** The associated k-space form of Figure A.3, after a BPF mask has been applied to the relevant section ........................................................................ 224

# List of Tables

**Table 2.1** Categorisation of a selection of surface topography measuring methods...13
**Table 2.2** A categorisation of a selection of CSI models. ..........................................38
**Table 3.1** Specifications of the sphere measurements................................................86
**Table 3.2** Nominal (as-designed) specifications of the surfaces. ................................87
**Table 5.1** Surfaces measured and modelled for this paper.......................................153
**Table 6.1.** Instrument specification ...........................................................................167

# List of Abbreviations

Throughout this thesis abbreviations are used for certain key terms. While these abbreviations are reintroduced the first time they are used in every chapter and in the chapter summary, they are also included here for reference. Acronyms for the names of organisations and specific instruments are excluded from this list.

| | |
|---|---|
| **1D/2D/3D** | One/two/three-dimensional |
| **NA** | Numerical aperture |
| **FOV** | Field of view |
| **OPD** | Optical path difference |
| **CSI** | Coherence scanning interferometry |
| **PSI** | Phase-shifting interferometry |
| **FV** | Focus variation |
| **AFM** | Atomic force microscopy |
| **SEM** | Scanning electron microscope |
| **SNR** | Signal-to-noise ratio |
| **HWR** | Height-to-wavelength ratio |
| **SRL** | Specular reflection limit (a.k.a. NA slope limit) |
| **EM** | Electromagnetic |
| **CEM** | Computational electromagnetic |
| **BEM** | Boundary element method |
| **FEM** | Finite element method |
| **FDTD** | Finite difference time domain methods |
| **RCWA** | Rigorous-coupled wave-equation methods |
| **TE / TM** | Transverse electric/magnetic |
| **3sBSM** | 3s boundary source method |
| **EFO** | Elementary Fourier optics |

| | |
|---|---|
| **KA** | Kirchhoff approximation |
| **LED** | Light-emitting diode |
| **PZT** | Piezoelectric transducers |
| **RAM** | Random-access memory |
| **TF** | Transfer function |
| **ITF** | Instrument transfer function |
| **OTF** | Optical transfer function |
| **STF** | Surface transfer function |
| **PSF** | Point-spread function |
| **IF** | Inverse filter |
| **BPF** | Band-pass filter |
| **PV** | Peak-to-valley surface amplitude |
| **FWHM** | Full width at half maximum |
| **RMS** | Root-mean-square deviation |
| **BRDF** | Bidirectional reflectance distribution function |
| **ASD** | Angular scattered intensity distribution |
| ***k*-space**[1] | Spatial frequency domain |
| **FFT** | Fast Fourier transform |
| **DFT** | Discrete Fourier transform |
| **FDA** | Frequency-domain analysis |
| **EBPBF** | Electron beam powder bed fusion |
| **GUI** | Graphical user interface |

[1] At times in this thesis **ξ**-space is used for the spatial-frequency space of the fringes, to distinguish it from the spatial-frequency space of the wavevectors, denoted by *k*-space.

# Declaration

I, Matthew Thomas, hereby declare that this thesis is written by me, and the work presented within it a result of my own original work except where otherwise stated. Where I have consulted the published work of others attribution is always clearly given. Between the text and acknowledgments section of this thesis I have acknowledged all my main sources of help; primarily my supervisors Dr Rong Su and Prof. Richard Leach. I received guidance throughout the project from Rong and Richard, with the work presented in Chapter 3 being produced in collaboration with Rong. Contributors to the work presented in specific chapters are acknowledged in the text of the chapters and in the publications associated with each chapter, as referenced at the beginning of each chapter.

The contents of this thesis have not been submitted in whole or in part for consideration for any other degree or qualification in this, or any other university. Papers arising from the research undertaken have been published in advance of submission of this thesis with the understanding that prior publication should not prejudice the assessment of this thesis.

This thesis contains fewer than 100,000 words including appendices, the bibliography, footnotes, tables, and equations.

# Acknowledgements

I would like to thank the University of Nottingham for funding my PhD with stipend support under a Faculty of Engineering funded scholarship. I am also thankful to the University for providing a 6-month extension to the registered period of study including 12 weeks of stipend support to mitigate the impact COVID-19 had on my project. I would finally like to thank the various funding bodies who supported the production and publication of my research work, as noted in the funding section of each publication.

Over the course of my PhD and as part of the University of Nottingham's Manufacturing Metrology Team (MMT) I have been blessed with the opportunity to meet and spend time with so many fantastic people from across the world. From those who have helped me with my work to those who have supported me outside of it, there are too many to name. Nonetheless, I would still like to name a few.

I would like to thank my internal supervisors, Prof. Richard Leach and Dr Rong Su, for their support and supervision throughout. Richard has provided rapid and experienced advice whenever needed, and at times valuable pastoral support and encouragement. He has taught me to be more confident, to be proud of my successes, and to try to worry less. He has also imparted some of his rigor towards grammar and formatting, as I can frustratingly no longer avoid noticing small mistakes in much of what I read! I would never have heard about the PhD project had he not reached out to me. Rong has been essential in helping me improve my technical skills and knowledge and has consistently provided meaningful technical feedback and guidance throughout my project. While the way we approached things was often opposed and I have sometimes struggled to follow his example, I nonetheless value every lesson I have learnt. I admire his uncluttered and rational approach to efficiently producing meaningful scientific research work, and in retrospect appreciate his "tough love" in guiding me not just in learning, but on learning how to better learn. Things such as limiting scope, iteratively improving, focusing on results, knowing what you do not need to know, prioritising areas of exploration, and asking better shorter questions. More than anyone Rong has been a mentor to me and has challenged me, providing an invaluable opportunity for improvement and development, the impact of which will affect me forever.

I would like to thank my industrial supervisor Dr Peter de Groot for Zygo's industrial support, for the opportunity to visit his workplace and home, for his guidance from an industrial perspective, and for the fantastic lectures he gave us. To reach his quality of writing on topics of complexity has become a personal goal, and he has shown me what it means to really be an expert. I would like to thank Prof. Jeremy Coupland, who despite not formally being my

supervisor and despite being busy as both Head of Optical Engineering Research & Teaching and as an Associate Dean for Research at Loughborough University, still found some time over the years to help answer my technical questions. All my work has built upon or been inspired by Jeremy's work; I only regret I could not have worked more with him directly. I must also thank Dr Nikolay Nikolaev, also from Loughborough University, who in collaboration with Jeremy provided me with the two-dimensional rigorous optical scattering code essential to my project. I would also like to thank all the other researchers who have authored publications with me and collaborated with me on research work.

To my colleagues and friends from MMT, thank you for your help and good company over the years – I hope I have been able to return some of it in kind. In particular: to Adam Thompson, for introducing me to everyone on day one, befriending me, and enduring my many stupid questions; to Lewis Newton, for the conversations and good times we had living together and that we've had from that point since; to Waiel Elmadih, who started his PhD with me with the fate of forever sitting next to me, whom I talked with much and whom became my friend; to Carlos Gómez, who likewise started with me, who I almost lived with, and who was always so friendly – I am sorry I could not attend your wedding!; to Helia Hooshmand, who became a sounding board for some of my strangely written sentences, who caught typos in some equations, and who unintentionally rekindled my passion for problem solving during the monotony of write-up; and to Ifeanyichukwu Echeta, who I only really got to know thanks to COVID-19, and who helped keep my head on straight during write-up and beyond. I must also thank Chung Han Chua and Liz Birchall, who similarly helped me keep things together with their support and company, especially during the periods of lockdown where only meeting outside in small groups was allowed. I also cannot thank Kerri Lindley enough for being a ray of sunshine, being my first port of call for any administrative questions or issues and keeping the entire building ship-shape. The whole place would sink without her!

To my friends outside my PhD life, thanks for all the fun we have had and for putting up with my rambles and rants. Thanks to Cat, Jon, Catriona, and Ian; I'll really miss seeing you guys so often. Thanks to Sam, Ed, Josh, Luke, and Joe for all the jokes and games since ~2011; a decade goes by fast! Finally, thanks everyone I met at UoN's SFFA student society, including those on the committee in 2018-19 and especially including James Thackway; being able to work with you and the committee to improve the society and get to see the fruits of our labour really renewed my motivation when I needed it the most.

Finally, I cannot thank my family enough for their continued and unwavering support in all aspects of life. I could not have done this without you.

# Chapter 1: Introduction

## 1.1 Background

While the shape of manufactured parts typically dictates their function, for some parts the small-scale surface topography present on key surfaces critically determines the part's capability [1], a principle also found in nature [2]. Advanced fabrication techniques that determine the small-scale surface topography, including new kinds of tools and techniques for surface grinding, polishing, finishing, etching, and coating, can be used to manufacture parts tailored for specific applications [1,3]. The surface topography present can determine properties related to tribology, such as friction, traction, lubrication, and wear [4–6]. They can affect physical properties, including optical properties such as reflectance and thermal properties such as those involved in passive and active cooling [1]. They can affect biological properties, involved in successful integration of manufactured parts with host physiology and extending part lifetime [7,8]. They can also control certain mechanical and hydrodynamic properties of the part [1,9,10]. Examples include wear-resistant cutting tools used for steel cutting [11,12], anti-reflective glazing coatings in the automotive industry [13], antiviral surfaces to suppress the spread of COVID-19 [14], aspherical microlens arrays in freeform optics manufacture [15], and fuel flow cavitation of a fuel injector nozzle [16]. Some examples are shown in Figure 1.1.

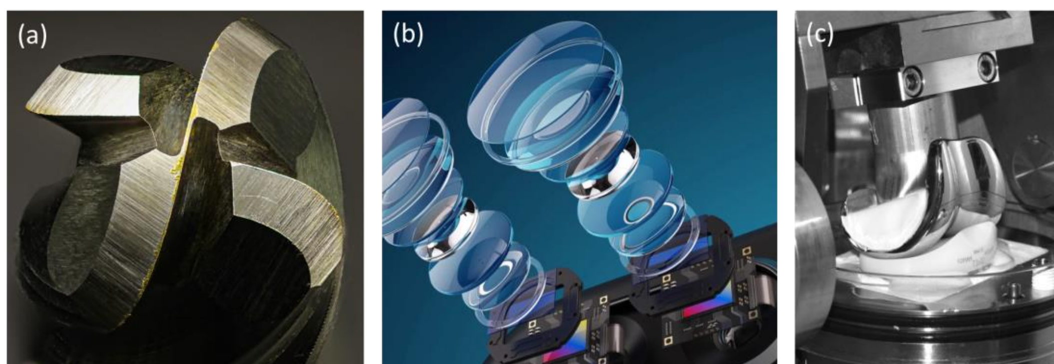


**Figure 1.1.** (a) A milling cutter tool, (b) exploded-view of aspherical microlens arrays found in smart phone cameras, and (c) total knee replacement part mounted in a wear simulator from [17]. Copyright: (a) "10 mm Ball End Milling Cutter" (https://flic.kr/p/2jgLFSm) by Tudor Barker under a CC BY-NC-SA 2.0 license. (b) Used with permission from ZYGO Corporation (AMETEK). (c) Reproduced from [17] with permission from Prof. Philippe Kretzer and Elsevier via CCC RightsLink publisher request (No. 5310851305781).

To provide comprehensive information about a surface's topography, or to conduct quality inspection of surface-engineered parts, surface topography measurement methods are required [18]. Compared to traditional mechanical contact methods, optical techniques have many advantages, such as their non-contact nature and the ability of areal optical methods to rapidly capture two-dimensional (2D) height information over an area of the surface [19,20]. Using interferometry for certain surfaces can even provide height data with sub-nanometre noise levels [21]. However, optical methods are typically more complex than contact methods due to the difficult-to-model physics of the light-surface interaction and the optics of the instrument. The interaction between the instrument and the sample results in the instrument accuracy being partially dependent on the measured surface itself, connected to the distribution of spatial frequencies that comprise the surface and the surface slopes present.

Engineered functional surfaces often feature varying slopes on macro- and micro-scales. For a mirror-like surface that only reflects light in the specular direction, the highest surface slope that can be measured by a far-field three-dimensional (3D) optical surface measuring instrument is determined by the numerical aperture (NA) of the objective lens. Light that is specularly reflected by a surface that has a slope larger than one-half of the maximum reflected ray angle ($\theta_{NA} = \sin^{-1} A_n$, where $A_n$ is the NA) will fall outside of the acceptance cone of the instrument and not be captured [19], as shown in Figure 1.2. However, many surfaces are not mirror-like and produce a distribution of scatter when illuminated (see Figure 1.3); under the Abbe theory of image formation, it is the capture of this scatter that provides image contrast [22,23]. More information about the object being measured can be recorded in the image if more scattering/diffraction orders can be captured. The limited NA captures only a portion of the scatter, which determines the upper limit to both the resolution of the instrument and to the surface spatial frequencies transferred by the instrument. As a large amount of the scatter is still in the specular direction for many surfaces, measurement of surfaces tilted at angles greater than $\theta_{NA}$ can be challenging, referred to as the specular NA slope limit or specular reflection limit (SRL).

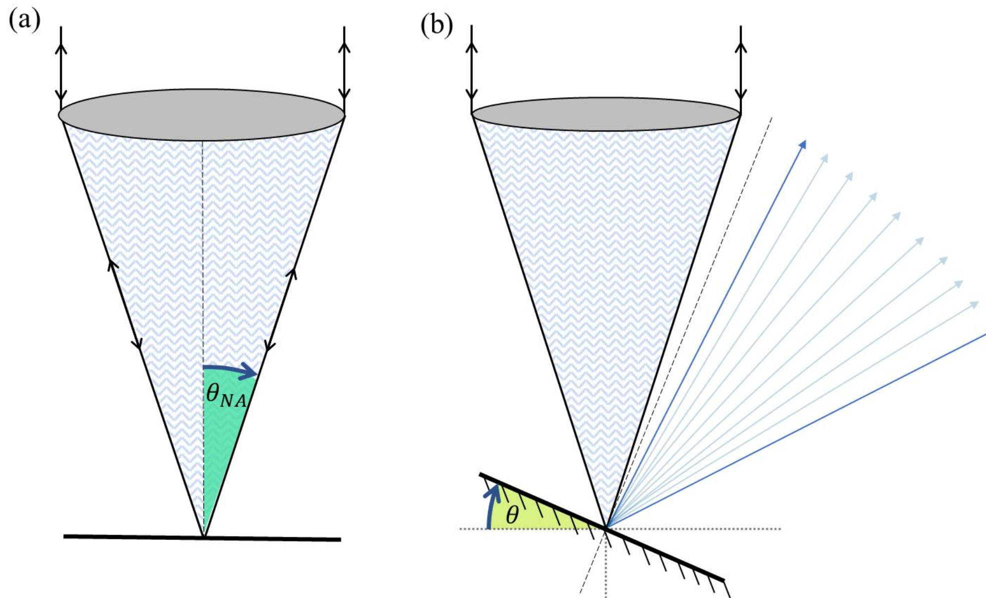


**Figure 1.2.** Diagram of the measurement of a mirror-like surface which only specularly reflects, shown (a) untilted (surface normal parallel to the optical axis) and (b) tilted at angle $\theta$. In (b) it is the case that surface slope $\theta \geq \theta_{NA}$, causing all the specular scatter to be lost.

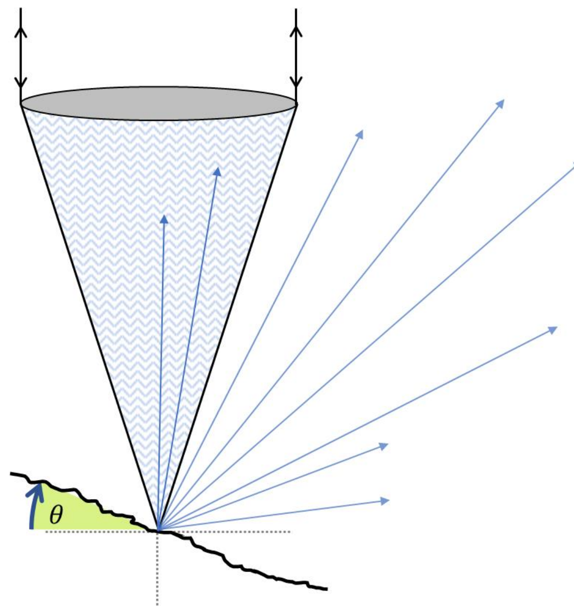


**Figure 1.3.** Diagram of the measurement of a rough surface which produces some specular and diffuse scatter, with similar arrangement to Figure 1.2(b).

Using optical surface topography measuring instruments, information from tilted or steep surfaces beyond the specular limit can naturally be acquired by making the surfaces less steep (relative to the optical axis of the instrument). This can be done by adjusting or making use of multiple viewing angles with respect to the sample, through

the use of tilt or multi-axes stages [24–28], rotating both the sample and the sensor [29], or making use of multiple sensors [30,31]. Unfortunately, such approaches are comparatively expensive, due to the additional moving parts (or additional sensors), can be slower (moving stage and making multiple measurements), require an accurate combination of measurement data, and have increased difficulty in retaining stability during a measurement.

Nonetheless, various instruments are capable of imaging and obtaining topography information from surfaces with slope angles well outside the specular acceptance cone, without repositioning the sample or instrument. This capability is attributed to the capture and detection of diffuse and back-scattered light from the microstructures found on the surface slopes [32–35], which is possible due to recent advances in instrument technology and design, including baseline sensitivity. Technology improvements for a coherence scanning interferometry (CSI) instrument include, e.g. dynamic noise reduction through signal oversampling, and high dynamic range measurement [35–37]. For a focus variation instrument, improvements include, e.g. the use of ring light illumination to essentially increase the illumination NA [33,38].

Typically, image formation from surface slopes that are steep enough that specular reflections are lost, obtain surface information with a low signal-to-noise ratio (SNR), which can lead to non-measured points [19,39] and high uncertainty. There is currently a lack of understanding about the instrument response to surfaces with steep slopes outside the NA cone. In particular, it is unclear over what surface spatial frequencies accurately reported surface texture and fine surface-feature details can be expected. The reliability of topography from these regions is unknown. Through theory, instrument modelling and experiment, measurement of steep surface slopes are investigated in this thesis. This is covered in more detail in the state-of-the-art review in section 2.6, and investigated in Chapter 6.

Understanding the optical and topography response through both experiment and modelling is also of great value towards understanding measurement uncertainty, in the context of measurement traceability and calibration infrastructure for optical topography instruments. Accurate measurement for any instrument requires traceability, i.e., an unbroken series of calibrations that relate through comparison the measurement(s) of an instrument to stated references, such as national or international

standards. It is essential that each comparison have stated uncertainties for the comparison to be meaningful: traceability and uncertainty are inseparable [40]. However, uncertainty evaluation is difficult for optical instruments due to the complexity of the measurement process, especially for complex surfaces [32]. Calibration by material measures, such as a step height, while calibrating the scales of the instrument, alone reveals little about how the instrument responds to different slope angles, spatial frequencies, or surface reflectivities [41–43].

The International Organization for Standardization (ISO) have published numerous specification standards related to areal topography measurement methods under ISO 25178, outlined in Table 1 of [41]. This includes ISO 25178-600 [44], titled “Nominal characteristics of areal surface topography instruments”, which covers the so-called metrological characteristics that are common (instrument-independent) across the different areal topography methods [45]. Under the ISO 25178 framework, through the quantitative determination of several metrological characteristics, each comprised of one or more underlying influence factors that affect the uncertainty, an evaluation of measurement uncertainty can in principle be obtained. The metrological characteristic that captures all the influence factors of the measurement uncertainty not already captured by other metrological characteristics is topography fidelity, which includes the majority of the surface-dependent errors such as surface slope-dependent errors [45]. Through understanding the results of optical topography measurement methods for complex and steep surfaces, the design of material measures for calibration of topography fidelity can in principle be better specified by making use of accurate modelling prior to artefact manufacture. Note that the ISO document that describes calibration and verification procedures using metrological characteristics is still under-development and subject to change [46].

In addition to the metrological characteristic framework, an alternative approach to measurement uncertainty evaluation that considers the results of a virtual instrument can be used [45,47], complimentary to the direct use of metrological characteristics. Through a stochastic method such as a Monte Carlo method, where for each influence factor appropriate probability distributions have been set, a virtual instrument can produce results across the range of input values and from these results a combined uncertainty can in principle be obtained [40,48]. In this thesis, for a specific optical measurement method an instrument model that accounts for multiple scattering and can

handle surface undercuts is developed and presented. Further development would allow for evaluating measurement uncertainty through stochastic virtual instrument modelling, even for complex surfaces.

## 1.2 Aims and objectives

The aim of the work in this thesis is to advance methods that enable extending the range of surface slopes that can be reliably measured by optical surface topography measurement, and to investigate the reliability of the current capability. This is to be done without altering instrument hardware or the use of rotation stages. The work focuses on topography measurement using a CSI instrument, and investigation of its response through the development and use of instrument modelling. Through the development of instrument models, the current understanding of topography errors and methods of evaluating measurement uncertainty can be improved. This work was inspired by a paper by Coupland et al. [49], which suggests that surface topography estimation methods for CSI could be improved through the use of rigorous CSI modelling. By iteratively adjusting a virtual surface, initially obtained from a priori manufacturing data, until differences between the experimental and modelled fringes are minimised, the surface topography can be obtained even for vertical surfaces or for surfaces that multiple scatter strongly when measured.

To pursue this aim, the following objectives are considered:

1. Characterise an instrument's linear transfer characteristics to allow for compensating the effect of lens aberration, to enhance signal quality and reduce errors that occur where the surface slope is close to the SRL of the objective lens used, as defined in sections 1.1 and 2.6.
2. Develop a computational CSI model to generate accurate fringes for complex surfaces which may contain slopes beyond the SRL. Experimental verification and demonstration of the model's non-linear capability, e.g., accurately predicting multiple scattering, is required. Non-linear models are defined and described in section 2.4.3.
3. Demonstrate the effect of surface slope on CSI fringes and topography, including slopes beyond the SRL, and improve the current understanding of the effect using both experimental measurement and the developed non-linear CSI model.

As part of following these objectives, publications were produced and are referred to in the thesis at the beginning of each chapter when relevant. A full list of publications by the author of this thesis can be seen at the end of the thesis prior to the appendices (pg. 219).

## 1.3 Novelty

In this thesis, error correction of fringe data through instrument characterisation and linear modelling is first described. When measuring complex and rough surfaces, the errors in CSI can be several orders of magnitude larger than when measuring relatively flat and smooth surfaces. So far it appears that all previous error correction methods attempt to amend the measured surface topography, where the topography is derived from the fringe data. For the first time, an error correction method is demonstrated that acts on the raw fringe data without any digital data processing, and the method is developed into a practical solution for a state-of-the-art commercial CSI system. The error correction requires accurate information about the 3D surface transfer function of the CSI system. The first experimental verification of the characterisation of the 3D surface transfer function is provided by using two types of precision spheres, through comparison of measurements of these spheres to modelled fringes. Instrument manufacturers have shown interest in integrating this method into commercial CSI systems.

Following the linear modelling methods for CSI, non-linear modelling methods are developed. Through advanced modelling of a CSI instrument and comparison to experiment, the instrument's capability is investigated for the measurement of steep (or tilted) complex surfaces. To some degree, the capability of any optical surface topography instrument is also demonstrated. Of special interest is the effect on the interference signal and measured topography when tilting the object at angles larger than the SRL of the instrument. Traditionally, information could not be collected from such steep surfaces, but often modern instruments still collect scatter, attributed to small-scale surface topography present along the steep surface. There is a lack of understanding in the literature about the reliability of optical topography produced from these surfaces, which this thesis helps to address. Filling this gap is clearly of value and such work has high industrial impact to instrument manufacturers and users: by providing techniques and tools that can accurately predict the response of the

instrument, the reliability of proposed surface measurement configurations can be investigated in advance and measurement parameters optimised for the parts in question. The need to rapidly measure surface topography in industry and the value it brings has already been discussed: the functional properties of functional surfaces are affected significantly by their topographies and can have complex geometries and high surface slopes while needing measurement for quality inspection, e.g. the fuel cavitation of fuel injector nozzles [1,16]. For the first time to the author's knowledge both fringe data and resulting height estimates are used to illustrate the capabilities and limitations of interference microscopy to measure beyond the SRL, accompanied with results from a suitable modelling method.

The CSI model used, based on a rigorous boundary element method (BEM), has been presented previously in the following publications [50–52], and is to the author's knowledge the only CSI model based on a BEM optical scattering model. Modelling results are verified directly with experimental measurements. For accurately handling arbitrary surface topography, BEMs are understood to be faster in principle than many alternative computational electromagnetic techniques, such as finite element methods (FEM), with more details given in section 2.4.3.

## 1.4 Thesis structure

In Chapter 1, the motivation of the thesis alongside a description of the problem it tackles is presented, the aims and objectives selected to investigate and address the problem are outlined, and the novelty of the chosen approach is stated.

In Chapter 2, a review of relevant literature is presented, and an overview on appropriate background material is made. This covers topics such as metrology; surface topography metrology; the principles, instrument design, and capability of CSI; linear and non-linear modelling of CSI; and topography measurement of steep surfaces.

In Chapter 3, through characterisation of a CSI instrument's capability to transfer surface topography, the effect of lens aberration on topography results at steeper regions is mitigated. The characterisation follows an established 3D linear shift-invariant theory for optical imaging, called the "foil model"; an overview of this theory and how it is applied to compensate for aberrations is presented here.

In Chapter 4, a rigorous BEM-based optical scattering model is verified through experiment and theory. The theory, implementation, and limitations of the model are outlined here.

In Chapter 5, the theory and implementation of a CSI model that uses this BEM model is described, and the model is verified against experimental results for both a range of gratings and a step height. Evidence of multiple scatter model capability is also shown for a vee-groove.

In Chapter 6, measurements of steeply-sloped surfaces beyond the specular NA limit are presented, with experimental measurements and BEM-CSI modelling results compared. With a focus on blazed grating measurement, the effect of surface tilt on the CSI fringes and resulting topography is investigated.

In Chapter 7, in the context of the aims and objectives set out above, the conclusions of the thesis are stated, and the possible future work discussed.

# Chapter 2: Background & State of the art

In this chapter, the state of the art relevant to this thesis is discussed, and where appropriate the accompanying background presented. The chapter begins with a brief overview on metrology and specifically surface topography metrology, which is followed by both the background and state of the art for coherence scanning interferometry (CSI), with a focus on instrument principles and capability. A review of CSI models in the literature is then given, to provide context for the modelling work presented in Chapter 3, Chapter 4, and Chapter 5, and why a non-linear model is developed for verification. An introduction to scalar scattering and imaging theory is also given, referenced in Chapter 3 and Chapter 5. Finally, the state-of-the-art on the capability of optical surface topography measurement methods for measurement of steep and tilted surfaces is reviewed, with a focus on CSI measurement and the effect on the measured topography when tilting the measured object at angles larger than the specular reflection slope limit (SRL) of the instrument, determined by the instrument's numerical aperture (NA). This is investigated later in Chapter 6.

## 2.1 Metrology

Metrology is the science of measurement, encompassing the definition and realisation of units of measurement and the traceability chain that links measurements to these realisations, and is essential for manufacturing [53]. To quantify the otherwise qualitative difference between something short and something long, a standard of length is required to use as a unit for measurements. The metre is defined by the distance travelled by light in a vacuum in 1/299,792,458 of a second[2], and from this any other measured lengths can simply be expressed as a scaling of this 'unit' length of 1 m. Using the same measurement units as others allows measurements and designs to be effectively communicated and worked on separately, so that different groups of people can accurately manufacture the same sized part or parts designed to fit together. Not following the same units when collaborating can lead to costly or even dangerous

[2] This definition, by definition, fixes the speed of light in vacuum at exactly 299,792,458 metres per second

incidents [54]. The units now used in almost all developed countries are the International System of Units (SI units) [55], which define base metric scaling units for distinct measurable quantities: time, length, mass, electric current, thermodynamic temperature, amount of substance, and luminous intensity. For example, time, length, and mass are given units of the second (s), metre (m), and kilogram (kg) respectively. Derived units are also defined in the SI units, e.g. frequency, force, and capacitance are given units of hertz (Hz), newton (N), and farad (F) respectively. The derived units can each be expressed in terms of combinations of the base units, such as $[N] = [kg\ m\ s^{-2}]$.

Once the definition of a unit can be realised, accurate artefacts (known as transfer artefacts) can be produced. These artefacts are more easily transported than the instruments that calibrated them and realised the unit, and are therefore used to calibrate measurement devices or to produce additional artefacts in other locations; this chain of comparisons that use calibration artefacts to link an instrument's measuring scale back to the realisation of the definition of a unit is called traceability [56]. To calibrate an instrument and confirm its measurements are 'correct', we compare it against a more accurate instrument via measurement of such an artefact. To ensure the calibration is meaningful and to parameterise what is meant by "more accurate", it is necessary for all measurements to have stated uncertainties [56,57]. Uncertainty is described in more detail in the context of virtual instruments and their significance to metrology and industry in section 1.1, with methods of uncertainty calculation described in [40,48], and an introduction to uncertainty as whole described elsewhere [58,59].

## 2.2 Surface metrology

Information about how a surface was manufactured or processed can also be seen 'fingerprinted' as part of the surface topography [60], and surface topography plays an important role in determining surface functional aspects such as friction, adhesion lubrication and wear [6,61,62]. Advanced production of surfaces with small scale form and height tolerances requires the ability to accurately measure these surface topographies as part of verifying the manufacturing process and the suitability of the parts. More information on this can be found in section 1.1. Surface metrology is the branch of metrology involved in obtaining this kind of information about a surface, typically involving the measurement of small surface features and information on surface texture, i.e., concerning topography measurement.

Surface topography measuring instruments may be separated into three broad classes as specified by ISO 25178 part 6 (2010) [63]: line profiling, areal topography measuring, and area-integrating. Line profiling methods produce a topographic profile $z(x)$, areal topography methods produce topographic images $z(x,y)$, and area-integrating methods can produce numerical results that depend on area-integrating properties of the surface via measurement of a representative area. An overview of the categorisation of several surface topography measuring methods is given in Table 2.1. The categorisation presented in Table 2.1 has been changed slightly from that given in ISO 25178 part 6 [63], as in the ISO standard the majority of the measurement methods considered are given as areal topography methods, even when they obtain topography by combing multiple parallel profiles. Only a few methods are considered as line-profiling, half of which are still also categorised as areal-topography methods; at the same time, no clear distinction is made between full-field areal-topography measurement methods and those that rely on combining sequential profiles, despite significant differences in measurement time.

**Table 2.1** Categorisation of a selection of surface topography measuring methods.

| **Line-profiling methods** (including areal methods that rely on taking sequential profiles) | **Areal-topography methods** (full-field measurement) | **Area-integrating methods** |
|---|---|---|
| Contact stylus scanning | Imaging confocal microscopy | Total integrated scatter |
| Chromatic confocal probes | Focus variation microscopy | Angle-resolved scatter |
| Point autofocus profiling | Phase-shifting interferometry | |
| Phase-shifting interferometer (initial designs [64]) | Coherence scanning interferometry | |

Stylus type instruments typically consist of a stylus in contact with the surface travelling across the surface in a line (profile), where the stylus's vertical movements are recorded and used to obtain the topographic profile and describe the surface texture. While these instruments can act in an areal scanning mode, measurement can be time consuming due to the number of profiles that must be taken to produce high resolution topographic images [20], as detailed in the following paragraph.

Stylus instruments are common for measuring surface texture and are trusted due to their relative simplicity and long-term usage in the industry [20,65]. However, they do suffer from a few disadvantages. By taking only profile measurements, i.e. measurement along a line, the instrument captures surface height from along only a

small proportion of the surface, from which surface parameters that characterise the surface texture can be derived. When a profile measurement of a functional surface is taken, it is possible that problems with the surface that lead to part failure can remain undetected, such as when the measurement axis does not intersect the surface defect [26]. As discussed above, measuring an areal topography is possible but time consuming. While measurement of a 1 mm profile sampled 1000 times may take only 10 s to measure (0.1 mm $s^{-1}$), measurement of a square grid of points for an areal measurement requires measurement of 1,000,000 points which can take several hours. The force applied to the surface during a measurement as part of the tactile (i.e. contact) nature of the instrument can also cause damage to the surface, and the finite size of the contacting tip acts as a filter for higher spatial frequency surface features [20]. In comparison, optical instruments can typically capture surface data from multiple positions simultaneously and with no contact with the surface.

Optical instruments can be placed into two main groups: those that measure surface topography (profile or areal methods), and those that infer statistical parameters of the surface from the distribution of scattered light (area-integrating methods). Both approaches rely on the capture and analysis of optical far-field scatter. Scanning optical techniques typically scan a light spot across a surface to obtain topographical profiles; areal optical techniques measure the surface over a field of view (FOV), typically moving the focus by scanning vertically over the surface and taking full-field measurements to produce topographic images; and area-integrating methods typically illuminate a surface and analyse the distribution of scattered light to obtain statistical parameters [66]. A brief review of some of the common optical instruments and their measurement methods follows, with a more complete list found in ISO 25178 part 6 [63] and the instruments discussed in detail in [19].

Both point autofocus profiling and chromatic confocal probes operate in a similar way to a stylus instrument, obtaining the surface height at specific points on a surface one point at a time and moving a probe along the surface to form profiles. For point autofocus profiling, the point of focus for a laser beam at some coordinate is found automatically through a scanning process to determine the surface height [67]. Chromatic confocal probes in contrast require no vertical scanning, and instead detect height changes by the change in the peak of the spectral response focussed on the

sensor [68]. Both techniques obtain the surface height at a single position of the surface; by using motion stages both profile and areal surface height data can be obtained.

Focus variation (FV) instruments use focus to ascertain the height of a surface but do so over the entire FOV by combining the vertical scanning of a microscope system with a small depth of focus. By continuously capturing image data as the instrument is vertically scanned, each region of the surface is captured in focus; analysing the variation of focus across the stack of image data for each imaged point allows for true colour full depth of field topographical images to be produced [69,70]. Imaging confocal microscopy similarly obtains a stack of areal image data; due to the instrument's confocal aperture each image captured contains very little light not originating from the focal plane of the instrument, which is used to obtain surface height data [71]. Phase-shifting interferometry (PSI) uses an interferometric objective lens to split the light into two parts, illuminating both the surface and a reference surface. While this reference surface is typically a mirror, other options for the surface include a transmission flat or a sphere. By using a narrow-band source for illumination, the scattered light from the surface and reference surface interferes and forms fringes. By introducing several known shifts between the optical path to the measured surface and the optical path to the reference surface, changes in the fringe pattern are produced [72]. The ensuing phase map, constructed from the ensemble of shifted interferograms [73], can in general be analysed to deduce the vertical height data.

However, unambiguous height measurement using PSI is limited to a range of one fringe, or approximately half the central wavelength of the light source. This is because the phase information is wrapped [72], making larger changes in height indistinguishable from smaller changes, i.e. $2\pi$ ambiguities. While phase unwrapping methods can allow for measurements of surfaces with overall height variations greater than this distance, local changes must remain small for these methods to remain accurate. Instruments therefore usual require that adjacent points on a surface have a height difference of less than $\lambda/4$, for illumination wavelength $\lambda$. With a similar design, coherence scanning interferometry (CSI) also uses an interferometric microscope objective and relies on the interference of light. However, the use of low-coherence broadband illumination localises the fringe pattern, removing the fringe order ambiguity and allowing for the measurement of rougher surfaces. A review on selected

topics in interferometric optical metrology, including discussion on PSI and CSI, can be found elsewhere [27].

CSI is specifically chosen for this thesis for further investigation into its steep slope capability. Because the steep slope problem has a wide scope, it is difficult to investigate without considering a specific measurement method, especially if development of a rigorous instrument model is desired; it is not feasible to investigate multiple measurement methods in parallel. The measurement method CSI is chosen over alternative methods for several reasons: CSI's methods of surface height estimation rely on interferometric information such as coherence and phase and are well defined; the interferometric nature of CSI provides instruments with high accuracy height measurements to a high precision for several surfaces; recent publications present an apparent high capability of CSI instruments for steep slope measurement for certain surfaces, but the reliability of the results and the range of applicable surfaces are not entirely understood [35,36]; and because work on linear (non-rigorous) modelling of CSI instruments had already been undertaken by colleagues [74]. An overview on CSI including a more detailed description of its principles and operation is made in section 2.3, a summary and categorisation of existing CSI models including linear and rigorous modelling is made in section 2.4, and an introduction to the slope measurement problem for optical surface topography instruments is given in section 2.6. One linear method of modelling CSI is discussed in Chapter 3, and a non-linear rigorous method is discussed in Chapter 5.

It is possible to apply summary statistics to these topographic profiles and topographic images, characterising a particular aspect of the surface by a single quantitative value. These are especially useful for surfaces textures that are relatively homogeneous across the overall surface, e.g., allowing for simple comparison of the texture of differently turned surfaces [75]. There are a wide variety of profile and areal surface texture parameters suited for emphasising and characterising slightly different surface texture properties; perhaps too many than is useful [76,77]. The most well-known profile parameters begin with the letter R, while areal parameters typically begin with the letter S. In this thesis the root mean square height $Sq$ is used at times to parameterise the roughness of a surface; taking the $Sq$ of a surface area is a simple extension to taking the $Rq$ of a surface profile. The $Sq$ gives a measure of the "deviation" of the surface from a perfectly flat plane in the same way that the standard deviation is a measure of

the dispersion of a set of values away from the mean value. Other common parameters include *Sa*, the arithmetic mean height, and *Sz*, the maximum surface height (from highest peak to lowest trough).

All parameters should be calculated after appropriate filtering of the measured surface has been performed: always including the removal of short-scale components associated with the instrument or environmental noise and including the removal of a nominal surface shape or form. In addition, a low-pass filter or high-pass filter can be applied before parameter calculation to select the band of spatial frequencies from which the parameters are calculated from; it is therefore essential that when the parameters are calculated and presented that the filters used in the calculation are also stated. A more detailed discussion about profile and areal surface texture parameters and their filtering requirements is beyond the scope of this thesis. The majority of these parameters and the required filtering processes are defined in the ISO documents for profile measurements [78] and areal measurements [79], and are also described in [80,81], with further detail for areal parameters given in [82].

## 2.3 Coherence scanning interferometry

CSI is an interferometric surface topography measurement method, defined in ISO 25178-604:2013 §2.5.1 as a "surface topography measurement method wherein the localisation of interference fringes during a scan of optical path length provides a means to determine a surface topography map" [83]. The term CSI collates older and more specific terms that share the basic functional principles of CSI; a list of alternative terms that relate to the definition of CSI can be seen in Table 3 of [83], and a list of recognised terms from technical, patent or commercial literature can be found in Table 9.1 of [84]. CSI primarily encompasses instruments with spectrally broadband and spatially extended light sources, wherein the limited coherence length of the illumination source leads to the localisation of the fringes. One of the more prevalent terms in older literature for CSI is "white light interferometry" (WLI) [49,85,86], or sometimes "scanning white light interferometry" (SWLI) [49,87,88].

As described in section 2 of [89] and in [90], WLI has a long history. In 1665, Robert Hooke observed the variation of white light interference patterns with the different thicknesses of thin plates of muscovite (common mica or potash mica) [91], even before Isaac Newton demonstrated that white light is comprised of different colours [92]

(which Hooke disputed [93]). An article on using interferometry for metrology, including using white light, is also discussed by Albert Michelson in 1893 [94]. However, it took a long time for machine technology, electronics and precision mechanics to improve to a level where automated measurement devices utilising these principles could be realised (such as in [95]), with earlier interferometers simply being converted conventional microscopes via a change of objective [96]. It took until around 1990 for what would now be recognised as CSI to be applied to profilometry, used for measuring surface topography [97–99]. More recent improvements in computer technology, such as processing power and random-access memory (RAM) capacity, have allowed for considerably sizeable arrays of signal data to be taken and rapidly processed by an instrument. Even in 1996 where sets of 4MB data arrays required what was then a significant memory storage capacity, memory was getting cheaper fast enough to stimulate renewed interest in WLI [85][3]. The incorporation of digital instrumentation for CSI was further assisted by development of computationally efficient theoretical signal models [101]. CSI instruments' uses are varied: CSI instruments have been shown to be capable as a flexible measurement instrument for in-line metrology for semiconductor manufacturing [102]; can be used for measuring silicon photovoltaic cells over a wide range using stitching, while handling thin and thick film thickness [103]; can be used to measure steep-surface fuel injection nozzles for maintaining quality control [104]; and can be used to fingerprint manufacturing processes used via measurement of surface texture [60]. More examples are given in a recent review [105].

The following subsections are primarily background on CSI. Section 2.3.5 focuses on the current capability of CSI instruments and is of some value even to the familiar reader, with some aspects directly connected to the topic of outside-NA measurement discussed in section 2.6.

### 2.3.1 Principles of CSI

Described simply, CSI is a technique that can measure how an object's surface topography varies by utilising the interference of light. In the same way as a Michelson interferometer, the light amplitude is divided into two beams by a beam splitter, and

---

[3] In 1995 costs for RAM were roughly \$30 per MB, while in 2021 they are roughly \$0.003 per MB (\$3.07 per GB), smaller by a factor of $10^4$ [100].

these two beams separate and travel to the object's surface and a reference surface respectively. The light that scatters from the object's surface and from the reference surface are collected and recombined, leading them to interfere at the image plane. The intensity recorded by each imaging pixel due to this interference is determined by the group-velocity optical path difference (OPD) between these two beams for some region of the surface. A scan of the measuring instrument along the axial direction changes this OPD by bringing the sample closer or further away from the objective lens of the instrument, resulting in each pixel's intensity varying up and down, mapping out a fringe pattern. This fringe pattern is localised around the position of zero OPD due to the use of the broadband illumination source and/or the illumination source's spatial extent, allowing for the height of the surface imaged by each pixel to be determined from both phase and coherence information. The use of coherence information is an improvement over PSI, which only has access to phase information.

### Basics of interferometry – the two-beam interferometer

As an interferometric device, CSI relies on the wave phenomena known as interference. This is the phenomenon where two waves that pass through each other "superpose", producing a wave with an amplitude larger or smaller than the original wave, i.e. constructive and destructive interference. The amplitude $\Psi_{\mathrm{T}}$ where the waves overlap is given by the (vector) sum of the amplitudes of the individual waves at that point, due to the principle of superposition:

$$\Psi_{\mathrm{T}} = \Psi_1 + \Psi_2. \tag{2-1}$$

A monochromatic electromagnetic (EM) plane wave that has propagated over distance $z_j$ can be described by a cosine function

$$\Psi_j = A_j \cos\left(kz_j - \omega t\right), \tag{2-2}$$

where $A_j$ is the maximum amplitude of the wave, the angular wavenumber $k$ is a function of wavelength $\lambda$ given by $k = 2\pi/\lambda$, $\omega$ is the angular wavenumber given by $\omega = 2\pi f$ for wave frequency $f$, and $t$ is time. The rate at which the crest of this plane wave propagates, i.e. the phase velocity, is given by $v_p = \omega/k$, which can be seen readily from Eq. (2-2).Note that the arbitrary phase offset $\phi_j$ that is often included has been left out for simplicity.

Eq. (2-2) can conveniently be described as the real part of a complex function, such that

$$\Psi_j = \Re\{A_j e^{ikz_j} e^{-i\omega t}\} = \Re\{U_j e^{-i\omega t}\}, \tag{2-3}$$

where $i = \sqrt{-1}$ is the imaginary number, $\Re\{\ \}$ denotes taking the real part of a complex number, and the complex wave amplitude $U_j(z_j)$ is defined, given by the phasor $U_j = A_j e^{ikz_j}$, where the time and position dependency are separated into two terms. This formulation is convenient because operations on the electric field $\Psi_j$ that are linear end up operating directly on the complex amplitude $U(z_j)$; due to this, the expression for taking the real part is sometimes omitted.

The intensity of light $I$ at the detector, defined as the mean rate of energy flow per unit area, can be shown to be related to the complex amplitude of a single wave by

$$I_j = |U_j|^2, \tag{2-4}$$

where $|\ \ |^2$ is the absolute square, and the associated scaling constant and the vector aspects of energy flow have both been omitted for clarity [106]. Let us then consider two plane waves $\Psi_1$ and $\Psi_2$ with the same polarisation, which have complex amplitudes $U_1(z_1)$ and $U_2(z_2)$ at the detector, having travelled distances $z_1$ and $z_2$ respectively to reach it. It is assumed that the two paths taken have the same optical properties such that only the path difference, $\Delta z = z_2 - z_1$ need be considered. The intensity of light $I$ at the detector, due to the principle of superposition, can be shown to be related to these two complex amplitudes by

$$I = |U_1 + U_2|^2 = |U_1|^2 + |U_2|^2 + 2|U_1||U_2|\cos(k\Delta z)\,, \tag{2-5}$$

which can also be expressed in terms of either the waves' maximum amplitudes $A_j$, i.e., the norms (magnitudes) of the phasors

$$I = A_1^2 + A_2^2 + 2A_1A_2\cos(k\Delta z), \tag{2-6}$$

or by the expected intensity of each independent beam $I_j$ by using Eq. (2-4), given by

$$I = I_1 + I_2 + 2\sqrt{I_1 I_2}\cos(k\Delta z). \tag{2-7}$$

When $I_1$ and $I_2$ are equal, Eq. (2-7) simplifies further to

$$I = 2I_1(1 + \cos(k\Delta z)) = 4I_1\cos^2(k\Delta z/2)\,. \tag{2-8}$$

From Eq. (2-7), it is clear that small variations in path difference $\Delta z$ map out a fringe pattern for the measured intensity at the detector.

The description of the wave propagation can also be extended by considering the waves travelling through a homogeneous media of refractive index $n$. When travelling through a vacuum, the phase velocity is equal to the speed of light in a vacuum $c$, i.e., $v_p = c$, but when travelling through a material like air or glass, the phase velocity is reduced, such that the refractive index is (by definition) given by $n = c/v_p$. As the frequency $f$ (and therefore angular frequency $\omega$) of the light must remain constant when light travels from one media to another, such as from a vacuum to glass, the reduced phase velocity must be accounted for by a reduction in the wavelength of the light. Therefore, the wavelength $\lambda$ can be made a function of vacuum wavelength $\lambda_0$ and refractive index $n$, where $\lambda = \lambda_0/n$, such that the wavenumber is given by $k = 2\pi n/\lambda_0$. Then, the variation of the fringe pattern can be better described as being based on the OPD $n\Delta z$.

An in-depth derivation for the expression for the interference of two monochromatic waves which properly treats the waves as vector quantities can be found in Born and Wolf [106,107], which also rigorously explores interference with partially coherent light, including that from spatially extended sources [108]. A detailed treatment of the coherence of extended sources and partial coherence under statistical optics is given by Goodman [109].

### Optical principles of CSI

The use of a broadband light source, potentially one that is also spatially extended, results in the short coherence length of the light. This in turn localises the fringes around the point of zero OPD, the so-called “stationary phase position” [89], with an envelope width that scales with coherence length. The resulting fringe pattern can be considered to be comprised of an incoherent superposition of many independent fringe patterns, each formed by a specific wavelength of light within the broadband light source [101,110]. Such a superposition causes the fringes to destructively interfere everywhere except near the point of zero OPD, forming the interferogram around this location, i.e., the localised fringes. This is shown in Figure 2.1. In a general sense, the localisation is a consequence of the fringes unavoidably containing spatial frequency content related directly to the illumination spectrum, and therefore the extent of the real space fringes scales inversely with that of the illumination spectrum. For example, a

single wavelength laser (monochromatic) produces fringes across all space, while a broadband source limits the extent of the fringes. Why this occurs can be understood through the results and theory of a simple model, presented in section 2.4.1.

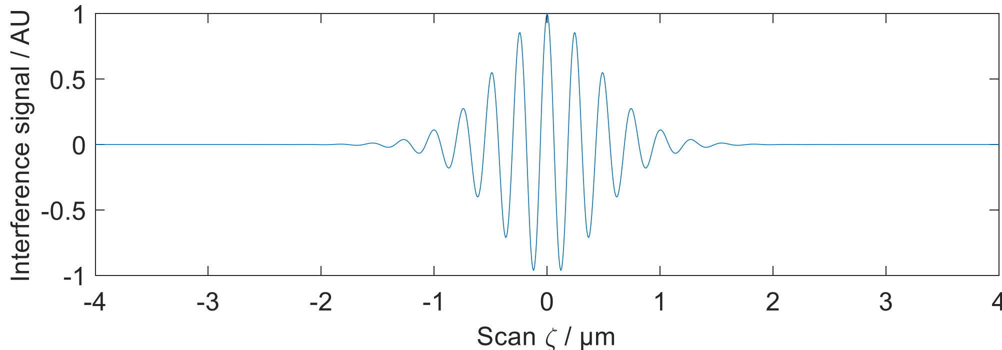


**Figure 2.1**. Modelled interferogram using a simple model based on that in [101] and described in section 2.4.

CSI actively utilises this property of fringe localisation, using the localisation of the amplitude modulated fringes, i.e., using the fringe contrast, in order to derive the height of the object at each point imaged by the detector pixels. While phase information is also used to calculate the topography, being able to utilise the localisation of the fringes allows CSI to avoid $2\pi$ ambiguity errors common in other types of coherent interferometry, such as PSI, resulting in it being better suited for scanning rough surfaces and large steps. The process of height estimation is described in section 2.3.4, while information about surface suitability and instrument capability is discussed further in section 2.3.5.

With the exception of the interferometric elements, the instrument images in the same way as a widefield optical microscope and follows the same overall design. Information on microscope imaging is given in [111], and information on microscopy in general in [112].

## 2.3.2 Instrument design

CSI encompasses a variety of different design approaches that utilise localised fringes to acquire topographical information, with examples of three very different designs described in [86]. The device used in this project was the ZYGO NewView 8300 CSI system [113], and later replaced by the Nexview NX2 [114], both of which mostly follow the common vertical scanning interferometer design schematically displayed in Figure 2.2 (based on figures in the literature including [84,105,110]). As stated earlier,

all interferometric microscope systems require the replacement of a regular microscope's primary objective with an interferometric objective, within which a beam splitter and reference surface must be present. It is the combination of the reference beams (which reflect from the reference surface) and the object beams (which reflect from the object being measured) that produce interference at the camera detector as the OPD of these beams varies.

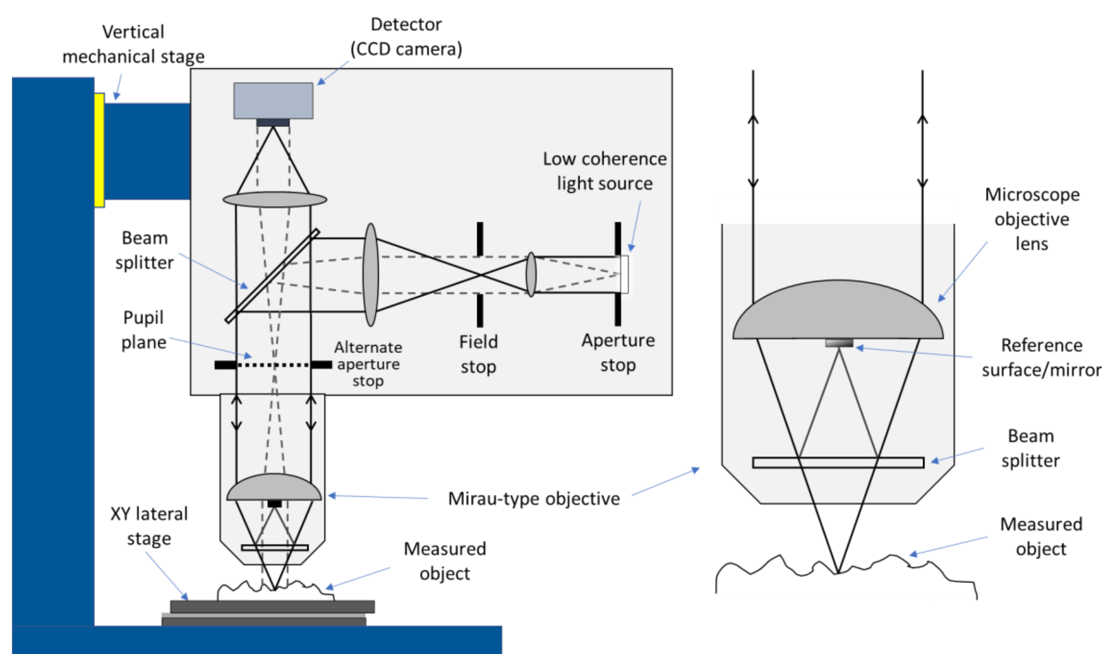


**Figure 2.2**. Schema of a vertical scanning style CSI instrument, equipped here with a Mirau-type interferometric microscope objective. Not to scale. Lens shapes are for illustration and are not accurate. Note that it is possible for the lateral and vertical motion stages to be positioned differently, so that either the object's stage or the microscope assembly would be completely immobile.

There are two primary designs for interference objectives: the Michelson-type which uses a reference arm perpendicular to the optical axis; and the more compact Mirau-type [96] whose reference arm is within the objective's assembly, with the reference mirror at the centre of the objective lens. Linnik-type interferometers do not use interference objectives: instead, the beam splitter is placed before the objective lens, and the interferometer uses two non-interferometric objective lenses, which are usually identical, to capture light from the object and reference surface [110,115].

Mirau objectives are best suited for high magnifications (~10× to 100×) since the associated high NA and high acceptance angle under spatially extended illumination reduce the influence of the central obscuration of the in-line reference mirror. Linnik

interferometers are also well suited for high magnifications but are less frequently used than interferometers with a Mirau objective, for two main reasons: their relatively higher sensitivity to vibration, and due to the additional cost of needing two objective lenses. The higher sensitivity to vibration is caused by the comparatively longer path length between the beam splitter and the object or reference surface.

At lower magnifications (~2× to 10×), Michelson objectives are typically used instead of Mirau objectives, due to the increased negative influence at lower NAs of the central obscuration present in Mirau objectives. In contrast, Michelson objectives are rarely used at higher magnifications due to design constraints that occur when attempting to combine a high NA with a perpendicular reference mirror arm. For magnifications below 2×, the geometry of the Michelson objectives becomes difficult to manage, and the recently developed wide-field objectives are more suitable [116,117]. These so-called "de Groot-Biegen" objectives [105] follow a similar design to a Mirau-type, but the coaxial beam splitter plate and partially transparent reference mirror are both tilted slightly to prevent unwanted reflections from travelling through the imaging pupil, improving fringe contrast. This design is best used for NA<0.1, with the asymmetric design somewhat compromising the image quality at higher NAs. Different interference objectives are mounted on an automated turret and are made parfocal to allow for switching between different magnifications. For interference objectives, it is usually best that the optical focus and the so-called "interferometric focus" are made the same, to avoid errors associated with interferometric defocus [118,119]. Therefore, objectives are designed to allow the distance to the reference mirror to be adjustable, typically by hand.

The illumination light source is incoherent (or has low coherence) due to both the broadband illumination spectrum and the illumination source's spatial extent. Typically, the spectrum is produced by white-light light-emitting diodes (LED), and the LED spectrum is filtered with a yellow filter to remove the undesired blue peak and form the desired Gaussian spectral distribution [110]. Alternatively, LED sources with separate red, blue and green filters can be combined and balanced to produce the same distribution [120,121]. Additional filters can be applied to narrow the spectral bandwidth when a longer coherence length is desired [122]. As seen in Figure 2.2, Köhler illumination is used such that the surface is uniformly illuminated and the illumination source is imaged in the objective's pupil plane. By filling the pupil plane,

the spatial coherence is reduced, resulting in a larger maximum lateral resolution compared to fully coherent illumination [84,123,124].

The light illuminating the sample is scattered from the surface, and the scatter is captured by the objective lens and imaged onto the detector. This detector is typically a monochrome detector array, such as a CCD or CMOS sensor, as only the light's intensity is necessary for CSI, and using equivalently sized colour sensitive sensors sacrifices sensor resolution [120]. Details about electronic image sensors, sensor resolution, and digitisation of image signal data can be found in [125].

Similar to typical microscopes, the axial distance $z$ between the objective and the scanned object is varied, either via motion of the objective or the stage, until the object is brought into focus. Typically, this is along the vertical direction. To take a measurement, an axial scan moves the focus while capturing multiple images, resulting in information captured at the "best focus" for each pixel separately. Typically, piezoelectric transducers (PZTs) are used to make small scale adjustments precisely over a scan, but with a limited range ($\approx$ 10 μm to 200 μm) [84]; sometimes a separate coarser adjustment mechanism can move the overall microscope assembly upwards or downwards over a larger range. Typically, the stage can be moved mechanically in either lateral ($x$-$y$) direction, i.e. the plane perpendicular to the axial optical axis, and can also be tilted slightly around these lateral axes. With this capability in place, a surface can automatically be scanned in its entirety by stitching multiple axial scans made at different $x$-$y$ positions, however this can lead to error in the surface topography due to the lateral distortion of the system and the increased measurement uncertainty due to stitching [126,127].

### 2.3.3 Fringe acquisition

An instrument scan produces a sequence of images taken at known $z$ positions, with the fringes forming in the images wherever the OPD is close to zero, almost as though the fringes are projected onto the surface only in regions that are in focus, producing surface contours. An example of how this appears is shown in Figure 2.3.

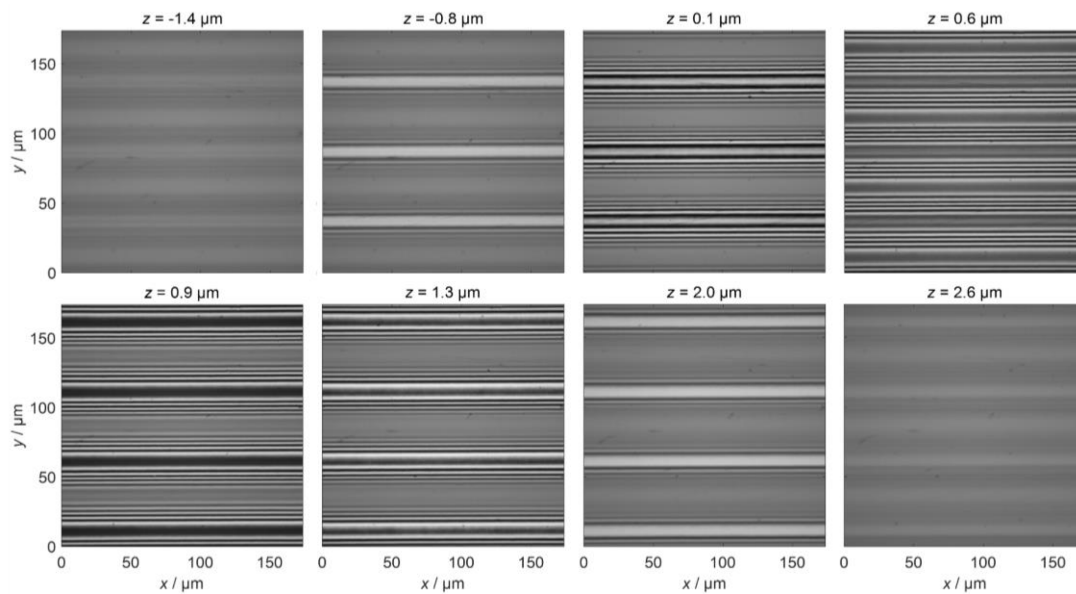


**Figure 2.3**. A subset of the images captured by a CSI instrument during a scan of a sinusoidal grating. Note that from these images we can tell that the sample is effectively flat relative to the lateral axes, and the midpoint between the two peaks is at about $z = 0.6$ μm. The same data is presented in Figure 2.4

The resulting image frame data can be considered a three-dimensional (3D) cuboid of fringe data. Taking slices of this data parallel to the optical axis reveals clearly how the topography has been encoded into the signal data. This is displayed in Figure 2.4, using the same data set at Figure 2.3.

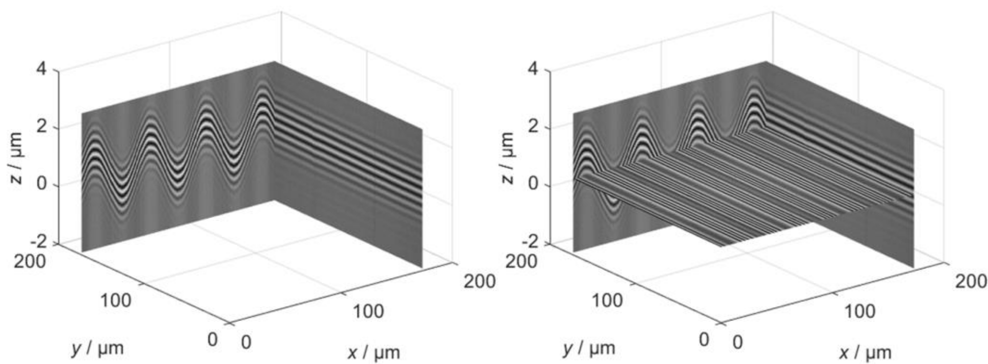


**Figure 2.4**. Slices of the 3D fringe data obtained from measurement of a sinusoidal grating. Both plots have slices at $x = 173$ μm and $y = 173$ μm, while the plot on the right also has a slice at $z = 0.6$ μm, also seen in Figure 2.3. This is to illustrate the connection between the vertically scanned images and the axial slices of data shown throughout this thesis.

Each data column of these axial fringe slices is effectively a single interferogram, like that in Figure 2.1, which has encoded the surface height for a location on the surface; this is shown in Figure 2.5.

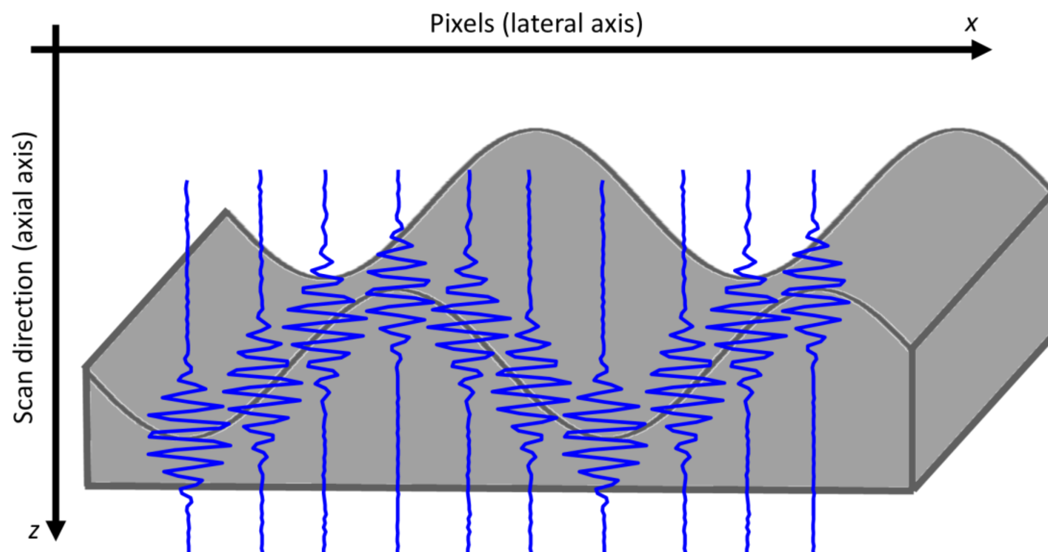


**Figure 2.5**. A diagram to present how the fringe data can be considered as columns of adjacent interferograms, each of which encode the surface height at a particular position. The same kind of axial slice can be seen in Figure 2.4, where the bright white and dark black fringes represent the peaks and troughs of the interferograms shown here.

### 2.3.4 Surface reconstruction methods

At one time circa 1977, interferometry for surface topography measurement was considered limited to polished optical surfaces that created simple interference patterns: such patterns could be interpreted with manual fringe tracing or by phase shifting methods [90]. However in the 1990s, interferometric methods based on optical coherence were shown to be capable of providing meaningful results from rough surface textures [98,99,110]. Improvements in technology since then have led to the development of CSI instruments as they currently appear, which capture fringe information digitally as a stack of image data. This 3D data is then processed by software or dedicated hardware to obtain a height estimation, with the quality of the analysis directly impacting the accuracy and capability of the instrument. Therefore, much work has been carried out on surface reconstruction and height estimation.

The analysis of localised fringe patterns to obtain precise height information is a detailed topic of study, for which a full discussion is beyond the scope of this thesis. However, it appears simple to extract surface height information from a cross-section

of measured fringe data wherever fringes are present, such as in Figure 2.6, by finding the bright centre of the fringes (fringe centroid) for each pixel's scan. The envelope that contains the fringes and limits their extent is called the coherence envelope. Generally, the position of the coherence envelope provides an estimate of the height and indicates the approximate location of the zeroth fringe order; the estimate can be further improved by considering phase information as in PSI.

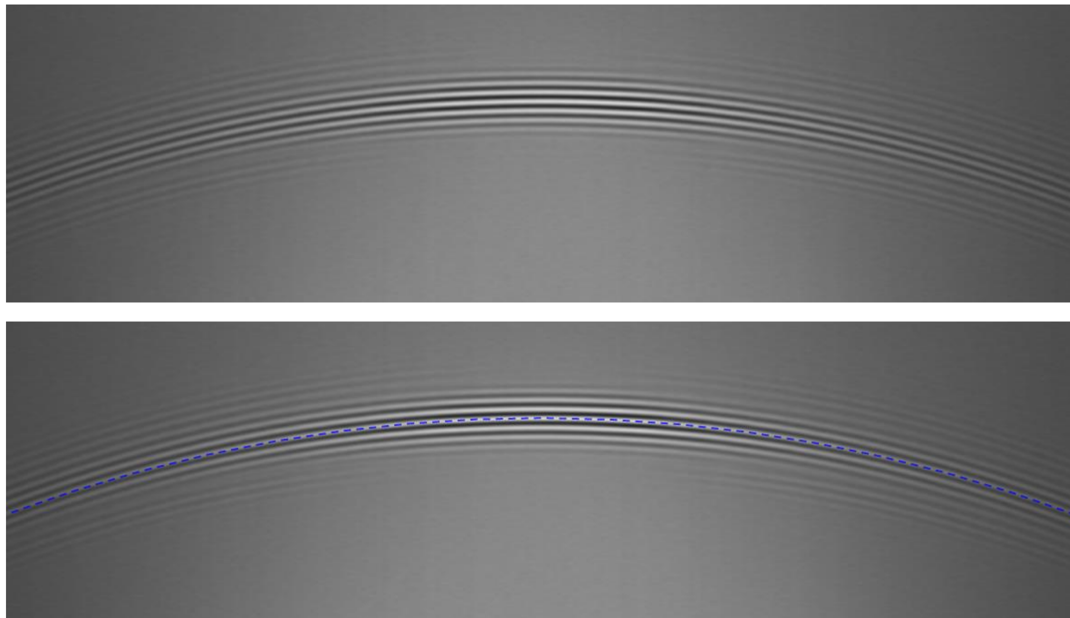

**Figure 2.6**. Axial cross section of fringe data from measurement of a microsphere. Above are the fringes alone, and below the same fringes with a simple height estimation overlayed.

The presence of this surface information in the fringe data is by design as, through the optical principles of the CSI instrument, the surface height information is encoded in the fringe data produced. This 'encoding' can usually be reasonably assumed to be linear: each instrument pixel collects an interferogram over an axial scan that is considered as being determined only by the height of the surface at a single *x*-*y* position. This 'pixel-by-pixel' assumption is one that, to the author's knowledge, all current height estimation algorithms rely on, but the exact method used to obtain the height for each pixel varies considerably. In section 9.5 of [84], an idealised expression for the interference signal is stated, where a cosine carrier signal with fringe frequency $K_0$ is modulated by a slowly varying modulation envelope function. In the same section, it states that while only an approximation, this model is a useful starting point for many signal processing strategies, listing a series of approaches in the literature from 1982 to 1997.

Surface height information can be obtained just from finding the position of the coherence envelope [85]. Initially, many height estimation methods relied on finding the position of maximum fringe contrast to obtain height information from the coherence envelope, but this method is computationally inefficient due to the large number of samples required and is sensitive to random noise (among other disadvantages). These disadvantages motivated the development of analysis in the spatial frequency domain [89]. Known as Fourier frequency-domain analysis (FDA), this analysis obtains phase and coherence information in the Fourier domain via Fourier transforming the signal data, from which surface height can be estimated. The FDA method is also capable of handling changes in the sample interval that occur due to environmental effects [89,128], and accurate height estimates can even be obtained from measurement data sampled at sub-Nyquist frequencies, so long as the sample rate chosen avoids segmenting or overlapping the frequency bandwidth [128,129].

FDA provides two outputs from the measurement data: a coherence profile and a phase profile. The information from the coherence profile corresponds to that from the coherence envelope; the information from the phase profile corresponds to the phase information obtainable using PSI methods for many (20 to 30) data frames [110]. While height information from the coherence profile is connected to the scan velocity, phase information obtained from a PSI analysis relies on the fringe frequency, which is a function of the illumination wavelength(s) and optical geometry. Therefore, phase information has a different traceability chain to the metre than that of the coherence profile. This difference in traceability chains can be avoided with FDA, as the phase profile can be obtained without any assumptions about the fringe frequency, using the scan velocity as a fundamental metric [110].

Calibration of the scan velocity for the instrument is typically performed via measurement of a material measure such as a step height standard [41,43,130,131]. However, an alternative method that uses a calibrated spectrometer to calibrate the microscope illumination, and from this the scan velocity, is also possible for CSI [132,133]. Such a method preserves the inherent high accuracy of interference microscopes through the traceability chain, and separates errors related to scanner linearity. This "wavelength standard" method can be used for traceable certification of step height standards, and for instruments calibrated in this way, step height artefacts can still be used for verification [43]. The method is used commercially: all interference

microscopes produced by Zygo are calibrated with the wavelength standard at their factory; NIST uses the wavelength standard when calibrating their Zygo interference microscope; and end users of Zygo Compass™ instruments who have demanding calibration requirements require calibration via the wavelength standard instead of step height standards due to the decreased uncertainty[4]. Alternative "self-calibration" approaches for the *z*-scale also acknowledge that a CSI instrument's high repeatability and accuracy is undercut by the comparatively large uncertainties in traceable calibration artefacts [134].

FDA can be used to acquire just the coherence envelope for analysis, which is more robust to low signal-to-noise ratios (SNR) from rough surfaces [37,39,135]; equally FDA can obtain both phase and coherence information together, which can be combined while applying corrections for inconsistencies to give a more refined height value [87]. However, these inconsistencies when left uncorrected can lead to fringe order errors [87,136], discussed further in section 2.3.5. In addition, there is a difference between the coherence envelope's peak position and the central bright fringe, called the phase gap. The phase gap is produced by the combined phase shifts from transmission and reflection properties of the components of the instrument, in addition to the effect of surface structures. Determining the phase gap across the entire FOV also increases the difficulty of combining coherence and phase information. Rather than using a mean phase gap everywhere, significant efforts in software development have been made to infer the specific phase gap at each pixel's location [84,87,110]. One approach to obtain the phase gap across the FOV and resolve fringe order errors is to interpret the surface structure assuming some range of possible variability, from which the nominal phase gap can be assumed and the fringe order at each pixel obtained [87]. Of course, this is only relevant when at least phase information is considered in the height estimation, making coherence-only methods more reliable for rough and unusual surfaces for which the expected phase gap can be misleading.

More recently, other techniques involving coherence correlation have been demonstrated [137], though this is not a new idea [138–140]. The spatial frequency-domain can also be used for signal modelling, with an efficient theoretical model

---

[4] Source of commercial usage from correspondence with Peter de Groot, Chief Scientist at Zygo Corporation

predicting the expected fringes from low-coherence interference instruments outlined and explored in [101], and demonstrated in section 2.4.1. For further reading, including the mathematical foundations, a detailed explanation of the FDA technique is described as part of [87], and is also detailed within [84] and [105]. The quality of the surface reconstruction depends on the capability of the instrument to obtain information from the surfaces considered, on the impact of environmental effects, and on the real-world imperfections in the instrument such as optical aberrations. This is discussed in section 2.3.5.

### 2.3.5 Current capability

As an optical technique, CSI is a non-contacting method, capable of measuring materials too soft to be measured by contact methods. Its non-destructive nature also avoids damaging a surface during the scanning process. Usually, CSI obtains an areal scan of the surface from a full-field scan, allowing for fast scans over a wide FOV. Compared to non-interferometric optical surface topography methods, such as FV microscopy, CSI also has the advantage that the surface topography is found independently of the objective lens used. While many optical techniques must sacrifice their vertical sensitivity to increase the FOV, CSI retains the same vertical sensitivity at any FOV, allowing for wide-range surface height measurements [123]. Due to CSI's interferometric nature, instruments can provide uncertainties of the order of nanometres [39] and sub-nanometre noise level for surface topography measurement of certain surfaces [21]. As an interferometer, CSI's closer connection to the realisation of the metre can at least in principle be exploited to provide calibration to the metre through a wavelength standard, removing the dependency on material measures for the relevant metrological characteristic [132].

However, compared to contact methods, CSI is more complex to model, and the fringe analysis required for high precision with a low measurement uncertainty has only become viable with improvements in computation. The complexity of the instrument modelling, combined with the high tolerances of the lenses used, leads to CSI typically being more expensive than contact methods. This complexity and sheer computational difficulty in modelling and analysing the light-matter interaction and scattering rigorously also means that various approximations are typically made when modelling the instrument, such as neglecting the effect of multiple scattering or considering less

spatial dimensions [141]. Reconstruction methods effectively rely on a simple optical/instrument model to make the mathematics of the height estimation tractable, which fortunately remains effective for many types of surfaces.

Additionally, all optical systems have certain inherent limitations, which prevent them from fully determining the surface topography. An instrument's lateral resolution is fundamentally limited by the diffraction limit: an inevitable blurring of lateral points due the wave nature of light and our limited ability to capture scatter. Imaging an ideal point-source of light produces an Airy disk, and our ability to distinguish one point-source from two closely positioned point-sources in our image is what is meant by the diffraction limit. This is parameterised by criteria such as the Rayleigh criterion or Sparrow criterion, whose values differ between the coherent and incoherent illumination cases [123]. The amount of blurring that occurs for each wavelength of light is typically determined by the NA of the instrument's objective lens used, as it is this aperture that restricts the range of angles of scattered light that the instrument can capture (see Figure 2.7). The capture of light scatter at larger angles is required to provide accurate height information for higher spatial frequency surface features. For incoherent imaging systems, the magnitude of the surface features obtained decreases as spatial frequency increases, effectively until the diffraction limit is reached. This is parameterised by the instrument transfer function (ITF) [142–146], and leads to an issue when measuring rough and steep surfaces.

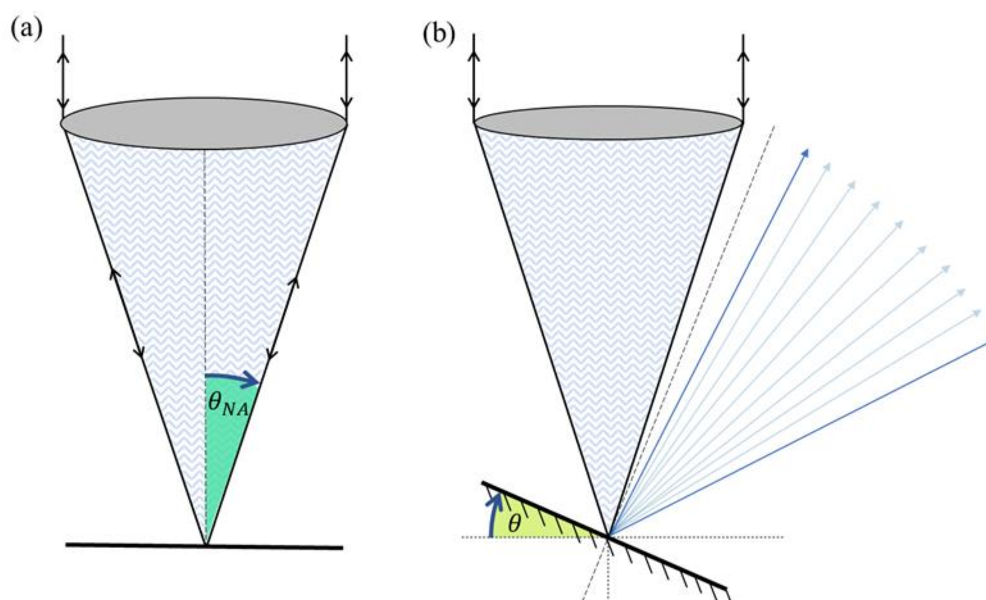


**Figure 2.7.** Schematic illustrating the concept of a maximum collection angle for a microscope system (repeated from Figure 1.2). Note that it is conventional for the collection angle $\theta_{\mathrm{NA}}$ to refer to the half-angle of the collection cone, as this angle is equal to the surface tilt at and above which a specular surface no longer scatters any light back into the objective.

Re-entrant features (i.e. overhangs) cannot be imaged easily via optical instrumentation, due to the geometry of the applied illumination and the objective lens' angle of acceptance (or "cut-off angle") relative to the surface; however this difficulty is not unique to optical systems as contact probes struggle due to similar line-of-sight geometric reasons. Such re-entrant features are usually masked in surface scans, being difficult to differentiate from small surface steps. There is even some evidence to suggest that optical instruments with larger NAs can obtain information from vertical walls and re-entrant wall features [36,49,147,70], and this is discussed in more detail in section 2.6.

In addition, real optical instruments inevitably suffer from some optical aberrations and other real-world imperfections. For the lens system these can be separated into monochromatic aberrations, higher-order aberrations and chromatic aberrations [148], derived from differences from the paraxial geometrical optics model of lenses. While some aberrations can be corrected, it is the case that lateral distortion [134,149,150], dispersion [151–153], retrace error [154–157], the effects of defocus and interferometric defocus [118,119,158], and higher-order aberrations can all contribute to errors in CSI, often errors dependent on the shape of the surface measured [159]. Real optical instruments also suffer for environmental noise such as vibration and air

turbulence, and have limitations in their sensor sensitivity and dynamic range; enhancements in technology and correct use of the instrument can reduce their impact on the measured topography [37,39,135,154,160,161].

### Instrument errors and reducing them

CSI is capable of being accurate with a high precision, with three measurements of the same step-height artefacts taken across a 3-year period providing an average standard deviation (i.e., repeatability) of 2.0 nm and 13.0 nm for 1.8 µm and 24 µm step-height artefacts respectively [133]. However, it is harder to retain this level of accuracy for any surface. This is because, among other things, the accuracy of CSI is dependent on the properties and attributes of the surface measured. Under a certain threshold, poor quality fringes lead to data dropout of the topographic map of the surface. This can be seen when using objective lenses with different NAs to measure a rough surface: lenses with a lower NA cannot capture enough light from the steeper areas of the surface to form visible fringe patterns from which height data can be confidently obtained; lenses with a higher NA have a wider acceptance angle and can capture light from steeper surfaces, reducing data dropout. This is discussed further in section 2.6, and an exploration of tilt and curvature dependent errors is carried out in [74]. Data dropout occurs not only when the fringe data's SNR falls below some threshold, where a low SNR can be caused by the low proportion of scatter that can be captured when scattering from steep surfaces [37], but also due to misconfiguration of the optical components, such as a poor optical focus. The lower limit for such noise is derived in [162] using the Cramer-Rao inequality. For rough surfaces with heights that exceed the coherence length under a single pixel (i.e. low magnifications), narrowing the illumination bandwidth with filters increases the coherence length and therefore reduces data dropout, at the cost of a loss in precision related to obtaining height information from a wider coherence envelope [37,39,122]. An evaluation of the measurement uncertainty associated with surfaces with such high spatial frequency texture, i.e., those that have sufficient variation in surface height within a region of the surface that when imaged is smaller than a sensor pixel in the image plane, has also been made and compared to experiment [163]. An examination of CSI's ability to complete a series of varied measurement tasks is carried out in [164].

Data dropout is not the only result of low SNR, the effect of real-world imperfections, or other limitations of the instrument. In certain situations, the central fringe order can be misclassified, leading to a jump in the height data corresponding to half the mean effective wavelength of the illumination, i.e., a change in phase by $2\pi$. This kind of error is therefore called a $2\pi$ or fringe order error. The causes of fringe order errors are relatively diverse, with very smooth surfaces sometimes producing so-called "ghost steps" due to field dependent dispersive aberrations [160], and rough surfaces sometimes exhibiting the effect at regions of high surface gradient [39]. Fringe order errors can occur even when the surface tilt is within the angle of acceptance. Note that all fringe-order errors are fundamentally only present when analysis attempts to combine both the coherence envelope and phase information, so utilising only the coherence envelope for height analysis is an effective way of reducing data dropout and fringe-order errors for rough, low SNR, surfaces [37,135].

Measurements of step discontinuities can produce the "batwing" effect. While similar looking to fringe order errors, the batwing effect occur due to interference of the step-edge diffracted waves with the regular top and bottom surface reflected waves, alongside shadowing effects [39,165]. These erroneous height values near the step discontinuities occur even when the step is much taller than the coherence length, though these errors are usually smaller. While the batwing errors can be related to a shifted coherence envelope [165,166], they do not have to be, and can appear entirely from phase evaluation methods [167]. For step height structures, the batwing effect is strongly dependent on the height-to-wavelength ratio (HWR) of the surface, as well as the effective illumination wavelength used, determined by the instrument's NA [168,169]. Rigorous modelling has also been performed to investigate these errors, comparing results against those from both simpler models and experiment [170]. With a choice of processing that depends more on the phase information, these batwing errors can be attenuated [166,171]. Furthermore, for certain step height geometries, careful tuning of the evaluation wavelength used in phase evaluation can also allow for accurate measurements of rectangular phase gratings, supressing the batwing artefacts and rounding of grating edges even when higher-order diffraction components are lost [167,172].

In [173], some of the parameters and properties of CSI that affect measurement results are investigated across three categories: transfer characteristics and resolution limits;

dispersion effects; and temporal and spatial coherence effects. Diffraction and temporal coherence effects were simulated and experimentally measured, with strong non-linear transfer characteristics observed for rectangular gratings, dependent on both instrument configuration and surface structure, with batwings appearing and disappearing depending on the HWR of the rectangular gratings used, revealing that adapting the centre wavelength can reduce the strength of batwings seen [168]. Investigation into dispersion effects, i.e., chromatic aberration, show that while fringe contrast is weakened and the coherence envelope is shifted by dispersion, phase information is barely influenced. The low impact of dispersion on phase information allows accurate topography to be obtained if the surface height variation is small, i.e., no fringe order ambiguity is present. Dispersion errors can also be reduced by adding corrective lenses designed with ray tracing software next to the beam splitter cube. It is also possible to reduce the prevalence of $2\pi$ errors that occur due to dispersion effects and lateral chromatic aberrations of the imaging system by first measuring a known standard surface and capturing information on the effect of the dispersion on the envelope position and phase and compensating for it [174]. Finally, temporal and spatial coherence effects were studied, using more accurate modelling. Batwing effects can be more accurately studied and in more detail when the spatial coherence (and therefore the NA of the instrument) is better accounted for, revealing maximum batwings occurring at HWR = 0.25. Polarisation was also studied, with stronger batwings seen when using transverse electric (TE) polarisation. The underestimation of profile height from measurement of a chrome structure on a glass substrate was also accurately predicted, with the cause due to the different phase shifts between reflections for the two different media.

As discussed earlier, all optical instruments are limited by their objective lens's NA, which determines a maximum acceptance angle at which light scattered or reflected from the surface can be captured by the system (see Figure 2.7). For artefacts with inclines steeper than this angle, such as a 70° silicon vee-groove, widely inaccurate height values can be obtained rather than data dropout occurring [39]. Errors of several hundred micrometres can be found for the sloped region, the resulting topographical data unrecognisable as a vee-groove even with the lower error magnitudes present around the trough of the groove [175]. This effect is attributed to multiple reflections (scattering) off the two sides of the groove [176,177], and further work has been carried

out to utilise this phenomenon to measure the dihedral angle of the vee-grooves [178]. This error is due to the inherent assumption that only single scattering events take place in a CSI scan, i.e., the ‘pixel-by-pixel’ assumption.

Relative to other types of surface measurement, CSI can sometimes overestimate the texture of rough surfaces. The reason for this can for example be explained by considering rough surfaces as being made up of differently orientated groove-like objects at the small-scale. Due to multiple scattering, each of these small-scale steep “grooves” that make up the rough surface are incorrectly interpreted as significantly modulating topography, increasing the apparent surface texture. Note that these surface texture effects are typically not a problem if coherence and phase information are both used [160]. In cases where the surface is simply tilted or has high slopes without significant texture, only a small proportion of the scattered light can be collected by the objective lens, leading to a low SNR and consequently data dropout. Capturing enough of the specular reflections from these surfaces to increase the SNR requires a larger NA, and for some surfaces is effectively impossible irrespective of the NA. A more detailed discussion on the optical measurement of surface topography for tilted and steep surfaces, especially with slopes or tilt angles beyond the acceptance angle of the objective lens, is given in section 2.6.

## 2.4 Overview of CSI models

Modelling is at the heart of understanding physical phenomena, and for CSI instruments is especially valuable due CSI’s complexity and the need to analyse signal data for height estimation. This thesis presents two main CSI modelling approaches: the foil model and the BEM-CSI model. The foil model treats the surface as a thin foil, which under certain approximations can be combined with an appropriate transfer function to generate CSI fringes for that surface. The BEM-CSI model instead calculates fringe data using a rigorous numerical boundary element method (BEM) of optical scatter, derived from Maxwell’s equations without significant approximation. The BEM method solves for a given illumination the surface boundary fields and surface-normal derivatives along a surface, and consequently can calculate the scatter from the surface, which can be used to produce fringes. A review on the state of art of CSI models including their limitations, as well as background on their assumptions and principles, is given in this section, while the foil model, BEM model, and BEM-CSI model are

described later in their respective chapters (Chapter 3, Chapter 4, and Chapter 5). Several of the models discussed in this section are categorised in Table 2.2, though alternative categorisations by dimensionality can be found in [105,179]. Note that a simple one-dimensional (1D) model can be readily extended to produce virtual fringe data for an entire surface, and is therefore not limited to just 1D, but extending the model does not account for the real measurement method as well as a less-approximate higher-dimensional model can. In addition, the dimensionality of the surface and the imaging process can differ in general and between different models [179], and models can be comprised of a combination of approximate and rigorous parts, which complicates categorisation.

**Table 2.2** A categorisation of a selection of CSI models.

| | |
|---|---|
| **Simple 1D signal modelling** | Cosine intensity with envelope [101,180]<br>Numerical integration of a cosine intensity interference signal over parameter space [101] |
| **Linear two-dimensional (2D) and 3D modelling** | Cosine intensity with envelope, extended to higher dimensions, filtered by the traditional optical transfer function [181]<br>Elementary Fourier optics (thin phase object approximation) [182]<br>Extended Richards-Wolf model (Debye approximation, vectorial variant) [168,169,173,183]<br>Kirchhoff approximation combined with filtering by coherent amplitude transfer function [168]<br>Foil model (Kirchhoff approximation, transfer function model) [88,184–186]<br>Double foil model (Kirchhoff approximation, transfer function model) [187] |
| **Non-linear modelling** | Finite element methods [49,179,188]<br>Boundary element methods [51,52]<br>Finite difference time domain methods [170]<br>Rigorous-coupled wave-equation methods [179,189] |

## 2.4.1 A simple linear cosine intensity CSI model

A CSI model that takes a cosine intensity function summed over multiple wavelengths and incident angles, can still predict the main features of an interference signal, including signals from thin films [101,180]. Effectively, both the surface-light interaction and resulting scatter are not considered in a cosine intensity model; instead, the height of the surface is included simply by setting the phase origin of the cosine to the height of the surface along the optical axis. To help explain this approach, its theory

and some simple results are outlined below, with more advanced linear models discussed in section 2.4.2.

A basic CSI intensity signal for measurement of single surface point for a single sensor pixel is modelled, to examine some of the fundamental dependencies of the fringes on the optical configuration. This model follows that described in [101], an established method in older literature per section 3.2 of [110].

Starting from Eq. (4) of [101]

$$I(\zeta) = \int_0^\infty \int_0^1 g(\beta, k, \zeta) U(\beta) V(k) \beta \, d\beta \, dk, \tag{2-9}$$

where $\beta = \cos(\psi)$ is the directional cosine for incident angle $\psi$; $k = 2\pi\lambda$ is the angular wave number for illumination wavelength $\lambda$; $g(\beta, k, \zeta)$ is the interference contribution for a single ray bundle, at some specific axial scan position $\zeta$, for some directional cosine $\beta$ and some specific wave number $k$; $U(\beta)$ is the intensity distribution in the pupil plane of the objective lens, also known as apodization factor; and $V(k)$ is the optical spectrum distribution. The factor $g(\beta, k, \zeta)$ is given by

$$g(\beta, k, \zeta) = R + Z + 2\sqrt{RZ} \cos\big(2\beta k(h - \zeta) + (v - \omega)\big), \tag{2-10}$$

where $R$ is the reference reflectivity, $Z$ is the effective object intensity reflectivity, $h$ is the height of surface at the point considered, $v$ is the reference path phase contribution, and $\omega$ is the object path phase contribution. In general, $Z, R, v, \omega$ all vary with a change in $\beta$.

Next, Eq. (2-9) is simplified by reducing the intensity distribution profile to a point source at the centre of the pupil plane, such that $U(\beta) = 0$ when $\beta \neq 1$, i.e., equivalent to low NA illumination. Furthermore, it is assumed that $(v - \omega) = 0$ for all $k$, and that reflectivities $R$ and $Z$ are independent of both $k$ and $\beta$, so that these factors can be neglected in the analysis. This gives

$$I(\zeta) = U_1 \int_0^\infty g(1, k, \zeta) V(k) \, dk, \tag{2-11}$$

where $U_1 = U(1)$. Substituting this equation into Eq. (2-10) gives

$$I(\zeta) = U_1(R+Z)\int_0^\infty V(k)\,dk + 2U_1\sqrt{R+Z}\int_0^\infty V(k)\cos\big(2k(h-\zeta)\big)\,dk. \tag{2-12}$$

As only the fringe patterns (produced as the axial scan position $\zeta$ varies) are of interest, the first term can be neglected. The equation can then be evaluated numerically.

The optical distribution $V(k)$ is modelled as a Gaussian with a full width at half maximum (FWHM) of 100 nm and mean of 500 nm, such that numerical integration of the cosine is achieved at each desired $\zeta$. A height value $h$ of 1 μm was chosen and the results are displayed in Figure 2.8. Even with such a simple model, it is easy to see how the fringe envelope changes under a narrower bandwidth illumination, shown in Figure 2.9.

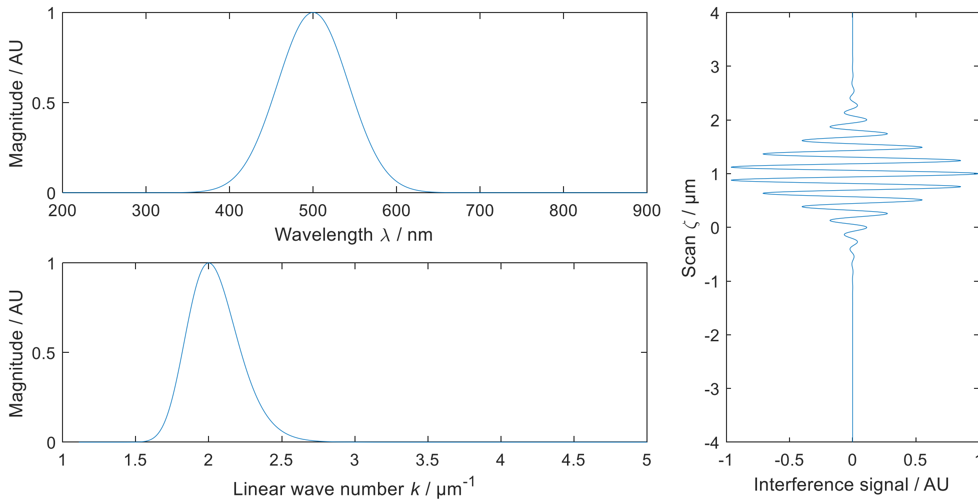


**Figure 2.8**. Modelled interference signal (interferogram) for CSI (right) using a Gaussian optical distribution with FWHM of 100 nm and mean of 500 nm (left), where a point source is considered at the centre of the pupil plane. Note that the chosen surface height of 1 μm is clearly visible due to the localisation of the fringe pattern produced.

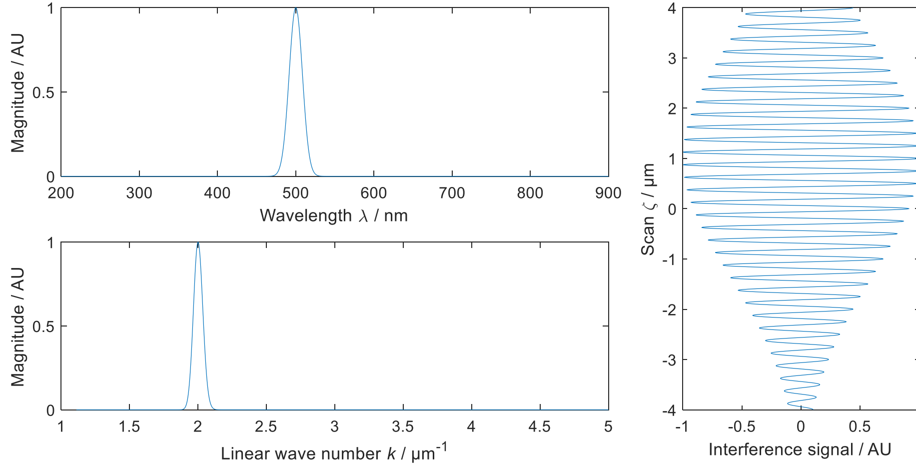


**Figure 2.9**. Modelled interferogram for CSI (right) using a Gaussian optical distribution with FWHM of 20 nm and mean of 500 nm (left). The fringe signal is visually cropped to preserve the same 8 µm scan range as in Figure 2.8.

Of course, when the illumination is not only normally incident, i.e. for NAs that are not small, the fringe spacing is also affected. In other models this aspect is captured and simplified by an NA-factor or "obliquity factor" [190]. A more general case using an extended light source, limited by the NA ($A_n$) of the objective lens, can also be considered. Without the simplifying assumption of a central point source of light in the pupil plane, Eq. (2-9) is considered, where the intensity distribution $U(\beta)$ is chosen to be constant for $\beta < \theta_{\mathrm{NA}}$ where $\theta_{\mathrm{NA}} = \sin^{-1}(A_n)$, and zero elsewhere. While it is possible to evaluate Eq. (2-9) significantly more efficiently by combining $\beta$ and $k$ to a common spatial frequency parameter, and rewriting the equation in the Fourier domain [101], the equation can still be evaluated directly. Shown in Figure 2.10 are two interferograms calculated in this way with similar coherence lengths, despite the large differences in illumination bandwidth and NA. With comparison to Figure 2.9, it can be seen that a larger NA also causes the coherence envelope to shrink. Clearly a combination of temporal and spatial coherence together produces the localised fringes seen in CSI.

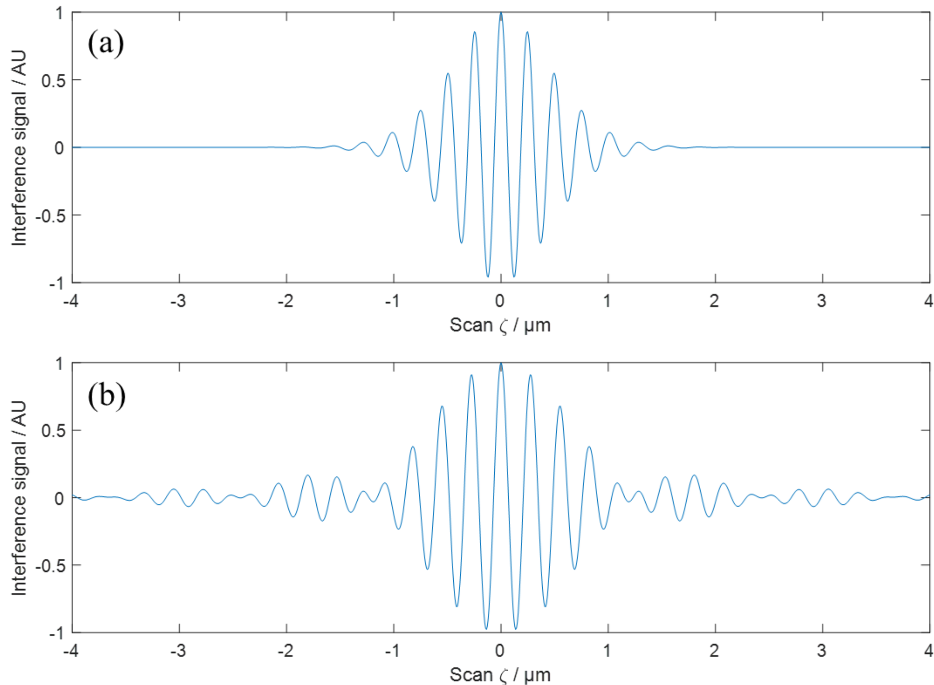


**Figure 2.10**. Modelled interferogram for CSI using a Gaussian optical distribution with a mean wavelength of 500 nm, where: (a) the FWHM is 100 nm and the NA is 0.2, and (b) the FWHM is 20 nm and the NA is 0.6. In both cases the pupil plane is uniformly filled for the chosen NA.

## 2.4.2 More advanced linear models

A similar approach to the cosine intensity model described in section 2.4.1 was made to predict the effects of multiple reflections within a surface film [181], although a number of aspects, such as the variation of the angle of incidence, were neglected. The cosine intensity model has also been extended to a 2D model by others, combining a group of 1D interferograms for an areal region of surface heights with a traditional 2D optical transfer function (OTF), effectively accounting for the diffraction and spatial frequency filtering associated with the measurement instrument [191]. This is equivalent to convolving the intensity image at each scan position with the lateral optical point-spread function (PSF) of the instrument. Note that the surface here is effectively "2.5D", in that each lateral coordinate $(x,y)$ may have only one surface height $(z)$. Rectangular gratings were considered in the referenced work, to investigate both the linear and non-linear transfer characteristics associated with the gratings, and with the OTF determined the ITF was evaluated by modelling a range of gratings with different grating heights and periods.

The so-called "elementary Fourier optics" (EFO) approach instead treats the surface as a thin phase grating whose phase is linear with the surface height; valid only for surfaces

with heights small relative to the depth of field, referred to as the "thin phase object approximation" [182]. Image formation occurs using Fourier optics field propagation along the optical axis [192], with filtering by an ITF applied laterally to the spectrum. Unlike the simpler cosine intensity model, EFO requires a range of surface height points; each point of the scattered spectrum formed is comprised of scatter from points across the entire surface. Only the interferometric response is considered, with the conventional non-interferometric imaging of the object neglected. While not essential, an obliquity factor [190] is used to average the effect of different illumination angles and simplify the calculation; this reduces the accuracy of the model for high NAs. For surfaces with small heights that meet the thin phase object approximation, the model can rapidly predict the main features of surface topography measurements by CSI.

The so-called "extended Richards-Wolf" model requires numerical integration similar to the cosine intensity model. The theory of the extended Richards-Wolf model is detailed in [168,169,173,183], the vectorial case explained further in [183], vectorial comparisons made to other linear models in [188], and the model used for instrument characterisation in [193]. The approach is based on the Debye approximation [194–196], and the modelling method was first developed by Richards and Wolf [197]. The approach considers the distribution of the electromagnetic field due to diffraction at and near to the focus of an aberration-free system imaging a point source, for an incident field considering vectorial linear polarisation. This is then adapted and extended to an interferometric configuration with spatially incoherent illumination.

Some CSI models are based on the Kirchhoff (or physical optics) approximation (KA) [141,198,199]. The KA primarily requires that surfaces vary slowly on the optical scale; more detail on the assumptions taken are given later in this section, including expressions such as Eq. (2-13) as criteria for the KA. One CSI model based on the KA, called the foil model, characterises the instrument's imaging as a 3D linear filtering operation on surface spatial frequencies, and has been used to produce a virtual CSI instrument for instrument and error characterisation [186]. The foil model's theory is presented in [185], and the exact approximations made listed in [184], following Beckmann and Spizzichino [141]. The foil model is used throughout Chapter 3 and detailed further there. Other CSI models based on the KA can be seen in [168,187], used to estimate the strength of the batwing effect for different configurations. In the case of [187], the foil model is modified and the so-called "double foil model"

presented, named due to explicitly modelling the response of both the sample and the reference mirror. This modification has a larger impact for instrument modelling with larger NAs, and a smaller impact with lower NAs. Issues with the assumption that an instrument has a universal PSF independent of the surface are suggested and explored analytically, and issues demonstrated for several surfaces, which are further expanded on in more recent work [200].

Both the foil model and double foil model are examples of 3D transfer function models, which model the interference response of the instrument as a filtering in frequency space of an object surface spectrum by a transfer function, equivalent to a convolution of an instrument intensity PSF with an object surface function (the so-called "foil"). The use of 3D transfer functions in the area of surface topography measuring instruments is reviewed in [201]. This review also clarifies the differences between the various lower-level kinds of transfer functions used in optics to transfer scattered optical field to the optical field measured by an instrument, such as the OTF. The ITF, which maps input surface to measured surface, can also be related to the 3D transfer function [144,146].

There are many publications on regions of validity of the KA for different scattering problems, often including modifications to account for neglected phenomena and widen the region of validity [198,199,202–207]. This can make recognising the limitations of some specific KA-based CSI models difficult, without looking in-depth at the specific implementation and through exploratory use of the model. An overview on the early history of analytical optical scattering models and associated approximations, the origin of the KA to the anglosphere, and certain empirical modifications to the classical Beckmann-Kirchhoff scattering model [208], can be found in [199]. In [199], the author states that the Beckmann-Kirchhoff model contains a paraxial assumption that confines its applicability to small incident and scattering angles, and with inspiration from the non-paraxial Harvey-Shack scattering theory, can be empirically modified to reduce the effect.

In some of the earlier literature for the Brekhovskikh variant of the KA, it states that while the KA model used is valuable in predicting scatter for sinusoidal surfaces with small amplitude-to-period ($h/d$) ratios (i.e. shallow slopes), the model became less accurate with increasing angles of incidence, with the threshold of where this occurs

dependent on $h/d$ [198]. With some dependence on the ratio of period to illumination wavelength, the scattering theory was also shown to fail for any surface spatial frequency and incident angle for $h/d \gtrsim 0.13$ (sinusoid maximum slope $\gtrsim 47°$) as an absolute upper limit; this was shown to be related to the predicted occurrence of multiple scattering under geometrical optics. A similar result on the differences between an analytical approach and a rigorous one with changing sinusoid slope, as well as the same geometrical optics upper limit, was shown in the author's own work [209] and is briefly presented in Chapter 4.

The primary limitation for the validity of the KA can be parametrised by the well-known Brekhovskikh criterion [186,198,208,210]:

$$4\pi r_c \cos\theta \gg \lambda\,, \tag{2-13}$$

where $\lambda$ is the wavelength of light, $r_c$ is the radius of curvature at some surface point, and $\theta$ is the local angle of illumination incidence, i.e. between the plane that the KA assumes and the incident wavevector. Other criteria that have been used are given in Ogilvy [211], including one criterion that depends on the cube of the cosine of the angle of incidence relative to the mean plane, and another simply stating $r_c \leq 3\lambda$. However, Ogilvy argues that these criteria are all the result of geometrical arguments, and therefore that more rigorous arguments are required for a more accurate understanding. Ogilvy states that the literature (up to 1991) demonstrated that the most important requirement is that the wavelength is much greater than the surface correlation length ($\lambda/\lambda_0 > 1$), with the ratio of wavelength to surface root-mean-square deviation (RMS) also being important ($\lambda/\sigma > 1$). In either case, while criteria can be useful, establishing the regions of validity of the KA for a range of surface geometries is best done by comparing results from a KA-based model to experimental measurements or to a rigorous model that has been verified experimentally.

While the primary limitation of the KA is a lower limit to the surface's radius of curvature, KA-based CSI modelling approaches almost always make some other simplifications to make the problem tractable and the model easier to calculate. They often neglect multiple scattering and cannot readily handle shadowing, cannot handle surface overhangs or undercuts, typically neglect angular and polarisation-dependence of the reflection coefficient (an acceptable assumption for a perfect conductor), and neglect for metals, metal-specific interactions such as surface plasmons. While

modifications can be made to compensate for some of these assumptions, they cannot fundamentally be overcome for all surfaces. For more complex or rough surfaces for which the KA is not entirely valid, the use of non-linear models based on Maxwell's equations is necessary to obtain accurate scatter.

### 2.4.3 Non-linear models

The analysis applied to fringe patterns recorded by CSI instrumentation typically acquires the height at each point on the surface by assuming linear specular scattering of the illumination off the surface, collected by the objective optic and focussed onto a detector. This approach assumes that multiple scattering is negligible and ignores other wave effects that could occur; for some surfaces these effects can distort or mask the expected "linear" fringe pattern, leading to data dropout or erroneous height values [39]. One example of this is for vee-groove structures [49,175,178], with fringes shown in Figure 2.11. The inverted vee-shaped fringes are produced by multiple reflections and are misinterpreted by surface reconstruction methods [49]. For more advanced methods of surface reconstruction to be developed that can handle these surfaces, such as iteratively improving the estimate by minimising the difference between measured and modelled data [49], fast and accurate fringe models for such surfaces must first be developed. As described in Chapter 1, such a model is also valuable for evaluating measurement uncertainty.

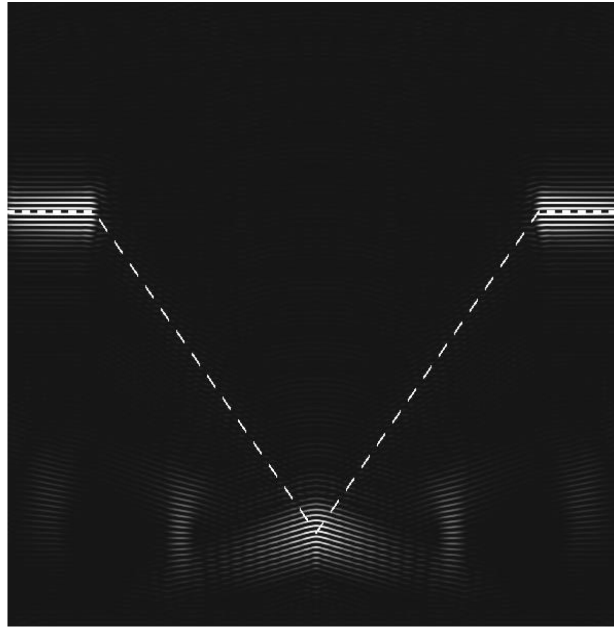

**Figure 2.11**. Modelled CSI fringes using a rigorous method for a vee-groove surface (Silicon vee-groove, 70° dihedral angle, 20 μm deep, NA = 0.55, λ = 600 nm to 700 nm). Only the positive parts of the fringes are shown, with the dashed-white line marking the true surface topography. Figure first used in [49] and is re-used in [209]; reproduced here with permission.

For complex arbitrary surfaces, including those with step heights or discontinuities, a rigorous model based on numerical techniques that solve Maxwell's equations must be used, especially in the case where multiple scattering is not negligible. Here "rigorous" means "based on Maxwell's equations, with solutions that converge towards those that Maxwell's equations would predict as the number of sample points is increased towards infinity". Using computational electromagnetic (CEM) approaches [212,213] such as finite element methods (FEM) [49,179,188], boundary element methods (BEM) [51,52], finite difference time domain methods (FDTD) [170], and rigorous-coupled wave-equation methods (RCWA) [179,189], rigorous CSI models have been made to predict fringe data more accurately. Such models have been used as a reference to compare simpler analytical models against, and to investigate complex and high-aspect ratio surfaces [49,170,188,179,189,214–216]. Rigorous models from other kinds of interferometry can also be adapted for CSI [217–219][5]. Note that some of these CSI models have only been published in the last few years, and that each model tends to

[5] The cited references primarily cover rigorous modelling of phase-shifting polarization interferometry. Information concerning adaption of the RCWA model used there for CSI was provided in private correspondence with Peter de Groot.

come with certain fundamental or computational limitations: e.g., reduced dimensionality of input surfaces or the imaging process [188], which may include compensating for the missing dimensionality with a less-rigorous approach [179]. In some cases, the model may handle multiple dimensions and polychromatic CSI illumination in principle, but the calculation of scatter for the surfaces of interest can take too long without artificially limiting the scope of the model [179,188]. In other cases, dimensionality is intentionally reduced at the theory stage to make the computational modelling faster, such as considering the scalar Helmholtz equation [49,51]; extending these models to 3D requires further theory development [220]. Each model tends to handle scatter propagation and imaging slightly differently, implemented to differing degrees of rigour, suiting the specific problem considered. The modelling code used is also typically not publicly available.

The work carried out by Coupland et al. [49] makes use of FEM to produce CSI interferograms expected for measuring vee-grooves and step artefacts, demonstrating the multiple scattering effect (seen in Figure 2.11). These predicted fringes are in good agreement with the measurements of real vee-grooves [175]. Other work has shown that analysis of the scattering can provide the dihedral angle of the vee-groove [178]. Similarly, diffraction effects found in CSI measurements of trenches have been examined in [221], with rigorous numerical evaluations of vector diffractions for a trench compared to experimental results. Later on in [49], from an initial FEM model of the horizontal parts of a step artefact, with the initial geometry of the artefact provided by a priori manufacturing data, a so-called "second order" interferogram can be calculated that is able to reveal the vertical wall of the step. Furthermore, this process can be applied iteratively to produce better estimates of the surface for more complex step artefact geometries.

In work by de Groot et al. [189], CSI measurement of optically-unresolved features is achieved through the use of RCWA modelling, for etched silicon surfaces with depths and pitches less than the wavelength of light. In general, CSI measurement will underestimate the etch depth (or step height) for these high spatial frequency grating structures, but by predicting through modelling the measured step heights for a range of "true" etch depths, the relationship between them can be found and a look-up table produced. CSI measurements can be corrected using this look-up table, and these

corrected measurements are compared against atomic force microscopy (AFM) measurements with good agreement.

In the last two years, a number of different approaches for modelling CSI have also been developed by Pahl et al. [170,188,179,216]. Both an FEM and RCWA scattering model are considered in [179], using the open source FEM software Netgen/NGSolve [222] and RCWA commercial software Unigit [223] to solve the surface-light interaction. The image formation in CSI is then calculated by an analytical approximation based on Kirchhoff's diffraction integral. Results are compared to each other, to simpler models, and to measurement data for grating structures. They conclude that rigorous models can be more useful than analytical approaches even when the number of dimensions considered are limited.

In [170], rigorous 2D modelling is used to compute the scattered near field, which is then combined with a Fourier optics treatment of image formation. FEM modelling is again achieved using NGSolve (but here for the near field), while a commercial FDTD called Lumerical [224] is used for comparison, with identical results obtained. The paper introduces models based on these two methods and points to potential areas of application, including for rectangular gratings. In [188] the work in [170] is improved on, with different CEM modelling approaches discussed in detail and comparisons made between different combinations of surface structure dimensionality and image formation dimensionality. The image formation approach is improved to 3D, and the FEM model extended to conical illumination and detection and for arbitrary materials, by considering the 2D case of the vector wave equation rather than the scalar Helmholtz equation. The near-field scatter is found using FEM along a line near to the surface, and the far-field scatter found through eigenvalue expansion (similar to a Fourier transform), though other methods are acknowledged. While the FEM model effectively remains 2D, by considering a prismatic grating surface, the vector electric field can still be considered, and the 3D problem tackled. In their latest relevant publication [216], the model is extended to describe the entire measuring process including the depth scan, and this extended model (alongside measurement data) is used as a reference for comparisons between three different analytical approaches previously mentioned in section 2.4.2 [183].

Presented in this thesis is a new CSI model, based on a rigorous 2D BEM optical scattering model produced at Loughborough University. To synthesise CSI fringe images such as in Figure 2.6, this BEM-CSI model obtains the scatter from the BEM model for illumination from multiple angles and multiple wavelengths, combines them together, and considers some basic imaging theory. Publications involving the BEM model directly include [209,225–228], while publications that use the BEM model directly include [50–52]. Details about the BEM model are given in Chapter 4, while details about the CSI model are given in Chapter 5.

## 2.5 Scalar scattering and imaging theory

Scalar scattering theory is the common foundation of the foil model used in Chapter 3, the BEM model used in Chapter 4, and the imaging theory of the BEM-CSI model used in Chapter 5 and Chapter 6. In addition, the backpropagation imaging theory is for the most part common between the foil model and the BEM-CSI model. As such, the scalar scattering theory and imaging by backpropagation is outlined here, and the expressions given referred to across subsequent chapters.

### 2.5.1 Scalar scattering theory

Following the method outlined in [229] (and repeated partially in [88,184,185]), the scalar Helmholtz equation (aka the time independent wave equation) is taken as

$$\nabla^2 E(\mathbf{r}) + k_0^2 n^2(\mathbf{r}) E(\mathbf{r}) = 0, \tag{2-14}$$

where the dependence on the wavelength of light for electric field $E(\mathbf{r})$ and refractive index $n(\mathbf{r})$ has been omitted, and where the angular wavenumber is given by $k_0 = \frac{2\pi}{\lambda_0}$ for illumination wavelength $\lambda_0$. This equation is found considering a monochromatic electromagnetic field incident on a linear isotropic nonmagnetic medium occupying some finite domain that contains no electromagnetic sources (the illuminated object), surrounded by a vacuum. The electric field $E(\mathbf{r})$ can without approximation be considered as the sum of two electric fields, the incident field $E_r(\mathbf{r})$ and the scattered field $E_s(\mathbf{r})$:

$$E(\mathbf{r}) = E_r(\mathbf{r}) + E_s(\mathbf{r}). \tag{2-15}$$

The incident field is chosen to be the field that would exist were the illuminated object to be absent, while the scattered field is defined directly by Eq. (2-15) and effectively represents the additional field produced by the presence of the illuminated object. From this description, the incident field $E_r(\mathbf{r})$ can be defined by

$$(\nabla^2 + k_0^2)E_r(\mathbf{r}) = 0, \tag{2-16}$$

as $n(\mathbf{r}) = 1$ for all $\mathbf{r}$ in the absence of the object. By also making the substitution

$$n^2(\mathbf{r}) = \big(1 - 2\Delta(\mathbf{r})\big), \tag{2-17}$$

$$\Delta(\mathbf{r}) = \big(1 - n^2(\mathbf{r})\big)/2, \tag{2-18}$$

where $\Delta(\mathbf{r})$ is the refractive index contrast, and substituting Eq. (2-16) and Eq. (2-17) into Eq. (2-14), the inhomogeneous Helmholtz equation is obtained

$$(\nabla^2 + k_0^2[1 - 2\Delta(\mathbf{r})])E_s(\mathbf{r}) = 2k_0^2\Delta(\mathbf{r})E_r(\mathbf{r}), \tag{2-19}$$

$$(\nabla^2 + k_0^2)E_s(\mathbf{r}) = 2k_0^2\Delta(\mathbf{r})\big(E_r(\mathbf{r}) + E_s(\mathbf{r})\big), \tag{2-20}$$

$$(\nabla^2 + k_0^2)E_s(\mathbf{r}) = -4\pi F(\mathbf{r})E(\mathbf{r}) = U(\mathbf{r}). \tag{2-21}$$

Note that Eq. (2-19), (2-20) and (2-21) are all the same equation written in different forms, where for Eq. (2-21) the scattering potential of the medium $F(\mathbf{r})$ is given by

$$F(\mathbf{r}) = \frac{1}{4\pi}k_0^2[n^2(\mathbf{r}) - 1] = -\frac{1}{2\pi}k_0^2\Delta(\mathbf{r}). \tag{2-22}$$

In Eq. (2-21) the substitution $U(\mathbf{r}) = -4\pi F(\mathbf{r})E(\mathbf{r})$ is also introduced for convenience, as it can be considered the source term for a free-space scalar wave equation with source terms present. Also note that $\Delta(\mathbf{r})$, and thus both $F(\mathbf{r})$ and $U(\mathbf{r})$, are 0 for values of $\mathbf{r}$ not within the object. Next, the inhomogeneous Helmholtz equation is converted into an integral equation by making use of Green's functions. First, the Green's function $G(\mathbf{r})$ associated with the inhomogeneous Helmholtz equation is, by definition, a solution of

$$(\nabla^2 + k_0^2)G(\mathbf{r}) = -\delta^{(3)}(\mathbf{r}), \tag{2-23}$$

where $\delta^{(3)}(\mathbf{r})$ is the 3D Dirac delta function. By combining this with Eq. (2-21), considering the geometry described in Figure 2.12, and applying Green's theorem (Green's second identity), the expression

$$E_s(\mathbf{r}) = +4\pi \int_{\Omega} F(\mathbf{r}')E(\mathbf{r}')G(\mathbf{r}-\mathbf{r}')\,\mathrm{d}^3r' - \int_{S_R} \left[E(\mathbf{r}')\frac{\partial G(\mathbf{r}-\mathbf{r}')}{\partial n'} - G(\mathbf{r}-\mathbf{r}')\frac{\partial E(\mathbf{r}')}{\partial n'}\right]\mathrm{d}S_R, \tag{2-24}$$

is obtained. Within the surface integral, $\mathbf{r}'$ is limited to the boundary of $S_R$; within the volume integral, $\mathbf{r}'$ is integrated over all space (denoted by $\mathrm{d}^3r'$) but non-zero contributions to the integral occur only when $F(\mathbf{r}') \neq 0$, i.e., when $\mathbf{r}'$ is inside the scatterer. Here the $\frac{\partial}{\partial n'}$ operator is an outward surface normal derivative. Note that Eq. (2-24) is strongly connected to Eq. (4-1) and Eq. (4-2).

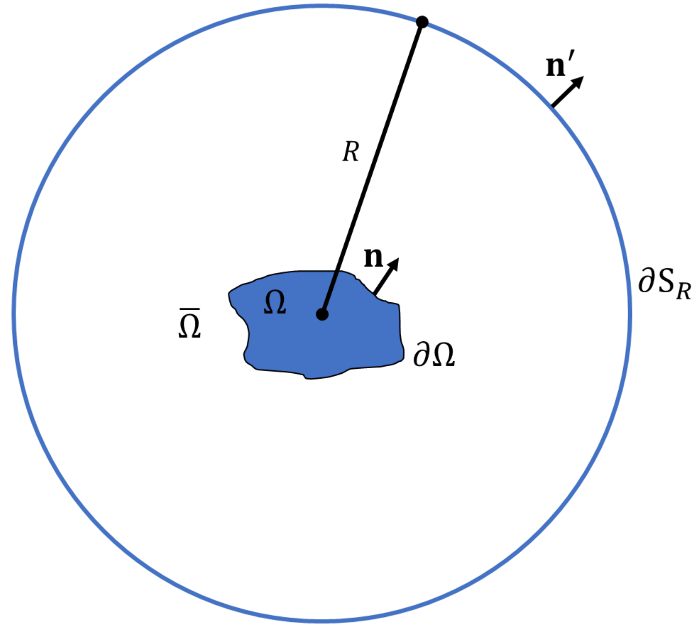


**Figure 2.12.** Geometry used for the derivation of Eq. (2-24) following the approach in [229], where a large sphere $S_R$ with radius $R$ and surface element $\partial S_R$ contains a volume $\Omega + \bar{\Omega}$ (which includes the scatterer volume $\Omega$).

As outlined in [229], by choosing a specific Green's function that satisfies Eq. (2-23) and considering that the scattered field will act as a spherical wave sufficiently far away from the scatterer, i.e. by assuming the Sommerfeld radiation condition, this expression can be simplified to just

$$\begin{aligned} E_s(\mathbf{r}) &= 4\pi \int_{-\infty}^{+\infty} G(\mathbf{r}-\mathbf{r}')F(\mathbf{r}')E(\mathbf{r}')\,\mathrm{d}^3r' \\ &= -\int_{-\infty}^{+\infty} G(\mathbf{r}-\mathbf{r}')U(\mathbf{r}')\,\mathrm{d}^3r' \\ &= -G(\mathbf{r}) \otimes U(\mathbf{r}). \end{aligned} \tag{2-25}$$

where here $\otimes$ is the operator for a convolution, and where

$$G(\mathbf{r}) = \frac{e^{ik_0|\mathbf{r}|}}{4\pi|\mathbf{r}|} \tag{2-26}$$

was chosen, where $i = \sqrt{-1}$. Eq. (2-26) is known as outgoing free-space Green's function of the Helmholtz operator, as the phase increases as $|\mathbf{r}| \to \infty$. Note that the function is symmetrical, i.e., $G(\mathbf{r}) = G(-\mathbf{r})$. The form of this solution depends on the dimensions of space considered, with the 3D form given in Eq. (2-26). Note that despite this simpler expression, the scattered field (or total field) for some chosen incident illumination in general must first be found within the volume of the object, from which the field outside the volume can then be found. Also note that the $4\pi$ in the denominator is a consequence of choosing the RHS of Eq. (2-23) to be $-\delta(\mathbf{r})$, rather than $-4\pi\delta(\mathbf{r})$ as seen elsewhere [229]; this is connected to choosing to neatly express the solution in terms of either $F(\mathbf{r})E(\mathbf{r})$ or in terms of $U(\mathbf{r})$.

A far-field approximation for this Green's function is then considered, shown in Figure 2.13. First, the coordinate origin is chosen without loss of generality to lie within the object. Second, it is assumed that the object is small relative to the distance considered for the far field, i.e., all $\mathbf{r}$ vectors that lie within the object are small relative to any $\mathbf{r}$ vectors to be chosen to calculate the scattered far field at. Then, for object coordinate $\mathbf{r}'$ and far field coordinate $\mathbf{r} = r\hat{\mathbf{s}}$ from the origin (for scalar radius $r$ and unit vector $\hat{\mathbf{s}}$), then $|\mathbf{r}-\mathbf{r}'| \approx |\mathbf{r}| - \frac{\mathbf{r}\cdot\mathbf{r}'}{|\mathbf{r}|} = r - \hat{\mathbf{s}}\cdot\mathbf{r}'$.

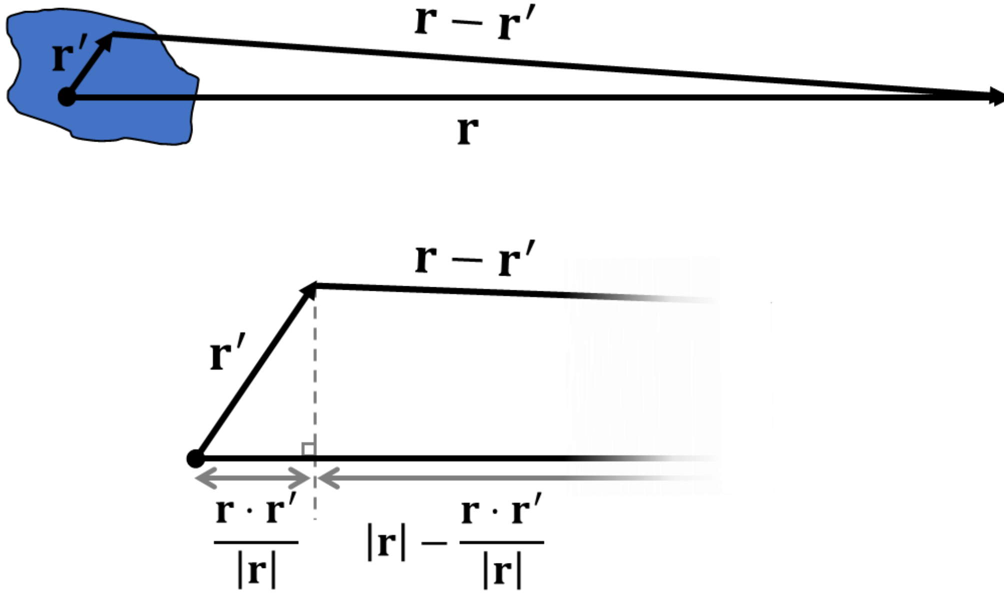


**Figure 2.13.** Geometry used for the derivation of Eq. (2-27) , where $\mathbf{r}$ is much larger than $\mathbf{r}'$, showing geometrically how $|\mathbf{r}-\mathbf{r}'| \approx |\mathbf{r}| - \frac{\mathbf{r}\cdot\mathbf{r}'}{|\mathbf{r}|}$ for approximately parallel lines.

From this approximation for $|\mathbf{r}-\mathbf{r}'|$, the Green's function can be approximated to

$$G(\mathbf{r}-\mathbf{r}') = \frac{e^{ik_0|\mathbf{r}-\mathbf{r}'|}}{4\pi|\mathbf{r}-\mathbf{r}'|} \approx \frac{e^{ik_0 r}}{4\pi r} e^{-ik_0\hat{\mathbf{s}}\cdot\mathbf{r}'}, \tag{2-27}$$

and therefore, from Eq. (2-25), under this far-field approximation, the far-field scatter can be described as

$$\begin{aligned} E_s(r\hat{\mathbf{s}};\hat{\mathbf{s}}_\mathrm{i}) &= -\frac{e^{ik_0 r}}{4\pi r}\int_{-\infty}^{+\infty} U(\mathbf{r}';\hat{\mathbf{s}},\hat{\mathbf{s}}_\mathrm{i})\, e^{-ik_0\hat{\mathbf{s}}\cdot\mathbf{r}'}\mathrm{d}^3 r' \\ &= \frac{e^{ik_0 r}}{r}\int_{-\infty}^{+\infty} F(\mathbf{r}')E(\mathbf{r}';\hat{\mathbf{s}},\hat{\mathbf{s}}_\mathrm{i})e^{-ik_0\hat{\mathbf{s}}\cdot\mathbf{r}'}\mathrm{d}^3 r' \\ &= f(\hat{\mathbf{s}},\hat{\mathbf{s}}_\mathrm{i})\frac{e^{ik_0 r}}{r}, \end{aligned} \tag{2-28}$$

where the single indefinite integral and $\mathrm{d}^3 r'$ represents a 3D integral of vector $\mathbf{r}'$ over all space along the components of $\mathbf{r}'$ (i.e. $\iiint \cdot\, \mathrm{dx\,dy\,dz}$), and where the scattering amplitude $f(\hat{\mathbf{s}},\hat{\mathbf{s}}_\mathrm{i})$ has been defined above as

$$\begin{aligned} f(\hat{\mathbf{s}},\hat{\mathbf{s}}_{\rm i}) &= -\frac{1}{4\pi}\int_{-\infty}^{+\infty} U(\mathbf{r}';\hat{\mathbf{s}},\hat{\mathbf{s}}_{\rm i})\, e^{-ik_0\hat{\mathbf{s}}\cdot\mathbf{r}'}\mathrm{d}^3r' \\ &= \int_{-\infty}^{+\infty} F(\mathbf{r}')E(\mathbf{r}';\hat{\mathbf{s}},\hat{\mathbf{s}}_{\rm i})e^{-ik_0\hat{\mathbf{s}}\cdot\mathbf{r}'}\,\mathrm{d}^3r'. \end{aligned} \tag{2-29}$$

The parameter $\hat{\mathbf{s}}_{\rm i}$ is introduced in Eq. (2-28) to denote that the scattering amplitude (and therefore the far-field scattered field) is dependent on the incident field chosen; here a plane wave incident field given by $E_r(\mathbf{r}) = e^{ik_0\hat{\mathbf{s}}_{\rm i}\cdot\mathbf{r}}$ with wavevector $\mathbf{k}_{\rm inc} = k_0\hat{\mathbf{s}}_{\rm i}$ has been reasonably assumed. This dependence originates simply because the total field $E(\mathbf{r}';\hat{\mathbf{s}},\hat{\mathbf{s}}_{\rm i})$ is equal to the sum of the scattered field and the incident field per Eq. (2-15). Also note that $k_0\hat{\mathbf{s}}$ in Eq. (2-28) likewise can be considered as the observation wavevector $\mathbf{k}_{\rm s} = k_0\hat{\mathbf{s}}$, and as such, the scattering amplitude $f(\hat{\mathbf{s}},\hat{\mathbf{s}}_{\rm i})$ can also equally be described using $f'(\mathbf{k}_{\rm s},\mathbf{k}_{\rm i})$ where $f'$ is defined by $f'(k_0\hat{\mathbf{s}},k_0\hat{\mathbf{s}}_{\rm i}) = f(\hat{\mathbf{s}},\hat{\mathbf{s}}_{\rm i})$.

The approach that provides Eq. (2-25) and the resulting expression for the scattered field $E_s(\mathbf{r})$ given in Eq. (2-28) are not the only result for scattered field that can be obtained. By taking care to handle the Green's function's singularity at $\mathbf{r} = \mathbf{r}'$ for Eq. (2-24) and considering different geometries, different expressions are obtained, given elsewhere [141,230]. Typically, these expressions describe the scattered field at a specific point inside a volume, determined by a surface integral over the surface boundary of the scatterer, or the specific field at some point in space by the boundary field. The approach taken to obtain Eq. (2-25) and Eq. (2-28) following that in [229] is nonetheless presented here as Eq. (2-25) remains the basis for much of the work that some of this thesis is based on, e.g. Chapter 3 and in [88,184,185].

If Eq. (2-28) is considered in reverse, it states that from measurements of the scattered field, information about the source spectrum $U(\mathbf{r})$ or scattering amplitude $f(\hat{\mathbf{s}},\hat{\mathbf{s}}_{\rm i})$ can be obtained. Due to the presence of the exponential term $e^{-ik_0\hat{\mathbf{s}}\cdot\mathbf{r}'}$, the integral can be considered a Fourier transform to $k$-space coordinate $\mathbf{k}_{\rm s} = k_0\hat{\mathbf{s}}$ such that, from Eq. (2-28) the expression

$$\begin{aligned} E_s(r\hat{\mathbf{s}};\hat{\mathbf{s}}_{\rm i}) &= -\frac{e^{ik_0r}}{4\pi r}\int_{-\infty}^{+\infty} U(\mathbf{r}';\hat{\mathbf{s}}_{\rm i})\, e^{-ik_0\hat{\mathbf{s}}\cdot\mathbf{r}'}\mathrm{d}^3r' \\ &= -\frac{e^{ik_0r}}{4\pi r}\widetilde{U}(k_0\hat{\mathbf{s}};\hat{\mathbf{s}}_{\rm i}), \end{aligned} \tag{2-30}$$

is obtained, which can be rewritten as

$$\widetilde{U}(k_0\hat{\mathbf{s}};\hat{\mathbf{s}}_\mathrm{i}) = -4\pi r\, e^{-ik_0 r} E_s(r\hat{\mathbf{s}};\hat{\mathbf{s}}_\mathrm{i}). \tag{2-31}$$

Here the tilde over a function denotes the relationship $\tilde{B}(\mathbf{k}) = \mathcal{F}\{B(\mathbf{r})\}$, where $\mathcal{F}\{\cdot\}$ denotes taking the Fourier transform. Clearly the function $\widetilde{U}(\mathbf{k};\hat{\mathbf{s}}_\mathrm{i})$ for any $\mathbf{k}$ is given values by Eq. (2-31) only along the surface of a sphere of radius $k_0$ in $k$-space, and is undefined elsewhere. Note that Eq. (2-31) can also be expressed in terms of $f(\hat{\mathbf{s}},\hat{\mathbf{s}}_\mathrm{i})$ as

$$\widetilde{U}(k_0\hat{\mathbf{s}};\hat{\mathbf{s}}_0) = -4\pi f(\hat{\mathbf{s}},\hat{\mathbf{s}}_\mathrm{i}) = -4\pi f'(k_0\hat{\mathbf{s}},k_0\hat{\mathbf{s}}_\mathrm{i}). \tag{2-32}$$

The approach taken in explaining the theory typically diverges here when considering an approximate linear model. For a linear model, an approximation such as the Born approximation or KA is taken, reducing the total field $E(\mathbf{r}';\hat{\mathbf{s}},\hat{\mathbf{s}}_\mathrm{i})$ present in Eq. (2-28) or (2-29) to remove its explicit dependence on the scattered field, from which further expressions and relations can be obtained. In the Kirchhoff case in particular, the integral theorem of Helmholtz and Kirchhoff is used to obtain an expression for the scattered field, instead of Eq. (2-28) [141,230]. Then the scattering potential $F(\mathbf{r})$, which is a function of the object only, can be related to the scattering amplitude $f(\hat{\mathbf{s}},\hat{\mathbf{s}}_\mathrm{i})$, such that the scattering amplitude in the direction $\hat{\mathbf{s}}$ for incident light $\hat{\mathbf{s}}_\mathrm{i}$ is given entirely by $f(\hat{\mathbf{s}},\hat{\mathbf{s}}_\mathrm{i}) = \tilde{F}(\mathbf{K})$ where $\mathbf{K} = k_0(\hat{\mathbf{s}} - \hat{\mathbf{s}}_\mathrm{i})$ and $\tilde{F}(\mathbf{k}) = \mathcal{F}\{F(\mathbf{r})\}$. In this case, the scattering amplitude is dependent only on the object function and on $\hat{\mathbf{s}} - \hat{\mathbf{s}}_\mathrm{i}$, rather than on $\hat{\mathbf{s}}$ and $\hat{\mathbf{s}}_\mathrm{i}$ separately. Some of this theory is given in Chapter 3. This $k$-space approach to describing the theory of optical instruments is similar to that used in optical coherence tomography, which is described in detail elsewhere [231].

For non-linear models, the scattering amplitude cannot be so simply related to the object function, which prevents the combined scattering and imaging process from being simply described as just a linear filtering operation of instrument transfer function with object spectrum function, as in the linear case [185]. However, even without this capability, it is still possible to make use of the same scalar theory mathematical framework to describe the imaging of an object by an optical instrument in the non-linear case where neither the Born or Kirchhoff approximations have been taken.

### 2.5.2 Imaging theory by back-propagation of far-field scatter

A reconstructed field $E_m(\mathbf{r}_\mathrm{m})$ can be considered to represent the measured field a microscope instrument can capture from the object. In other words, the measured field measured by a CCD sensor at the image plane of an instrument can be considered the

same as the reconstructed scattered field present at object plane. For an instrument that scans the object axially, the reconstructed scattered field at each scan location is collected in focus, so that the measured field across a scan can be obtained just by finding the reconstructed scattered field over the volume scanned, i.e., for each object plane considered. However, a filter must also be applied to the field to account for the limited NA of the instrument. The reconstructed scattered field, and therefore the measured field, is obtained through back-propagation of the far-field scattered field back to the object, while also accounting for this limited NA. The integral theorem of Helmholtz and Kirchhoff, also known as the Kirchhoff integral theorem, which can be derived from Eq. (2-24) through different geometric considerations [230], is given in [184] by the expression

$$E_m(\mathbf{r}_\mathrm{m}) = -\int_\Sigma \left[ E_s(\mathbf{r}_\mathrm{s}) \frac{\partial G^*(\mathbf{r}_\mathrm{m} - \mathbf{r}_\mathrm{s})}{\partial n} - G^*(\mathbf{r}_\mathrm{m} - \mathbf{r}_\mathrm{s}) \frac{\partial E_s(\mathbf{r}_\mathrm{s})}{\partial n} \right] \mathrm{d}\Sigma. \tag{2-33}$$

This expression describes the back-propagation for the geometry given in Figure 2.14, where $\mathbf{r}_\mathrm{s}$ is bound to the surface of sphere $\Sigma$ and $\mathbf{r}_\mathrm{m}$ is a point near or within the scatterer. As back-propagation is considered from the far field, the complex conjugate of the outgoing Green's function $G^*(\mathbf{r})$ is used, i.e., a point sink, given by

$$G^*(\mathbf{r}_\mathrm{m} - \mathbf{r}_\mathrm{s}) = G^*(\mathbf{r}_\mathrm{s} - \mathbf{r}_\mathrm{m}) = \frac{e^{-ik_0 r_\mathrm{s}}}{4\pi r_\mathrm{s}} e^{ik_0 \hat{\mathbf{s}}_\mathrm{s} \cdot \mathbf{r}_\mathrm{m}}, \tag{2-34}$$

where $\mathbf{r}_\mathrm{s} = r_\mathrm{s} \hat{\mathbf{s}}_\mathrm{s}$.

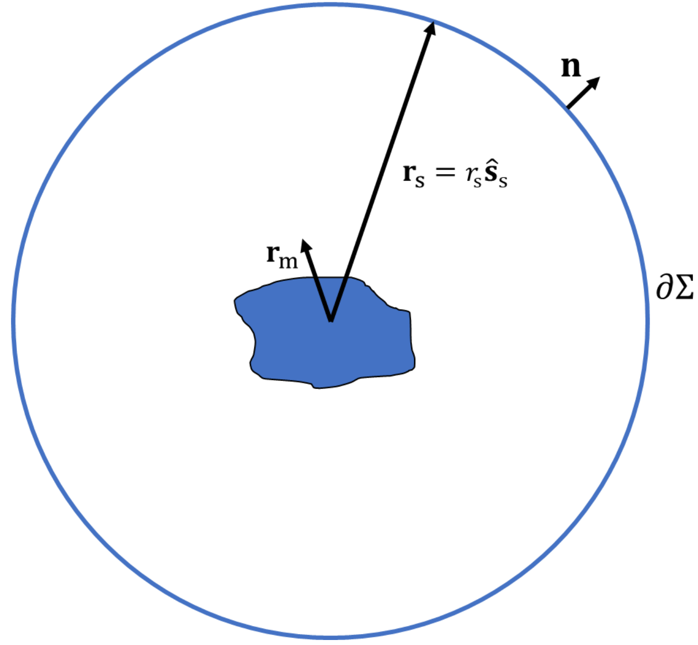


**Figure 2.14.** Geometry used for the derivation of Eq. (2-33). Not to scale.

Given the boundary surface Σ can be freely considered as a sphere with radius $r_\mathrm{s}$, i.e., $\mathbf{r}_\mathrm{s} = r_\mathrm{s}\hat{\mathbf{s}}_\mathrm{s}$, and as $|\mathbf{r}_\mathrm{m}| \ll |\mathbf{r}_\mathrm{s}| = r_\mathrm{s}$ under the far-field approximation, then

$$\frac{\partial G^*(\mathbf{r}_\mathrm{m} - \mathbf{r}_\mathrm{s})}{\partial n} = -ik_0 G^*(\mathbf{r}_\mathrm{m} - \mathbf{r}_\mathrm{s}), \tag{2-35}$$

$$\frac{\partial E_s(\mathbf{r}_\mathrm{s})}{\partial n} = ik_0 E_s(\mathbf{r}_\mathrm{s}), \tag{2-36}$$

where in the far field, the expression

$$\begin{aligned} \frac{d}{dr}\left(\frac{\exp(ik_0 r)}{r}\right) &= ik_0 \frac{\exp(ik_0 r)}{r} - \frac{\exp(ik_0 r)}{r^2} \\ &\approx ik_0 \frac{\exp(ik_0 r)}{r} \text{ as } r \to \infty, \end{aligned} \tag{2-37}$$

has been used, and the scattered field from Eq. (2-28) is given by $E_s(\mathbf{r}_\mathrm{s}) = f(\hat{\mathbf{s}}_\mathrm{s}, \hat{\mathbf{s}}_\mathrm{i}) \frac{e^{ik_0 r_\mathrm{s}}}{r_\mathrm{s}}$.

Substituting Eq. (2-35) and Eq. (2-36) into Eq. (2-33) gives

$$E_m(\mathbf{r}_\mathrm{m}) = 2ik_0 \int_\Sigma G^*(\mathbf{r}_\mathrm{m} - \mathbf{r}_\mathrm{s}) E_s(\mathbf{r}_\mathrm{s})\, \mathrm{d}\Sigma. \tag{2-38}$$

Note that for an NA limited instrument, only a limited range of far-field scatter will be present, which can be described by modifying the Green's function to describe only a cap of a spherical shell. However, doing this will be postponed.

Substituting $E_s(\mathbf{r}_\mathrm{s})$ in terms of $U(\mathbf{r}';\hat{\mathbf{s}}_\mathrm{i})$ as given in Eq. (2-30), and $G^*(\mathbf{r}_\mathrm{m}-\mathbf{r}_\mathrm{s})$ given in Eq. (2-34), gives

$$E_m(\mathbf{r}_\mathrm{m}) = -\frac{ik_0}{8\pi^2 r_\mathrm{s}^2}\int_\Sigma\left[\iint_{-\infty}^{+\infty} U(\mathbf{r}')e^{-ik_0\hat{\mathbf{s}}_\mathrm{s}\cdot\mathbf{r}'}\,\mathrm{d}^3r'\right]e^{ik_0\hat{\mathbf{s}}_\mathrm{s}\cdot\mathbf{r}_\mathrm{m}}\,\mathrm{d}\Sigma. \tag{2-39}$$

Note that the dependence on the direction of incident illumination $\hat{\mathbf{s}}_\mathrm{i}$ for $U(\mathbf{r}';\hat{\mathbf{s}}_\mathrm{i})$ has been omitted for clarity. The integral of $\mathbf{r}_\mathrm{s} = r_\mathrm{s}\hat{\mathbf{s}}_\mathrm{s}$ over the shell $\Sigma$ can be more explicitly expressed as an indefinite integral,

$$E_m(\mathbf{r}_\mathrm{m}) = -\frac{ik_0}{8\pi^2 r_\mathrm{s}^2}\int_{-\infty}^{+\infty}\left[\iint_{-\infty}^{+\infty} U(\mathbf{r}')e^{-ik_0\hat{\mathbf{s}}_b\cdot\mathbf{r}'}\,\mathrm{d}^3r'\right]e^{ik_0\hat{\mathbf{s}}_b\cdot\mathbf{r}_\mathrm{m}}\delta(|\mathbf{r}_b|-r_\mathrm{s})\,\mathrm{d}^3\mathbf{r}_b, \tag{2-40}$$

where $\mathrm{d}^3\mathbf{r}_b$ has been used to represent the three-dimensional integral over all real space by parameter $\mathbf{r}_b$, where the general position vector $\mathbf{r}_b$ is a replacement to the limited $\mathbf{r}_\mathrm{s}$ (in general $\mathbf{r}_b \neq r_s\hat{\mathbf{s}}_\mathrm{s}$ for constant $r_s$, and $\hat{\mathbf{s}}_\mathrm{s} = \hat{\mathbf{s}}_b$), and a 1D Dirac delta function is used to limit the contributing values of the integral to only $\mathbf{r}_b$ that lie on the shell $\Sigma$. Note that $r_b$ in the polar representation of the coordinate $\mathbf{r}_b = r_b\hat{\mathbf{s}}_b$ is not a constant. Also note that the 1D Dirac delta $\delta(|\mathbf{r}|)$ takes only scalar arguments; when the arguments are exclusively the modulus of a vector then the function can be related to the 3D Dirac delta by $\delta^{(3)}(\mathbf{r}) = \delta(|\mathbf{r}|)$.

By further making the substitution $\mathbf{r}_b/r_s = \mathbf{k}'/k_0$ (where in general $\mathbf{r}_b/r_s = \mathbf{k}'/k_0 \neq \hat{\mathbf{s}}_b$), which defines $\mathbf{k}'$ and implies that $\mathbf{r}_b/|\mathbf{r}_b| = \hat{\mathbf{s}}_b = \mathbf{k}'/|\mathbf{k}'|$, Eq. (2-40) becomes

$$E_m(\mathbf{r}_\mathrm{m}) = -\frac{i}{8\pi^2 k_0}\int_{-\infty}^{+\infty}\left[\iint_{-\infty}^{+\infty} U(\mathbf{r}')e^{-ik_0\frac{\mathbf{k}'}{|\mathbf{k}'|}\cdot\mathbf{r}'}\,\mathrm{d}^3r'\right]e^{ik_0\frac{\mathbf{k}'}{|\mathbf{k}'|}\cdot\mathbf{r}_\mathrm{m}}\delta(|\mathbf{k}'| - k_0)\,\mathrm{d}^3\mathbf{k}'. \tag{2-41}$$

Due to the Dirac delta function, the only values of $\mathbf{k}'$ that provide contributions to the integral are when $|\mathbf{k}'| = k_0$. Therefore, while retaining the Dirac delta function, Eq. (2-42) can equally be written as

$$E_m(\mathbf{r}_\mathrm{m}) = -\frac{i}{8\pi^2 k_0}\int_{-\infty}^{+\infty}\left[\int_{-\infty}^{+\infty} U(\mathbf{r}')e^{-i\mathbf{k}'\cdot\mathbf{r}'}\mathrm{d}^3r'\right]e^{i\mathbf{k}'\cdot\mathbf{r}_\mathrm{m}}\delta(|\mathbf{k}'| - k_0)\,\mathrm{d}^3\mathbf{k}' = -\frac{i}{8\pi^2 k_0}\int_{-\infty}^{+\infty}\widetilde{U}(\mathbf{k}')\delta(|\mathbf{k}'| - k_0)e^{i\mathbf{k}'\cdot\mathbf{r}_\mathrm{m}}\,\mathrm{d}^3\mathbf{k}', \quad (2\text{-}42)$$

where the inner-most integral has been recognised as a Fourier transform of $U(\mathbf{r}')$ from $\mathbf{r}'$to $\mathbf{k}'$. Taking the Fourier transform from $\mathbf{r}_\mathrm{m}$ to $\mathbf{k}$ on both sides of the equation gives

$$\begin{aligned}\tilde{E}_m(\mathbf{k}) &= -\frac{i}{8\pi^2 k_0}\int_{-\infty}^{+\infty}\left[\int_{-\infty}^{+\infty}\widetilde{U}(\mathbf{k}')\delta(|\mathbf{k}'| - k_0)e^{i\mathbf{k}'\cdot\mathbf{r}_\mathrm{m}}\,\mathrm{d}^3\mathbf{k}'\right]e^{-i\mathbf{k}\cdot\mathbf{r}_\mathrm{m}}\,\mathrm{d}^3\mathbf{r}_\mathrm{m} \\ &= -\frac{i}{8\pi^2 k_0}\int_{-\infty}^{+\infty}\widetilde{U}(\mathbf{k}')\delta(|\mathbf{k}'| - k_0)\delta(|\mathbf{k}-\mathbf{k}'|)\,\mathrm{d}^3\mathbf{k}' \\ &= -\frac{i}{8\pi^2 k_0}\widetilde{U}(\mathbf{k})\delta(|\mathbf{k}| - k_0),\end{aligned} \quad (2\text{-}43)$$

where $\int e^{i(\mathbf{k}-\mathbf{k}')\cdot\mathbf{r}}\,\mathrm{d}^3\mathbf{r} = \delta(|\mathbf{k}-\mathbf{k}'|)$ and $\int_{-\infty}^{+\infty} X(\mathbf{k}')\delta(|\mathbf{k}-\mathbf{k}'|)\mathrm{d}^3\mathbf{k}' = X(\mathbf{k})$ were used. This expression tells us that the spectrum of the measured field, assumed equal to the spectrum of the reconstructed scattered field, is the result of a linear filtering operation on the source spectrum. For an optical system limited by a NA, the expression $\delta(|\mathbf{k}| - k_0)$ can be replaced by $\delta(|\mathbf{k}| - k_0)H\left(\hat{\mathbf{k}}\cdot\hat{\mathbf{z}} - \sqrt{1 - A_n^2}\right)$, where $H(x)$ is the Heaviside step function and $\hat{\mathbf{z}}$ a unit vector parallel to the optical axis in the direction from the object towards the instrument.

Given that $\widetilde{U}(\mathbf{k})\delta(|\mathbf{k}| - k_0)$ is non-zero only for specific $\mathbf{k}$, then the far-field scattered field wavevector $\mathbf{k}_\mathrm{s} = k_0\hat{\mathbf{s}}_\mathrm{s}$ can once again be considered which satisfies $\widetilde{U}(\mathbf{k}_\mathrm{s})\delta(|\mathbf{k}_\mathrm{s}| - k_0) = \widetilde{U}(\mathbf{k}_\mathrm{s}) = \widetilde{U}(k_0\hat{\mathbf{s}}_\mathrm{s})$. Then, Eq. (2-43) can be given by

$$\tilde{E}_m(\mathbf{k}_\mathrm{s}) = -\frac{i}{8\pi^2 k_0}\widetilde{U}(\mathbf{k}_\mathrm{s}), \quad (2\text{-}44)$$

where, as in Eq. (2-31), the source spectrum at $\mathbf{k}_\mathrm{s}$ is given by

$$\widetilde{U}(k_0\hat{\mathbf{s}}_\mathrm{s}) = -4\pi r_s e^{-ik_0 r_s}E_s(r_s\hat{\mathbf{s}}_\mathrm{s}). \quad (2\text{-}45)$$

Combining Eq. (2-44) and Eq. (2-45) gives

$$\tilde{E}_m(k_0\hat{\mathbf{s}}_\mathrm{s}) = \frac{ir_s}{2\pi k_0} e^{-ik_0 r_s} E_s(r_s\hat{\mathbf{s}}_\mathrm{s}). \qquad (2\text{-}46)$$

In summary, the measured field spectrum along a shell in $k$-space can be obtained from the scattered field from the object obtained along at arc in the far field. Note again that this expression is for some specific incident illumination with direction $\hat{\mathbf{s}}_\mathrm{i}$, which is a factor in the determining the values of $E_s(r_s\hat{\mathbf{s}}_\mathrm{s})$. This expression for the measured field spectrum underpins both the foil model and the BEM-CSI model.

## 2.6 Outside-NA measurement

Engineered functional surfaces often feature varying slopes on macro- and micro-scales. For a mirror-like surface that only reflects light in the specular direction, the highest surface slope that can be measured by a far-field 3D optical surface measuring instrument is determined by the NA ($A_n$) of the objective lens. Light that is specularly reflected by a surface that has a slope larger than one-half of the maximum reflected ray angle ($\theta_\mathrm{NA} = \sin^{-1} A_n$) will fall outside of the acceptance cone of the instrument and not be captured [19], shown previously in Figure 2.7. However, many surfaces are not mirror-like and produce an angular distribution of scatter when illuminated; under the Abbe theory of image formation, it is the capture of this scatter that provides image contrast [22,23]. This difference is shown in Figure 2.15, and has previously been shown elsewhere [39,110,177]. The slope angle at which all the specularly scattered light is lost is referred to here as the "specular reflection slope limit" or "specular reflection limit" (SRL) for short [52]. It has previously been referred to as the "NA slope limit", "NA limit", and "specular limit" [225]. More information about the object being measured can be recorded in the image if more scattering/diffraction orders can be captured. The limited NA captures only a portion of the scatter, which determines the upper limit to both the resolution of the instrument and to the surface spatial frequencies transferred by the instrument. For interferometry specifically, an additional slope effect related to the relative size of the fringe spacing to the Airy disk can also impact the modulation depth [232]. Steeper surface slopes can also lead to a shift of signal spectra to higher wavelengths due to the larger effective wavelength of light and increasing angles of incidence and reflection, which can negatively impact surface reconstruction methods [172]. Further information on the current capability of CSI is given in section 2.3.5.

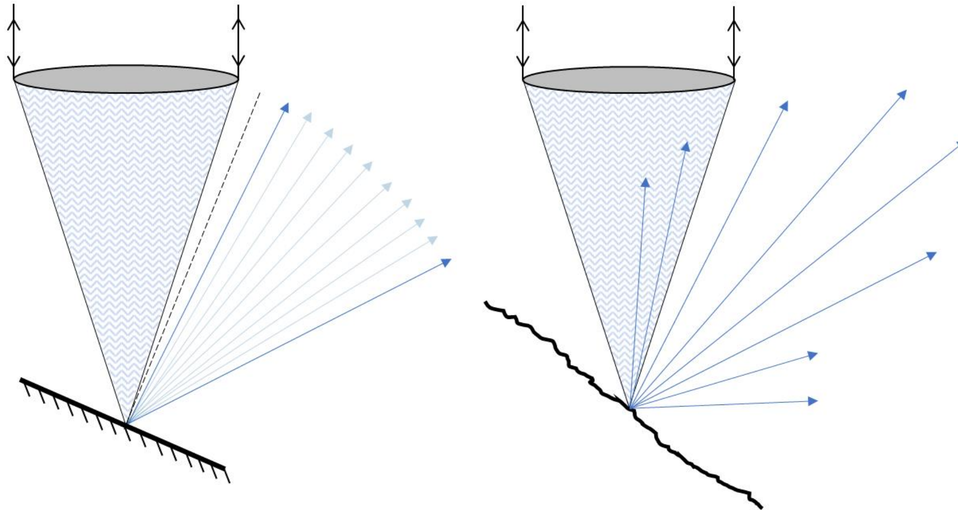

**Figure 2.15**. Diagrams illustrating the concept of collection angle for a microscope system for a tilted surface tilted beyond the acceptance angle, for a perfectly flat surface that specularly scatters (left), and for a rough surface which produces some scatter that the objective can collect. See Figure 2.7 for a diagram illustrating the connection between collection angle and a maximum tilt angle.

## 2.6.1 State of the art for outside-NA measurement

It is more difficult to obtain information from surfaces with slopes steeper than the SRL using surface topography measuring instruments than those without, as described in the previous section. One approach to solving this problem and acquiring the missing surface information is by adjusting or making use of multiple viewing angles with respect to the sample, through the use of tilt or multi-axes stages [24–26,28,233], rotating both the sample and the sensor [29], and making use of multiple sensors [30,31]. Unfortunately, such approaches are comparatively expensive, due to the additional moving parts (or additional sensors), can be slower (moving stage and making multiple measurements), require an accurate combination of measurement data, and have increased difficulty in retaining stability during a measurement. The mathematical foundations of data fusion from multiple measurements in surface metrology, including some of the challenges involved and current solutions, is reviewed in [234].

However, various instruments are capable of imaging and obtaining topography information from surfaces with slope angles well outside the specular acceptance cone, without repositioning the sample or instrument. This capability is attributed to the capture and detection of diffuse and back-scattered light from the microstructures found

on the surface slopes [32–35], which is possible due to recent advances in instrument technology and design. While this can include the capture of surface luminescence produced by, e.g. application of a fluorescent film [235], the scope here is limited to instruments that illuminate the surface and capture the resulting backscatter without the need for sample preparation. For a CSI instrument, high dynamic range measurement of parts with wide reflectance ranges can be performed through the alternation of light levels during a measurement or between sequential measurements, and dynamic noise reduction for detection of weak signals can be achieved through signal oversampling [35–37]. In [35], topography measurement of both a polymer micro-lens and a retroreflector array is achieved with measured slopes of up to 60° through the use of dynamic noise reduction, despite the 33° acceptance (half-)angle. In [36], an even wider range of surfaces with steep slopes are measured, with measurements made of a diamond-turned cone, a 3 mm diameter dealing ball, an end-mill, a fuel injector shoulder region, an electrical feed-through assembly, and a hypodermic needle. This included surfaces with recessed high slopes, and even those nearly vertical. Nevertheless, these measurements provided surface topography with slopes beyond the so-called “specular limit” of the objective lens used, for a range of different NAs. In a FV instrument, the use of ring light illumination can essentially increase the illumination NA, consequently extending the range of measurable slope angles [33,34,38]. FV instruments have also been used to measure lateral distances by detecting the location of a vertical wall precisely using a technology called “vertical focus probing” [70,147,236]. In section 3.3.2.1 and Figure 3.18 of [70], this technology is shown capturing surface texture information from a vertical wall, with results comparable to that obtained from the same surface when measured with the surface perpendicular to the optical axis.

Typically, image formation from surface slopes that are steep enough that specular reflections are lost, obtain surface information with a low SNR, which can lead to non-measured points [19,39] and high uncertainty. There is currently a lack of understanding about the instrument response to surfaces with steep slopes outside the NA cone, and in particular it is unclear over what surface spatial frequencies we can expect to accurately report texture and fine surface-feature details. The reliability of topography from regions with slopes near to and beyond the SRL is unknown [237].

Measurement of deep trenches (a.k.a. high-aspect ratio holes) is also related to outside-NA measurement. For example, patterned wafers with trenches made up of different materials present a problem for CSI, which can be handled by matching signal patterns to libraries of modelled signal signatures associated with each material and compensating for their effects to give a “true” topography [238]. The correlation between interference microscopy and scanning electron microscope (SEM) measurement of semiconductor etch depth also allows interference measurements to be taken and corrected for during the manufacturing process, where use of SEM would not be suitable [102]. In both cases, knowledge of the expected instrument response, via modelling or comparative measurement, is used to improve instrument capabilities.

### Investigation through modelling

In past literature, there has been interest in understanding the results produced from measurement of fine structures and steep surfaces, primarily through image modelling. For example, examining the diffraction orders produced from isolated step structures using a rigorous modal method, relating surface geometry parameters to the scatter produced [239]; applying the same method for square-wave gratings and isolated edges in the context of confocal imaging [240]; using a RCWA method and volume holography for image modelling of striated muscle fibres [241]; examination of periodic relief structures through differential modelling methods, improving understanding on the impact of shadowing, multiple scatter, and polarisation [242]; and generating monochromatic interferograms of step features by rigorous electromagnetic modelling, allegedly for the first time, to examine the resolution limit of interferometric measurement [243]. In particular, [243] focused on trapezoidal objects with non-vertical edges and of other structures with slanted slopes, and considered the effect of limiting the collection NA.

However, most of this older work typically involved only monochromatic, single incidence illumination, held back by the relatively limited computer hardware available in the 1990s and consequently relying on approximate first-order methods alongside the rigorous modelling. In addition, their focus was on the effect of changing the surface geometry parameters on the predominantly non-interferometric images generated by rigorous modelling, with the aim of allowing for information to be obtained from features below the lateral resolution of the instrument. A modern equivalent of this

work with less limitations considers CSI measurement of optically-unresolved features through the use of modelling in [189].

This thesis is instead concerned more with the capability and reliability of surface topography obtained from surfaces with texture and steep slopes that are challenging to optical surface topography instruments, topographies with potentially any shape, and with a focus on obtaining topography using CSI specifically (as explained in section 2.2). Capability here refers to the scope of the domain of surfaces and surface slopes for which a topography instrument can obtain accurate height information, while reliability here refers to how accurate the reported height data is for specific surfaces with varying surface slopes and spatial frequencies.

A summary of CSI models is described in section 2.4. For complex arbitrary surfaces, including those with step heights or discontinuities, a rigorous model based on numerical techniques that solve Maxwell's equations must be used, especially when multiple scattering is not negligible. Using CEM approaches such as FEM and RCWA, rigorous CSI models have been made to predict fringe data more accurately. They have been used as a reference to compare simpler analytical models against, and to investigate the fringes produced by complex and high-aspect ratio surfaces [49,170,188,179,189,214–216]. More information in the literature on CSI models and the underlying optical scattering models is given in section 2.4, with non-linear modelling specifically in section 2.4.3. In [49], a method of obtaining information from vertical slopes using iterative rigorous modelling was suggested. The work in [49] is in part the inspiration for this PhD project, and is discussed in more detail in section 2.4.3.

Presented in this thesis is a newly developed CSI model based on a rigorous BEM optical scattering model, referred to as BEM-CSI, which is used in [50–52]. In principle, BEM scales better with surface size compared to FEM and is therefore more readily extended to 3D surfaces, being better suited to the surface boundary scattering problem. The BEM and BEM-CSI models are discussed briefly in section 2.4.3 and are covered in more detail in Chapter 4 and Chapter 5 respectively. This model is used to investigate the scatter obtained by complex surfaces in Chapter 6.

## 2.7 Summary

Interferometry for surface topography measurement was previously considered to be limited to polished optical surfaces that created simple interference patterns that could be interpreted with fringe tracing or by phase shifting methods [90]. This changed in the 1990s, when it was shown that interferometric methods based on optical coherence could provide meaningful results from rough surface textures [98,99,110]. This has led to impressive growth in applications for coherence scanning interferometry (CSI), today serving the needs of many industries that rely on quality control of parts ranging from machined automotive components to additively manufactured parts [37,104,105].

Qualifying CSI instruments for specific applications often involves an empirical evaluation of measurement capability, such as a gauge repeatability and reproducibility tests [133]. Such tests do not necessarily provide insight into the best configuration of the instrument for a given measurement, nor can they predict how accurate a measurement will be for a specific part type and measurand in advance of exhaustive testing. For this reason, there are on-going efforts to build theoretical models [51,184,185,188] that represent the physical principles of measurement well enough to serve as core engines for virtual instruments [186]. The resulting virtual instruments would duplicate the response of real instruments with enough confidence to pre-configure an instrument for optimum performance, and to evaluate the associated uncertainty of measurement without a potentially lengthy empirical test. Measurement capability for various surfaces can also be investigated and identified using the theoretical models, even without uncertainty calculation. These models can be based on analytical approximations of the optical scattering problem such as the Kirchhoff approximation, or be derived rigorously from Maxwell's equations, providing greater accuracy for surfaces with sharp edges or with features that produce multiple scattering.

In recent years, technological enhancements to measurement sensitivity have extended CSI measurement capabilities to parts having surface slope angles that exceed the specular acceptance angle, defined for incoherent microscope illumination by $\theta_{\mathrm{NA}} = \sin^{-1} A_n$, where $A_n$ is the numerical aperture of the objective. This is a significant next step in the technology, allowing for measurements of spheres, cones and pyramidal structures, even with light directed at near normal incidence, using weakly-reflected light at high scattering angles [35,36]. This new practical capability poses a theoretical

challenge for researchers in an applications area where the requirement is clear: instrument users need to know under what circumstances measurement results for steeply-sloped surfaces are meaningful and have a quantifiable uncertainty. The answer to these questions will be highly dependent on the specific part type and measurement configuration, hence the need for appropriate physical models.

# Chapter 3: Lens aberration compensation of CSI using the foil model

In this chapter, an approximate coherence scanning interferometry (CSI) model is introduced, based on the Kirchhoff approximation (KA). The theory is first outlined, describing the optical process of a CSI instrument as a three-dimensional (3D) linear shift-invariant filtering operation that maps surface geometry to imaged fringes. Under this theory the instrument response of a CSI instrument is described by a 3D surface transfer function (STF). The 3D STF accounts for aspects of the optical system such as numerical aperture (NA), lens aberration, and reference mirror defocus [119,159]. A method to obtain an instrument's 3D STF through measurement of a microsphere is described and the resulting experimental 3D STFs are presented. From these experimental 3D STFs, inverse filters (IF) are generated that should compensate for the effects of lens aberration when applied to signal data captured by the instrument. From measurements of a sinusoidal grating, the topographies obtained from before and after compensation by an IF are compared both to each other and to measurements of the grating by a traceable contract stylus instrument.

Much of the work presented in this chapter was published in [159] (journal paper), with preliminary results presented earlier at SPIE Optical Engineering + Applications 2019 [244]. This work for the first time provided experimental verification of the characterisation and correction of an instrument through use of the foil model theory, reducing measurement errors through fundamental correction of the fringes. While not presented here, supporting work on the effects of interferometric defocus and on determining the lateral resolution of an instrument was published in [119] (journal paper) and presented at the 33rd ASPE Annual Meeting [144], respectively. This work was performed in collaboration with Dr Rong Su, who was an author of these publication alongside the author of this thesis.

Figures from [159] are reused here under a CC BY 4.0 license[6] without modification.

[6] https://creativecommons.org/licenses/by/4.0/

## 3.1 Introduction

As discussed in section 2.3, interference microscopy is an effective measurement method for measuring surface topography for a range of surfaces of industrial interest. As given in section 2.4, various linear and non-linear models have been developed to model CSI instruments; modelling is at the heart of understanding physical phenomena, and for CSI instruments is especially valuable due CSI's complexity and the need to analyse signal data for height estimation. For example, modelling can be used to investigate and potentially correct for instrument errors; potential instrument errors and approaches to mitigate them are discussed in section 2.3.5.

While the simplest CSI models do not even explicitly consider the propagation of light, their results are nonetheless useful in understanding real instrument data and in informing the design of height estimation algorithms [101]; this method is described in section 2.4.1. In addition, while non-linear methods can accurately model the CSI response from the widest range of surfaces, including those that are complex and produce multiple scattering (section 2.4.3), these rigorous CSI models are accompanied by some practical challenges. Not only are rigorous optical instrument models difficult to develop and verify, but their computationally demanding nature and associated hardware requirements present a serious practical problem; a specific example is briefly discussed later in section 5.6. Consequently, rigorous models are frequently accompanied by fundamental or computational limitations: e.g., reduced dimensionality and/or the use of only a monochromatic light source. There is therefore still great value in developing linear modelling methods without these limitations, capable of accurately modelling instrument response for a more limited range of surfaces but in a fraction of the time a rigorous approach would take.

More advanced linear methods, as discussed in section 2.4.2, include a method called elementary Fourier optics (EFO) [145,182,245,246], which models the scatter from a surface as the transmission of light though a thin phase grating with phase delay proportional to the corresponding surface topography. EFO is however valid only for surfaces with heights small relative to the depth of field, referred to as the "thin phase object approximation" [182]. A different linear method that is valid for a wider range of surfaces, referred to as the foil model, describes the optical process of CSI as a 3D linear shift-invariant filtering operation that maps surface geometry to imaged fringes

using a 3D STF as a filter. This filtering method is equivalent to a convolution of the surface geometry with a point spread function (PSF), obtained by a 3D inverse Fourier transform of the 3D STF. The name "foil model" is used as the surface is modelled using an infinitely thin foil-like object which follows the surface topography [88]. The foil model requires that the surface vary slowly, i.e. it relies on the KA and is based on scalar scattering theory, given in sections 2.4.2 and 2.5 respectively; the model's theory is outlined later in section 3.2 and is given in detail elsewhere [88,184,185]. The specifics of the assumptions taken by the foil model follow those originally taken by Beckmann for the KA [208], which are also given elsewhere [184,185].

Under the foil model, the effects of the instrument on the measurement process are entirely contained within a 3D STF. The 3D STF naturally includes the demodulation of the scatter from the object of interest by that from the reference mirror, producing fringes in the image plane. The values and passband (support) of the 3D STF are entirely determined by the optical system, including the illumination and collection NA (which may differ), and the spectral distribution of the illumination used in the instrument. In general, both the 3D STF and the surface spectrum can be complex valued. However, an ideal 3D STF will be exclusively real-valued, resulting in the phase of the fringe spectrum within the passband of the 3D STF matching the phase of the surface spectrum. In a real CSI instrument, problematic aspects such as optical aberration can cause retrace errors, dispersion errors, $2\pi$ errors and other slope- and spatial frequency-dependent errors in the measured height data, given in section 2.3.5. The presence of lens aberration introduces phase variation across the passband of the 3D STF, altering the phase of the measured fringe spectrum compared to the ideal case. This change to the phase of the fringes can lead to errors in height reconstruction methods as previously described, especially in regions of high slopes and low signal-to-noise ratio (SNR) [159]. In addition, the effect of non-zero reference mirror defocus can also introduce undesired phase shifts and reduce the lateral resolution of fringe images, which can lead to errors in the height estimation; this effect has been predicted by the foil model and experimentally demonstrated [119].

By obtaining through experiment the 3D STF of a real instrument, it is in principle possible to compensate for these undesired phase effects at a fundamental level by removing them from measured signal data, before height estimation methods and post-processing operations are applied [74,247]. In contrast, most error correction methods

that tackle errors such as $2\pi$ errors are applied only to the surface height data as post-processing operations. One convenient method of obtaining an experimental 3D STF is by measurement of the spherical cap of a precision microsphere [247]. Information on the tolerances of the sphere chosen are given in [248], while the use of silica microspheres manufactured through different methods are compared in [159]. Obtaining the experimental 3D STF of an instrument through measurement of a precision microsphere has been used repeatedly by Rong Su et al. with success [74,119,144,159,186,185,244]; however, any surface can be used as long as it is well known and contains all possible spatial frequencies (at least up to those that are captured by the passband of the instrument). It is therefore essential that the spheres measured do not deviate significantly from an ideal sphere, are smooth, and can be measured to accurately obtain the sphere diameter.

In this chapter, the use of the foil model to produce IFs from microsphere measurements to compensate for the phase effects of lens aberration in CSI signal data is demonstrated, including the resulting reduction of topography height errors. By capturing CSI signal data from measurements of precision microspheres and modelling the expected response using the foil model, experimental 3D STFs are generated. From these 3D STFs, an IF is formed that can compensate for the non-zero phase present in the experimental 3D STFs, attributed to lens aberration. Measurements of a sinusoidal grating are then taken, and the topographies obtained from before and after application of the IF. These topographies are compared to each other and to measurements of the grating by a traceable contract stylus instrument, to verify the foil model and CSI signal improvement by application of an IF.

## 3.2 Theory

### 3.2.1 Scattering under the KA

The foil model relies on the assumptions described in [184,185,208], which allow the scattering process to be linearised and ultimately allow the overall scattering, demodulation and imaging process to be described by the filtering of the surface spectrum by a single 3D STF. As discussed in section 2.5.1, the total field present in Eq. (2-28) or Eq. (2-29) must be approximated to enable an analytical solution for the scattered field elsewhere to be obtained. The Born approximation, which assumes only weak scattering occurs and therefore requires that there are only small objects present

or only small changes in refractive index, is not applicable for the typical usage of CSI instruments [184]. Instead, the KA is taken, which assumes that the surface varies slowly compared to the wavelength of light, such that the total field at each point on the boundary surface can be approximated by that obtained by a tangent plane at each point, given by

$$E(\mathbf{r}_\mathrm{b}) = (1+R)E_r(\mathbf{r}_\mathrm{b}), \tag{3-1}$$

where $\mathbf{r}_\mathrm{b}$ is a point on the surface boundary, $E(\mathbf{r}_\mathrm{b})$ is the total field at that point, $E_r(\mathbf{r}_\mathrm{b})$ the incident field at that point, and $R$ is a reflection coefficient, assumed constant over the range of scattering angles considered for all points on the boundary. The choice for the value of $R$ is given in detail in section 2.D. of [185], but in summary, is given by the Fresnel reflection coefficient or by an average of Fresnel reflection coefficients for different polarisations. An approximation for the Fresnel reflection coefficients in terms of the refractive index contrast across multiple angles of incidence can also be taken [185,249].

The KA requires that the surface slowly varies, equally expressed as requiring the radius of curvature at each point of the surface being significantly greater than the wavelength of light, as discussed in section 2.4.2. However, the KA also requires the following: the reflection coefficient must be constant or approximately constant, and the shadowing and multiple scattering effects must be negligible or compensated for [184,185,208]. For illumination by a plane wave with angular wavevector $\mathbf{k}_\mathrm{i}$ such that $E_r(\mathbf{r}) = e^{i\mathbf{k}_\mathrm{i}\cdot\mathbf{r}}$ (exponential function $e^{(\cdot)}$, imaginary unit $i=\sqrt{-1}$), the total field and the surface normal derivate of the total field along the boundary is given by

$$E(\mathbf{r}_\mathrm{b}) = (1+R)e^{i\mathbf{k}_\mathrm{i}\cdot\mathbf{r}_\mathrm{b}}, \tag{3-2}$$

$$\frac{\partial E(\mathbf{r}_\mathrm{b})}{\partial n} = i\mathbf{k}_\mathrm{i}\cdot\hat{\mathbf{n}}\,(1-R)e^{i\mathbf{k}_\mathrm{i}\cdot\mathbf{r}_\mathrm{b}}, \tag{3-3}$$

where $\hat{\mathbf{n}}$ is the unit surface normal vector at $\mathbf{r}_\mathrm{b}$. Following the Beckmann–Kirchhoff solution to surface scattering [208], these KA boundary conditions can be combined with the integral theorem of Helmholtz and Kirchhoff (a.k.a. the Kirchhoff integral theorem)

$$E_s(\mathbf{r}_\mathrm{s}) = -\int_\mathrm{B}\left[E(\mathbf{r}_\mathrm{b})\frac{\partial G(\mathbf{r}_\mathrm{s}-\mathbf{r}_\mathrm{b})}{\partial n} - G(\mathbf{r}_\mathrm{s}-\mathbf{r}_\mathrm{b})\frac{\partial E(\mathbf{r}_\mathrm{b})}{\partial n}\right]\mathrm{dB}, \tag{3-4}$$

where the scattered field $E_s(\mathbf{r}_\mathrm{s})$ at some far-field position $\mathbf{r}_\mathrm{s}$ is given by the summation of terms as $\mathbf{r}_\mathrm{b}$ varies over the surface B, where B represents the object's surface boundary, and where $G(\mathbf{r}_\mathrm{s}-\mathbf{r}_\mathrm{b})$ is the outgoing Green's function for the Helmholtz equation given in Eq. (2-26). As in Eq. (2-27), a far-field approximation is taken such that

$$G(\mathbf{r}_\mathrm{s}-\mathbf{r}_\mathrm{b}) = \frac{e^{ik_0|\mathbf{r}_\mathrm{s}-\mathbf{r}_\mathrm{b}|}}{4\pi|\mathbf{r}_\mathrm{s}-\mathbf{r}_\mathrm{b}|} \approx \frac{e^{ik_0|\mathbf{r}_\mathrm{s}|}}{4\pi|\mathbf{r}_\mathrm{s}|} e^{-ik_0\frac{\mathbf{r}_\mathrm{s}}{|\mathbf{r}_\mathrm{s}|}\cdot\mathbf{r}_\mathrm{b}}, \tag{3-5}$$

and where

$$\frac{\partial G(\mathbf{r}_\mathrm{s}-\mathbf{r}_\mathrm{b})}{\partial n} = -i\mathbf{k}_\mathrm{s}\cdot\hat{\mathbf{n}}\, G(\mathbf{r}_\mathrm{s}-\mathbf{r}_\mathrm{b}) \tag{3-6}$$

for $\mathbf{k}_\mathrm{s} = k_0\frac{\mathbf{r}_\mathrm{s}}{|\mathbf{r}_\mathrm{s}|}$. Substituting Eqs. (3-2), (3-3), and (3-6) into Eq. (3-4) gives

$$E_s(\mathbf{r}_\mathrm{s}) = i\int_\mathrm{B} G(\mathbf{r}_\mathrm{s}-\mathbf{r}_\mathrm{b})e^{i\mathbf{k}_\mathrm{i}\cdot\mathbf{r}_\mathrm{b}}[R(\mathbf{k}_\mathrm{s}-\mathbf{k}_\mathrm{i}) + (\mathbf{k}_\mathrm{s}+\mathbf{k}_\mathrm{i})\,]\cdot\hat{\mathbf{n}}\,\mathrm{dB}. \tag{3-7}$$

For only a portion of the surface being illuminated, a function $A(\mathbf{r})$ is introduced to represent the upper surface of the object that is illuminated, given by

$$A(\mathbf{r}) = W(\mathbf{r})\,\delta\big[\mathbf{r}\cdot\hat{\mathbf{z}} - s\big(r_x, r_y\big)\big], \tag{3-8}$$

where $W(\mathbf{r})$ is a window function, $\delta[\cdot]$ a one-dimensional (1D) Dirac delta function, and $s\big(r_x, r_y\big)$ the height of the surface in the direction of the optical axis $\hat{\mathbf{z}}$ at each lateral coordinate $(r_x, r_y)$. This allows Eq. (3-5) to be converted into an indefinite volume integral given by

$$E_s(\mathbf{r}_\mathrm{s}) = i\int_{-\infty}^{+\infty}\Bigg(G(\mathbf{r}_\mathrm{s}-\mathbf{r}_\mathrm{b})e^{i\mathbf{k}_\mathrm{i}\cdot\mathbf{r}_\mathrm{b}}[R(\mathbf{k}_\mathrm{s}-\mathbf{k}_\mathrm{i}) + (\mathbf{k}_\mathrm{s}+\mathbf{k}_\mathrm{i})\,] \cdot\hat{\mathbf{n}}\frac{A(\mathbf{r}_\mathrm{b})}{\hat{\mathbf{n}}\cdot\hat{\mathbf{z}}}\Bigg)\,\mathrm{d}^3 r_b. \tag{3-9}$$

From Eq. (3-9), the scattering amplitude for the foil model as given in Eq. (2-28) can be given as

$$
\begin{aligned}
f_K(\hat{\mathbf{s}}, \hat{\mathbf{s}}_\mathrm{i}) &= r_s \cdot E_s(r_s\hat{\mathbf{s}})e^{-ik_0 r_s} \\
&= \frac{i}{4\pi}\int_{-\infty}^{+\infty} e^{-i(\mathbf{k}_\mathrm{s}-\mathbf{k}_\mathrm{i})\cdot\mathbf{r}_\mathrm{b}}[R(\mathbf{k}_\mathrm{s}-\mathbf{k}_\mathrm{i}) + (\mathbf{k}_\mathrm{s}+\mathbf{k}_\mathrm{i})\,] \\
&\qquad \cdot \hat{\mathbf{n}}\frac{A(\mathbf{r}_\mathrm{b})}{\hat{\mathbf{n}}\cdot\hat{\mathbf{z}}}\,\mathrm{d}^3 r_b
\end{aligned}
\qquad (3\text{-}10)
$$

where the far-field Green's function given by Eq. (3-5) has been used for $\mathbf{r}_\mathrm{s} = r_s\hat{\mathbf{s}}$. Under Eq. (2-29), the expression for the source term $U_K(\mathbf{r}_\mathrm{b}; \hat{\mathbf{s}}, \hat{\mathbf{s}}_\mathrm{i})$ is then given by

$$
U_K(\mathbf{r}_\mathrm{b}; \hat{\mathbf{s}}, \hat{\mathbf{s}}_\mathrm{i}) = -i\left(e^{i\mathbf{k}_\mathrm{i}\cdot\mathbf{r}_\mathrm{b}}[R(\mathbf{k}_\mathrm{s}-\mathbf{k}_\mathrm{i}) + (\mathbf{k}_\mathrm{s}+\mathbf{k}_\mathrm{i})\,]\cdot\hat{\mathbf{n}}\frac{A(\mathbf{r}_\mathrm{b})}{\hat{\mathbf{n}}\cdot\hat{\mathbf{z}}}\right). \qquad (3\text{-}11)
$$

### 3.2.2 Scalar theory imaging

Imaging is then considered in the exact same way as in section 2.5.2, using the Kirchhoff integral theorem to apply back-propagation of the far-field scatter $E_s(\mathbf{r}_\mathrm{s})$ over the far-field surface $\Sigma$ to some region of space near to or within the scattering object at position $\mathbf{r}_\mathrm{m}$. This results in the expression

$$
E_m(\mathbf{r}_\mathrm{m}) = 2ik_0\int_\Sigma G^*(\mathbf{r}_\mathrm{m}-\mathbf{r}_\mathrm{s})E_s(\mathbf{r}_\mathrm{s})\,\mathrm{d}\Sigma, \qquad (3\text{-}12)
$$

where Eq. (2-38) has been repeated for clarity. Just as in section 2.5.2, the far-field boundary $\Sigma$ is assumed with no loss of generality to be a spherical shell with fixed sphere radius $r_\mathrm{s}$, such that $|\mathbf{r}_\mathrm{s}| = r_\mathrm{s}$ for all $\mathbf{r}_\mathrm{s}$. The integral over the spherical shell d$\Sigma$ can then be replaced by an indefinite integral over the new parameter $\mathbf{r}'_\mathrm{s}$, by replacing all $\mathbf{r}_\mathrm{s}$ by $\mathbf{r}'_\mathrm{s}$ and by including a Dirac delta function $\delta(|\mathbf{r}'_\mathrm{s}| - r_\mathrm{s})$ within the indefinite integral.

$$
E_m(\mathbf{r}_\mathrm{m}) = 2ik_0\int_{-\infty}^{+\infty} G^*(\mathbf{r}_\mathrm{m}-\mathbf{r}'_\mathrm{s})E_s(\mathbf{r}'_\mathrm{s})\,\delta(|\mathbf{r}'_\mathrm{s}| - r_\mathrm{s})\,\mathrm{d}^3\mathbf{r}'_s. \qquad (3\text{-}13)
$$

Considering the combination of Eq. (3-9) and Eq. (3-13), the exponential term and the two Green's functions can be reduced to

$$(4\pi|\mathbf{r}_\mathrm{s}|)^2 G^*(\mathbf{r}_\mathrm{m}-\mathbf{r}_\mathrm{s}')G(\mathbf{r}_\mathrm{s}'-\mathbf{r}_\mathrm{b})e^{i\mathbf{k}_\mathrm{i}\cdot\mathbf{r}_\mathrm{b}} = e^{ik_0\frac{\mathbf{r}_\mathrm{s}'}{|\mathbf{r}_\mathrm{s}'|}\cdot\mathbf{r}_\mathrm{m}} e^{-ik_0\frac{\mathbf{r}_\mathrm{s}'}{|\mathbf{r}_\mathrm{s}'|}\cdot\mathbf{r}_\mathrm{b}} e^{i\mathbf{k}_\mathrm{i}\cdot\mathbf{r}_\mathrm{b}}$$
$$= e^{-i\left(k_0\frac{\mathbf{k}_\mathrm{s}'}{|\mathbf{k}_\mathrm{s}'|}-\mathbf{k}_\mathrm{i}\right)\cdot\mathbf{r}_\mathrm{b}} e^{ik_0\frac{\mathbf{k}_\mathrm{s}'}{|\mathbf{k}_\mathrm{s}'|}\cdot\mathbf{r}_\mathrm{m}} \tag{3-14}$$
$$= e^{-i(\mathbf{k}_\mathrm{s}-\mathbf{k}_\mathrm{i})\cdot\mathbf{r}_\mathrm{b}} e^{i\mathbf{k}_\mathrm{s}\cdot\mathbf{r}_\mathrm{m}},$$

where just as in Eq. (2-41) and Eq. (2-42), the substitution $\mathbf{r}_\mathrm{s}'/r_s = \mathbf{k}_\mathrm{s}'/k_0$ is first made, which defines $\mathbf{k}_\mathrm{s}'$ and implies that $\mathbf{r}_\mathrm{s}'/|\mathbf{r}_\mathrm{s}'| = \hat{\mathbf{s}}_s = \mathbf{k}_\mathrm{s}'/|\mathbf{k}_\mathrm{s}'|$; and second, that $k_0\frac{\mathbf{k}_\mathrm{s}'}{|\mathbf{k}_\mathrm{s}'|}$ can be replaced by $\mathbf{k}_\mathrm{s}$ where $\mathbf{k}_\mathrm{s}$ remains limited to only values with magnitude $k_0$. While strictly this integration is still performed by $\mathbf{k}_\mathrm{s}'$ over infinity, the equality $\delta(|\mathbf{r}_\mathrm{s}'| - r_\mathrm{s}) = \frac{k_0}{r_s}\delta(|\mathbf{k}_\mathrm{s}'| - k_0)$ results in only the values of $\mathbf{k}_\mathrm{s}'$ where $|\mathbf{k}_\mathrm{s}'| = k_0$ contributing to the integral.

The phase term $e^{-i(\mathbf{k}_\mathrm{s}-\mathbf{k}_\mathrm{i})\cdot\mathbf{r}_\mathrm{b}}$ given in Eq. (3-14) changes phase in the direction of $\mathbf{k}_\mathrm{s} - \mathbf{k}_\mathrm{i}$ as $\mathbf{r}_\mathrm{b}$ is varied, and therefore does not vary at all when $\mathbf{r}_\mathrm{b}$ varies in the direction perpendicular to $\mathbf{k}_\mathrm{s} - \mathbf{k}_\mathrm{i}$. When the terms in Eq. (3-13) are integrated over various $\mathbf{r}_\mathrm{b}$ and $\mathbf{k}_\mathrm{s}$, many of the terms will add incoherently due to the rapidly changing phase of $e^{-i(\mathbf{k}_\mathrm{s}-\mathbf{k}_\mathrm{i})\cdot\mathbf{r}_\mathrm{b}}$. Only regions of the surface where the surface normal is parallel to $\mathbf{k}_\mathrm{s} - \mathbf{k}_\mathrm{i}$ will coherently contribute, as in these regions the vector difference between adjacent $\mathbf{r}_\mathrm{b}$ surface vectors will be approximately parallel with the surface tangent at $\mathbf{r}_\mathrm{b}$ and therefore perpendicular to the surface normal at $\mathbf{r}_\mathrm{b}$. This is known as the stationary phase approximation (or principle of stationary phase), and is particularly applicable under the KA where scattering is already assumed to come from a tangent plane; the stationary phase approximation assumes that the majority of the calculated scatter is from only the specular reflection from each tangent plane [184,208]. Under this approximation, the $(\mathbf{k}_\mathrm{s} + \mathbf{k}_\mathrm{i}) \cdot \hat{\mathbf{n}}$ from Eq. (3-9) is neglected, and the surface normal replaced with $\hat{\mathbf{n}} = \mathbf{k}_\mathrm{s} - \mathbf{k}_\mathrm{i}/|\mathbf{k}_\mathrm{s} - \mathbf{k}_\mathrm{i}|$, giving

$$E_m(\mathbf{r}_\mathrm{m}) = -\frac{R}{8k_0\pi^2}\int_{-\infty}^{+\infty}\left[\int_{-\infty}^{+\infty} e^{-i(\mathbf{k}_\mathrm{s}-\mathbf{k}_\mathrm{i})\cdot\mathbf{r}_\mathrm{b}}\left(\frac{|\mathbf{k}_\mathrm{s}-\mathbf{k}_\mathrm{i}|^2}{(\mathbf{k}_\mathrm{s}-\mathbf{k}_\mathrm{i})\cdot\hat{\mathbf{z}}}\right)A(\mathbf{r}_\mathrm{b})\,\mathrm{d}^3\mathbf{r}_b\right]\delta(|\mathbf{k}_\mathrm{s}| - k_0)e^{i\mathbf{k}_\mathrm{s}\cdot\mathbf{r}_\mathrm{m}}\,\mathrm{d}^3\mathbf{k}_s. \tag{3-15}$$

This is more compactly written as

$$E_m(\mathbf{r}_\mathrm{m}) = \int_{-\infty}^{+\infty} f_K(\mathbf{k}_\mathrm{s} - \mathbf{k}_\mathrm{i})\, \tilde{G}_\mathrm{ideal}(\mathbf{k}_\mathrm{s}) e^{i\mathbf{k}_\mathrm{s}\cdot\mathbf{r}_\mathrm{m}}\, \mathrm{d}^3\mathbf{k}_s, \tag{3-16}$$

where $f_K(\mathbf{K})$ remains consistent with Eq. (3-10) and is given here under the stationary phase approximation by

$$\begin{aligned} f_K(\mathbf{K}) &= \frac{i}{2\pi}\left(\frac{\mathbf{K}^2}{2\mathbf{K}\cdot\hat{\mathbf{z}}}\right) R \int_{-\infty}^{+\infty} A(\mathbf{r})\, e^{-i\mathbf{K}\cdot\mathbf{r}_\mathrm{b}}\, \mathrm{d}^3 r \\ &= \frac{i}{2\pi}\left(\frac{\mathbf{K}^2}{2\mathbf{K}\cdot\hat{\mathbf{z}}}\right) \int_{-\infty}^{+\infty} F_K(\mathbf{r})\, e^{-i\mathbf{K}\cdot\mathbf{r}_\mathrm{b}}\, \mathrm{d}^3 r \\ &= \frac{i}{2\pi}\left(\frac{\mathbf{K}^2}{2\mathbf{K}\cdot\hat{\mathbf{z}}}\right) \tilde{F}_K(\mathbf{K}), \end{aligned} \tag{3-17}$$

for $\tilde{F}_K(\mathbf{k}) = \mathcal{F}\{F_K(\mathbf{r})\}$ for the Fourier transform operator $\mathcal{F}\{\cdot\}$, and where $F_K(\mathbf{r})$ is the "foil" object function of the surface given by

$$F_K(\mathbf{r}) = R \cdot A(\mathbf{r}) = R\, W'(\mathbf{r})\, \delta\left[\mathbf{r}\cdot\hat{\mathbf{z}} - s\left(r_x, r_y\right)\right], \tag{3-18}$$

and where

$$\tilde{G}_\mathrm{ideal}(\mathbf{k}) = \frac{i}{4\pi k_0} \delta(|\mathbf{k}_\mathrm{s}| - k_0). \tag{3-19}$$

Here $W'(\mathbf{r})$ is used instead of $W(\mathbf{r})$ to denote that the window function can be combined with an appropriate shading function that may mitigate the impact of sharp points or the effect of shadowing at large angles to increase the accuracy of the model [185]. The function $\tilde{G}_\mathrm{ideal}(\mathbf{k})$ can be considered the 3D transfer function of the out-going propagating waves captured by an optical system that collects light for an entire spherical shell surrounding the object, and can be replaced by the NA limited $\tilde{G}_\mathrm{NA}(\mathbf{k})$ given by

$$\tilde{G}_\mathrm{NA}(\mathbf{k}) = \frac{i}{4\pi k_0} \delta(|\mathbf{k}| - k_0) H\left(\hat{\mathbf{k}}\cdot\hat{\mathbf{z}} - \sqrt{1 - A_n^2}\right), \tag{3-20}$$

where $H(x)$ is the Heaviside step function, and $A_n$ the NA of the instrument. Eq. (3-19) and Eq. (3-20) are shown visually in Figure 3.1.

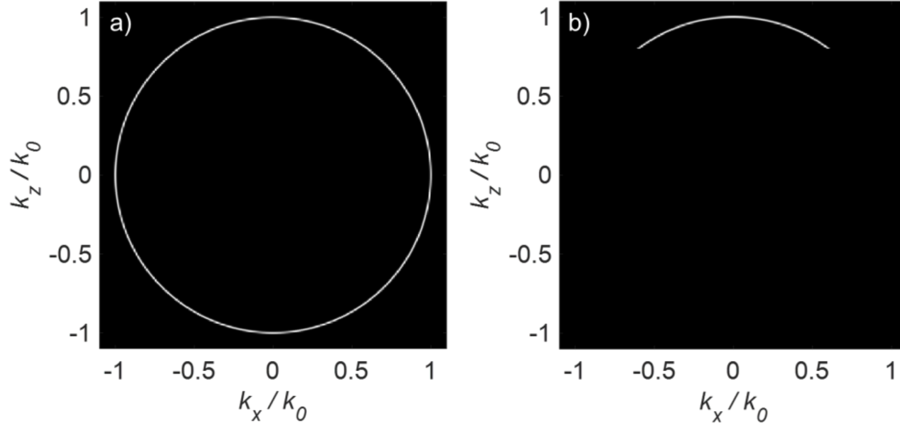


**Figure 3.1.** Visualisation in $k$-space of a $k_x$-$k_z$ slice of a) the ideal 3D transfer function given by Eq. (3-19) and b) the NA limited 3D transfer function for a NA of 0.6, given by Eq. (3-20). In both plots black denotes a value of zero and white non-zero.

Note that the exact forms of each of these equations varies between different publications [74,88,119,159,185,184] due to the ability to choose different Green's functions, different object functions, the choice of using linear or angular wavevectors, and different choices of optical transfer functions. Also note that the term 3D STF has not been used here for this transfer function; it has been reserved for CSI transfer functions, i.e., transfer functions that include the interference effects of the light from the reference mirror and that are typically not monochromatic.

The scattering amplitude that is in general dependent on $\mathbf{k}_\mathrm{s}$ and $\mathbf{k}_\mathrm{i}$ separately (as given in Eq. (2-29)) is shown in in Eq. (3-16) and Eq. (3-17) to depend only on $\mathbf{k}_\mathrm{s} - \mathbf{k}_\mathrm{i}$ under the foil model. This scattering amplitude is linear with the foil object function spectrum $\tilde{F}_K(\mathbf{K})$ evaluated only at $\mathbf{K} = \mathbf{k}_\mathrm{s} - \mathbf{k}_\mathrm{i}$, where the object spectrum is obtained from the foil object function $F_K(\mathbf{r})$ by Fourier transform. Notably, this foil function $F_K(\mathbf{r})$ is non-zero only along the surface boundary, i.e., where the refractive index changes rapidly, rather than the Born approximation, whose equivalent object function is non-zero throughout the entire volume of the object imaged.

### 3.2.3 Interferometric imaging

The intensity measured by the CCD or CMOS sensor of an interferometer for a single incident reference field is given in [88,184,185] by

$$\begin{aligned} I_d(\mathbf{r}) &= |E_m(\mathbf{r}) + E_r(\mathbf{r})|^2 \\ &= |E_m(\mathbf{r})|^2 + |E_r(\mathbf{r})|^2 + E_m(\mathbf{r})^* E_r(\mathbf{r}) + E_m(\mathbf{r}) E_r(\mathbf{r})^* \end{aligned} \tag{3-21}$$

where the measured scattered field $E_m(\mathbf{r})$ from the scattering object, for position vector $\mathbf{r}$, is combined with the reference field $E_r(\mathbf{r})$, where the reference field is the field reflected from the reference mirror in a real system. The fringes formed in the interferometer are caused by the last two terms of Eq. (3-21), which can be more concisely expressed as $2\Re\{E_m(\mathbf{r})E_r(\mathbf{r})^*\}$ where $\Re\{\cdot\}$ denotes taking the real part of a complex number. As such, the intensity of interest $I(\mathbf{r})$ is given by

$$I(\mathbf{r}) = 2\Re\{O(\mathbf{r})\} \tag{3-22}$$

$$O(\mathbf{r}) = E_m(\mathbf{r})E_r(\mathbf{r})^*, \tag{3-23}$$

where the generally complex $O(\mathbf{r})$ is called the "fringe field" in this chapter. Only the fringe field spectrum $\tilde{O}(\mathbf{k})$ is needed to calculate $I(\mathbf{r})$, where just as in Chapter 2, the tilde denotes the relationship $\tilde{X}(\mathbf{k}) = \mathcal{F}\{X(\mathbf{r})\}$ for any arbitrary function $X(\mathbf{r})$.

As the reference mirror should receive the same illumination as the object does, the reference field scattered from the mirror can be assumed equal to the incident illumination, given by $E_r^{(\mathrm{i})}(\mathbf{r}) = \mathrm{e}^{i\mathbf{k}_\mathrm{i}\cdot\mathbf{r}}$ for illumination wavevector $\mathbf{k}_\mathrm{i}$. Note that in the case where the sign of the $E_r^{(\mathrm{i})}(\mathbf{r})$ is made negative due to reflection from the reference mirror [88,184], the fringe pattern is the same but with the peaks and troughs flipped, which can be seen by considering Eq. (3-21) for $|E_m(\mathbf{r}) - E_r(\mathbf{r})|^2$. From the reference field the fringe field can be given as

$$O^{(\mathrm{i})}(\mathbf{r}) = E_m^{(\mathrm{i})}(\mathbf{r})\, \mathrm{e}^{-i\mathbf{k}_\mathrm{i}\cdot\mathbf{r}}. \tag{3-24}$$

Using Eq. (3-16), the expression

$$O_K^{(\mathrm{i})}(\mathbf{r}_\mathrm{m}) = \int_{-\infty}^{+\infty} f_K(\mathbf{k}_\mathrm{s} - \mathbf{k}_\mathrm{i})\, \tilde{G}_\mathrm{ideal}(\mathbf{k}_\mathrm{s}) e^{i(\mathbf{k}_\mathrm{s}-\mathbf{k}_\mathrm{i})\cdot\mathbf{r}_\mathrm{m}}\, \mathrm{d}^3\mathbf{k}_s, \tag{3-25}$$

is obtained, where the exponential term is now also in terms of $\mathbf{k}_\mathrm{s} - \mathbf{k}_\mathrm{i}$. By considering the new coordinate $\mathbf{K} = \mathbf{k}_\mathrm{s} - \mathbf{k}_\mathrm{i}$, the integral can be rewritten as

$$O_K^{(\mathrm{i})}(\mathbf{r}_\mathrm{m}) = \int_{-\infty}^{+\infty} f_K(\mathbf{K})\, \tilde{G}_\mathrm{ideal}(\mathbf{K} + \mathbf{k}_\mathrm{i}) e^{i\mathbf{K}\cdot\mathbf{r}_\mathrm{m}}\, \mathrm{d}^3\mathbf{K}, \tag{3-26}$$

where the integral can be recognised as the inverse Fourier transform, i.e., $O_K^{(\mathrm{i})}(\mathbf{r}_\mathrm{m}) = \mathcal{F}^{-1}\{f_K(\mathbf{K})\,\tilde{G}_\mathrm{ideal}(\mathbf{K}+\mathbf{k}_\mathrm{i})\}$. Therefore, the fringe field spectrum $\tilde{O}_K^{(i)}(\mathbf{K})$ for a single incident plane wave can be given by

$$\tilde{O}_K^{(i)}(\mathbf{K}) = f_K(\mathbf{K})\,\tilde{G}_\mathrm{ideal}(\mathbf{K}+\mathbf{k}_\mathrm{i}), \tag{3-27}$$

while for multiple plane waves is given by

$$\tilde{O}_K(\mathbf{K}) = f_K(\mathbf{K}) \sum_{\mathbf{k}_\mathrm{i}} \tilde{G}_\mathrm{ideal}(\mathbf{K}+\mathbf{k}_\mathrm{i})\,. \tag{3-28}$$

These equations state that the CSI fringe spectrum at the spatial-frequency ($k$-space) position $\mathbf{K}$ is dependent only on the scattering amplitude at $\mathbf{K}$ for values of $\mathbf{K}$ that exist on a spherical shell with radius $k_0$ and centre $\mathbf{K} = -\mathbf{k}_\mathrm{i}$ for any acceptable $\mathbf{k}_\mathrm{i}$. For example, for normal incidence where $\mathbf{k}_\mathrm{i} = -k_0\hat{\mathbf{k}}_\mathrm{z}$, the values of $\mathbf{K}$ that contribute non-zero field spectrum to $\tilde{O}_K^{(i)}(\mathbf{K})$ are those on the spherical shell circle centred at $\mathbf{K} = +k_0\hat{\mathbf{k}}_\mathrm{z}$ with radius $k_0$, such as $\mathbf{K}_1 = 2k_0\hat{\mathbf{k}}_\mathrm{z}$, $\mathbf{K}_2 = k_0\left(\frac{1}{\sqrt{2}}\hat{\mathbf{k}}_\mathrm{x} + \left[1+\frac{1}{\sqrt{2}}\right]\hat{\mathbf{k}}_\mathrm{z}\right)$, $\mathbf{K}_3 = k_0\left(\hat{\mathbf{k}}_\mathrm{x} + \hat{\mathbf{k}}_\mathrm{z}\right)$, or $\mathbf{K}_4 = \mathbf{0}$. When $\tilde{G}_\mathrm{ideal}$ is replaced by $\tilde{G}_\mathrm{NA}$ the spherical shell is truncated to a cap, limiting the range of contributing values further.

### 3.2.4 3D transfer function

It is now useful to consider Eq. (3-28) with the scattering amplitude replaced by the object spectrum function as given in (3-17), giving

$$\tilde{O}_K(\mathbf{K}) = \tilde{F}_K(\mathbf{K})\,\tilde{H}_K(\mathbf{K}), \tag{3-29}$$

where the 3D STF $\tilde{H}_K(\mathbf{K})$ has been defined by

$$\tilde{H}_K(\mathbf{K}) = \frac{i}{2\pi}\left(\frac{\mathbf{K}^2}{2\mathbf{K}\cdot\hat{\mathbf{z}}}\right) \sum_{\mathbf{k}_\mathrm{i}} \tilde{G}_\mathrm{NA}(\mathbf{K}+\mathbf{k}_\mathrm{i})\,. \tag{3-30}$$

Eq. (3-29) states that the fringe field spectrum (and therefore the intensity fringes) can be found by a point-wise product in $k$-space of the object function $\tilde{F}_K(\mathbf{K})$ with the instrument's 3D STF $\tilde{H}_K(\mathbf{K})$, equally expressed by the convolution of the real-space object function $F_K(\mathbf{r})$ with PSF $H_K(\mathbf{r})$, where $H_K(\mathbf{r}) = \mathcal{F}^{-1}\{\tilde{H}_K(\mathbf{K})\}$.

For a range of different incident illumination vectors limited by a NA, the summation in Eq. (3-30) can be rewritten in terms of an indefinite integral, given in [185] by

$$\begin{aligned}\sum_{\mathbf{k}_\mathrm{i}} \tilde{G}_\mathrm{NA}(\mathbf{K}+\mathbf{k}_\mathrm{i}) &= \sum_{\mathbf{k}_\mathrm{i}} \tilde{G}_\mathrm{NA}(\mathbf{K}) \otimes \delta^{(3)}(\mathbf{K}+\mathbf{k}_\mathrm{i}) \\ &= \int \tilde{G}_\mathrm{NA}(\mathbf{K}-\mathbf{K}') \cdot \sum_{\mathbf{k}_\mathrm{i}} \delta^{(3)}(\mathbf{K}'+\mathbf{k}_\mathrm{i})\ \mathrm{d}^3K' \\ &= \frac{i}{k_0} \int \tilde{G}_\mathrm{NA}(\mathbf{K}-\mathbf{K}') \cdot \tilde{G}'_\mathrm{NA}(\mathbf{K}')\ \mathrm{d}^3K',\end{aligned} \qquad (3\text{-}31)$$

where the difference in pre-factors between Eq. (3-31) and Eq. (46) of [185] comes from the difference in the definition of $\tilde{G}_\mathrm{NA}(\mathbf{k})$ between this section and [185]. Note also that $\tilde{G}'_\mathrm{NA}(\mathbf{K})$ is equal to $\tilde{G}_\mathrm{NA}(\mathbf{K})$ when the illumination pupil is entirely filled, i.e., when the NA for illumination and observation are the same, but will vary if the illumination condenser's NA is smaller than the objective NA. When the two functions match, the integral can be considered a convolution between $\tilde{G}_\mathrm{NA}(\mathbf{K})$ with itself, and therefore can also be found numerically by the Fourier transform of $G^2_\mathrm{NA}(\mathbf{r})$, rather than numerically evaluating the convolution directly [88,184]. An example PSF and associated 3D STF, given by Eq. (3-30) and Eq. (3-31), calculated using this approach is shown in Figure 3.2.

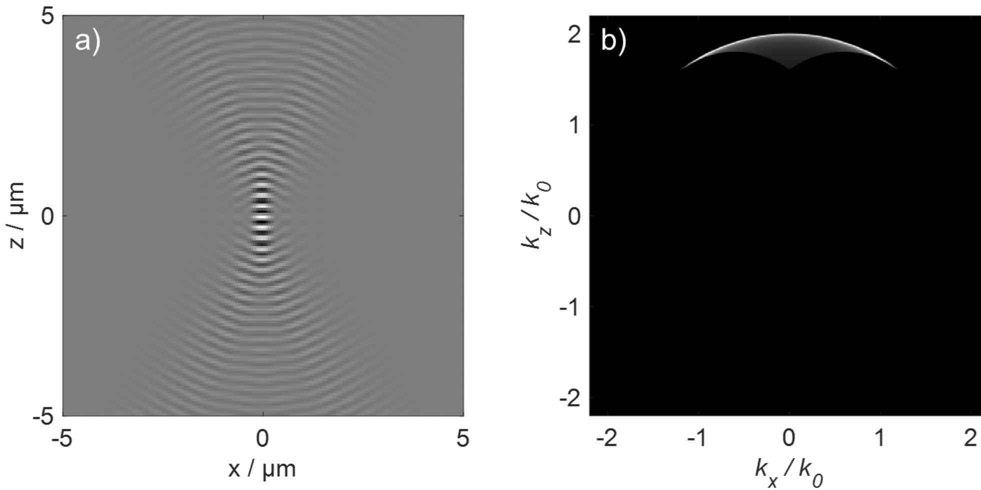


**Figure 3.2.** A lateral-axial 2D slice of a) the real part of the PSF $H_K(\mathbf{r})$ and b) the magnitude of the associated 3D STF $\tilde{H}_K(\mathbf{K})$ given by Eq. (3-30), for NA=0.6 and $k_0 = 2\pi/\lambda$, $\lambda = 0.5$ µm.

Finally, for an illumination source with multiple wavelengths, integration over a normalised power spectrum density $S(k_0)$ of the illumination source is perfomed, giving

$$\widetilde{H}_K(\mathbf{K}) = -\frac{1}{2\pi}\left(\frac{\mathbf{K}^2}{2\mathbf{K}\cdot\hat{\mathbf{z}}}\right)\int_0^{+\infty}\int_{-\infty}^{+\infty}\tilde{G}_{\mathrm{NA}}(\mathbf{K}-\mathbf{K}')\cdot\tilde{G}'_{\mathrm{NA}}(\mathbf{K}')\,\mathrm{d}^3K'\,\frac{S(k_0)}{k_0}\,\mathrm{d}k_0. \quad (3\text{-}32)$$

For an instrument with a well-specified illumination spectrum, a 3D STF can be generated and a PSF subsequently obtained that characterises the instrument in the case where no aberration is present. An example is shown in Figure 3.3. With adjustment, the same approach can be used to model the 3D STF of the instrument when reference mirror defocus is present [119]. Once a 3D STF is present, the foil model can be used as a virtual instrument and produce fringe signal data using Eq. (3-29), accurate for surfaces that are applicable under the KA and other foil model assumptions [186]. This remains the case with an experimentally obtained 3D STF, and from the 3D STF information about the instrument such as its lateral resolution can be obtained [144].

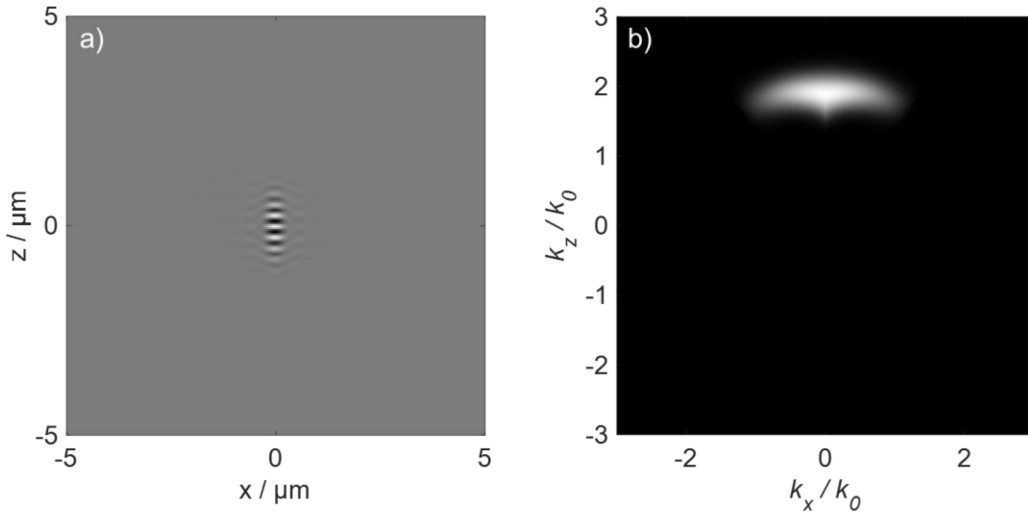


**Figure 3.3.** A lateral-axial 2D slice of a) the real part of the PSF $H_K(\mathbf{r})$ and b) the magnitude of the associated 3D STF $\widetilde{H}_K(\mathbf{K})$ given by Eq. (3-32), for NA=0.6 and a Gaussian spectrum illumination. The illumination has a mean wavenumber $k_0 = 2\pi/\lambda$ where $\lambda = 0.5$ µm, and full width at half maximum (FWHM) of $k_0/5$, approximately equivalent to a FWHM in wavenumber of 0.1 µm.

## 3.2.5 3D STF measurement and correction

Eq. (3-29) states that the fringes produced in a CSI instrument are a result of filtering the spectrum of an object function with a surface scattering 3D STF associated with the

instrument. When obtained experimentally this 3D STF is therefore able to effectively characterise the optical instrument, e.g. allowing for a comparison of the 3D measurement performance between different optical instruments [88,201]. An experimental 3D STF for a CSI instrument can be obtained by first measuring a surface with known topography, obtaining the intensity signal data from the instrument. As these intensity terms are separable in the frequency domain, the intensity is Fourier transformed and a band-pass filter applied to obtain the fringe spectrum $\tilde{O}_K(\mathbf{K})$. Next, the foil object function $F_K(\mathbf{r})$ is produced using Eq. (3-18) and knowledge of the surface's topography, and the object spectrum $\tilde{F}_K(\mathbf{K})$ is generated by Fourier transform. The 3D STF $\tilde{H}_K(\mathbf{K})$ can then be obtained by

$$\tilde{H}_K(\mathbf{K}) = \frac{\tilde{O}_K(\mathbf{K})}{\tilde{F}_K(\mathbf{K})}, \tag{3-33}$$

where Eq. (3-29) has been rearranged. Numerically, the Dirac delta function in Eq. (3-18) is non-zero only on the surface of the infinitely thin foil object, and must therefore be blurred axially to be handled numerically. Therefore, the Dirac delta function is given numerically as the limit of a Gaussian function [74]

$$\delta(z) = \lim_{\sigma \to \varepsilon} \frac{1}{\sqrt{2\pi}\sigma} \exp\left[\frac{-z^2}{2\sigma^2}\right], \tag{3-34}$$

where $\sigma$ is the standard deviation and $\varepsilon$ is a small positive number ($\varepsilon > 0$) chosen so that the variation of the magnitude of $F_K(\mathbf{r})$ near $z = 0$ due to the non-zero $\sigma$ can still be captured by the discrete sampling of $F_K(\mathbf{r})$ chosen. This experimentally measured 3D STF can be used to characterise the instrument, and information about the instrument transfer function (ITF) and lateral resolution of the system can be obtained [144].

From Eq. (3-32) it is apparent that $\tilde{H}_K(\mathbf{K})$ is a real-valued function for all **K** and should not contain any phase within the passband. However, phase variation is typically found in experimental measurements of $\tilde{H}_K(\mathbf{K})$, and is attributed to aberration in the optical system. Therefore, an inverse filter can be simply generated by phase inversion of the phase component of the experimentally measured 3D STF $\tilde{H}_K(\mathbf{K})$, such that

$$P_{\text{inv}}(\mathbf{K}) = \exp\left(-i \angle\{\tilde{H}_K(\mathbf{K})\}\right), \tag{3-35}$$

where $\angle\{\cdot\}$ denotes taking the phase, and where $P_{\text{inv}}(\mathbf{K})$ has unit magnitude throughout the passband. Then, for any measured intensity signal, the associated fringe field spectrum $\tilde{O}_K(\mathbf{K})$ can be obtained, and the inverse filter can be applied such that

$$\tilde{O}'_K(\mathbf{K}) = \tilde{O}_K(\mathbf{K})\, P_{\text{inv}}(\mathbf{K}) \tag{3-36}$$

$$I'(\mathbf{r}) = 2\Re\left\{\mathcal{F}^{-1}\{\tilde{O}_K(\mathbf{K})\, P_{\text{inv}}(\mathbf{K})\}\right\}, \tag{3-37}$$

where $I'(\mathbf{r})$ is the intensity fringes after inverse phase filtering. These filtered fringes are believed to provide more accurate topography data than that obtained from the unfiltered fringes, due to compensating for the effect of instrument aberration. This can be understood under the foil model as the phase encoded within the filtered fringes $I'(\mathbf{r})$ better reflecting the phase of the object spectrum $\tilde{F}_K(\mathbf{K})$ and therefore the surface topography described by the object function $F_K(\mathbf{r})$. Furthermore, computational adjustments can be made to the inverse filter to artificially adjust the 3D STF's magnitude, "flattening" it to give a potentially improved PSF associated with higher spatial frequencies [74,247].

Under the assumption that the foil model is valid, including the requirement of the KA being valid and multiple scattering being negligible, it is shown in [247] that the measurement of a microsphere can provide the 3D STF characteristic of the CSI measurement instrument. A microsphere was used because in principle, all spatial frequencies that the instrument can capture are present across the sphere. The microsphere must be close to an ideal sphere, as the diameter measured from the top of the sphere to its bottom is used to generate the surface geometry of the entire sphere. Details on the microspheres chosen for this work are given in section 3.3.1, and some additional requirements on the microspheres are given in section 3.1. Note that only the cap of the sphere is resolvable due to the limited NA causing data dropout at steeper surface angles.

## 3.3 Materials and methods

Discussed in the following subsections are the methods and materials used to obtain information on the 3D STF of a CSI instrument by measurement of a microsphere. However, from the many microsphere measurements taken, the fringe data had to be converted into a usable format, filtered by an appropriate band-pass filter (BPF), aligned to the foil of the surface, and together processed to generate 3D STFs.

Exploration on the effect of the choice of window size, the capability of different alignment methods, the effect of misalignment, and the effect of other parameters also needed to be explored. Easy application of the inverse filters to fringe data from measurements of many different freeform surfaces was also required. To enable and support this (and prior) work, a graphical user interface was created, utility functions added, and the existing code modified to be more modular to support the use of the user interface.

Benefits of the interface included easy selection of data files to load and ensuring the choice of parameters made was visible; utility functions included rapid loading of slices of fringe data to preview fringes and the choice of cropping made; modularity included allowing the BPF to be independently generated and saved for a chosen lens configuration. More details including some figures of the interface are given in Appendix A; this work was developed further outside of the PhD project by the author of this thesis as a research associate.

### 3.3.1 Precision microspheres

To characterise the 3D STF, the use of four silica spheres that were manufactured by two different methods were investigated. The spheres chosen were of varying sizes and were repeatedly measured at different rotational angles. The specifications of the spheres are given in Table 3.1. In addition to silica spheres, mercury spheres have previously been measured by others to obtain a 3D STF [250]. In this work silica spheres are used instead of mercury spheres due to: the ease of re-measurement of the same sphere at different times without a change in the sphere’s size or shape; the ease of measurement of several differently-sized spheres to minimise the effect of any shape error; and the ease of transporting and handling the spheres in comparison to those involved in handling liquid mercury.

**Table 3.1** Specifications of the sphere measurements.

| **Sphere** | A2 | A5 | | B39 | B45 |
|---|---|---|---|---|---|
| **Diameter /µm** | 102.0 | 106.6 | | 39.4 | 45.0 |
| **Coating** | Yes | | | No | |
| **Lateral and vertical sizes[7] of the window $W$(r) /µm** | ($x$,$y$) ($z$)<br>20.3 5.2<br>23.1 5.9<br>26.0 6.7 | | | ($x$,$y$) ($z$)<br>11.6 3.0<br>14.5 3.7<br>17.4 4.5 | |
| **Rotation /°** | 0, 90, 180, 270[8] | | | | |
| **No. of repeats** | 3 | | | | |

The A-type spheres were produced using femtosecond laser structuring combined with a subsequent step of $CO_2$ laser melting. This method is known as 'laser morphing' and is further described elsewhere [251,252]. The radius of the A-type sphere was determined using an interferometric radius measurement procedure on an interferometer (a Twymann-Green interferometer). The spheres were coated with silver to enhance reflectivity. The radius is measured as the distance between the so-called cat's eye position, where the focus of the interferometric objective coincides with the vertex of the sphere, and the null test position of the sphere, where the focus of the interferometer objective coincides with the centre of curvature of the sphere. The radius is the displacement between the two positions, measured with a displacement measuring interferometer that uses a frequency stabilised helium-neon laser at 633 nm.

The B-type spheres are commercially available and produced by melting non-spherical $SiO_2$ particles in plasma to form spherical droplets, and then cooled to obtain solid spheres. As the B-type spheres directly sit on top of an optical flat, the diameters were measured as the distance between the top of the sphere and the surface of the optical flat. The standard deviation of the ten repeated diameter measurements is smaller than 10 nm. The influence of the accuracy of the diameter and sphericity on the 3D STF has been demonstrated elsewhere [74].

### 3.3.2 Surface measurement

In this work, characterisation and correction of a commercial CSI instrument was performed. This instrument had a Mirau objective lens (0.55 NA), 0.174 µm lateral

---

[7] Standard deviation. See section 3.2 for the definition of W(r), and section 3.4.1 for its implementation
[8] Sphere A2 is also measured at (45, 135, 225, 315)°

sampling distance, 1000×1000 lateral sampling points, 0.56 μm central wavelength, and bandwidth of approximately 100 nm FWHM. The field-dependent lateral distortion of the instrument was measured and corrected using a previously reported self-calibration technique [150]. In principle, the proposed technique can be applied to any CSI instrument.

Three reference surface samples (material measures manufactured by Rubert & Co Ltd, see Table 3.2 for specifications) and an AM surface were used for validating the proposed error correction method of surface measurement, given in section 3.2.5. Surfaces R521 and R527 have similar slope distributions but different spatial frequencies. R525 has a similar pitch as R527 but its maximum slope is close to the acceptance angle of the NA of the instrument. As shown in Figure 3.4, the sinusoidal surfaces not only feature varying slopes but also varying spatial frequencies and microscale machining marks. The AM surface of a Ti-6Al-4V sample was made using the electron beam powder bed fusion (EBPBF) technique (see [253] for more details). The roughness of this type of surface is usually of the order of several micrometres or higher. These surfaces are well-known challenges for optical instruments and are good representatives of surfaces in real-world applications.

**Table 3.2** Nominal (as-designed) specifications of the surfaces.

| | R521 | R527 | R525 |
|---|---|---|---|
| **Form** | Sine wave | Sine wave | Sine wave |
| **Pitch / μm** | 15 | 100 | 135 |
| **Peak-to-valley amplitude / μm** | 1.6 | 10 | 19 |

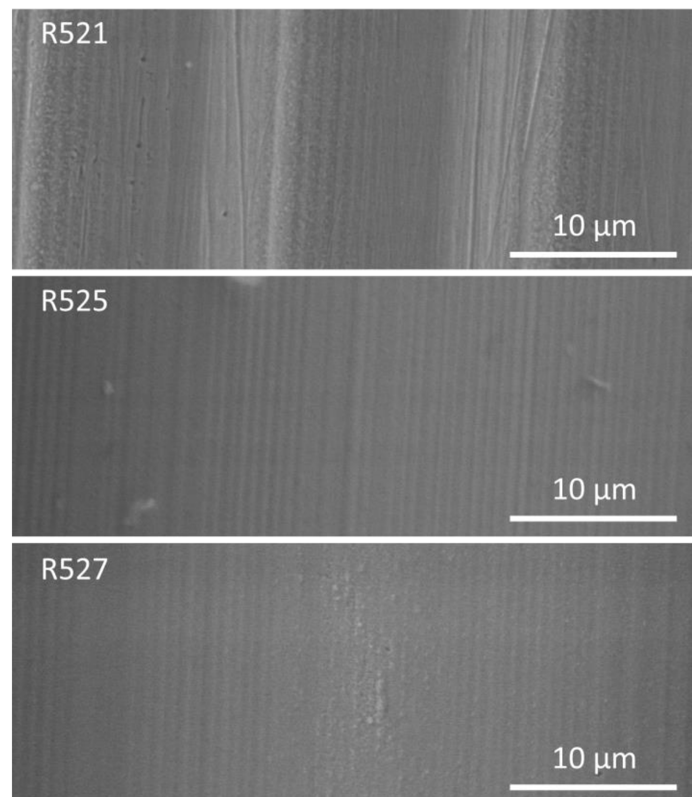


**Figure 3.4.** SEM images showing the micro textures in surfaces R521, R525 and R527.

A stylus instrument (Talysurf Intra 50) was used to provide reference measurements of these surfaces. The tip radius of the stylus is 2 µm. The measurement noise (root-mean-square [RMS] value) is 12 nm, which was evaluated using an optical flat by following the standard calibration procedure [254]. The primary profile length of the stylus measurement was 5 mm for the three sinusoidal surfaces. Each of the profiles was split into ten segments from which the mean profile and the standard deviation were calculated. The mean profiles of the stylus measurements were used for comparison, such that the impact of topographic outliers of the surface, e.g. dust particles, can be minimised. The reproducibility of the stylus measurements, calculated as the root sum of squares of the standard deviation value and the noise, are 30 nm, 30 nm and 24 nm for R521, R525 and R527, respectively. The root sum of squares is used when combining uncertainties from multiple uncorrelated contributors. The response of the stylus instrument to these surfaces is not expected to be affected by the slope-dependent errors experienced by the optical instrument thanks to the large pitch of the surface structure relative to the tip radius of the stylus.

To quantitatively compare the surface measurement results obtained by the optical and stylus instruments, surface profiles are extracted from different positions of the CSI areal topography maps and compared with the stylus-measured profiles. A registration algorithm that can specify any degrees-of-freedom [255] is used to match and register the profiles for direct comparison.

## 3.4 Result and analysis

### 3.4.1 Characterisation of 3D STF

The 3D STF can be calculated by dividing the 3D fringe data of a spherical cap by the corresponding foil function in the spatial frequency domain, as given in Eq. (3-33). In implementing the numerical calculation, the window function in Eq. (3-18), $W(\mathbf{r})$, is defined using a 3D Gaussian function with appropriate widths in the spatial domain to limit the foil function to the spherical cap of interest. The Dirac delta function is approximated by a 1D Gaussian function along the surface height direction ($z$-direction) and has a sufficiently small width, as given in Eq. (3-34).

The experimentally determined 3D STFs of the CSI instrument obtained by measuring the four spheres are shown in Figure 3.5. To minimise the characterisation error that may be caused by the size uncertainty, asphericity of the sphere [74,248] or other statistical error sources, the spheres were measured three times at four rotation angles (twelve measurements for each sphere). The measured 3D fringe data were processed using three different window sizes (see Table 3.1). Subsequently, seventy-two 3D STFs were obtained from the measurements of the A- and B-type spheres, respectively.

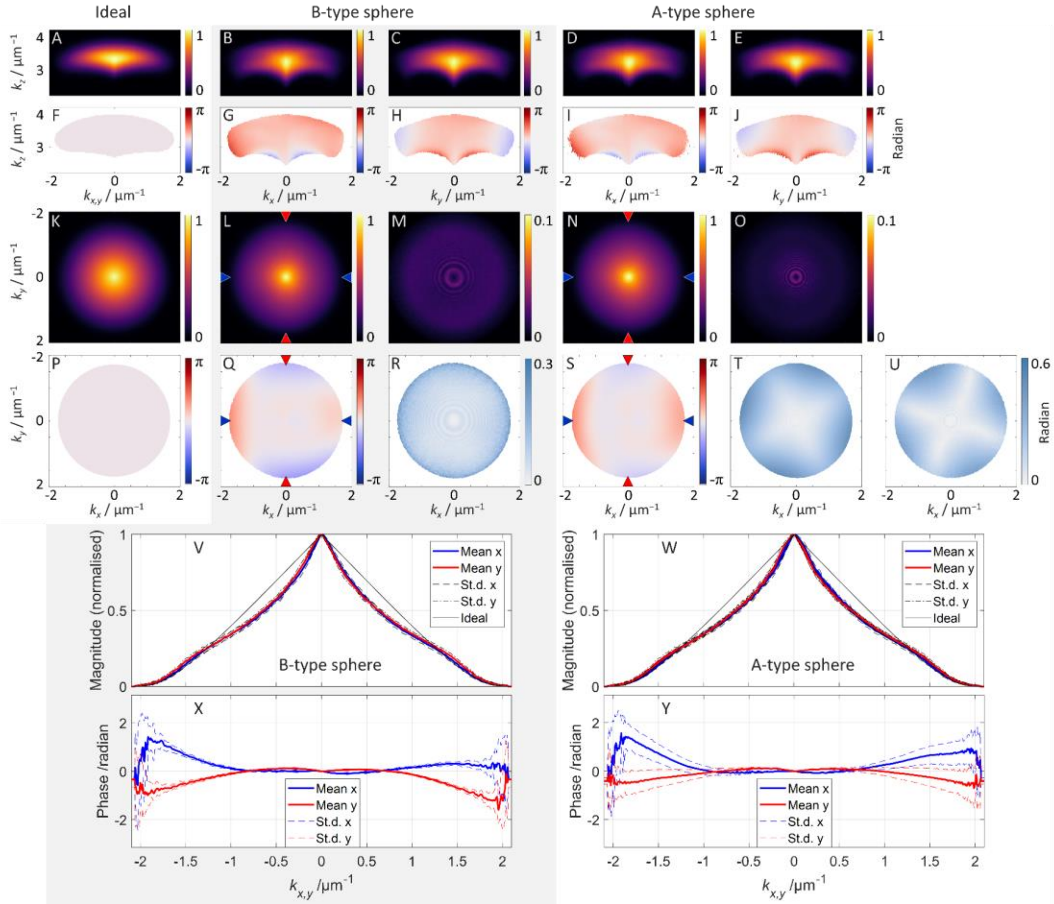


**Figure 3.5.** Experimentally characterised 3D STF of the CSI system. Row I shows the cross-sectional slices of the normalised magnitudes of the 3D STFs. Row II shows the corresponding phases. Row III shows the magnitudes of the in-pupil STFs. Row IV shows the corresponding phases. Row V and VI show the 1D profiles of the magnitudes and phases of the experimental in-pupil STFs. (A, F, K, P) ideal (diffraction-limited) case. (B, C, G, H, L, Q) the 3D STF and in-pupil STF obtained using B-type spheres. (M, R) the corresponding standard deviations of the in-pupil STFs. (D, E, I, J, N, S) the 3D STF and in-pupil STF obtained using A-type spheres. (O, T, U) the corresponding standard deviations of the in-pupil STFs. (U) is obtained when sphere A2 was rotated at 45°, 135°, 225° and 315°. (V, W, X and Y) the profiles are taken along the $k_x$ and $k_y$ axes as marked in (L, N, Q and S).

The 3D STF is a complex-valued quantity. Its magnitude determines the spatial frequency passband of the CSI, and the peak modulation of the magnitude is located at approximately the spatial frequency $2/\lambda_0$ on the $k_z$ axis, where $\lambda_0$ is the central wavelength of the light source in air. The 3D STF of an ideal instrument (diffraction-limited) should in principle be rotationally symmetric about the $k_z$ axis.

To make it easier to visualise and compare the measured 3D STFs, the mean and standard deviation of the in-pupil STF are evaluated, which is calculated by integrating

the 3D STF over the axial spatial frequency $k_z$ for each lateral spatial frequency $k_x$ and $k_y$ [256,257]. In this way, the in-pupil STF is similar to the in-pupil (2D) OTF that can be found at the back focal plane of the objective lens [192].

The magnitude of the experimental 3D STF [Figure 3.5(B), (C), and (L)] obtained using the B39 and B44 spheres deviates from the ideal magnitude [Figure 3.5(A), and (K)]. The degraded magnitude is likely to be due to the combined effect of defocus, high order aberrations, and the central obstruction due to the presence of the reference mirror in the optical axis of the Mirau objective.

The magnitude is effectively the weighting factor that determines the impact of the phase value on the measurement result. The phase of the real instrument [Figure 3.5(G), (H), and (Q)] deviates from zero, i.e. the ideal case [see Figure 3.5(F) and (P)], due to the presence of optical aberrations. The departure and variation of the phase become relatively larger at the edges of the passband but its impact on the measurement result is limited as the corresponding magnitude is small.

The asymmetry in both magnitude and phase is probably caused by the tilt and decentration of the optical components and other asymmetric aberrations in the optical system. The asymmetry indicates that the optical system would perform differently along different directions in terms of resolution and measurement accuracy.

The standard deviation of the seventy-two 3D STFs obtained using spheres B39 and B44 is plotted in Figure 3.5(M) and (R). The mean values of the standard deviations for the normalised magnitudes and phases of the corresponding in-pupil STFs are 0.004 (normalised value) and 0.06 rad, respectively. That these values are very small provides evidence that the characterisation result is stable and insensitive to the changes of the window function, is independent of the spheres, and the sphere form error is sufficiently small. The main cause of the residual variations in Figure 3.5(M) and (R) may be the result of the linearity of the axial scanning stage and the environmental mechanical vibration.

The 3D STFs that were obtained using spheres A2 and A5 using the same instrument working conditions has a magnitude almost identical to that obtained using the B-type spheres [Figure 3.5(L), (N), (V), and (W)]. However, the mean value of the phase slightly deviates from the result of B-type spheres [see Figure 3.5(Q), (S), (X), and (Y)],

and the mean values of the standard deviation in phase is 0.22 rad [calculated from Figure 3.5(T)], much higher than that shown in Figure 3.5(R).

The systematic phase variation in Figure 3.5(T) is mainly caused by an orthogonal anisotropy of the spherical form in the A-type spheres, i.e. the radius of the sphere slightly varies along two orthogonal horizontal directions. This hypothesis was further verified by measuring sphere A2 at four additional rotation angles, and the phase variation pattern in Figure 3.5(U) rotates with the sphere by 45° relative to Figure 3.5(T). This problem is not surprising as the laser-morphing process started with intrinsically asymmetric conditions, such as thermal gradient, asymmetric material geometry, and possible asymmetry in the heating profile. From this point, the rest of the experiments were carried out using B-type spheres.

### 3.4.2 Inverse filtering of 3D PSF

The experimentally characterised 3D STF is used to calculate the inverse filter through phase inversion, as given by Eq. (3-35). The 3D impulse response of the instrument to the surface, i.e. 3D PSF, can be calculated through the inverse Fourier transform of the 3D STF (Figure 3.6). It can be seen that the asymmetry and skewness of the original 3D PSF in both axial and horizontal directions were corrected after applying the inverse filtering. The effects of the aberration compensation on real surface measurement will be shown in section 3.4.3.

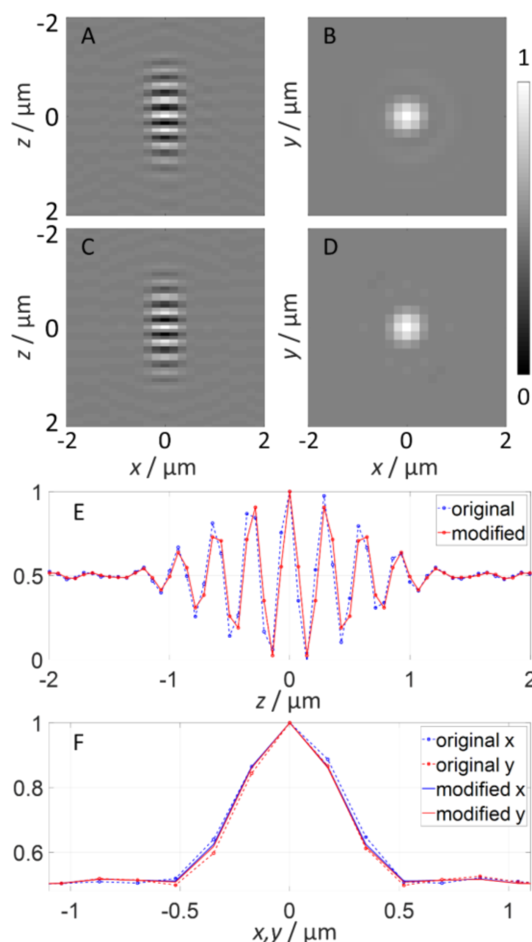


**Figure 3.6.** Experimentally characterised 3D PSF of the CSI system. (A, B) Cross-sectional slices through the origin of the original 3D PSF in the *x*-*z* and *x*-*y* planes, respectively. (C, D) Cross-sectional slices of the 3D PSF after the inverse filtering. (E) Interferogram profiles along the axial direction at $x,y = 0$ before and after the inverse filtering. (F) Profiles along the horizontal directions at $z = 0$ before and after the inverse filtering.

### 3.4.3 Improved surface measurement

The CSI-measured areal surface topography of R521, R527, and R525 are shown in Figure 3.7(A), Figure 3.8(A), and Figure 3.9(A), respectively. The topography is calculated pixelwise using the frequency-domain analysis method [87,110] without any filtering processes that connect phases of neighbouring pixels, i.e. algorithm-driven interpretation of surface structure is not used when resolving fringe order. The original and inverse-filtered measurement results are compared with the stylus measurements after alignment. The profiles at $y = 0$ are used for demonstrating the comparisons, as shown in Figure 3.7(C), Figure 3.8(C), and Figure 3.9(C). The CSI-measured profiles extracted from different *y* positions were also compared; similar results were obtained and, therefore, are not shown.

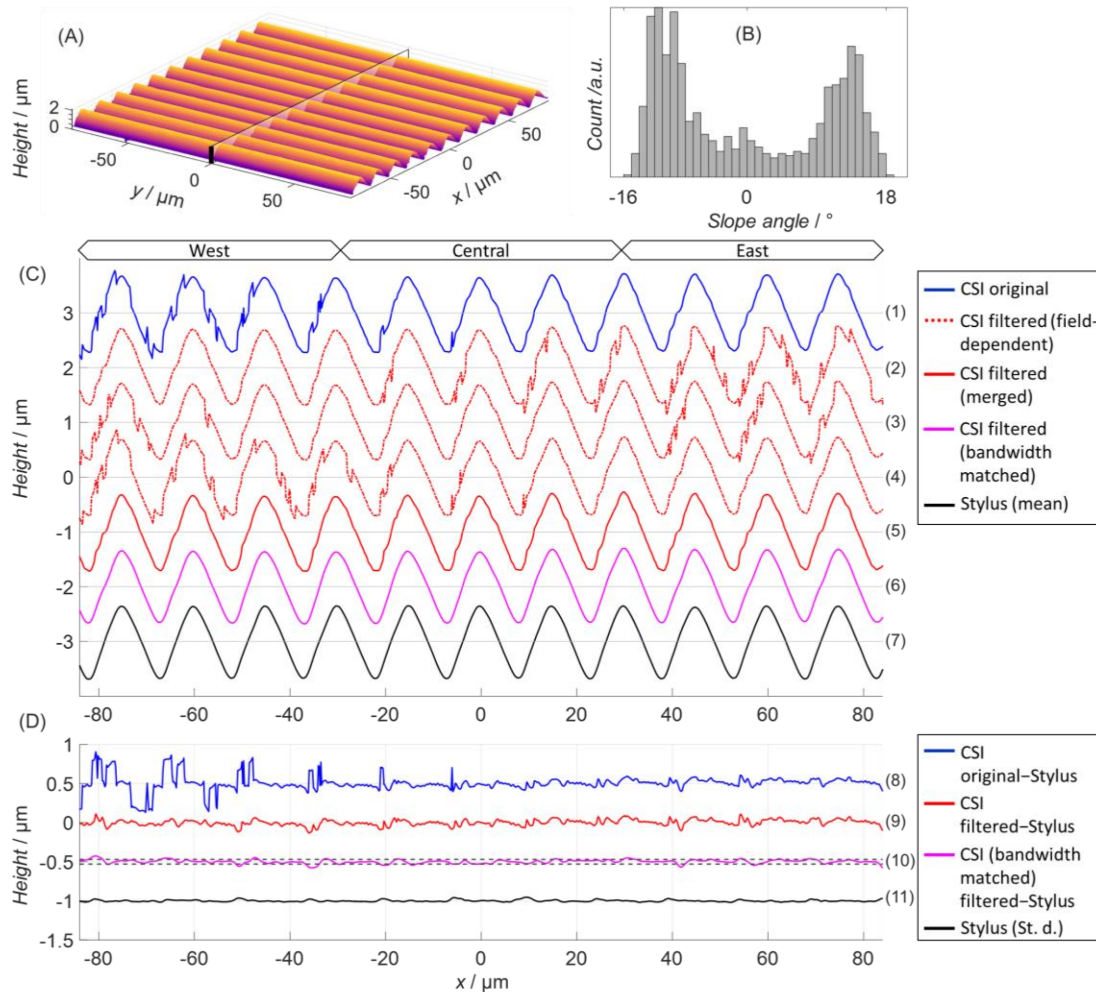


**Figure 3.7.** Measurements of surface R521. (A) 3D plot of the CSI-measured areal topography. (B) Slope angle distribution calculated from the 1D numerical gradient of the stylus profile. (C) CSI- and stylus-measured profiles, where for display purposes the seven profiles have been offset on the *y*-axis by {+3,+2,+1,+0,−1,−2,−3} µm respectively: (1) original CSI measurement, (2-4) CSI measurements modified based on the field-dependent 3D STFs, (5) final result of the inverse-filtered CSI measurement, (6) bandwidth matched and inverse-filtered CSI measurement, (7) mean value of the stylus-measured profiles. (D) Surface height differences between CSI- and stylus-measured profiles (8,9,10) and the standard deviation of stylus-measured profiles (11), where the dashed line indicates the 30-nm reproducibility of the stylus measurement. For display purposes these four difference profiles have been offset on the *y*-axis by {+0.5,+0,−0.5,−1} µm respectively. Note that all CSI profiles are calculated using both coherence profile and phase information, referred to as “high-precision CSI profile”.

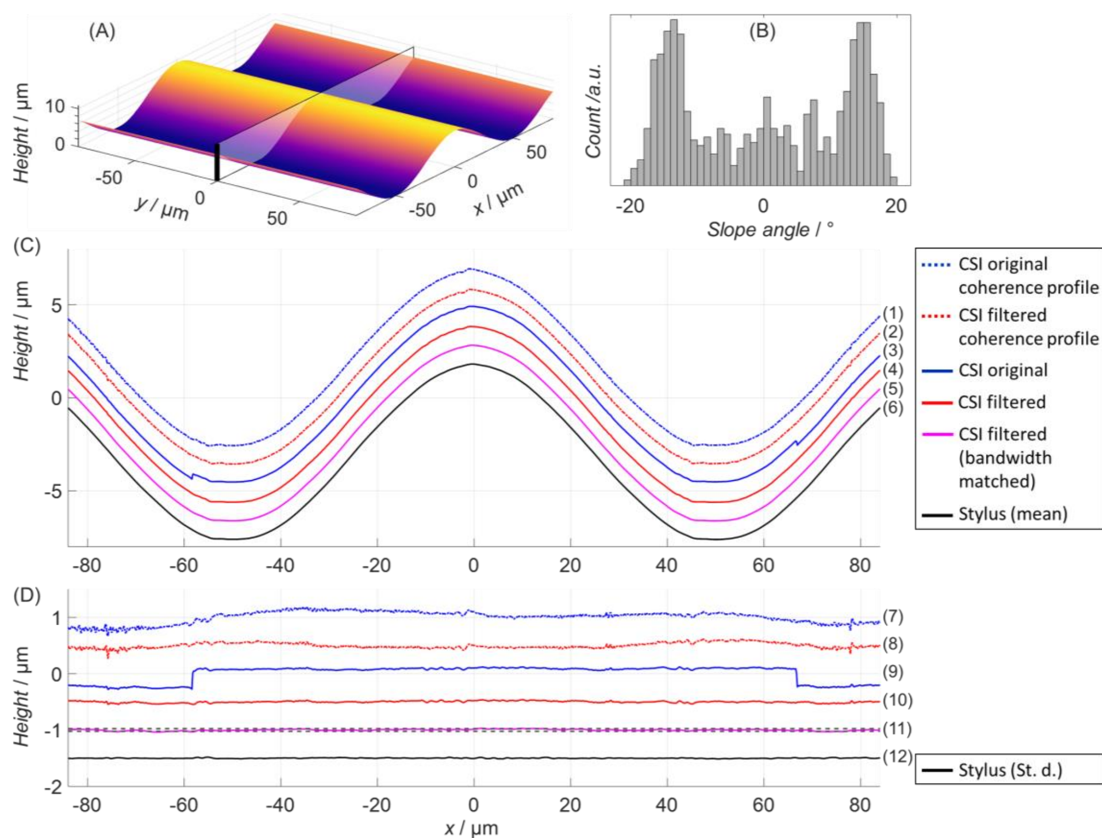


**Figure 3.8.** Measurements of surface R527. (A) 3D plot of the CSI-measured areal topography. (B) Slope angle distribution calculated from the stylus profile. (C) CSI- and stylus-measured profiles, where for display purposes the six profiles have been offset on the *y*-axis by {+2,+1,+0, −1,−2,−3} µm respectively. (D) Surface height differences between CSI- and stylus-measured profiles and the standard deviation of stylus-measured profiles, where the dashed line indicates the 24-nm reproducibility of the stylus measurement, and where for display purposes the six difference profiles have been offset on the *y*-axis by {+1.5,+1,+0,−0.5,−1,−1.5} µm respectively.

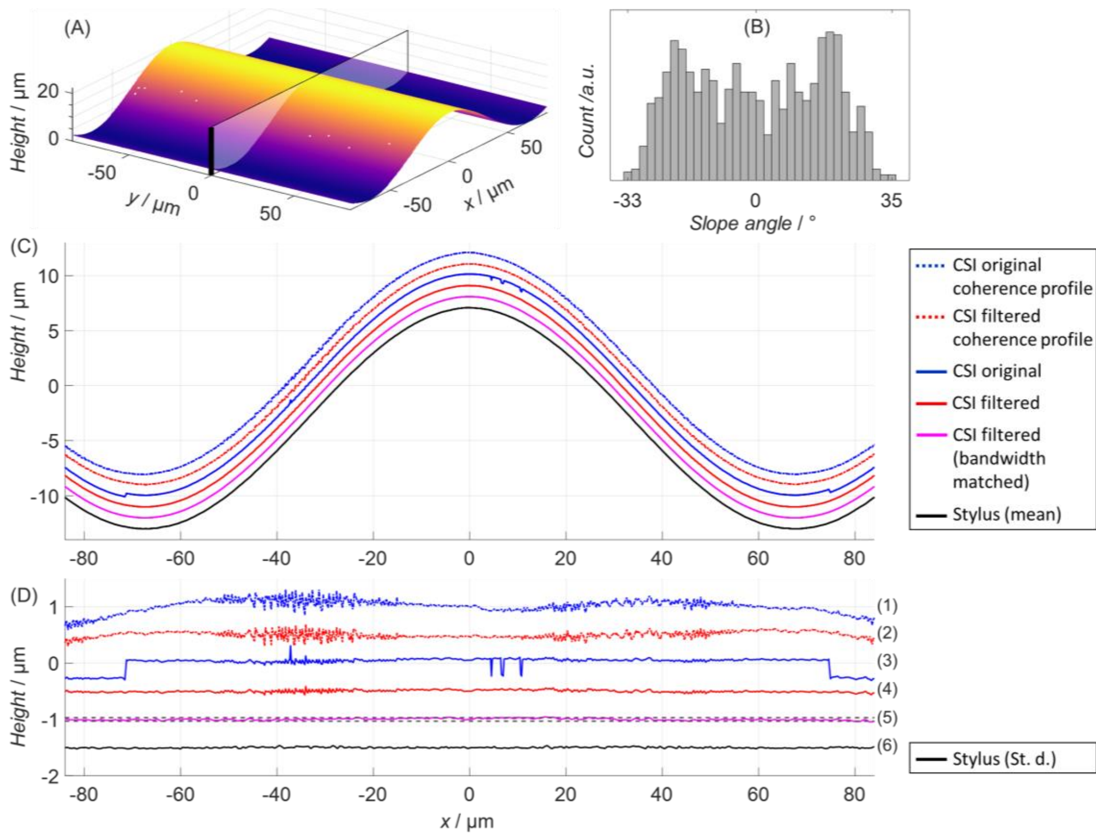


**Figure 3.9.** Measurements of surface R525. (A) 3D plot of the CSI-measured areal topography. (B) Slope angle distribution calculated from the stylus profile. (C) CSI- and stylus-measured profiles, where for display purposes the six profiles have been offset on the *y*-axis by {+2,+1,+0, −1,−2,−3} µm respectively. (D) Surface height differences between CSI- and stylus-measured profiles and the standard deviation of stylus-measured profiles, where the dashed line indicates the 30-nm reproducibility of the stylus measurement, and where for display purposes the six difference profiles have been offset on the *y*-axis by {+1.5,+1,+0,−0.5,−1,−1.5} µm respectively..

Considering that a real optical instrument is never precisely shift-invariant, the B-type spheres were also placed at two other locations in the field of view, $x = \pm 60$ µm (at $y = 0$), to characterise the 3D STFs locally. Three locations are found (i.e. west, central, and east) that are sufficient for the purpose of demonstrating the effectiveness of the inverse filtering for this work. Based on Eq. (3-35) and Eq. (3-36), three corresponding field-dependent inverse filters were calculated and applied to the original CSI fringe data separately to generate three filtered surface measurements, as shown in profiles (2 to 4) of Figure 3.7(C). Compared to the original CSI-measured profile, the measurement errors were effectively removed in the west, central, and east regions of the filtered profiles, respectively. Then, the filtered profiles were merged to generate profile (5) by

simply joining the corrected regions of profiles (2 to 4), where the boundaries of the three sub-regions were selected at $x = \pm 30$ μm, corresponding to approximately 1/3 and 2/3 of the field of view. To make appropriate comparison with the stylus measurement and match the spatial bandwidths of the different instruments [258,259], the corrected CSI profile is low-pass filtered with a 2 μm cut-off spatial wavelength [see profile (6) of Figure 3.7(C)]. Note that all CSI profiles in Figure 3.7 are calculated using coherence profile to determine the fringe order and phase information to refine the surface height measurement [87,110], here referred to as "high-precision CSI profile".

Figure 3.7(D) shows the differences between the CSI and stylus measurements and the standard deviation of the stylus measurements. Profile (8) clearly shows the presence of slope-dependent and 2π errors (due to an incorrect estimation of the fringe order by approximately half the mean wavelength [164]) in the original CSI measurements. The errors mostly occur at the upward slopes. Small bumps that periodically appears in profile (11) imply that the surface contains irregularities and high roughness in the regions of upward slopes. 2π errors are often removed using post-processing methods, such as phase unwrapping, if the surface is known to be smooth and continuous. However, the performance of such techniques is significantly limited for the surfaces considered that contain irregular features and roughness on high slopes. Profiles (9) and (10) shows the effective reduction of the errors after inverse filtering. The mean height deviation of profile (10) is 18 nm. As the comparison is made using the mean stylus profile, the deviation is mainly caused by the topographic reproducibility of the manufactured surface, which is of the order of 30 nm.

The slope distribution also shows that the upward slopes are steeper than the downward slopes. In the context of 3D imaging theory, high slopes may correspond to the high lateral spatial frequencies of the 3D STF. Based on an approximation, a 20° slope corresponds to a lateral spatial frequency of 1.22 $\mu m^{-1}$, calculated as $(2/\lambda_0)\times\sin(20°)$, where the magnitude of the in-pupil STF is slightly above 0.2 and the phase deviates from zero by 0.25 rad, as shown in Figure 3.5(V) and Figure 3.5(X). Therefore, the fringe contrast is reduced in the high slope region and the fringe pattern is distorted due to optical aberrations.

The same inverse filtering process was used for the case of R527 as shown in Figure 3.8. This surface has a similar maximum slope angle as the R521 case but a pitch of

100 μm, corresponding to a spatial frequency of 0.010 $\mu m^{-1}$. Profiles (1) and (2) are the coherence profiles and (3) and (4) show the high-precision CSI profiles. By the nature of the surface reconstruction method in CSI, coherence profiles do not have 2π errors but are sensitive to noise, as the coherence envelope is slowly varying and its width correlates with the coherence length of the light source, as discussed in section 2.3.1 and shown in section 2.4.1. It is more precise to determine the surface height using the phase information as the fringe that carries the height information has approximately ten peaks under that coherence envelope.

The coherence profile can be significantly influenced by retrace error, dispersion error [87,151,153,156,174], and errors that are induced by other aberrations [see profiles (7) in Figure 3.8(D)], which causes the incorrect estimation of the fringe order and, therefore, cause 2π errors in the high-precision CSI profile [see profiles (9)]. It is evident from Figure 3.8(D) that the inversion of the 3D STF successfully compensates the optical aberrations and corrects the fringe order analysis. Consequently, agreement between the CSI and stylus measurements is improved. The mean height deviation of profile (11) is down to 11 nm.

Figure 3.9 shows the result for surface R525 which has a maximum slope angle close to the limit of the acceptance angle of the lens determined by the NA. 2π errors appearing in the high slope region are removed, leaving the mean height deviation of profile (5) in Figure 3.9(D) to 13 nm.

Figure 3.10 shows the CSI measurement of the Ti-6Al-4V AM surface and the comparison before and after the inverse filtering. Based on the findings obtained from the measurements of sinusoidal surfaces, the difference in the coherence topography [Figure 3.10(B)] is highly likely to arise from the correction of the slope- and spatial frequency-dependent errors in the original measurement that suffers from optical aberrations. The difference in the high-precision topography is mainly due to the removal of 2π phase jumps through the fringe order correction. Although there is no reference measurement for the AM surface, the observed phenomenon agrees with that concluded from the sinusoidal surface measurements.

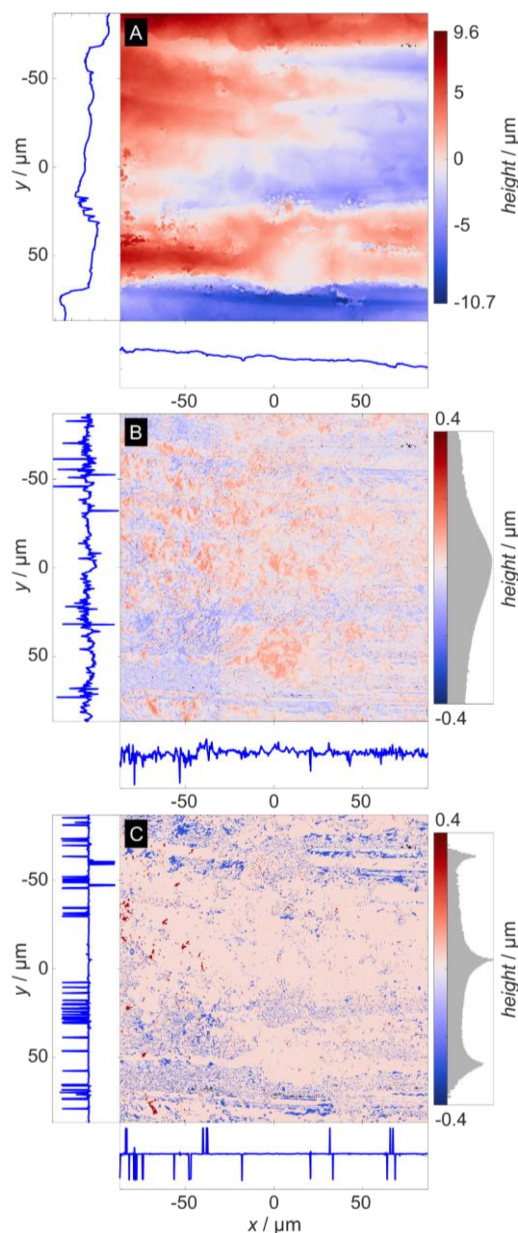


**Figure 3.10.** CSI measurements of the Ti-6Al-4V AM surface. (A) CSI high-precision areal topography. (B) Difference of the CSI coherence topography before and after the inverse filtering. (C) Difference of the CSI high-precision topography before and after the inverse filtering. Profiles are extracted through the origins. To improve the visibility, the magnitude of colourbar histograms in (B) and (C) are plotted in logarithmic scale and a threshold (−0.4 μm to 0.4 μm) of the height difference is used which removes outliers that account for 0.3% of the total number of measured points.

## 3.5 Conclusion and discussion

The 3D STF is an informative metric for quantitatively evaluating and comparing the performance of an optical surface measuring instrument in the linear regime, including the instrument's response to various slope angles and spatial frequencies. A real optical

3D imaging instrument is never ideal and always exhibits some degree of aberration. Optical aberrations cause retrace errors, dispersion errors, $2\pi$ errors, and other slope- and spatial frequency-dependent errors in a CSI instrument. Although these errors are well-known and have been corrected to some degree in the past, most of the correction methods are applied to the measured surface height data as post-processing approaches.

Here the experimental verification of the foil-model based characterisation of the 3D STF of a CSI instrument is demonstrated, and a practical method for compensating lens aberrations in CSI through phase inversion of the characterised 3D STF is presented. The error correction is carried out at a fundamental level by modifying the raw 3D fringe data prior to surface reconstruction and any post-processing.

Three freeform surfaces with varying slopes and spatial frequencies and an AM surface have been used as case studies to further validate the characterisation and error correction methods. Phase jumps have been largely removed, and the discrepancy between CSI and contact stylus measurement is reduced from a few tens of nanometres to 10 nm across a 170 µm field of view, which is commensurate with the noise floor of the stylus instrument. The change in topography is most significant in areas of high slopes as it is in these areas that the phase jumps are most prevalent, due to the lower SNR of the associated fringes produced by high slopes and due to the greater impact of lens aberration. In the context of 3D imaging theory, the high slopes may correspond to the high lateral spatial frequencies of the 3D STF, which have lower magnitudes and tend to be most affected by lens aberration than those with no lateral component (see Figure 3.5). In this way, the compensation of lens aberration is especially useful for measurements of surfaces with slopes close to the specular NA limit, as discussed in section 2.6.

Finally, this method may be applied to other 3D imaging modalities, e.g. imaging confocal microscopy and focus variation microscopy, which can also be treated as linear systems and are known to exhibit similar errors when presented with high surface slopes [88,260].

While the foil model assumes that a 3D linear shift-invariant filter applied to an object function is sufficient to accurately model the scatter produced by a range of surfaces [88], it is clear from Figure 3.7 that a real instrument may not be entirely shift-invariant, demonstrated by the field dependent differences in the phase of the STF.

From plot (2) of Figure 3.7(C), the application of a field-dependent inverse filter can be seen to be detrimental in regions that are characterised by a different STF. The use of three sphere measurements taken at different locations (west, central, and east) was used to resolve this issue, combining filtered results together from each region using data fusion methods [234]. Sphere measurements may need to be taken at multiple ($x$,$y$) FOV coordinates, depending on the isotropy and degree of variation of the STF across the FOV. For example, to correct an entire FOV, 5 sphere measurements taken at positions such as ⚄ may be necessary. This is in contrast to [247], which found improvement in measurement results from a single STF for surfaces measured at different locations in the FOV. The additional complexity involved in taking multiple measurements and combining partially overlapping differently-filtered topography data does somewhat lessen the ease and effectiveness of this technique compared to that described in [247]. The sphere size may also be more significant when field dependence is considered. Smaller spheres are likely better at producing an STF that characterises the instrument near to a specific field position as the sphere covers only a small portion of the FOV, but this can also lead to sampling issues and alignment issues; more information on sphere size can be found elsewhere [248].

Naturally, the foil model is incapable of accounting for multiple scattering effects or the effect of sharp edges, as neglecting these effects is a requirement of the KA. Surfaces must also have minimal shadowed regions when illuminated and typically cannot have overhangs or undercuts. Therefore, the accuracy of the foil model for tilted surfaces can be reduced compared to when untilted. To accurately model scatter from more complex surfaces, a more rigorous model is required, as developed over the following chapters of the thesis.

## 3.6 Summary

In this chapter, an approximate CSI model based on the Kirchhoff approximation (KA) was presented, known as the foil model. The model's theory was derived from scalar scattering theory and given in detail. The model states that the fringes produced by a CSI instrument can be predicted by filtering the spectrum of an object function (that follows the surface geometry) by a surface scattering transfer function (STF) associated with the instrument. The model is applicable for surfaces that are valid under the KA.

A method of obtaining the STF of an instrument though measurement of microspheres was described, and several STFs obtained from different microspheres. By obtaining an STF of an instrument experimentally the instrument can be characterised, and the effect of any lens aberration present can be found within the STF as non-zero phase. From the experimental STFs, inverse filters were produced that could be applied to measured fringes to compensate for the effect of lens aberration. This was demonstrated through application of inverse filters to several freeform surfaces, comparing the resulting topography data with that obtained from the unfiltered fringes and to the height data obtained from a traceable contract stylus instrument. The comparisons showed a reduction in fringe order errors, especially in areas of high slope, and a greater agreement of the topography data with the stylus instrument data. This provides experimental verification of the foil model and of the method of compensating for lens aberration by obtaining an STF experimentally.

In this chapter, an approximate coherence scanning interferometry (CSI) model is introduced, based on the Kirchhoff approximation (KA). The theory is first outlined, describing the optical process of a CSI instrument as a three-dimensional (3D) linear shift-invariant filtering operation that maps surface geometry to imaged fringes. Under this model the effects of the instrument on the measurement process are entirely contained within a surface transfer function (STF), including aspects of the optical system such as objective numerical aperture (NA), lens aberration, and reference mirror defocus [119,159]. A method to obtain an instrument's STF through measurement of a microsphere is described and the resulting experimental transfer functions are presented. From these experimental STFs, inverse filters (IF) can be generated that in principle can be applied to signal data captured by the instrument to compensate for the effects of lens aberration. From measurements of a sinusoidal grating, the topographies obtained from before and after compensation by an IF are compared both to each other and to measurements of the grating by a traceable contract stylus instrument.

# Chapter 4: Verification of a BEM optical scattering model

In this chapter, a rigorous two-dimensional (2D) model of electromagnetic surface scatter is presented, based on a boundary element method (BEM) established by Simonsen [261]. The model is experimentally verified by comparison of the simulated far-field scatter with measurements from a laser scatterometer for a sinusoidal grating, and by comparison of the model to known rigorous analytical solutions for certain surfaces via the Mie solution to Maxwell's equations (i.e., the Mie scattering theory). In addition, results from the BEM model are compared against those from an approximate approach for a wide range of sinusoidal grating surface wavelengths, and the regions of agreement investigated.

The work in this chapter is based on that presented at the European Optical Society Annual/Biennial Meeting (EOSAM) in 2018 [209]. Further verification work is performed as part of the following chapter (Chapter 5), which focuses on developing and verifying a model of coherence scanning interferometry (CSI) based on this chapter's BEM model.

## 4.1 Introduction

As discussed in section 2.4.3, non-linear rigorous models of optical scatter are necessary if accurate scatter for any arbitrary surface geometry is desired. While linear methods such as those based on the Kirchhoff approximation can provide accurate results for a wide variety of surfaces, they nonetheless make several assumptions about the surface so that the scattering problem is analytically tractable, limiting the range of applicability. Scatter from surfaces such as vee-grooves cannot be readily predicted by these linear methods, despite the strongly specular reflecting nature of the surface, due to the strong amount of multiple scattering (or more specifically multiple reflection) that occurs [175,178]. In general, rough surfaces and those with steep surfaces are more likely than flatter surfaces to produce multiple scattering, to have incident angle and polarisation dependent effects, and suffer more from geometric effects such as self-shadowing. Complex geometries that include overhangs are also impossible for linear methods to handle.

The BEM scattering model used in this chapter was implemented using MATLAB by collaborators at Loughborough University, based on the method described by Simonsen [261]; the underlying theory itself was developed earlier by Maradudin et al [262]. The method is derived from Maxwell's equations and can account for surface plasmons in metals. The method relies on the Ewald-Oseen extinction theorem, which states that the incident field is extinguished within an object by a component of the induced field, and the other component of the induced field then satisfies the wave equation for the object's refractive index [263–265]. For monochromatic, linearly polarised plane wave illumination, the BEM model solves linear partial differential equations along the surface boundary to obtain the field and its surface normal derivative, from which near-field and far-field scatter can then be calculated [261]. The numerical approach used is formally exact and is therefore in principle applicable to scattering from surfaces of any topography [261].

The BEM approach is in principle faster (decreased computational effort) for solving surface boundary problems than methods such as finite element methods (FEM) due to the BEM approach scaling better with surface size [188]. For example, for surface modelling for a surface made up of $N^2$ points, FEMs scale with $N^6$ while BEMs scale with $N^4$, despite both methods requiring matrix inversion [49]. Note that the BEM model considered in this chapter is limited to only 2D surfaces, i.e., limited to surfaces completely described only by a set of lateral and axial coordinates ($x$, $z$), where surface undercuts are allowed. A similar model that can handle three-dimensional (3D) surfaces is a boundary source method named 3sBSM, described elsewhere [220]; however use of the 3sBSM model is more complex and its computation time currently prohibitive for use in polychromatic NA illuminated instrument modelling.

Publications using this chapter's BEM model directly include [209,225–228], and this model has also been used to develop the BEM-CSI model presented in Chapter 5.

## 4.2 Theory

As already stated, the BEM model essentially follows that described by Simonsen in section 4.10 of [261], which details the 2D BEM surface scattering theory in full. However, following Simonsen's work, the following derivation is given here using a somewhat simpler notation and omitting the more complicated details. This has been carried out to explain the core of the BEM approach to a reader who may not have

access to Simonsen's paper or finds the simpler notation more accessible, and for completeness. To this aim, some steps of the derivation are omitted and at times expressions are simplified.

The surface is modelled as an object that occupies space $\Omega$ with permittivity $\varepsilon_-$ and permeability $\mu_-$, in a surrounding space $\overline{\Omega}$, with permittivity $\varepsilon_+$ and permeability $\mu_+$, where $\mathbf{n}$ is an outward vector normal to the boundary surface $\partial\Omega$ (pointing from $\Omega$ towards $\overline{\Omega}$), as shown in Figure 4.1.

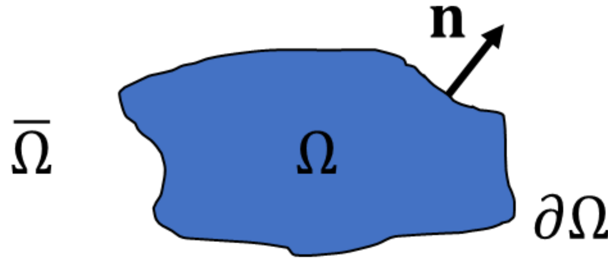


**Figure 4.1.** Geometry of the object considered for the scattering problem

If an incident electromagnetic wave $\Phi^{inc}(\mathbf{r})$ generated by some external source occupies space $\overline{\Omega}$, then the total electromagnetic field inside space $\overline{\Omega}$, i.e. $\mathbf{r} \in \overline{\Omega}$, can be represented by the surface integral

$$\Phi^{out}(\mathbf{r}) = \Phi^{inc}(\mathbf{r}) + \frac{1}{4\pi}\iint_{\partial\Omega}\left[\Phi^+(\mathbf{r}')\frac{\partial G^+(\mathbf{r}-\mathbf{r}')}{\partial n'} - G^+(\mathbf{r}-\mathbf{r}')\frac{\partial\Phi^+(\mathbf{r}-\mathbf{r}')}{\partial n'}\right]dS', \quad (4\text{-}1)$$

or equivalently, inside $\Omega$ ($\mathbf{r} \in \Omega$), as

$$\Phi^{inc}(\mathbf{r}) = -\frac{1}{4\pi}\iint_{\partial\Omega}\left[\Phi^-(\mathbf{r}')\frac{\partial G^-(\mathbf{r}-\mathbf{r}')}{\partial n'} - G^-(\mathbf{r}-\mathbf{r}')\frac{\partial\Phi^-(\mathbf{r}-\mathbf{r}')}{\partial n'}\right]dS', \quad (4\text{-}2)$$

where $\frac{\partial}{\partial n'}$ is the derivative of the function along the normal vector $\mathbf{n}$ at the point $\mathbf{r}'$, $\Phi^+(\mathbf{r}')$ and $\frac{\partial\Phi^+(\mathbf{r}')}{\partial n'}$ are values of the electromagnetic field and its surface normal derivative at the outer side of the boundary $\partial\Omega$, $\Phi^-(\mathbf{r}')$ and $\frac{\partial\Phi^-(\mathbf{r}')}{\partial n'}$ are values of the electromagnetic field and its surface normal derivative at the inner side of the boundary $\partial\Omega$, $G^+(\mathbf{r}-\mathbf{r}')$ and $\frac{\partial G^+(\mathbf{r}-\mathbf{r}')}{\partial n'}$ are the Green's function (of the Helmholtz wave equation) and its surface normal derivative in $\overline{\Omega}$, and $G^-(\mathbf{r}-\mathbf{r}')$ and $\frac{\partial G^-(\mathbf{r}-\mathbf{r}')}{\partial n'}$ are the Green's function and its surface normal derivative inside $\Omega$. Note that the $\mathbf{r}'$ is bound to the surface $\partial\Omega$ and the surface integral that varies this parameter for each surface

element $dS'$ forms a closed surface. The field $\Phi^{\pm}(\mathbf{r})$ is the electric component of the TE wave or the magnetic component of the TM wave, and the 2D outgoing Green's function $G^{\mp}(\mathbf{r},\mathbf{r}')$ can be given by

$$G^{\mp}(\mathbf{r},\mathbf{r}') = i\pi H_0^{(1)}(k_{\mp}|\mathbf{r}-\mathbf{r}'|)\,, \tag{4-3}$$

where $k_{\mp}$ is a wave vector of the medium, i.e. $k_{\mp} = n_{\mp}k_o$ for vacuum wave vector $k_o$ and refractive index of the media $n_{\mp}$, and $H_0^{(1)}(\cdot)$ is the Hankel function of the first kind and zeroth order. Note that the dependence of the fields and the Green's functions on the frequency of light has been omitted to simplify the notation, and that Sommerfeld's radiation condition [230,266] has been used to remove the need to integrate the exterior region at infinity, i.e. so that only the boundary between the object and the exterior space is relevant. Also note that Eq. (4-2) is the Ewald-Oseen extinction theorem, where the incident field is seen to be extinguished inside the object ($\Omega$) by the induced field. The equivalence of the extinction theorem and the boundary-value scattering problem is shown elsewhere [265].

To evaluate the fields everywhere by using Eq. (4-1) and Eq. (4-2), knowledge of the values of $\Phi^{+}(\mathbf{r}')$, $\Phi^{-}(\mathbf{r}')$, $\frac{\partial\Phi^{+}(\mathbf{r}-\mathbf{r}')}{\partial n'}$ and $\frac{\partial\Phi^{-}(\mathbf{r}-\mathbf{r}')}{\partial n'}$ at the boundary $\partial\Omega$ is needed. These terms can be approximately evaluated using the Fresnel equations, a method taken by Beckmann's Kirchhoff approximation (KA)-based approach to model surface scattering [141,208]. This KA-based approach is also a part of the Foil model, discussed in Chapter 3. This leads to a non-rigorous model of surface scattering that is valid only when the KA holds and multiple scattering is negligible [184,185]. To be able to solve the scattering problem rigorously, the field and its normal derivative on the surface can instead be calculated by taking advantage of the extinction theorem. An exact solution of the scattering problem first equates the fields and their derivatives on the boundary between two media, i.e.

$$\Phi^{+}(\mathbf{r}') = \Phi^{-}(\mathbf{r}'), \tag{4-4}$$

$$\frac{1}{\kappa^{+}}\frac{\partial\Phi^{+}(\mathbf{r}')}{\partial n'} = \frac{1}{\kappa^{-}}\frac{\partial\Phi^{-}(\mathbf{r}')}{\partial n'}, \tag{4-5}$$

where $\kappa_{TE}^{+} = \mu^{+}, \kappa_{TE}^{-} = \mu^{-}, \kappa_{TM}^{+} = \varepsilon^{+}$ and $\kappa_{TM}^{-} = \varepsilon^{-}$; $\kappa^{+}$ and $\kappa^{-}$ are here used without a subscript as $u^{\pm}(\mathbf{r})$ represents either the TE or TM case. These boundary conditions

given in Eq. (4-4) and Eq. (4-5) are applied to Eq. (4-1) and Eq. (4-2), coupling the two inhomogeneous integral equations.

These can then be solved by discretising the coordinates that comprise the boundary surface, and from this forming matrix equations that can be numerically solved as long as the step size adequately approximates the integrals. The boundary surface (contour) of the domain Ω is divided into *N* control points and, at these points, the fields $\Phi^{+}(\mathbf{r}')$ and their derivatives $\frac{\partial\Phi_j^{+}(\mathbf{r}')}{\partial n'}$, $j = 1, 2, \ldots, N$, at the side of the upper/external (+) medium are assumed unknown. By appropriately applying the boundary conditions given in Eq. (4-4) and Eq. (4-5) to the fields in Eq. (4-1) and Eq. (4-2), a system of 2*N* equations with 2*N* unknowns is obtained; *N* fields $\{\mathcal{F}_j = \Phi_j^{+}(\mathbf{r}')\}$ and *N* derivatives $\{\mathcal{N}_j = \frac{\partial\Phi_j^{+}(\mathbf{r}')}{\partial n'}\}$. If from $\mathcal{F}_j$ and $\mathcal{N}_j$ two vectors are formed with length *N* $\{\mathcal{F} = (\mathcal{F}_1, \mathcal{F}_2, \ldots, \mathcal{F}_N)$, $\mathcal{N} = (\mathcal{N}_1, \mathcal{N}_2, \ldots, \mathcal{N}_N)\}$, a system of two matrix equations can be formed.

$$-(\mathbf{A}^{+} - \mathbf{I})\mathcal{F} + \mathbf{B}^{+}\mathcal{N} = \mathcal{F}^{inc}, \tag{4-6}$$

$$-\mathbf{A}^{-}\mathcal{F} + \frac{\kappa_\nu^{-}}{\kappa_\nu^{+}}\mathbf{B}^{-}\mathcal{N} = 0, \tag{4-7}$$

where $\mathcal{F}^{inc}$ is a vector whose components are the incident fields at the *N* control points at the boundary surface contour, **I** is the identity matrix, and the components of the matrices $\mathbf{A}^{-}$, $\mathbf{A}^{+}$, $\mathbf{B}^{-}$ and $\mathbf{B}^{+}$ are best given in equations (138a) and (138b) of Simonsen's paper (and are derived in its appendix) [261]. However, note that they depend on the surface normal derivative of the Green's function and the Green's function respectively, as they are derived from Eq. (4-1) and Eq. (4-2).

The solutions to the system of equations (Eq. (4-6) and Eq. (4-7)) that provides values for the components of the vectors $\mathcal{F}$ and $\mathcal{N}$ can be represented by

$$\mathcal{F}_j = \boldsymbol{\mathcal{F}}\mathcal{F}^{inc}, \tag{4-8}$$

$$\mathcal{N}_j = \boldsymbol{\mathcal{N}}\mathcal{F}^{inc}, \tag{4-9}$$

where the matrices $\boldsymbol{\mathcal{F}}$ and $\boldsymbol{\mathcal{N}}$ are defined as:

$$\boldsymbol{\mathcal{F}} = \left[-(\mathbf{A}^{+} - \mathbf{I}) + (\mathbf{B}^{+})\left(\frac{\kappa_\nu^{-}}{\kappa_\nu^{+}}\mathbf{B}^{-}\right)^{-1}(\mathbf{A}^{-})\right]^{-1}, \tag{4-10}$$

$$\boldsymbol{\mathcal{N}} = \left[-(\mathbf{A}^{+} - \mathbf{I})(\mathbf{A}^{-})^{-1}\left(\frac{\kappa_\nu^{-}}{\kappa_\nu^{+}}\mathbf{B}^{-}\right) + (\mathbf{B}^{+})\right]^{-1}. \tag{4-11}$$

With these matrices defined, Eq. (4-8) and Eq. (4-9) can give the electromagnetic fields and their surface normal derivatives along the boundary on the outside of the object, from which near- and far-field field values could be calculated. By definition, the second term (i.e. the entire integral) of Eq. (4-1) is the scattered field outside the object, i.e. as $\Phi^{out}(\mathbf{r}) = \Phi^{inc}(\mathbf{r}) + \Phi^{sc}(\mathbf{r})$. Equivalently, from Eq. (4-6) the following expression can be obtained:

$$\mathcal{F} - \mathcal{F}^{inc} = \mathcal{F}^{sc} = \mathbf{A}^{+}\mathcal{F} - \mathbf{B}^{+}\mathcal{N}. \tag{4-12}$$

From this expression, the BEM model can be used to calculate scatter in the near field and far field, where $\mathbf{A}^{+}$ and $\mathbf{B}^{+}$ are in general dependent on $\mathbf{r}$ and $\mathbf{r}'$. However, for experimental verification and for CSI modelling it is only the far-field scattering distribution function that is of interest, which provides the intensity of the scattered light captured at some scattering angle. The far-field scatter at a position with vector $\mathbf{r}_j$ can be given by

$$\mathcal{F}^{sc}(\mathbf{r}_j) = \sum_{i=1}^{N} a_n(\mathbf{r}_j)\mathcal{F}_n - b_n(\mathbf{r}_j)\mathcal{N}_n, \tag{4-13}$$

where $F_n$ and $D_n$ are the components of the vectors $\mathcal{F}$ and $\mathcal{N}$, and $N$ is the number of control points, as previously defined. The coefficients in Eq. (4-13) are obtained the elements of $\mathbf{A}^{+}$ and $\mathbf{B}^{+}$ in the far field case and are given by

$$a_n(\mathbf{r}_j) = Q\frac{dl_n}{4}\exp(-i\mathbf{r}_n \cdot \mathbf{k}_j)\,\mathbf{n}_n \cdot \mathbf{k}_j, \tag{4-14}$$

$$b_n(\mathbf{r}_j) = iQ\frac{dl_n}{4}\exp(-i\mathbf{r}_n \cdot \mathbf{k}_j), \tag{4-15}$$

and

$$Q = \sqrt{\frac{-2\mathrm{i}}{\pi \mathrm{k}_{+}|\mathbf{r}_j|}}. \tag{4-16}$$

Here, $\mathbf{k}_j = \frac{\mathbf{r}_j}{|\mathbf{r}_j|}k_{+}$, $\mathbf{r}_n = (x_n, z_n)$, $\mathbf{n}_n$ is the surface normal vector of the $n^{\text{th}}$ element, $dl_n$ is the length of the $n^{\text{th}}$ element of the scattering boundary, and $k_{+}$ is the wavevector of the light in the scattering medium.

Finally, the measured intensity is given by

$$I^{sc}(\mathbf{r}_j) = \frac{\varepsilon_{+}\mu_{+}\varepsilon_0}{2}\left|\mathcal{F}^{sc}(\mathbf{r}_j)\right|^2, \tag{4-17}$$

where $\varepsilon_0$is the permittivity of free space.

An alternative approach for the far field case taken in Simonsen's paper uses the Fourier representation of the Green's function (instead of Eq. (4-3)), where the surface coordinate considered is neglected in the Green's function. This then provides an expression for $\Phi^{sc}(\mathbf{r})$ as an integral of a scattering amplitude function over all scattering angles, where the scattering amplitude function is itself a function of the field and its surface normal derivative along the entire boundary, and weighted by the specific scattering angle considered. In general care must be taken when numerically evaluating the Hankel function directly (or by using built-in functions) in the far field due to issues with numerical instability [267]. In the BEM scattering model used in this thesis, for far-field calculations, an asymptotic expression for large arguments is used for the Hankel function, while the built-in Hankel function in MATLAB is used for near-field calculations.

## 4.3 Methodology

To verify the BEM model, several comparisons were made. The model had already been tested for simple surfaces, such as a flat and a low-amplitude sinusoidal grating (PV $\ll \lambda$ for peak-to-valley surface amplitude PV and illumination wavelength $\lambda$), and the results compared against those obtained from Fourier optics [192,245], giving good agreement. To compare the BEM model against an exact reference, near-field scatter for a transmissive cylinder was calculated and compared against that predicted by Mie scattering theory, which is an exact solution of Maxwell's equations for spheres and cylinders [268,269]. Experimental verification was also performed, comparing the model against scatterometer measurement of a higher amplitude sinusoidal grating (PV $> 10\lambda$), for which Fourier optics modelling would not be valid. Results from the BEM model for this surface were therefore also compared against a KA-based model. Finally, results from the BEM model and KA-based model were compared for a wide range of sinusoidal gratings with different surface wavelengths, and their region of agreement investigated.

### 4.3.1 Scatterometer measurement method

As the BEM model is a 2D model, a sinusoidal grating was measured. The grating used was produced by Rubert & Co Ltd and was produced using nickel electroforming, with a nominal amplitude of 9.5 μm and a nominal wavelength of 135 μm (i.e., a maximum slope angle of ~23.9°). Using a stylus profile instrument, an equivalent grating was

measured and several profiles along the direction of sinusoidal variation were collected. From this data, a curve fitting the profile to a sine function gives a measured peak-to-mean amplitude of 10.05 µm (i.e. PV of 20.1 µm) and surface wavelength of 134.8 µm (a maximum slope angle of ~25.1°). This surface geometry is shown in Figure 4.2.

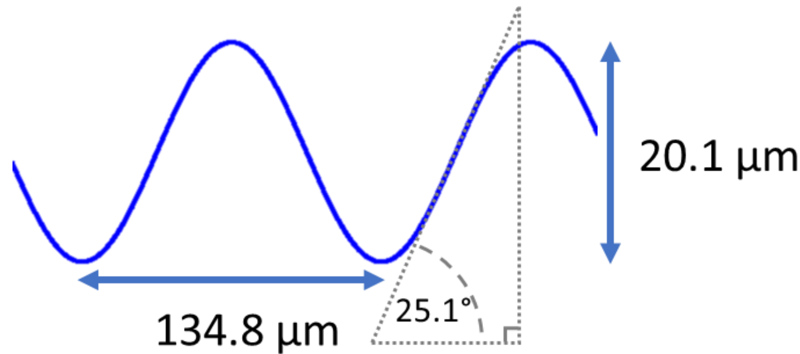


**Figure 4.2.** Illustration of the surface geometry of the measured sinusoidal grating. Not to scale, as the height of the grating has been exaggerated.

The bidirectional reflectance distribution function (BRDF) from this grating was measured by collaborator Hamidreza Aryan with a high-accuracy angular scatterometer at the University of North Carolina at Charlotte (UNCC), named CASI [270,271]. A block diagram of the scatterometer is shown in Figure 4.3. More information on BRDF can, for example, be found in [272]. BRDF measurement of the grating using the CASI scatterometer was made over a range of angles spanning a semicircle centred on the point of sample illumination. The general geometry of BRDF measurement is shown in Figure 4.4. The semi-circular scanning path was chosen to lie on the plane of incidence, i.e., the plane in which both the grating's surface normal and the incident illumination's propagation vector lies. Since this incident propagation vector can be freely chosen, the plane of incidence can be aligned so that its normal is parallel to the grating's ruling direction. The incident illumination was a p-polarised (i.e. transverse magnetic (TM) polarisation) beam produced by a laser source ($\lambda = 632.8$ nm) which illuminates the grating at an angle of incidence of 5° from the grating's surface normal. The illumination's beam diameter on the surface was approximately 1.5 mm, having been reduced from 6 mm by application of an illumination aperture.

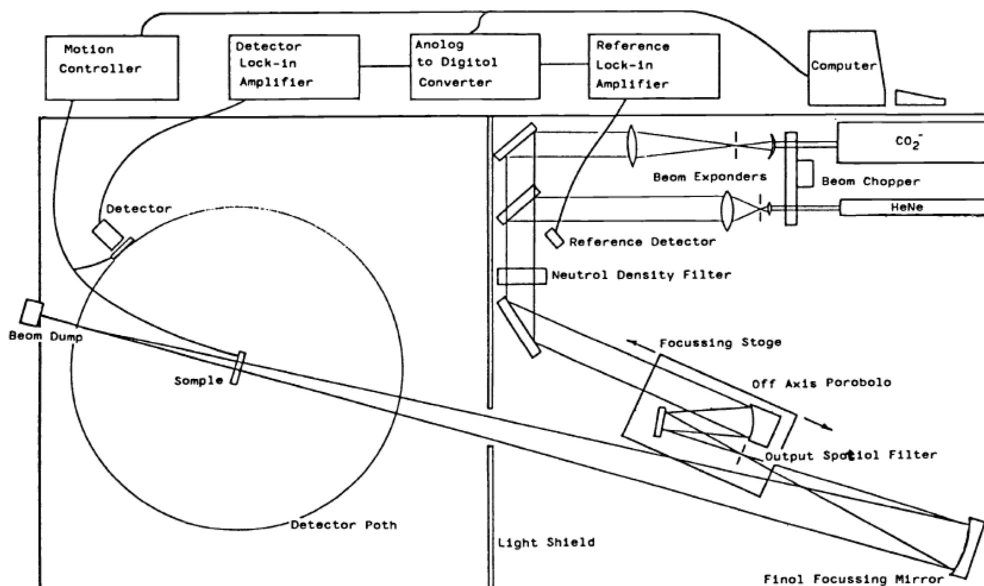


**Figure 4.3.** Overall block diagram for the CASI scatterometer. Reproduced from [270] with permission from author Dr John Stover and publisher SPIE.

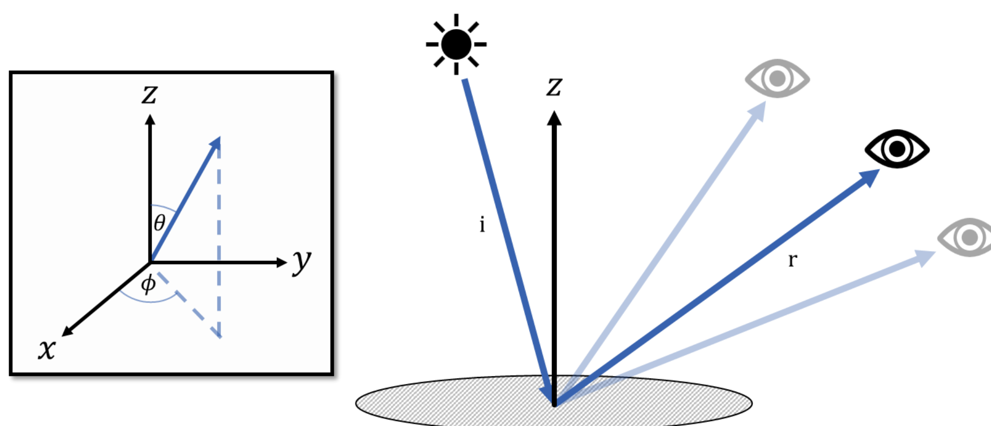


**Figure 4.4.** Geometry of BRDF measurement. Incident illumination with a fixed irradiance is applied with angles $\theta_\mathrm{i}$, $\phi_\mathrm{i}$ to a surface, and the radiance of the resulting scatter is measured at angles $\theta_\mathrm{r}$ and $\phi_\mathrm{r}$, where $\theta$ and $\phi$ are the zenith and azimuth angle respectively. The BRDF has units of inverse steradians, where steradians are a unit of solid angle. In general, the BRDF is a four-dimensional function of $\theta_\mathrm{i}$, $\phi_\mathrm{i}$, $\theta_\mathrm{r}$, and $\phi_\mathrm{r}$. In this work, only an arc along $\theta_\mathrm{r}$ is measured for constant $\theta_\mathrm{i}$ and $\phi_\mathrm{i} = \phi_\mathrm{r} = 0$. Note here that the surface normal is aligned with the $z$ axis of the optical geometry.

A scan of BRDF values along this semi-circular path was taken from -95° to 85° with the 0° position of the data set in the instrument to be the "specular region" as part of the pre-measurement alignment procedure. This specific measurement path was chosen under the assumption that the illumination was located at $-10°$ and the normal of the surface's mean plane at $-5°$, and therefore the specular region (centred at 0°) includes

the angles close to the angle at which light would be primarily reflected if the surface were perfectly smooth. Illumination with normal incidence to the surface mean plane could not be used as the placement of the detector would obscure the source of illumination during the necessary alignment procedure, which was why an incidence angle of 5° was used.

Measurements of the BRDF were taken in steps of 0.478° across the semicircle, where the goniometric component of the CASI has a lateral resolution of 0.001° (0.01 mm linear) [270]. A fixed collection aperture of 12.525 mm was used across the range, except for the specular region. Around this region, the measurements were taken using smaller apertures (4.846 mm and 1.640 mm) and using smaller angular steps (steps of 0.185°, 0.063° and 0.013°), likely following a default configuration optimised for surfaces that strongly scatter in the specular direction. The smaller aperture was likely used in this region due to the much larger signal strength expected. However, as this data is filtered out, only the fixed collection aperture and default angular step used outside the specular region are relevant.

To compare the BRDF to an angular scattered intensity distribution (ASD) produced by a model, a cosine correction must be applied to the BRDF, as described in [272]. The cosine correction to the BRDF allows easier examination of the ratio between the scattered light power per unit solid angle and the incident power. As the incident power and the detector's aperture are fixed for all angles considered in the comparison, the definitions of the cosine corrected BRDF and the ASD only differ by a fixed constant amount, allowing for meaningful comparison. Note that the intensity ordinate has been normalised for this comparison to avoid considering these scale factor differences; in this work, the priority was comparing how the shape of the distribution of the ASD varies compared to the cosine corrected BRDF.

### 4.3.2 Comparison with BEM modelling

The ASD from the BEM computational model was obtained, matching where possible the experiment and experimental grating's specification for the modelled surface. We used a virtual sinusoidal grating with the previously measured amplitude and wavelength (10.05 µm, 134.8 µm); plane wave illumination with wavelength $\lambda$ = 633 nm and p-polarisation was used at an incident angle of 5°; the surface is treated as having the electromagnetic boundary conditions of an ideal conductor; and the input

beam was chosen to be a plane wave of infinite extent. While the final ASD is shown later in section 4.4.2, it is useful in explaining the method taken to present some preliminary results here, shown Figure 4.5. In Figure 4.5, the 0° position is the direction of the mean plane's surface normal, and the incident illumination arrives at the +5° position. Note that the asymmetry of the result comes from the incident angle of +5°; the intensity peaks at roughly +45° and −55° can be predicted using geometrical optics for this angle of incidence.

The total length of the illuminated grating was 1.4828 mm (eleven surface wavelengths), chosen to match CASI's beam diameter of 1.5 mm. Control points along this surface are chosen automatically, ensuring the surface is sufficiently sampled to produce accurate scattering results: the distance between control points was set to be a maximum of $\lambda/5$= 127 nm apart. The scattering problem is solved computationally, and the far-field field strength calculated across 50,000 uniformly distributed angles between −80° and +80° (an angular step size of 0.0032°). This high angular sampling easily guarantees that even the thin intensity peaks will be well represented; each fine peak in Figure 4.5 on average being made up of twelve points.

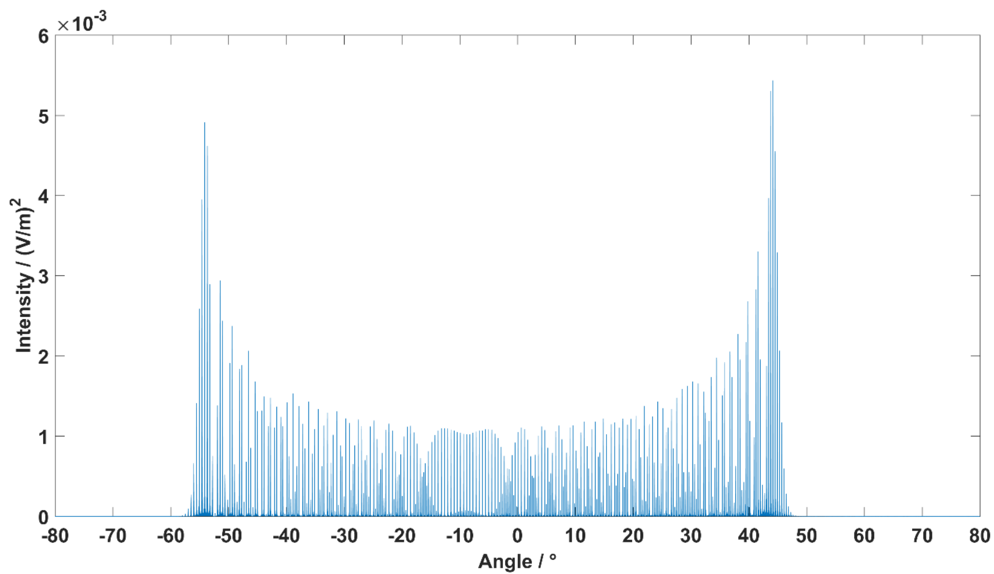


**Figure 4.5.** Simulated far-field scattered intensity due to illumination of a sinusoidal grating (peak-to-mean amplitude: 10.05 μm, surface wavelength: 134.8 μm) with $\lambda$ = 633 nm p-polarised light incident at 5° from the surface normal

This ASD model data must also be filtered for effective comparison with experimental scatterometer measurement data, as the measured data represents the scatter collected at each angular position over a small range of angles that are simultaneously collected

by the aperture of the sensor. Therefore, convolution of the ASD data with an aperture function is performed. The 12.525 μm aperture corresponds to a ~1.2° angular "width", however a simple rectangular convolution kernel of this width resulted in a noisy output due to the unphysical hard cut-off. By additionally considering that the detector will not equally collect light across its aperture to its sensor, a combination of a rectangular function of width 0.9° with a Gaussian function with standard deviation of 0.2° was chosen as a convolution kernel, shown in Figure 4.6. Since the intensity ordinate of the ASD will be normalised, the scale of this aperture convolution kernel is not considered. The result of the convolution is shown in Figure 4.7.

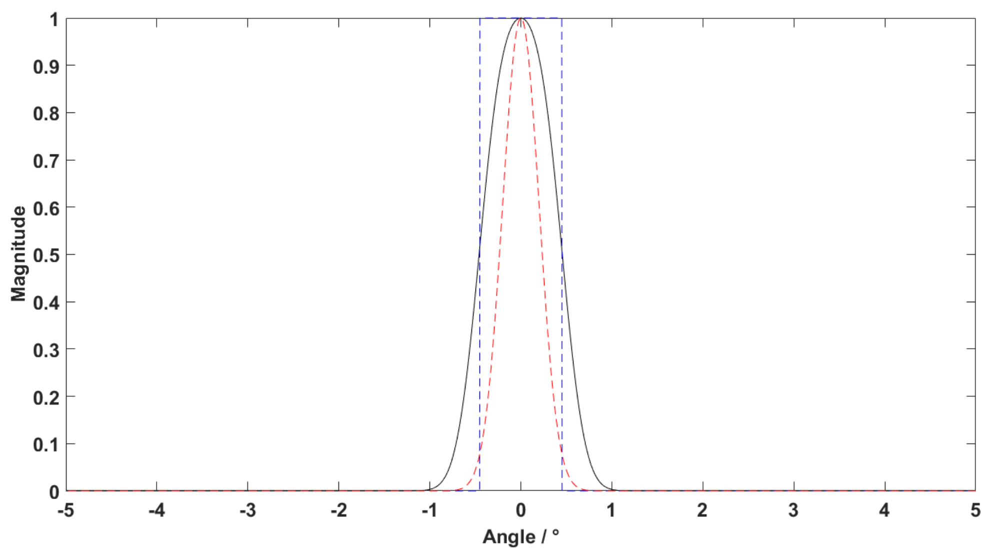


**Figure 4.6.** Convolution function (black line) obtained by convolution of a rectangular function of width 0.9° (blue dashed line) with a Gaussian function with standard deviation of 0.2° (red dashed line). This function is applied to the simulated ASD when it is compared with experimental data.

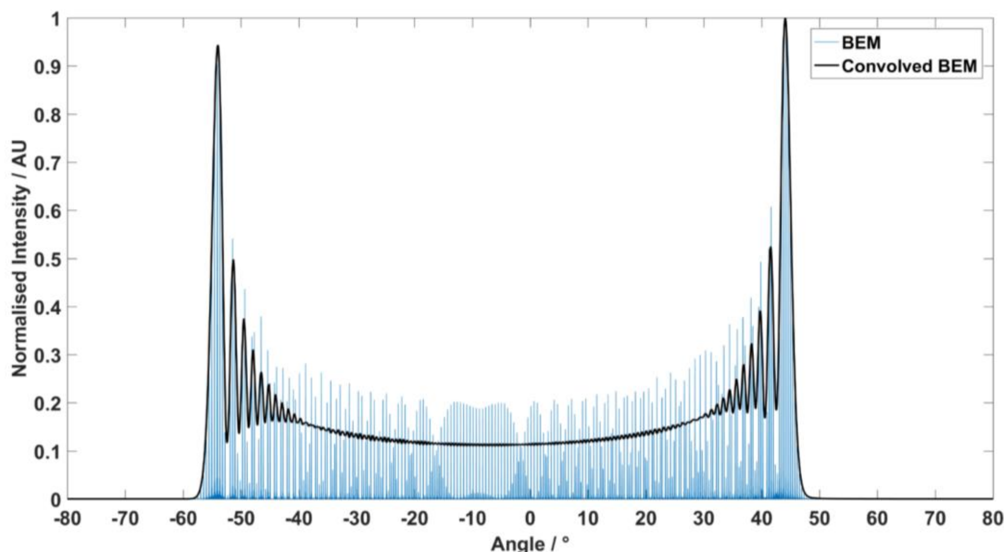


**Figure 4.7.** Result of convolution of the ASD calculated using BEM

### 4.3.3 Model comparison for a range of sinusoids

Because the aforementioned ideal sinusoidal grating is not expected to produce multiple scattering, the results from the rigorous BEM model for scatter from this grating can also be compared to those from a KA-based (i.e. non-rigorous) model, where agreement between the two is expected for this specific surface geometry, providing evidence of the BEM model's validity. The comparisons made for this surface geometry are discussed in section 4.4.2. However, it is interesting to investigate for which surface slopes the expected agreement would begin to fail, i.e., when the KA no longer holds. While this does not verify that the BEM model provides accurate scatter for this domain, a disagreement between the KA and the BEM model where the KA is expected to fail is nonetheless expected, given that multiple scattering will begin to contribute to the scatter more significantly in this region. Comparisons are made between the models using a sinusoidal grating similar to that used for Figure 4.5, except here the nominal surface parameters are used, with a total surface length of 810 µm (six surface wavelengths), and illuminated with normal incidence light. While the surface peak amplitude is held constant at 9.5 µm, the surface period is varied from 135 µm down to 11 µm in steps of 1 µm. The results are shown in section 4.4.3, with select examples and an overview of the entire range presented.

## 4.4 Results & Discussion

### 4.4.1 Comparison to Mie scattering

The results of the comparison between the BEM model and the Mie scattering theory are shown in Figure 4.8. Here the illumination was a p-polarised plane wave with wavelength of 0.5 µm travelling along the $z$-direction towards positive $z$, for a dielectric cylinder of radius 0.5 µm, and the refractive index of the medium outside and inside the cylinder was 1.0 and 1.5 respectively.

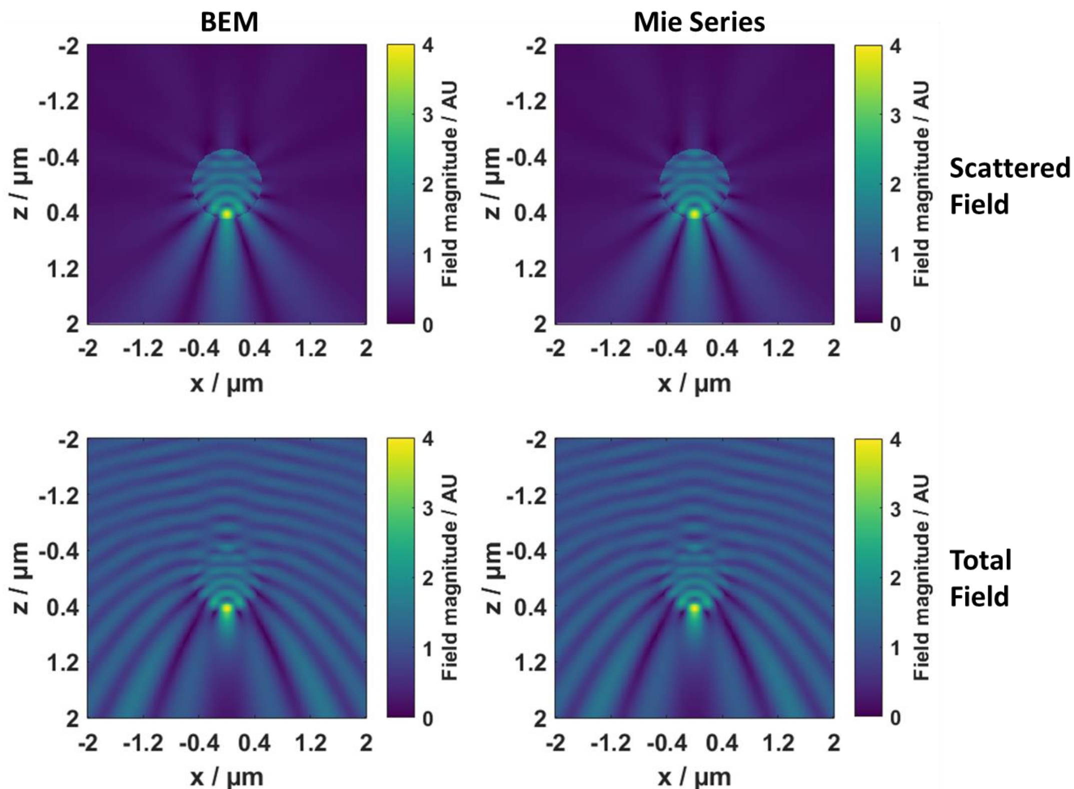


**Figure 4.8.** Magnitude of the scattered field and total field for the BEM model and the Mie solution for a homogenous cylinder.

No significant differences were seen between the results from the BEM model and the Mie theory. Away from the surface boundary, the maximum difference between the results in the plots in Figure 4.8 were approximately 200 times smaller than the maximum field magnitude inside the cylinder, and outside the cylinder the maximum difference is approximately 2000 times smaller than the maximum field magnitude. Along the surface boundary there are some artefacts present in the results from the BEM model that differ more significantly from the Mie scattering theory, that occur due to the BEM model having to discretely sample the cylinder. As the number of samples for

this cylinder boundary increases, the presence and magnitude of these artefacts decreases.

This overall agreement provides strong evidence that the BEM model can accurately predict scatter and do so beyond the linear regime, given that Mie scattering theory is a direct solution of Maxwell's equations and the relatively high curvature of the cylindrical surface.

### 4.4.2 Comparison to scatterometer

The measurement as reported by the CASI instrument is shown in Figure 4.9. Negligible values of BRDF at high angles are removed from the data to allow for easier viewing of the data, and a small number of points with extreme BRDF values around −70° were removed as outliers. The two gaps in BRDF values around −10° and 0° are caused respectively by the receiver obscuring the illumination, for which no measurements were taken, and in the defined specular region, where the data is filtered out due to the use of different apertures and angular steps.

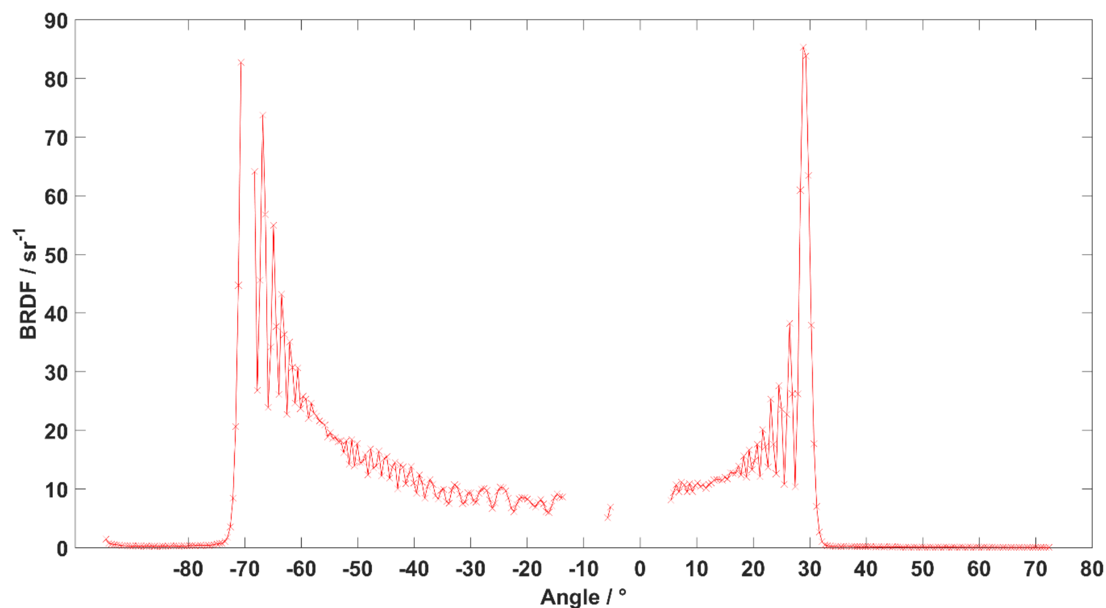


**Figure 4.9.** Measurement of the BRDF (in units of inverse steradians) produced by the CASI scatterometer at UNCC. The axis Angle has values reported by the instrument, as described in section 4.3.1.

The measurement that produced the data in Figure 4.9 was taken with the assumption that, as the illumination was at −10° and the surface normal at −5°, the specular region was therefore at 0°; i.e., illumination with an incident angle of −5° from the surface normal was used. This choice is reiterated by the measurement data being collected

from −95° to 85°, i.e., placing the centre of the measurement data range at −5°, where the surface normal is believed to be, collecting an equal amount of scatter from either side of the semicircle. However, this measurement configuration should not produce peaks at −70° and 30°, and this misconfiguration issue in the data and metadata provided by UNCC had to first be investigated.

### CASI misconfiguration

Under geometrical optics, scatter of light from the chosen sinusoidal grating for an illumination incident angle of −5° from the surface normal was considered. The scatter from the regions of the grating with the steepest slopes should produce scatter at angles of −45.1° and 55.1° from the surface normal, and intuitively scatter is expected to be strong in these regions. In the horizontal axis of Figure 4.9, where the origin is aligned with the supposed specular region, these peaks would be located at the −50.1° and 50.1° positions respectively. This result does not match the data shown in Figure 4.9, with effectively no scatter measured at 50°.

For the same measurement configuration, both the BEM model and KA-based model were used to produce scatter, and after filtering the scatter compared to the experimental CASI data. The results from the two models were almost identical to each other, so only results from the BEM model are shown in Figure 4.10. The location of the two peaks in intensity are located at approximately −45° and 55°, matching the values obtained from geometrical optics. This strongly suggests some of the information about the CASI data is incorrect.

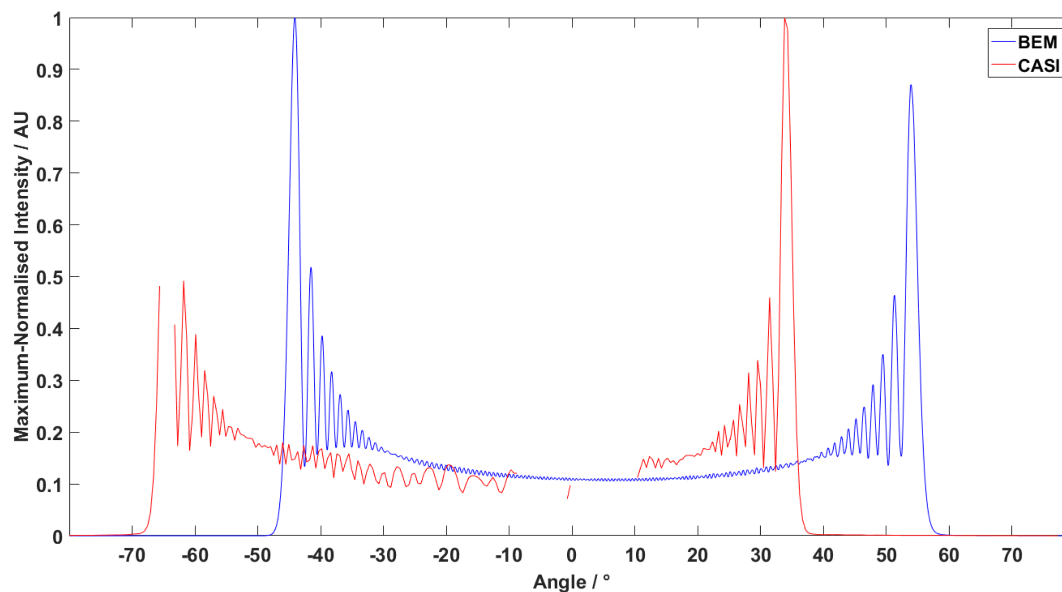


**Figure 4.10.** Comparison of BEM scatter data (after convolution with an aperture kernel function) against CASI measurement data, under the assumed measurement configuration. Note that in this figure the CASI data is shifted by 5°, so that here 0° represents the supposed location of the surface normal for both sets of data.

While the data shown in Figure 4.9 has been filtered, before this filtering was applied the data had both non-zero values and had multiple changes in sample spacing (and potentially aperture) around 0°; in contrast, no data was collected at all from around −10°. This strongly suggests that the instrument was configured expecting the specular region to be located at 0° due to incident illumination located at −10°, incident at an angle of −5° from the surface normal. The full measurement data range of −95° to 85° also supports this conclusion. It would be difficult to mistake the location of the incident illumination when setting up the instrument, and it is also unlikely that the incident angle of the illumination from the surface normal is significantly different from the stated 5° incidence from the surface normal.

Therefore, the case where the instrument was configured backwards was considered, with the incident illumination still located at −10° (as seen in Figure 4.9) but the surface normal instead located at −15°, i.e., the direction of incident illumination is flipped, with an incident angle of +5° rather than −5°. In this case, the specular region would be at −20°. When the horizontal axis is shifted by +20° so that this specular reflection is located at 0°, the two peaks in the data are located at −50° and 50°; this agrees with the expected result under geometrical optics. This result, alongside good agreement with the BEM and KA method modelling results using this measurement configuration

(shown in section 4.4.3), is the basis for the decision to consider this flipped configuration as the correct illumination configuration. Except for Figure 4.10, this configuration has already been used for the modelled results of the sinusoidal grating presented so far, to reduce the confusion caused by presenting incorrectly configured modelling data.

### Comparison of CASI and BEM

Figure 4.11 shows the cosine corrected BRDF (i.e. the angle-resolved scatter) as measured by CASI, compared to the ASD obtained from our computational model after convolution with an aperture function. Under the correct measurement configuration, the CASI data's surface normal is located at −15° in Figure 4.9, and so the CASI data is shifted by +15° before being included in Figure 4.11 so that the surface normal is placed at 0°.

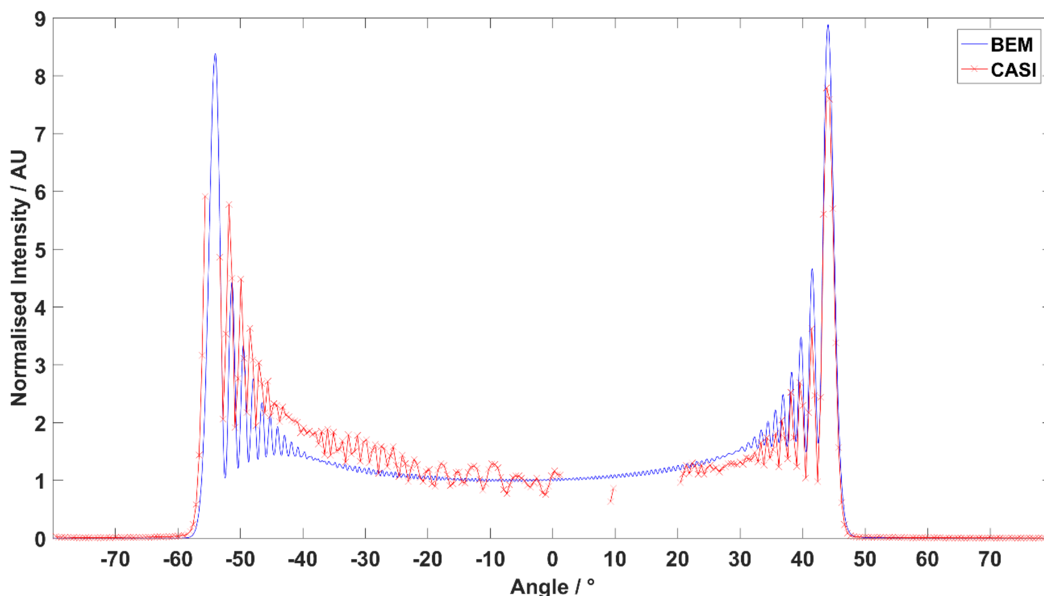


**Figure 4.11.** The cosine corrected BRDF as measured by CASI, compared to the ASD obtained from our BEM computational model (after convolution with an aperture function).

Figure 4.11 shows close agreement between our BEM simulation and the experimental measurement: the mean absolute difference between the two sets of data is 0.22 AU, equivalent to 3% of the peak intensity. In particular, the agreement is good at the retrograde (positive) angles along the lobes of varying intensity. However, a finer angular sampling step size around this region would have improved the clarity of the comparison and reduced the aliasing effects present around each peak. The closely

matching gap between the two intensity peaks, and the predicted shift of the CASI data by +15° correctly aligning the two datasets without additional fine-tuning, both provide additional evidence for model verification. Some of the differences between the shapes of the intensity curves are believed to be caused by the noise produced by reducing the beam width with a pinhole to 1.5 mm, since some scattered light from the edges of the pinhole could be seen on the sample. Additionally, it appears that a small systematic increase in intensity has occurred during the CASI measurement for the negative angles; the cause of which is unclear. Differences originating from the simulation could include simulating a perfect grating rather than the "real" grating (in terms of surface smoothness, PV and period), the differences between the 2D surface model and the 3D real grating, the hardware-limited resolution limits of our model, and other model approximations such as treating the illumination as a p-polarised plane wave.

### 4.4.3 Survey of agreement with KA method

Figure 4.12 shows the scatter produced by the KA-based method and the BEM model for a sinusoidal grating using the same conditions as used for Figure 4.5, except here nominal surface values and normal incidence light is used, and a surface length of 810 μm (six surface wavelengths) considered, i.e. a specific case of that described in section 4.3.3.

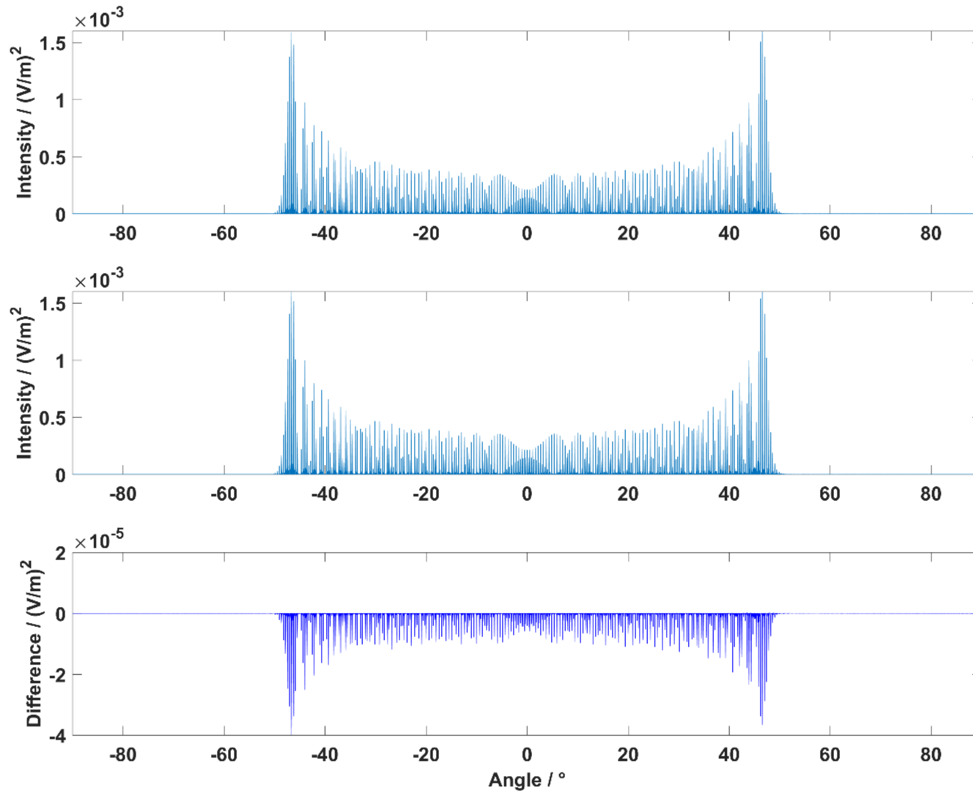


**Figure 4.12.** ASD produced using (top) the KA-based method, (middle) using the BEM model, and (bottom) the difference between these results. The ASD is produced from scatter from a perfect sinusoidal grating with 135 μm surface wavelength and 9.5 μm amplitude illuminated with normal incidence polarised plane wave illumination. Note the vertical axis scale for the difference plot is 100 times smaller than the two plots above it.

The two methods give almost identical results. Note that the slight asymmetry here occurs due to the choice of the initial phase of the sinusoidal grating ($+\pi$) and low number of integer surface wavelengths, such that the resulting asymmetry of the surface produces a visible asymmetry in the far-field ASD. However, since both the BEM and KA-based models take as input the same biased surface, the comparison between the ASDs produced is valid.

As the virtual sinusoidal grating's wavelength (or period/pitch) ($d$) is decreased from 135 μm while retaining the peak-to-mean amplitude ($h$) of 9.5 μm (with 0.633 μm wavelength illumination ($\lambda$)), the two models give results in close agreement until around $d = 76$ μm, corresponding to $h/d = 0.125$ and $d/\lambda \approx 213$. Surface wavelengths shorter than this cause the ASDs of the BEM method and KA-based method to rapidly diverge, corresponding to surface geometries whose scattering distribution for normal incident light would, under geometrical optics, produce multiple reflections and, therefore, no longer be sufficiently characterised by the KA. This is

illustrated in Figure 4.13. This condition is equivalent to requiring the local radius of curvature to be much larger than the wavelength of light for the KA to hold, as discussed in section 2.4.2. Interestingly, this result shows similarities to that given in [198], which discusses the boundaries to the regions of validity of a KA-based model for monochromatic scattering from a sinusoidal grating. The paper shows that the KA begins to fail when $h/d$ exceeds 0.13 for any incident angle and for any optical wavelength, and that this specific limit is related to the occurrence of multiple reflection under geometrical optics; the approximation can fail for lower values of $h/d$ in reality, and is reduced both for non-normal angles or incidence and at longer illumination wavelengths relative to the surface wavelength.

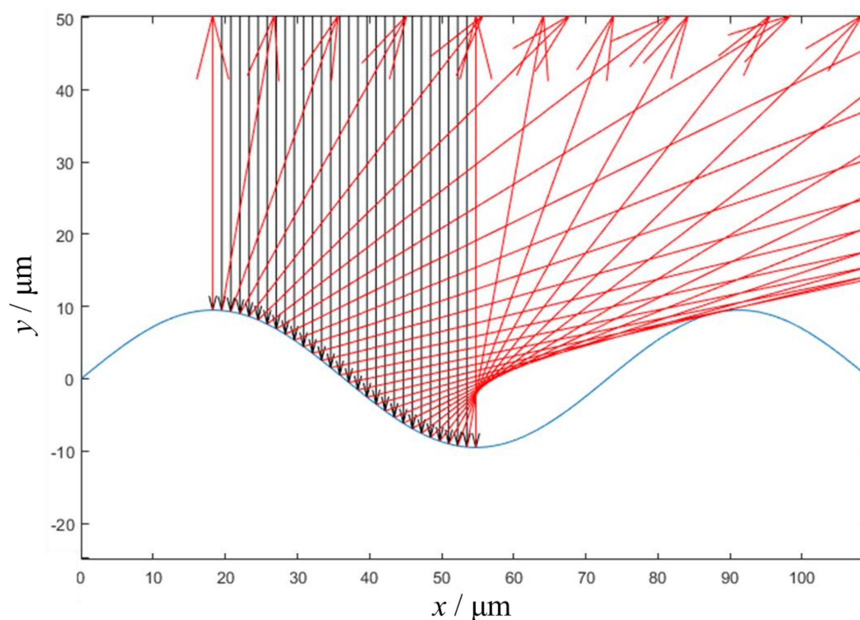


**Figure 4.13.** Geometrical optics reflections from a sinusoidal grating with surface period $d = 76$ μm and peak-to-mean amplitude $h = 9.5$ μm, illuminated at normal incidence.

The following figures (Figure 4.14, Figure 4.15, and Figure 4.16) display comparisons between the two models at selected surface wavelengths; note that for each figure the plots share the same $y$-axis scale for that figure. The divergence is shown across the entire range more abstractly in Figure 4.17.

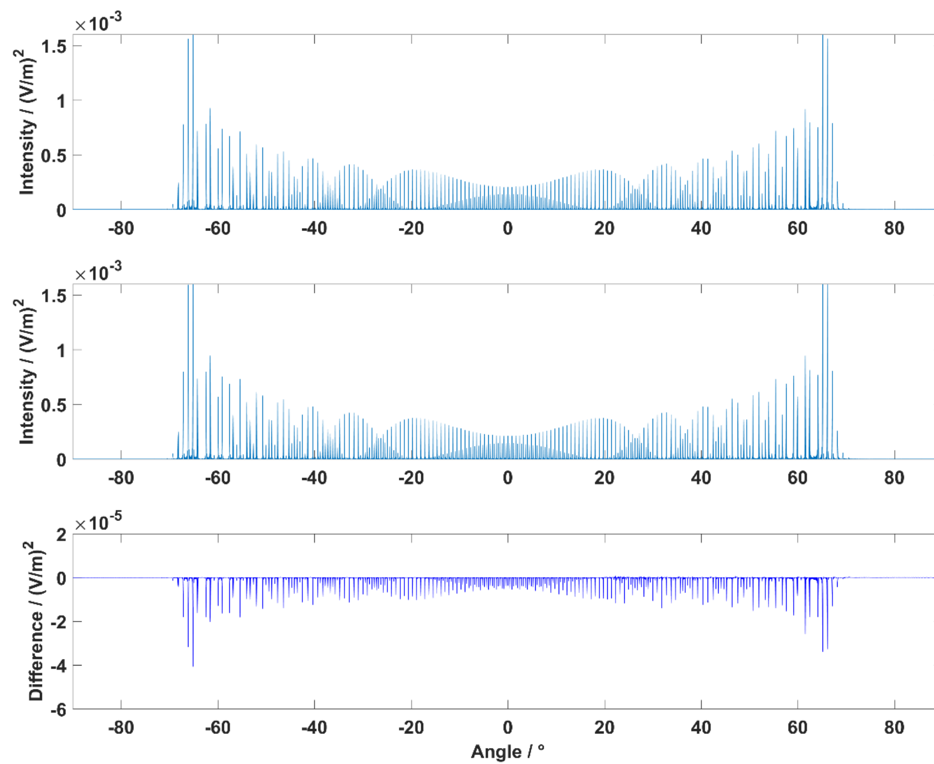


**Figure 4.14.** ASD for a perfect sinewave for surface wavelength of 90 µm and amplitude of 9.5 µm, (top) using a KA-based method, (middle) using the BEM model, and (bottom) the difference between these results.

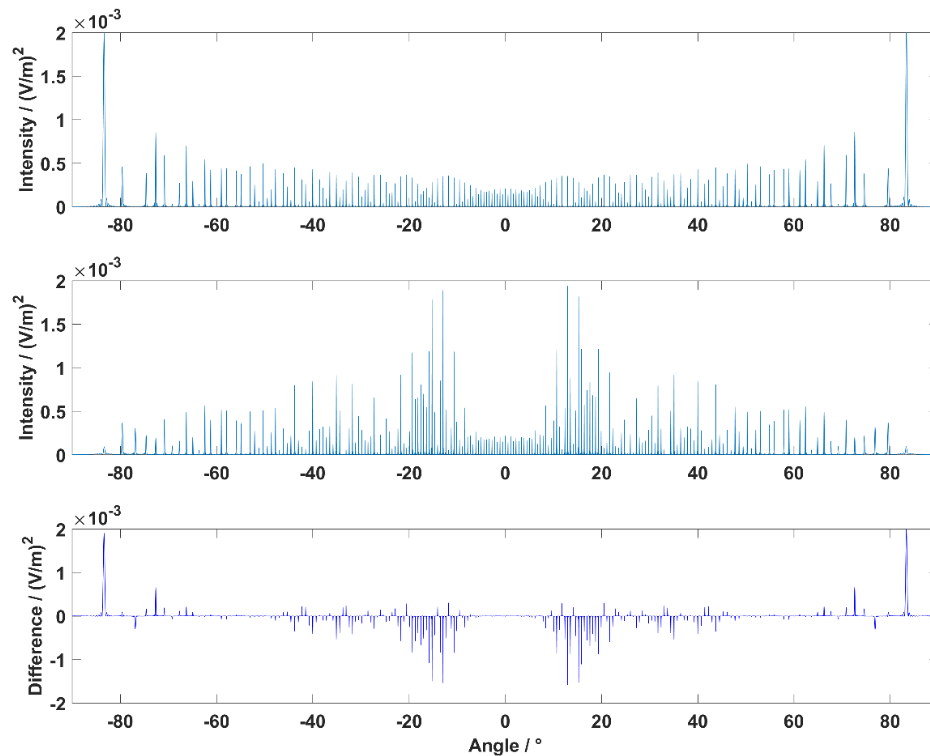


**Figure 4.15.** ASD for a perfect sinewave for surface wavelength of 65 µm and amplitude of 9.5 µm, (top) using a KA-based method, (middle) using the BEM model, and (bottom) the difference between these results. Note the change in the scale of the *y*-axis of the difference plot.

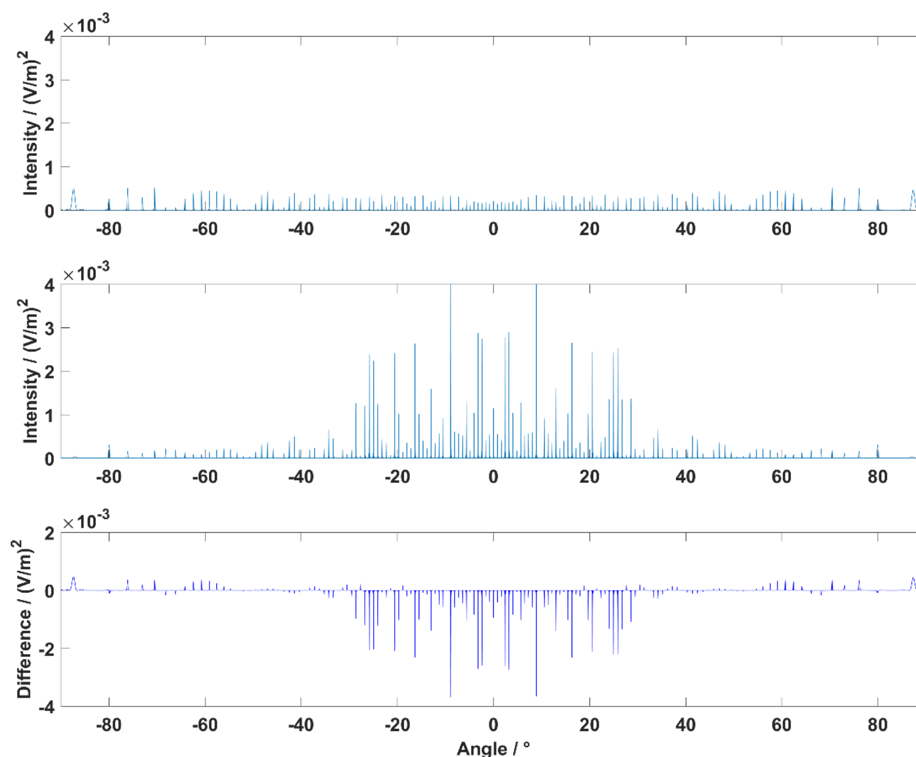


**Figure 4.16.** ASD for a perfect sinewave for surface wavelength of 45 µm and amplitude of 9.5 µm, (top) using a KA-based method, (middle) using the BEM model, and (bottom) the difference between these results. Note the change in the scale of the *y*-axis of the difference plot.

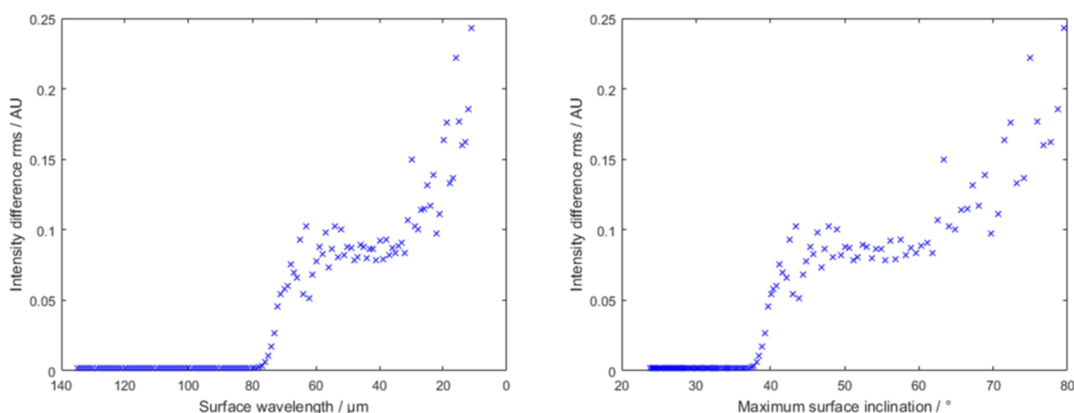


**Figure 4.17.** Differences between the KA-based linear model and the BEM rigorous model for a sinusoidal grating with amplitude 9.5 µm and 0.633 µm wavelength illumination for a range of different surface wavelengths (left). The same data is shown using maximum surface inclination as the horizontal axis for an alternative viewpoint (right).

## 4.5 Conclusion and discussion

The agreement of the results presented in section 4.4 provides evidence that the BEM model can produce accurate scattering results. While there was some confusion related to the alignment of the experimental set-up and data (discussed in detail in section

4.4.2), this was ultimately resolved, providing agreement between the BEM model and experiment. Comparisons with a KA-based linear model also gives good agreement for the chosen sinusoidal function, and the agreement with Mie scattering theory supports the BEM model's capabilities for more complex surfaces. However, the approach taken is worth discussing.

Naturally, the comparison work was limited by the sinusoidal grating used. A grating was chosen due to the BEM model being limited to only 2D surfaces, i.e., limited to surfaces completely described only by a set of $(x, z)$ coordinates. A sinusoidal grating was chosen due to its simplicity, the wide range of existing scattering literature that involves them, and the ease of obtaining a suitable sinusoidal grating for measurement. In some scattering theories, the sinusoidal is also fundamental, in the sense that an arbitrary surface (with no undercuts) can be made up of a combination of sinusoids, and the resulting scattering from the arbitrary surface is closely connected to the combination of the scattering from the surface's decomposition into different wavelength sinusoidal gratings.

While the sinusoidal grating chosen had high amplitude relative to the wavelength of illumination used, the surface wavelength used was also large such that the surface was not too steep, so that a KA-based model would be expected to accurately calculate scatter for the surface. This was carried out to improve the ability of this work to verify the BEM model through comparison to a more readily understood method, for a surface that was, effectively, simpler to model. However, this choice of simpler surface does mean that this work does not strongly verify the model's capability to handle multiple scattering, besides the comparison to the Mie solution for a cylinder. Obtaining experimental sinusoidal gratings that were known to produce multiple scattering was difficult and was ultimately avoided, especially given that this work relied on collaborators at UNCC, who made the experimental scatterometry measurements also having access to the same surface. Even if such a surface could be measured, the ability to rely on a simple reference model to compare to in addition to experimental data was valuable to minimise experimental mistakes, such as the misalignment problem discussed.

A comparison to another rigorous model, one that is already established and can be used as a reference, is difficult to do for several reasons. First, understanding a different

rigorous model enough to trust its theoretical foundation is naturally difficult, compared to a simple KA-based method, as such methods must necessarily be complex. For this reason, comparison to another numeric rigorous model is also less convincing, compared to comparison to exact analytical solutions or to experimental measurement. Due to the large amount of effort in creating implementations of rigorous approaches, much existing software in the literature is also inaccessible due to being proprietary, bespoke or commercial. For example, some early attempts to compare the BEM model to a commercial FEM model were made, specifically JCMsuite from JCMwave GmbH. However, access was provided only to results of the FEM model, where virtual surfaces were sent by email to the author of the model and scatter data sent back. Due to problems with ensuring the same surface and illumination conditions were modelled, and disagreements with the model's author about the direction of the work and the contents of the associated publications, the FEM comparison work had to be discarded.

As previously discussed, the scatterometer used was not configured correctly, which caused some confusion. Other parts of the experimental work could have also been improved. The high precision of the goniometric component of the scatterometer (angular resolution of 0.001°) was unfortunately not used effectively; instead, the majority of the data was collected with an angular spacing of 0.478°. This led to aliasing problems in the data. As the sinusoidal grating was not expected to scatter specularly strongly, the choice to change the aperture and angular spacing in the expected specular region made this region of the data unsuitable for model comparison. Ideally, a smaller aperture and a smaller angular spacing would have been used equally throughout the entire semi-circular scan.

## 4.6 Summary

In this chapter, a two-dimensional rigorous boundary elements method (BEM) solution to Maxwell's equations was presented and verified. First, the theory of the model was outlined, where the model should be able to accurately predict scattering from any surface. To verify this, scattering data from the BEM model was compared to various analytical models for different surfaces with good agreement, including an exact analytical Mie scattering solution for a cylinder, providing evidence of the BEM model's ability to accurately calculate scatter for surfaces with high surface curvature and slopes. The BEM model was also verified by comparison to experiment, comparing

the model to measurements of a rough but slowly varying sinusoidal grating by a high accuracy scatterometer, resulting in good agreement when differences in the scatterometer set-up and the physical modelling are considered. These comparisons provide evidence that verify the accuracy of the BEM model, and provide some evidence of its capability to accurately predict scatter from complex surfaces, including those surfaces that linear models cannot accurately model. Finally, the BEM model was compared against a Kirchhoff approximation-based method for the sinusoid geometry measured experimentally, providing further agreement, and for a range of different sinusoidal grating geometries, to investigate the domain within which the two models agree and disagree.

# Chapter 5: Modelling of CSI beyond the linear regime

In the previous chapter (Chapter 4), a rigorous two-dimensional (2D) boundary element method (BEM) model of electromagnetic surface scatter was presented. The BEM scattering theory was outlined, and the model was verified for a sinusoidal grating through comparison to experiment and to an approximate analytical method, and for a cylinder through comparison to an exact analytical solution. In this chapter, a coherence scanning interferometry (CSI) model that was developed based on this BEM model is presented. This model is intended to be capable of accurately modelling the CSI signal for complex surfaces which contain steep surfaces and can produce multiple scattering. The BEM-CSI theory is first outlined, where CSI fringes are produced by considering the holographic recording and reconstruction of the scattered field produced by the BEM model from a range of illumination wavelengths and incident angles. The computational implementation of the model is discussed, including the discrete sampling of continuous ranges and on the grid interpolation chosen. The BEM-CSI model is verified through comparison to experimental CSI measurements of various surfaces, and through comparison of results of modelling a vee-groove to those seen in the literature, which demonstrates the model's capability to predict multiple scattering.

The work in this chapter is based in part on that published in [51] (journal paper), the majority of which is based on the work presented earlier at the SPIE: Optical Metrology 2019 conference [50].

## 5.1 Introduction

Detailed information about a part's surface topography is valuable in manufacturing, as described in section 1.1. Optical surface topography measurement methods such as CSI have traditionally struggled with measurements of surfaces with slopes steeper than the specular slope limit, as described in section 2.6. Despite modern improvements in instrument technology allowing for an extended range of measurable slopes, the reliability of surface topography obtained from these slopes is unknown. However, a virtual instrument can be used to improve a user's understanding of the measurement process and investigate the reliability of surface topography data by providing

uncertainty evaluation [41], as described in section 1.1 and 1.3. The value of a virtual instrument is also discussed elsewhere [186,273,274].

A CSI model like that described in [186], which uses the foil model (described in section 2.4.2 and 3.2), can be useful for a range of surfaces for which the model is valid (given in section 2.4.2). However, a CSI model based on a rigorous optical model would be capable of predicting instrument response for a wider range of surfaces, including those that are complex and produce significant multiple scattering. The fringe data that such surfaces produce are typically not correctly handled by reconstruction methods. Reconstruction methods for CSI must rely on an assumed relationship between the measured field and the true surface topography, with reconstruction methods typically assuming that the phase of the measured field at a point is proportional to the surface height at that point. While CSI models based on this simple assumption can still predict the main features of an interference signal [101,275], and reconstruction methods that assume this are effective [87], this approximation only truly holds for sufficiently smooth surfaces ($\mathrm{PV} \ll \lambda$ for peak-to-valley amplitude (PV) and illumination wavelength ($\lambda$)). Despite the mitigating effect of a finite spatial frequency bandwidth, the effect of multiple scattering and loss of diffraction orders cannot be neglected and remains a problem for surfaces that are rough at the optical scale, or when coherent features such as vee-grooves or sharp edges are present [49,164]. For such complex surfaces, the CSI measurement process is fundamentally non-linear, and consequently the linear reconstruction methods cannot reconstruct accurate surface topographies. Only an advanced reconstruction method that accounts for these effects could provide an accurate surface topography estimate for these surfaces, and such a method must be based on a rigorous scattering model.

Rigorous models for optical scattering typically use numerical methods to solve Maxwell's equations, methods which are discussed in section 2.4.3. To solve the scattering problem for arbitrarily complex surfaces efficiently, a rigorous BEM-based optical scattering model has been chosen, the details of which are presented in Chapter 4, including model verification. The BEM scattering method described is formally exact, and accounts for surface plasmons, polarisation effects, and structures which contain overhangs and other complex re-entrant features. As this BEM model is two-dimensional (2D), it is restricted to surfaces that only scatter within the plane of incidence, i.e. surfaces fully described by lines on the plane of incidence (*x*-*z* plane) and

considered to infinitely extend along the third dimension (*y* direction) perpendicular to the plane of incidence. Due to limited development time and the increased computational demand, a three-dimensional (3D) scattering model was not considered here.

In this chapter, a new way of modelling CSI images by using a BEM-based rigorous surface scattering model and synthesising images in the spatial frequency domain (*k*-space) is demonstrated. The model considers the effects of multiple scattering and works for surfaces with arbitrary geometries. The fringes produced by the CSI model are compared to those measured by a real instrument for a range of surfaces, to verify the model, and a vee-groove was also modelled to verify the multiple scattering capability. Since the CSI model is limited to 2D but the experimental instrument generates 3D image data, qualitative comparison between simulation and experiment is provided. Publications using this chapter's CSI model include [50–52], and this model is used in Chapter 6 to investigate scatter from tilted complex surfaces.

## 5.2 CSI modelling theory

To obtain equations that describe the signal synthesis for CSI, the theory of scalar scattering of scattering must first be revisited, as described in section 2.5. The far-field scattered field that scatters from an illuminated object encodes information about the object itself. Back-propagation of this far-field scatter can provide the reconstructed scattered field in the vicinity of the instrument's object plane, which an optical instrument effectively images, i.e., providing an expression for the field measured by the instrument. This back-propagation provides the reconstructed measured field spectrum in *k*-space.

The following section describes how this measured field is then demodulated by the reflected reference field, and the effect of this demodulation on the field spectrum generated in *k*-space for a specific incident illumination wavevector. From this, an expression for the measured fringes for a broadband light source, i.e., from a range of different incident angles and illumination wavelengths, can be obtained.

### 5.2.1 CSI signal synthesis

The intensity fringes measured by an interferometer for a single incident reference field is given in [88,185,184] by

$$I(\mathbf{r}) = 2\Re\{O(\mathbf{r})\}, \tag{5-1}$$

where $\Re\{\cdot\}$ denotes taking the real part, and the fringe field $O(\mathbf{r})$ is given by

$$O(\mathbf{r}) = E_m(\mathbf{r})E_r(\mathbf{r})^*. \tag{5-2}$$

Here the measured scattered field $E_m(\mathbf{r})$ from the scattering object, for position vector $\mathbf{r}$, is demodulated by the conjugate of the reference field $E_r(\mathbf{r})$, where the reference field is the field reflected from the reference mirror in a real system. The location of $\mathbf{r}$ can be thought of being near to the image plane, or alternatively as corresponding to the associated region near the object plane, which an instrument scans through to obtain field information. From the arguments presented in section 2.5.2, the scattered field from the scattering object measured at the instrument's sensor can be considered equal to the reconstructed scattered field present near to the object, which is why $E_m(\mathbf{r})$ as given by Eq. (2-38) and (2-46) has been used in Eq. (5-2) to represent the measured scattered field. Note that the expression for coherent demodulation given in Eq. (5-2) is the same as that in Eq. (3-23), used in the derivation for the foil model.

Considering Eq. (5-2) more generally, the fringe field $O^{(\mathrm{i})}(\mathbf{r})$ for a specific incident illumination wavevector $\mathbf{k}_\mathrm{i}$, where the reference field is given by a plane wave $E_r^{(\mathrm{i})}(\mathbf{r}) = \mathrm{e}^{i\mathbf{k}_\mathrm{i}\cdot\mathbf{r}}$, can be given by

$$O^{(\mathrm{i})}(\mathbf{r}) = E_m^{(\mathrm{i})}(\mathbf{r})\, \mathrm{e}^{-i\mathbf{k}_\mathrm{i}\cdot\mathbf{r}}, \tag{5-3}$$

where $E_m^{(\mathrm{i})}(\mathbf{r})$ denotes for a specific incident wavevector the resulting reconstructed scattered field that can be measured at the image plane, which is generated by the scattering object and can be calculated from the far-field scatter produced by the object as given by Eq. (2-46). Here it is assumed that the reference field is a perfect reflection of the incident field, so that neither the reference surface nor its scatter need to be directly considered. For an instrument with optical axis $\hat{\mathbf{z}}$ pointing from the surface towards the instrument, with the NA given by $A_n$, the incident wavevectors allowed satisfy the inequality $-\hat{\mathbf{k}}_\mathrm{i} \cdot \hat{\mathbf{z}} > \sqrt{1 - A_n^2}$ (where any vector $\mathbf{v}$ satisfies $\mathbf{v} = |\mathbf{v}|\hat{\mathbf{v}}$ for $|\hat{\mathbf{v}}| = 1$).

The total intensity measured from a range of incident illumination wavevectors can then be given by

$$I_{\text{total}}(\mathbf{r}) = \sum_{\text{i}} I^{(\text{i})}(\mathbf{r}) = \sum_{\text{i}} 2\Re\{O^{(\text{i})}(\mathbf{r})\}, \tag{5-4}$$

which can equally be expressed by

$$I_{\text{total}}(\mathbf{r}) = 2\Re\{O_{\text{total}}(\mathbf{r})\}, \tag{5-5}$$

where $O_{\text{total}}(\mathbf{r})$ is given by

$$\begin{aligned} O_{\text{total}}(\mathbf{r}) &= \sum_{\text{i}} O^{(\text{i})}(\mathbf{r}) \\ &= \mathcal{F}^{-1}\left\{\sum_{\text{i}} \tilde{O}^{(\text{i})}(\boldsymbol{\xi})\right\} \equiv \mathcal{F}^{-1}\{\tilde{O}_{\text{total}}(\boldsymbol{\xi})\}, \end{aligned} \tag{5-6}$$

where the tilde denotes taking the Fourier transform such that $\tilde{O}^{(\text{i})}(\boldsymbol{\xi}) = \mathcal{F}\left\{O^{(\text{i})}(\mathbf{r})\right\}$, and where the spatial frequency coordinate $\boldsymbol{\xi}$ has been used to denote the spatial frequencies of the interferogram. Notably, the summation of intensity values in real space can be obtained from the summation of fringe field spectrum values, which are generally complex valued. These equations are given in more detail in Appendix B.

Eq. (5-5) and Eq. (5-6) state that the total fringe intensity can be obtained from calculating the summation of the fringe field terms for each incident wavevector in the spatial-frequency domain. Returning to Eq. (3-24), the fringe field can be Fourier transformed to obtain the fringe field spectrum

$$\tilde{O}^{(\text{i})}(\boldsymbol{\xi}) = \mathcal{F}\left\{E_m^{(\text{i})}(\mathbf{r})\, \mathrm{e}^{-i\mathbf{k}_{\text{i}}\cdot\mathbf{r}}\right\}. \tag{5-7}$$

Under the Fourier modulation / frequency shifting property given by

$$\begin{aligned} \mathcal{F}\{g(x)\} &= \tilde{g}(\xi) \\ \mathcal{F}\left\{g(x)\, \mathrm{e}^{-ik_{\text{i}}x}\right\} &= \tilde{g}(\xi + k_{\text{i}}), \end{aligned} \tag{5-8}$$

for any arbitrary function $g(x)$, the Fourier transform in Eq. (5-7) can be written as

$$\tilde{O}^{(\text{i})}(\boldsymbol{\xi}) = \tilde{E}_m^{(\text{i})}(\boldsymbol{\xi} + \mathbf{k}_{\text{i}}). \tag{5-9}$$

Expressing the measured scattered field spectrum $\tilde{E}_m^{(\text{i})}$ in terms of the source spectrum $\tilde{U}^{(\text{i})}$ or in terms of scattering potential $f'$ using Eq. (2-43) gives

$$\tilde{O}^{(\mathrm{i})}(\boldsymbol{\xi}) = -\frac{i}{8\pi^2 k_0}\tilde{U}^{(\mathrm{i})}(\boldsymbol{\xi}+\mathbf{k}_\mathrm{i})\delta(|\boldsymbol{\xi}+\mathbf{k}_\mathrm{i}|-k_0) \tag{5-10}$$

$$\tilde{O}^{(\mathrm{i})}(\boldsymbol{\xi}) = \frac{i}{2\pi k_0} f'(\boldsymbol{\xi}+\mathbf{k}_\mathrm{i},\mathbf{k}_\mathrm{i})\delta(|\boldsymbol{\xi}+\mathbf{k}_\mathrm{i}|-k_0), \tag{5-11}$$

where naturally the wavevector $\mathbf{k}$ in Eq. (2-43) has been replaced by $\boldsymbol{\xi}+\mathbf{k}_\mathrm{i}$.

These two expressions show that $\tilde{O}^{(\mathrm{i})}(\boldsymbol{\xi})$ is non-zero only where $|\boldsymbol{\xi}+\mathbf{k}_\mathrm{i}| = k_0$, i.e., non-zero values are present only on a shell in $\boldsymbol{\xi}$-space with radius $k_0$, centred at $\boldsymbol{\xi} = -\mathbf{k}_\mathrm{i}$. From Eq. (2-45), it can be seen that $\tilde{U}^{(\mathrm{i})}(\mathbf{k})$ only has values on a shell in $\mathbf{k}$-space where $\mathbf{k} = \mathbf{k}_\mathrm{s} = k_0\hat{\mathbf{s}}_\mathrm{s}$, where $\mathbf{k}_\mathrm{s}$ is the observation wavevector of the far-field scattered field. Therefore, by considering only the values of $\boldsymbol{\xi}$ that meet the equality $\boldsymbol{\xi} = \mathbf{k}_\mathrm{s} - \mathbf{k}_\mathrm{i}$, Eq. (2-45) or Eq. (2-46) can be combined with Eq. (5-10) or Eq. (5-9) respectively to provide $\tilde{O}^{(\mathrm{i})}(\mathbf{k}_\mathrm{s}-\mathbf{k}_\mathrm{i})$ in terms of far-field scatter $E_s(r_s\hat{\mathbf{s}}_\mathrm{s})$ or scattering amplitude $f'(\mathbf{k}_\mathrm{s},\mathbf{k}_\mathrm{i})$, given by

$$\tilde{O}^{(\mathrm{i})}(\mathbf{k}_\mathrm{s}-\mathbf{k}_\mathrm{i}) = \frac{ir_s}{2\pi k_0} e^{-ik_0 r_s} E_s^{(\mathrm{i})}\left(r_s\frac{\mathbf{k}_\mathrm{s}}{k_0}\right), \tag{5-12}$$

$$\tilde{O}^{(\mathrm{i})}(\mathbf{k}_\mathrm{s}-\mathbf{k}_\mathrm{i}) = \frac{i}{2\pi k_0} f'(\mathbf{k}_\mathrm{s},\mathbf{k}_\mathrm{i}). \tag{5-13}$$

Note that while these expressions appear to be in terms of constant wavenumber $k_0$, they also hold for treating $k_0$ as a variable, so long as $|\mathbf{k}_\mathrm{s}| = |\mathbf{k}_\mathrm{i}| = k_0$ for any choice of $\mathbf{k}_\mathrm{i}$. Also note that in general, the observation vector is also limited by the NA and must similarly satisfy the inequality $\hat{\mathbf{k}}_\mathrm{s}\cdot\hat{\mathbf{z}} > \sqrt{1-A_n^2}$ .

The expression given in Eq. (5-12) is already enough to explain the approach taken in this chapter to synthesise the CSI signal from far-field scatter, with the geometry visualised later in Figure 5.2. However, it is useful to obtain an explicit expression for the total fringe field $\tilde{O}_{\mathrm{total}}(\boldsymbol{\xi})$ as given by Eq. (5-6), and therefore an expression for $I_{\mathrm{total}}(\mathbf{r})$. Considering the unrestricted coordinate $\boldsymbol{\xi}$ using Eq. (5-6) and Eq. (5-10), the expression

$$\tilde{O}_{\mathrm{total}}(\boldsymbol{\xi}) = -\frac{i}{8\pi^2 k_0}\sum_{\mathrm{i}} \tilde{U}^{(\mathrm{i})}(\boldsymbol{\xi}+\mathbf{k}_\mathrm{i})\delta(|\boldsymbol{\xi}+\mathbf{k}_\mathrm{i}|-k_0), \tag{5-14}$$

can be obtained. When including a limiting NA, this can be written as

$$\tilde{O}_{\mathrm{total}}(\boldsymbol{\xi}) = -\frac{i}{8\pi^2 k_0}\sum_{\mathrm{i}} \tilde{U}^{(\mathrm{i})}(\boldsymbol{\xi}+\mathbf{k}_{\mathrm{i}})\tilde{G}_{\mathrm{NA}}(\boldsymbol{\xi}+\mathbf{k}_{\mathrm{i}}), \tag{5-15}$$

where a transfer function $\tilde{G}_{\mathrm{NA}}(\mathbf{k})$ has been defined by

$$\tilde{G}_{\mathrm{NA}}(\mathbf{k}) = \delta(|\mathbf{k}| - k_0)H\left(\hat{\mathbf{k}}\cdot\hat{\mathbf{z}} - \sqrt{1-A_n^2}\right). \tag{5-16}$$

Unsurprisingly, the term that is summed in Eq. (5-15) only has non-zero values when $\tilde{G}_{\mathrm{NA}}(\boldsymbol{\xi}+\mathbf{k}_{\mathrm{i}}) \neq 0$, which for a valid $\mathbf{k}_{\mathrm{i}}$ fully determines the values of $\boldsymbol{\xi}$ where the term is non-zero. Therefore, neither a transfer function for the illumination nor an explicit summation of the observation values are needed for the expression; the former is implied by the summation over i, and the latter embodied in the expression for $\tilde{O}^{(\mathrm{i})}(\boldsymbol{\xi})$ (which includes $\tilde{G}_{\mathrm{NA}}(\boldsymbol{\xi}+\mathbf{k}_{\mathrm{i}})$).

For a broadband illumination source such as a white-light LED, multiple wavelengths are present. The normalised power spectrum density $S(k_0)$ of the illumination source can be included in Eq. (5-15), giving

$$\tilde{O}_{\mathrm{total}}(\boldsymbol{\xi}) = -\frac{i}{8\pi^2}\int_0^\infty \frac{S(k_0)}{k_0}\tilde{O}_{\mathrm{mono}}(\boldsymbol{\xi}; k_0)\,\mathrm{d}k_0, \tag{5-17}$$

where $\tilde{O}_{\mathrm{mono}}(\boldsymbol{\xi}; k_0)$ is given by one of either of:

$$\tilde{O}_{\mathrm{mono}}(\boldsymbol{\xi}; k_0) = \sum_{\mathrm{i}} \tilde{U}^{(\mathrm{i})}(\boldsymbol{\xi}+\mathbf{k}_{\mathrm{i}}; k_0)\tilde{G}_{\mathrm{NA}}(\boldsymbol{\xi}+\mathbf{k}_{\mathrm{i}}; k_0), \tag{5-18}$$

$$\tilde{O}_{\mathrm{mono}}(\boldsymbol{\xi}; k_0) = -4\pi r_s e^{-ik_0 r_s}\cdot\sum_{\mathrm{i}} E_s^{(\mathrm{i})}\left(r_s\frac{\boldsymbol{\xi}+\mathbf{k}_{\mathrm{i}}}{|\boldsymbol{\xi}+\mathbf{k}_{\mathrm{i}}|}\right)\tilde{G}_{\mathrm{NA}}(\boldsymbol{\xi}+\mathbf{k}_{\mathrm{i}}; k_0). \tag{5-19}$$

From the combination of Eq. (5-5), Eq. (5-17), and Eq. (5-19), a complete expression for the fringes measured by a broadband NA limited CSI instrument in terms of far-field scattered field is obtained.

## 5.3 Implementation

The procedure that allows a BEM-based CSI model to generate fringe signal data for surfaces can be broken into several steps, which are illustrated in Figure 3.1.

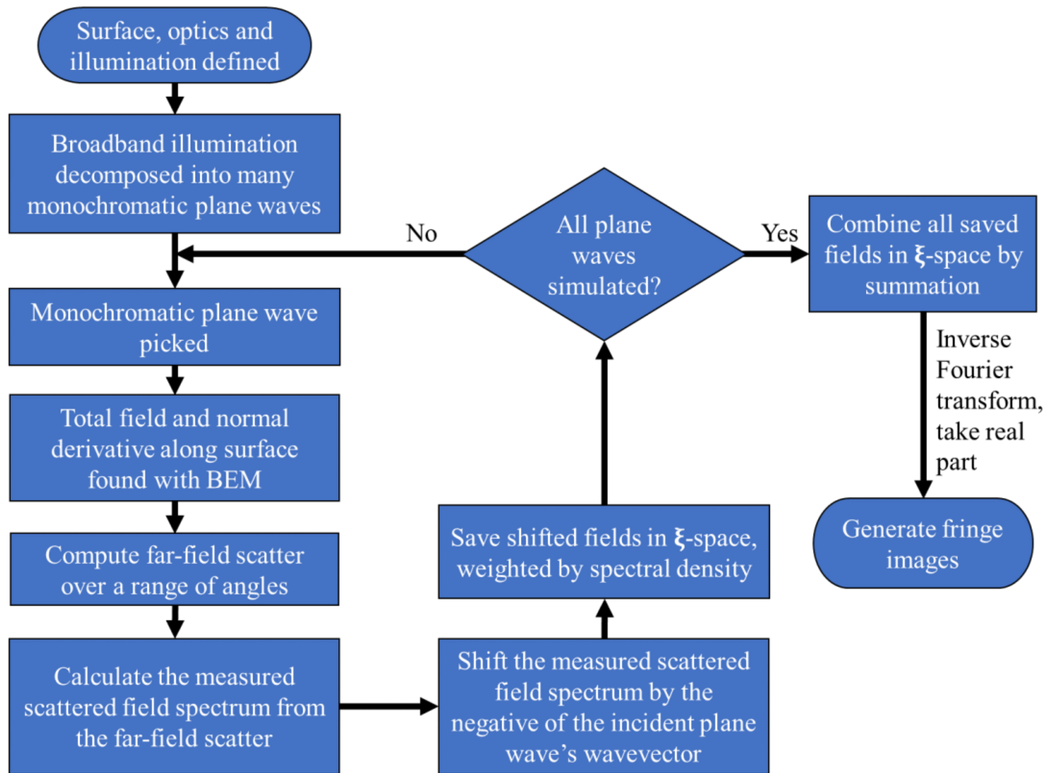


**Figure 5.1.** Flowchart describing the operation of the CSI model. In practice, the fields are summed together iteratively, rather than only once all plane waves have been considered.

The choice of model parameters and their limitations are described in section 5.3.1, and a brief overview on generation of BEM scatter is given in section 5.3.2. The method used to calculate CSI signal from the BEM scatter through addition in spatial frequency space is described in section 5.3.3, the implementation of which requires discrete sampling of multiple quantities and interpolation onto a rectangular grid, discussed in section 5.3.4 and 5.3.5.

### 5.3.1 Choice of inputs

A surface's coordinates along the lateral axis $x$ and the optical axis $z$ can be generated by an analytical function or numerically specified. Naturally, the surface described by these coordinates defines the boundary between two homogeneous mediums of different refractive indices, and for each medium, the complex refractive index must be specified. Next, the optical parameters, such as the NA of the lens, are chosen, providing the range of angles that the incident illumination can take and the acceptance angle for filtering of the scattered field. The polarisation of illumination is selected, between either the transverse electric (TE) or transverse magnetic (TM) polarisations

(i.e. s- or p-polarisations). The illumination's broadband spectrum can be defined by a Gaussian distribution with a given mean wavelength and full width at half maximum (FWHM). For each component of the illumination, the illuminating beam applied to the surface is modelled as either a Gaussian beam or a plane wave. In the case of a Gaussian beam, the diameter of the beam waist is set to be half the lateral width of the surface, where the lateral width of the surface is the width of the surface's projection onto the horizontal ($x$) axis.

### 5.3.2 BEM for surface scattering

Once the surface, optics and illumination have been defined, the broadband spectrum and the angles of illumination are sampled, and for each possible pairing of wavelength and incident angle, the surface field values are found using the BEM method described in Chapter 4, which provides the total field and its surface normal derivative along the surface. Details on the BEM model chosen can be found in sections 4.1 and 4.2. Details on the sampling is given in section 5.3.4. From these surface "source" fields, the scattered far-field at any point for each pairing can be found (e.g., Eq. (4-13)). As mentioned in section 4.3.2, for these far-field scatter calculations to be accurate, the surface must be resampled equidistantly before the surface field values are found, with the resampling distance typically set to $\lambda/5$ or smaller for illumination wavelength $\lambda$. To ensure that the same surface coordinates are used for each wavelength of light sampled from the spectrum, the smallest wavelength sampled is chosen to determine the resampling distance.

### 5.3.3 CSI signal synthesis in $\boldsymbol{\xi}$-space

To calculate the values of $\tilde{O}_{\mathrm{total}}(\boldsymbol{\xi})$ for the plane wave components of the illumination $\mathbf{k}_{\mathrm{i}}$, the demodulation can be carried out in the spatial frequency domain through a process similar to a convolution of the far-field scatter with the conjugate of the reference field, as described in section 5.2. For each $\mathbf{k}_{\mathrm{i}}$, the scattered field generated at a scattering/observation wavevector $\mathbf{k}_{\mathrm{s}}$ is iteratively added to $\tilde{O}_{\mathrm{total}}(\boldsymbol{\xi})$ at the position $\boldsymbol{\xi} = \mathbf{k}_{\mathrm{s}} - \mathbf{k}_{\mathrm{i}}$ to any existing value at that position, and this is repeated for each wavelength of the light source, weighted by its spectral density. The fringe field spectrum $\tilde{O}_{\mathrm{total}}(\boldsymbol{\xi})$ is obtained through the superposition of the signal for each

wavelength and angle of incidence, and the CSI fringe image in real-space is then given by the real part of $O_{\text{total}}(\mathbf{r}) = \mathcal{F}^{-1}\{\tilde{O}_{\text{total}}(\boldsymbol{\xi})\}$.

For a single incidence wavevector $\mathbf{k}_{\text{i}}$, the contribution to $\tilde{O}_{\text{total}}(\boldsymbol{\xi})$ is given by $\tilde{O}^{(\text{i})}(\boldsymbol{\xi})$, given in Eq. (5-9) in terms of the shifted measured field spectrum $\tilde{E}_m^{(\text{i})}(\boldsymbol{\xi} + \mathbf{k}_{\text{i}})$. The reference field, a reflection of the incident field, is the source of the $+\mathbf{k}_{\text{i}}$ term. The values of $\tilde{E}_m^{(\text{i})}(\mathbf{k}_{\text{s}})$ for $\mathbf{k}_{\text{s}} = k_0\hat{\mathbf{s}}_{\text{s}}$ can themselves be expressed in terms of the (real-space) far-field scatter from the illuminated object $E_s^{(\text{i})}(r_s\hat{\mathbf{s}}_{\text{s}})$ taken at the same angle, as given in Eq. (5-19). The values of the measured field spectrum $\tilde{E}_m^{(\text{i})}(\mathbf{k}_{\text{s}})$ are only defined on a spherical shell in *k*-space with a radius of $k_0 = 2\pi/\lambda_0$ (or $1/\lambda_0$ if $\mathbf{k}_{\text{s}}$ was a linear wavevector) [276], and likewise the spectrum of the reference field measured is also a spherical shell in *k*-space with the same radius. Both spherical shells are truncated due to the finite NA, and here it is assumed that the same NA limits both the illumination and observation angles available [88]. As shown in Figure 5.2, for a monochromatic source the two truncated spherical shells appear to be convolved, due to the demodulation process, i.e., the reflected reference field shifts the measured field values to higher spatial frequencies. Specifically, once a value for $\tilde{E}_m^{(\text{i})}(\mathbf{k}_s)$ is calculated, it can be shifted in *k*-space by $-\mathbf{k}_{\text{i}}$ to obtain its contribution to $\tilde{O}(\boldsymbol{\xi})$. The process is not a convolution, as the scattered field (and therefore the measured field spectrum) depends on the value of the incident wavevector $\mathbf{k}_{\text{i}}$. Therefore, for each $\mathbf{k}_{\text{i}}$ considered, a new set of scattered field values must be calculated along an arc of observation vectors $\mathbf{k}_{\text{s}}$, and each arc shifted accordingly in *k*-space by $-\mathbf{k}_{\text{i}}$ to be placed into $\boldsymbol{\xi}$-space. For this reason, different coloured arcs are used in Figure 5.2, indicating that each arc in general has different field values.

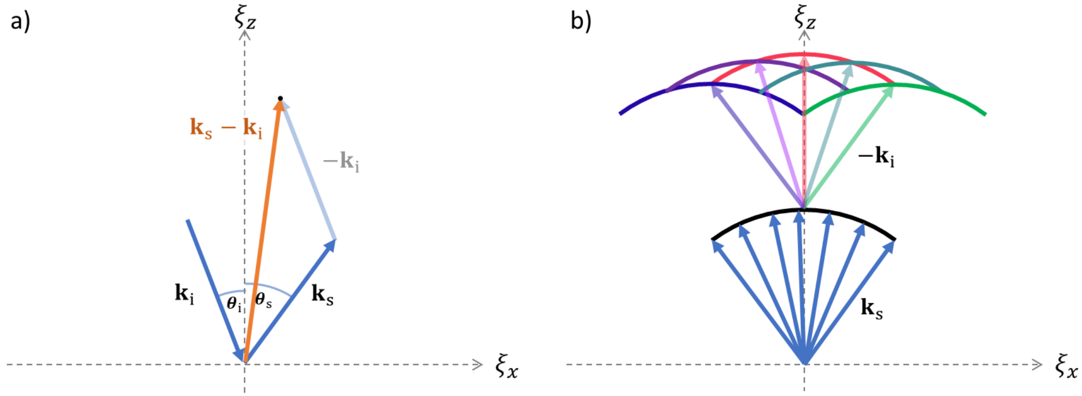


**Figure 5.2.** Diagram of construction of signal in $\boldsymbol{\xi}$-space at $\mathbf{k}_s - \mathbf{k}_i$ using $\mathbf{k}_s$ and $\mathbf{k}_i$. a) Construction of fringe field spectrum $\tilde{O}(\boldsymbol{\xi})$ is achieved by adding the computed scattered field values for each incident wavevector $\mathbf{k}_i$ across a range of scattering/observation wavevectors $\mathbf{k}_s$ at the positions $\mathbf{k}_s - \mathbf{k}_i$ in $\boldsymbol{\xi}$-space. The field values have been multiplied by the appropriate phase and scale factors and weighted by the illumination spectral density. b) For a specific wavenumber $k_0$, the non-zero field values of $\tilde{O}(\boldsymbol{\xi})$ for a limited set of $\mathbf{k}_i$ are shown as coloured arcs, with each colour associated with a different choice of $\mathbf{k}_i$. The value of $\tilde{O}(\boldsymbol{\xi})$ under the black arc is zero; the black arc is used to illustrate how the values of the far-field scattered field are first located along the black arc before they are shifted by $-\mathbf{k}_i$.

For each possible NA-limited pairing of $\mathbf{k}_i$ and $\mathbf{k}_s$ (where $|\mathbf{k}_i| = |\mathbf{k}_s| = k_0$), the far-field scattered field from the scatterer must first be found using the BEM model, and using Eq. (2-46) the corresponding values of the measured field spectrum $\tilde{E}_m^{(i)}(\mathbf{k}_s)$ for each calculated far-field scatter $E_s^{(i)}(r_s\hat{\mathbf{s}}_s)$ can be found. This is also shown in Eq. (5-19), and consists primarily of removing the phase contribution of the far-field propagation by distance $r_s$. No apodization function is used to weight the resulting scatter for each choice of $\mathbf{k}_i$ and $\mathbf{k}_s$, corresponding to the case of constant angular variation (i.e., uniform angular apodization) [185,190]. However, an apodization function could be readily introduced if desired. The other scale factors present in Eq. (5-19) are omitted in the implementation of the model, as there is no direct facility in the BEM model to control the intensity of the illumination used. It is also not easy to obtain the power of the illumination used for the real instrument, nor the power measured by the CCD sensor when imaging the fringes. Due to this, accounting for the scale factors that are constant for all $\tilde{O}(\mathbf{k})$ is unnecessary, and only qualitative comparison with experiment is desired.

To calculate the fringe spectrum $\tilde{O}(\boldsymbol{\xi})$ for broadband illumination, the process to obtain $\tilde{O}_{\text{mono}}(\boldsymbol{\xi}; k_0)$ as given in Eq. (5-19) is performed for each wavelength of the

illumination present. These are then weighted by the term $S(k_0)/k_0$ in the integral in Eq. (5-17), where $S(k_0)$ is the normalised power spectrum density of the illumination source. However, in the implemented model a different weighting factor $S'(k_0)$ is used instead of $S(k_0)/k_0$. This is done for two reasons.

First, the spectral density used in CSI instruments is typically close to a Gaussian distribution, with a mean and standard deviation such that $a \cdot S(k_0)/k_0 \approx S(k_0)$, where $a$ is a scalar constant normalisation factor defined as $S_{\text{max}} = S(a)$ where $S_{\text{max}}$ is the maximum of $S(k_0)$. In this way, it is equally reasonable to treat $S(k_0)/k_0$ as a Gaussian distribution in terms of $k_0$, such that $S'(k_0) = a \cdot S(k_0)/k_0$ can be modelled as a Gaussian.

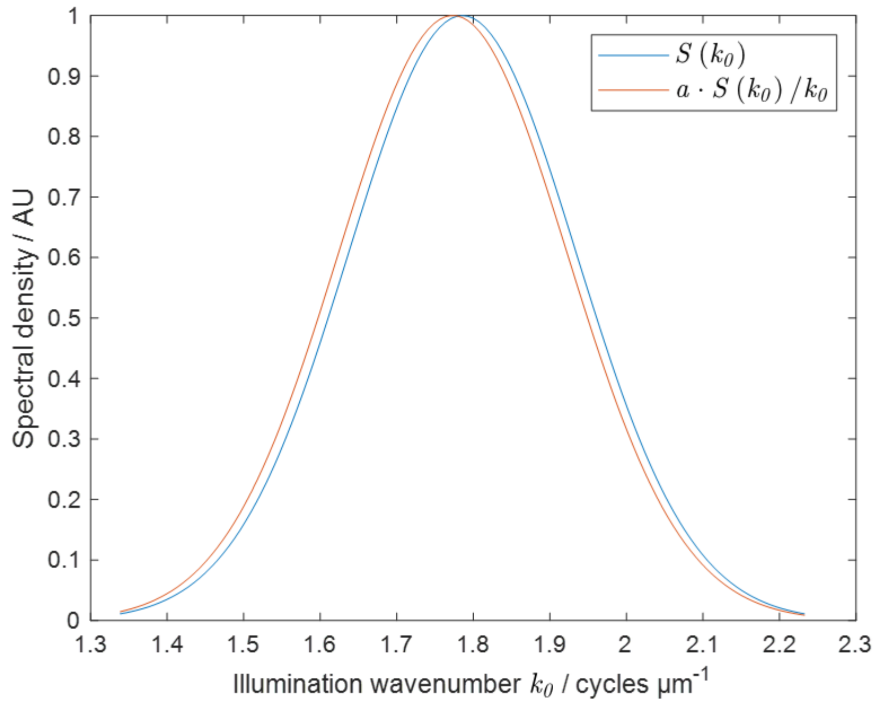


**Figure 5.3.** Spectral density $S(k_0)$ and weighting factor $S(k_0)/k_0$ for a Gaussian distributed $S(k_0)$ with a mean of 1.786 μm$^{-1}$ and FWHM of 0.351 μm$^{-1}$ (corresponding approximately to a mean of 0.56 μm and a FWHM of 0.11 μm for an approximately equivalent Gaussian distributed spectral density as a function of wavelength). Note that $k_0$ here is in units of cycles μm$^{-1}$, i.e., $k_0$ is a linear wavenumber, in contrast to using radians μm$^{-1}$ for an angular wavenumber.

Second, the spectral density of a real CSI instrument is, for this work, obtained through measurement of a low-NA measurement of a flat, where the fringe spectrum is obtained by Fourier transform of the measured fringe data. The flat surface acts as a mirror so that only specular scatter occurs. As the fringe spectrum $\tilde{O}(\boldsymbol{\xi})$ only has non-zero values

when $\boldsymbol{\xi} = \mathbf{k}_s - \mathbf{k}_i$, the specular scatter from the flat will exclusively lie in $\boldsymbol{\xi}$-space along the $\xi_z$ axis (where $\xi_x = 0$). The use of a low NA reduces the effect on the fringe spectrum of specular scatter produced by larger angles of incidence, approximately providing fringes that would be obtained if illumination was only normally incident. This ensures that the values of fringe spectrum along the $\xi_z$ axis are determined predominantly by the illumination spectral density. Therefore, a vertical slice along the $\xi_z$ axis of $\boldsymbol{\xi}$-space is taken from this spectrum to obtain a distribution relating to the spectral density of the illumination source. While the scale of the domain of this distribution is doubled compared to the illumination wavenumber ($\xi_z = 2k_0$), it is the case that this distribution represents the total weighting term that the illumination introduces i.e., it represents $S(k_0)/k_0$ in Eq. (5-17), which already includes the $1/k_0$ factor. It is therefore preferable in the implementation of the CSI model to not include a $1/k_0$ term, and to handle a Gaussian modelled or experimentally measured weighting function $S'(k_0)$ alone.

### 5.3.4 Discrete sampling considerations

While the descriptions for fringe synthesis in section 5.3.3 are accurate, it is necessary in a computational model for the various summations to be discretely sampled (or discretely generated). The sampling considerations related to BEM, such as the sample spacing of the surface geometry, have been discussed previously in Chapter 4. Those associated with the CSI fringe generation specifically are the illumination spectrum sampling and the angular sampling of the NA limited range of angles for the incident and observation vectors. In each case, if the sampling is too sparse to capture and characterise the underlying variation of the quantity being sampled, then the model cannot accurately model the resulting fringe signal. The sampling of the resulting real-space fringe signal generated must also be chosen, which can be chosen to match that of an instrument's imaged pixel size (i.e., spatial sampling per pixel) and scanning step.

Sampling of incident and observation angles are performed with equidistant angular spacing, as previously stated. The number of samples per degree (sample density) used for the incident and observation angles in general differ. The minimum number of observation angles required is determined in part by the surface's total width, as this determines the width of a scattered diffraction order; i.e. the Fourier transform of a rectangular function provides a sinc function whose width scales inversely with the

rectangular function's width [277]. For this condition, a sample density of approximately 3 samples per degree for a 25 μm wide surface appears appropriate, shown in Figure 5.4.

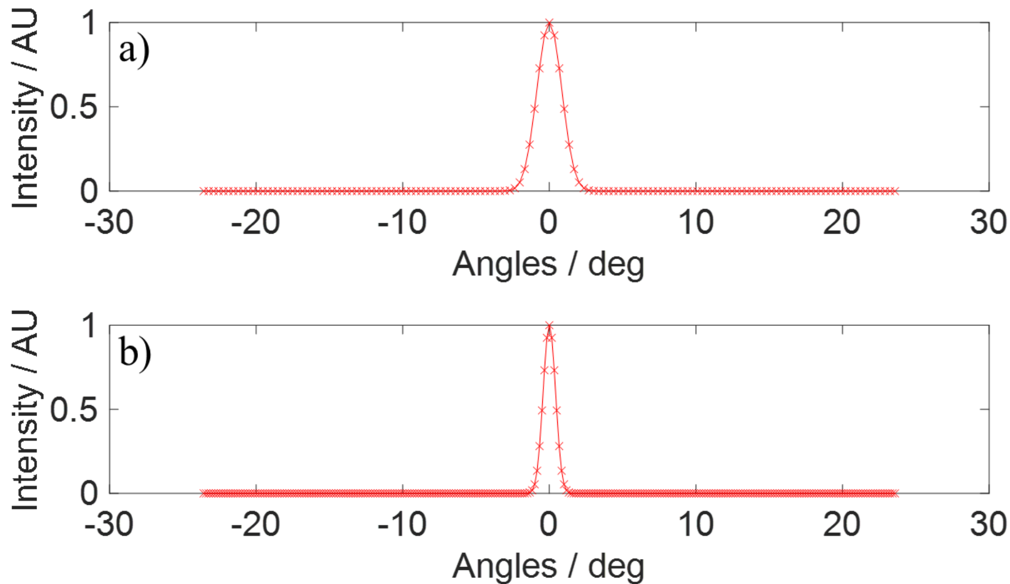


**Figure 5.4.** Intensity of angular scatter from monochromatic ($\lambda$=0.57 μm) normal incidence illumination of a flat surface with length a) 25 μm, and b) 50 μm. Samples where scatter values are calculated at are shown with a red x. The angular sample rate is a) 3 samples per degree, b) 6 samples per degree, automatically increased for the longer surface to proportionally account for the decreased peak width.

The minimum number of incident angles required is harder to generally determine, as it is determined by the variation of the relative distribution of surface scatter as the incident angle is varied for a specific surface. For some surfaces, very little variation of the distribution of scatter occurs (relative to the incidence direction), while for others more significant variation can occur, sometimes over only a small range of incident angles. Methods such as the foil model avoid this problem by design, by assuming a degree of independence between the object and the optical geometry, which allows the scattering amplitude to depend only on the object function and on $\mathbf{k}_s - \mathbf{k}_i$, with no dependence on $\mathbf{k}_i$ explicitly. This method is accurate for surfaces that are valid under the KA, which is satisfied sufficiently by many real-world surfaces. This means that for many surfaces, the minimum incident angle sampling density required is not dependent on the surface chosen and is related only on the need to sufficiently represent the extended support of the fringe spectrum $\tilde{O}(\boldsymbol{\xi})$ that occurs when the sample is illuminated by multiple incident wavevectors at different angles. This extended support

is especially significant when, due to a limited NA and a tilted surface, the majority of captured scatter originates from incident angles close to the acceptance angle. A sample density of approximately 0.6 samples per degree appears appropriate in practice for various surfaces, i.e., around 41 incident angles for an NA of 0.55.

Sampling of the illumination spectral density at a finite number of wavelengths must also be performed. The minimum sample density required is one that sufficiently represents the distribution of the spectral density and can sufficiently capture the change in the fringe field $\tilde{O}(\boldsymbol{\xi})$ as $k_0$ varies. In principle this sample density can be quite small for simple surfaces such as a flat; for the spectral density shown in Figure 5.3, taking 11 samples is sufficient (spacing of 0.08 cycles $\mu m^{-1}$), a choice commonly used in the foil model. However, for a range of illuminating angles for more complex or tilted surfaces, greater care must be taken, as monochromatic fringe spectrum values $\tilde{O}_{\text{mono}}(\boldsymbol{\xi}; k_0)$ are a result of the summation of field values from many different combinations of $\mathbf{k}_\text{i}$ and $\mathbf{k}_\text{s}$ where each field value is in general dependent on the specific $\mathbf{k}_\text{i}$ used. Ensuring that adjacent values of $\tilde{O}_{\text{mono}}(\boldsymbol{\xi}; k_0)$ from different $k_0$ are sufficiently close enough to each other to successfully capture the underlying variation can require larger illumination spectrum sampling densities. In Chapter 6, for a similar spectral density range to that in Figure 5.3, 61 samples were taken (a spacing of ~0.015 cycles $\mu m^{-1}$). This is shown in Figure 5.5. When a measured illumination spectrum is used in the model, the spectral density is interpolated at the chosen sampling density.

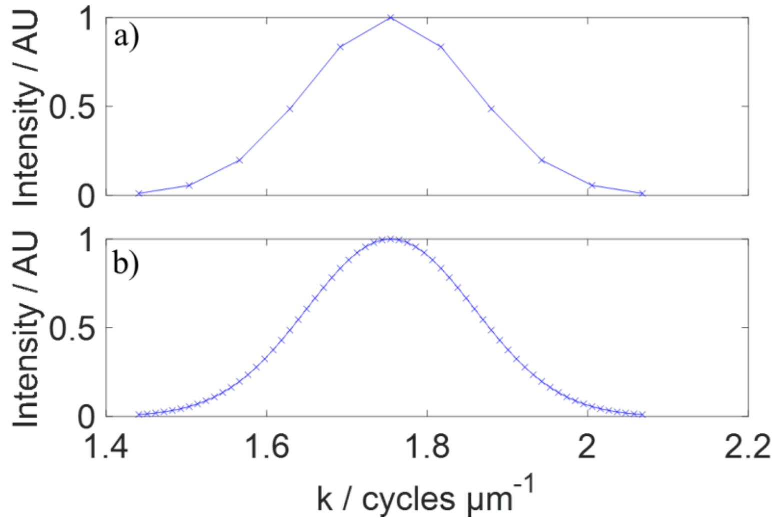


**Figure 5.5.** Modelled Gaussian spectral density with a mean wavenumber of 1.754 μm$^{-1}$ and FWHM of 0.246 μm$^{-1}$ (corresponding approximately to a mean wavelength of 0.57 μm and a FWHM of 0.08 μm), sampled at a) 11 positions, and b) 61 positions. Note that $k_0$ here is in units of cycles μm$^{-1}$, i.e., $k_0$ is a linear wavenumber.

## 5.3.5 Coordinate grid interpolation

After choosing the sampling of various continuous parameters across their ranges, an additional sampling issue must be resolved. The fringes in the model are generated over an *x*-*z* Cartesian plane, where the *z*-axis is the optical axis of the instrument. The fringe intensity values over this plane are discretely found over a rectangular grid of coordinates that span the plane. The values are stored in a 2D numerical array with the rows and columns of the array associated with the corresponding coordinate grid. The spacing of coordinates along the grid in the lateral (*x*) and axial (*z*) directions are constant, but the specific spacing in each direction in general differs. When imitating a real instrument, these values are the spatial sampling per pixel (accounting for magnification) and the scan step between images, respectively. To obtain the fringe field in real space $O(x,z)$ over this grid, the fringe field spectrum $\tilde{O}(\xi_x,\xi_z)$ must first be found over a corresponding rectangular grid of coordinates in the Fourier domain. An inverse Fourier transform is performed numerically by use of the Fast Fourier Transform (FFT) algorithm, a specific discrete Fourier transform (DFT) algorithm included in MATLAB, to obtain $O(x,z)$ from $\tilde{O}(\xi_x,\xi_z)$. An example grid is shown in Figure 5.6.

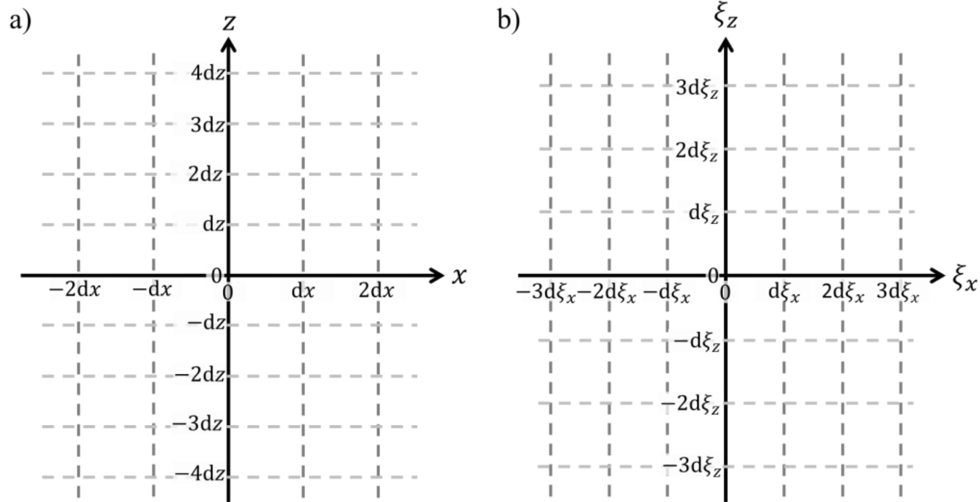


**Figure 5.6.** Discrete 2D rectangular grid in a) real space and b) $\boldsymbol{\xi}$-space, with constant spacing a) $\mathrm{d}x$ and $\mathrm{d}z$, and b) $\mathrm{d}\xi_x$ and $\mathrm{d}\xi_z$. For a real space axis $x$ containing $N_x$ discrete points, the corresponding frequency space axis under the FFT also has $N_x$ discrete points with spacing of $\mathrm{d}\xi_x = \frac{1}{(N_x \cdot \mathrm{d}x)}$ and a total extent of $N_x \mathrm{d}\xi_x = \frac{1}{\mathrm{d}x}$. Points range from $\xi_x = -\frac{1}{2\mathrm{d}x} + \frac{\mathrm{d}\xi_x}{2}$ to $\xi_x = \frac{1}{2\mathrm{d}x} - \frac{\mathrm{d}\xi_x}{2}$ when $N_x$ is odd, and from $\xi_x = -\frac{1}{2\mathrm{d}x}$ to $\xi_x = \frac{1}{2\mathrm{d}x} - \mathrm{d}\xi_x$ when $N_x$ is even. Corresponding expressions hold for the $z$ and $\xi_z$ axes.

The fringe spectrum $\tilde{O}(\xi_x, \xi_z)$ over a rectangular grid in the Fourier domain must be found to obtain real-space fringes. However, the fringe spectrum is formed by the combination of field values found at the locations where $\boldsymbol{\xi} = \mathbf{k}_\mathrm{s} - \mathbf{k}_\mathrm{i}$, for a discrete set of $\mathbf{k}_\mathrm{s}$ and $\mathbf{k}_\mathrm{i}$ considered. Naturally, any vector $\mathbf{k}_\mathrm{s} - \mathbf{k}_\mathrm{i}$ formed from the discrete set of available $\mathbf{k}_\mathrm{s}$ and $\mathbf{k}_\mathrm{i}$ generally will not lie on any of the $\boldsymbol{\xi}$-space rectangular grid coordinates, as shown in Figure 5.7. In the case of tomography where only $\mathbf{k}_\mathrm{s}$ is considered, the fringe spectrum could first be described in polar coordinates, and resampling to Cartesian coordinates using an established method could then be performed [278]. However, because of the effect of the $\mathbf{k}_\mathrm{i}$ term introduced by the demodulating reference field, an equivalent method here would first require creating many shifted polar coordinate grids for each $\mathbf{k}_\mathrm{i}$ (including for each $k_0$), where only the values along the arc $\mathbf{k}_\mathrm{s}$ (relative to a shifted origin of $-\mathbf{k}_\mathrm{i}$) are non-zero. Such an approach is not straightforward or especially efficient and may be difficult to implement due to the sparseness of each set of polar coordinates.

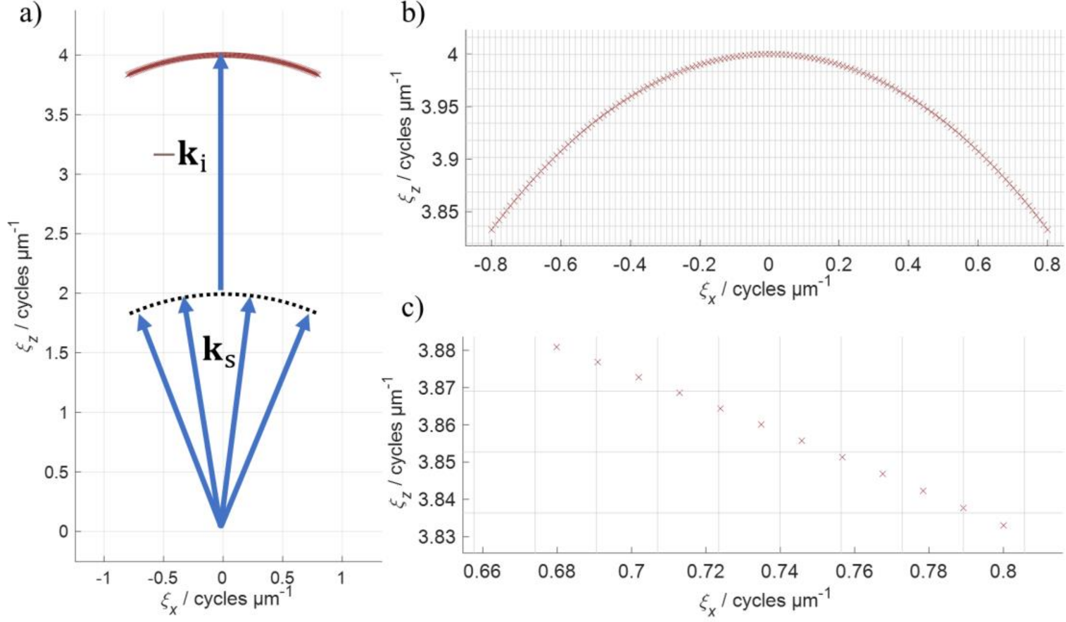


**Figure 5.7.** Locations of demodulated scatter in $\boldsymbol{\xi}$-space at $\boldsymbol{\xi} = \mathbf{k}_\mathrm{s} - \mathbf{k}_\mathrm{i}$ given by red cross marks for 141 equally spaced observation wavevectors $\mathbf{k}_\mathrm{s}$ (for a NA of 0.40), for monochromatic (λ=0.50 μm) normal incidence illumination ($\mathbf{k}_\mathrm{i} = -k_0\xi_z$). a) Shows the location of scatter relative to the origin where arrows for $\mathbf{k}_\mathrm{s}$ and $-\mathbf{k}_\mathrm{i}$ have been added for clarity, and where grid lines are tied to axes ticks. In b) and c) the locations of scatter are made more visible and the grid lines represent a rectangular grid of discrete coordinates $(\xi_x, \xi_z)$ at which values for $\tilde{O}(\xi_x, \xi_z)$ are found from the nearby scatter.

Here instead the contribution to $\tilde{O}(\xi_x, \xi_z)$ for a specific pair of $\mathbf{k}_\mathrm{s}$ and $\mathbf{k}_\mathrm{i}$ is found by multiplying the generated fringe field value by a function similar to a blurring convolution kernel. The kernel function used is a product of Gaussian functions with compact support and is evaluated in the region of $\boldsymbol{\xi} = \mathbf{k}_\mathrm{s} - \mathbf{k}_\mathrm{i}$ at coordinates near to $\mathbf{k}_\mathrm{s} - \mathbf{k}_\mathrm{i}$ that lie on the rectangular grid. A similar approach using sinc functions can be seen in section 4.4 of [279]. A one-dimensional (1D) simplification of the method used here is shown in Figure 5.8.

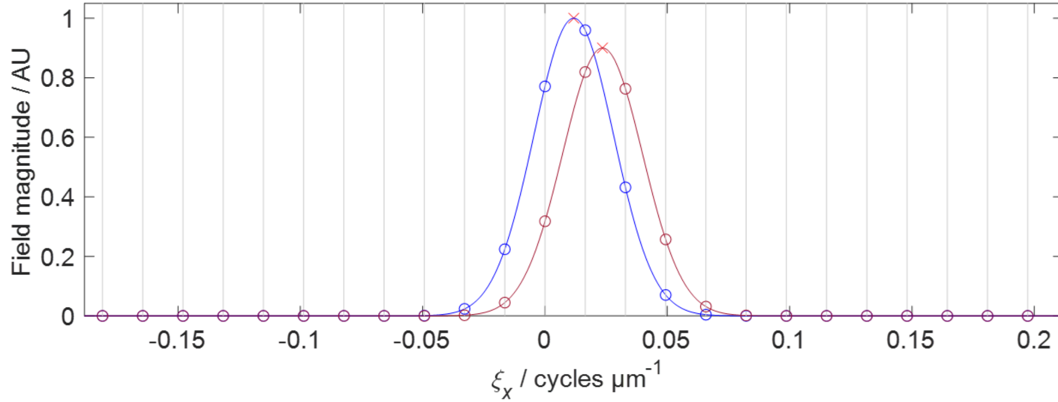


**Figure 5.8.** Diagram displaying a 1D simplification of the 2D blurring method. The magnitudes of two adjacent scattered fields are denoted by red cross marks, where the magnitudes here were arbitrarily chosen to be 1 AU (left) and 0.9 AU (right). The discrete coordinates of $\xi_x$ at which field values are to be found are shown by equally spaced vertical grey lines. Each scattered field contributes its field value to nearby discrete coordinates using a Gaussian "blurring" function centred on the scattered field, where the field magnitude of the contribution at each discrete coordinate is determined by the Gaussian function at that coordinate. For example, at $\xi_x = 0$ the field value found is the sum of the two scattered fields with magnitudes modified by the Gaussian function, given by the blue and burgundy circle marks at $\xi_x = 0$ (0.77 AU and 0.32 AU respectively). As the addition is complex, the resulting field value may have a smaller magnitude than the sum of the constituent field magnitudes.

The kernel function fulfils two purposes. The first purpose is to try to ensure that the field value at $\mathbf{k}_\mathrm{s} - \mathbf{k}_\mathrm{i}$ and adjacent field values found nearby are combined in such a way so that the field values at rectangular grid coordinates between the adjacent field values are correctly interpolated. For this purpose, the blurring extent should be related to spacing between the values of $\mathbf{k}_\mathrm{s} - \mathbf{k}_\mathrm{i}$ and how they are distributed (for a discrete set of $\mathbf{k}_\mathrm{s}$ and $\mathbf{k}_\mathrm{i}$). The distribution of $\mathbf{k}_\mathrm{s} - \mathbf{k}_\mathrm{i}$ values for a chosen number of $\mathbf{k}_\mathrm{s}$ and $\mathbf{k}_\mathrm{i}$ for the monochromatic case is shown in Figure 5.9. The blurring should in general scale inversely with the number of samples taken and should also be applied differently along different directions. This is shown by the difference in spacing between dots of the same colour and of similar but different colours in Figure 5.9b) to d). For example, reducing the number of observation angles sampled for $\mathbf{k}_\mathrm{s}$ spreads out the field values found across the NA-limited arc; these values need to be blurred more to compensate and this blurring should be made along the tangent to the arc.

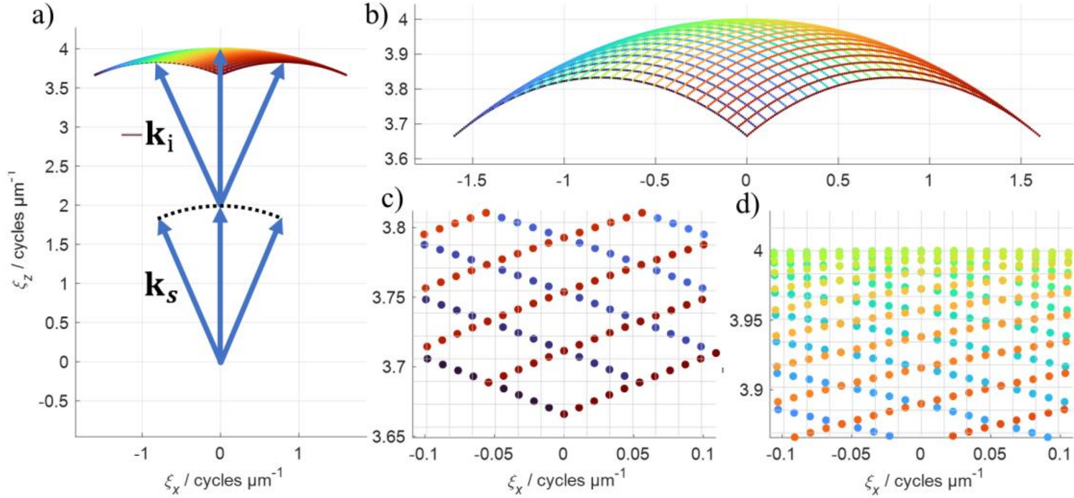


**Figure 5.9.** Locations of demodulated scatter in $\boldsymbol{\xi}$-space at $\boldsymbol{\xi} = \mathbf{k}_\mathrm{s} - \mathbf{k}_\mathrm{i}$ given by coloured dots, for monochromatic illumination (λ=0.50 µm) over a range of incident angles limited by a NA of 0.40, where 141 $\mathbf{k}_\mathrm{s}$ and 29 equally spaced incident wavevectors $\mathbf{k}_\mathrm{i}$ have been used. A different colour is used for each arc of scatter produced by a different $\mathbf{k}_\mathrm{i}$, as in Figure 5.2, and here similar values of $\mathbf{k}_\mathrm{i}$ use similar colours to indicate the structure of the demodulated scatter's distribution. In a) the location of scatter relative to the origin is shown, grid lines extend from the axes' ticks, and arrows for $\mathbf{k}_\mathrm{s}$ and $-\mathbf{k}_\mathrm{i}$ have been added for clarity. The black dotted line added represents the NA-limited shell of available $\mathbf{k}_\mathrm{s}$ before being shifted by $-\mathbf{k}_\mathrm{i}$. In b), c), and d) the gaps between locations of scatter are made more visible. In c) and d) the same field of view at different positions is displayed, and the grid lines represent a rectangular grid of discrete coordinates $(\xi_x, \xi_z)$ as in Figure 5.7b) and c).

The second purpose is to ensure that the field values at each specific $\mathbf{k}_\mathrm{s} - \mathbf{k}_\mathrm{i}$, which may be at any position within the passband of the instrument, are added to the rectangular grid of coordinates in the vicinity of $\mathbf{k}_\mathrm{s} - \mathbf{k}_\mathrm{i}$. For this purpose, the blurring extent should at a minimum be half the size of a rectangular grid "pixel", where the width and height of a "pixel" is the spacing between adjacent grid values along each dimension, otherwise the calculated fringe values that are not near to any single grid coordinate will not provide much contribution to any coordinate of $\tilde{O}(\xi_x, \xi_z)$. This can equally be considered a constraint on the maximum size of the $\boldsymbol{\xi}$-space grid pixels chosen for a specific blurring extent and sample density used.

The primary purpose of the kernel is the first purpose: correctly combining adjacent and overlapping calculated field values such that the field values provided at the rectangular coordinates chosen are accurate. When the rectangular grid of coordinates is fine relative to the sampling of $\mathbf{k}_\mathrm{s} - \mathbf{k}_\mathrm{i}$ chosen (i.e., the angular spacing and spectrum

spacing chosen), the kernel provides interpolation via blurring to ensure smooth variation of the fringe field values in regions between samples of $\mathbf{k}_\mathrm{s} - \mathbf{k}_\mathrm{i}$, for example filling in the gaps in Figure 5.9c). The values of $\tilde{O}(\xi_x, \xi_z)$ at these in-between grid points would otherwise be zero. However, the second purpose cannot be neglected. When the grid is both coarse relative to the sampling of $\mathbf{k}_\mathrm{s} - \mathbf{k}_\mathrm{i}$ and to the kernel extent, those field values near a specific grid coordinate would contribute almost exclusively to $\tilde{O}(\xi_x, \xi_z)$ at just that single coordinate, while values not near any specific coordinate contribute almost nothing to $\tilde{O}(\xi_x, \xi_z)$ at any coordinate. To resolve this, either the blurring must be increased (while the sampling of $\mathbf{k}_\mathrm{s} - \mathbf{k}_\mathrm{i}$ is simultaneously decreased), or the rectangular grid made finer, so that the blurring extent used is larger than half the size of a rectangular grid "pixel".

### Blurring modes

In the model, there are two modes implemented for the blurring kernel: Cartesian blurring and polar blurring. The first, used for the work presented in this chapter, blurs separately along the $\xi_x$ and $\xi_z$ directions, labelled as $k_x$ and $k_z$ in Figure 5.13 onwards for simplicity. This blurring along $\xi_x$ scales inversely with the observation angle sample density, and the blurring along $\xi_z$ scales inversely with the illumination spectrum sample density. Such an approach is simple and fast to implement and benefits from the two blurring directions being orthogonal. It also benefits when the diffraction orders in the fringe spectrum are parallel with $\xi_z$, which occurs when the mean plane of the modelled surface is parallel with $\xi_x$ (and therefore $x$). For surfaces that primarily scatter in and near to the specular direction, and at incident and observation angles from the normal that are relatively small ($|\theta| < \sim 30°$), most of the fringe spectrum is close to the line $\xi_x = 0$, such that blurring along $\xi_x$ and $\xi_z$ provides accurate results. Even in the case of Figure 5.15, where the scatter is spread out wider than in Figure 5.17, the blurring chosen remains suitable and any issues can be mitigated by increasing the number of angular and illumination samples taken. This blurring mode is shown in in Figure 5.10 in black.

The second blurring mode, used for the work presented in Chapter 6, blurs along the directions parallel and perpendicular to $\mathbf{k}_\mathrm{s}$, i.e., providing radial and tangential blurring at each point on the observation arc. This mode in general provides more accurate results for any surface but is slightly slower computationally and was more complicated

to implement. This mode is also shown in Figure 5.10 in red. Using this mode instead of the Cartesian blurring is necessary for titled surfaces, especially those titled at angles larger than 30°. This is because the fringe spectrum of a titled surface is approximately equal to the spectrum of the untilted surface rotated around $\boldsymbol{\xi} = \mathbf{0}$ by the same angle, so that for a periodic surface, the diffraction orders are also rotated. Performing blurring along $\xi_z$ that scales inversely with the illumination sample density fails when the diffraction orders no longer lie parallel with $\xi_z$, and instead leads to gaps in the diffraction orders, shown in Figure 5.11, which in turn lead to aliasing effects in the real-space fringes. The Cartesian blurring can only succeed for titled surfaces when the spectrum sampling is significantly increased, and the blurring extent reduced to a value that specifically suits the tilt chosen. In contrast, the polar blurring approach can use a constant number of samples and constant blurring parameters when untilted and tilted at any angle and give accurate results with similar appearances (besides the rotation of the diffraction orders).

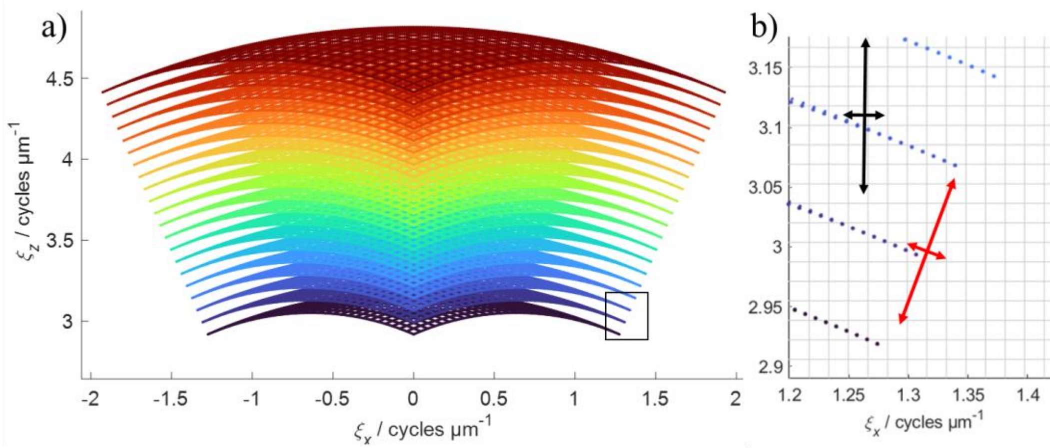


**Figure 5.10.** Locations of demodulated scatter in $\boldsymbol{\xi}$-space at $\boldsymbol{\xi} = \mathbf{k}_\mathrm{s} - \mathbf{k}_\mathrm{i}$ given by coloured dots, for polychromatic illumination (from λ=0.415 µm to λ=0.628 µm) over a range of incident angles limited by a NA of 0.40, where 141 $\mathbf{k}_\mathrm{s}$, 29 $\mathbf{k}_\mathrm{i}$, and 21 illumination wavenumbers $k_0 = |\mathbf{k}_\mathrm{i}| = |\mathbf{k}_\mathrm{s}|$ have been used. A different marker colour is used for different wavenumbers. In a) the region covered by $\boldsymbol{\xi} = \mathbf{k}_\mathrm{s} - \mathbf{k}_\mathrm{i}$ for the samples of $\mathbf{k}_\mathrm{s}$, $\mathbf{k}_\mathrm{i}$, and $k_0$ is shown, with a small black box denoting the region shown in b). In b), the FWHM in two directions are given for the Cartesian blurring in black and for the polar blurring in red, with the grid lines denoting the discrete coordinates $(\xi_x, \xi_z)$ at which values are interpolated at.

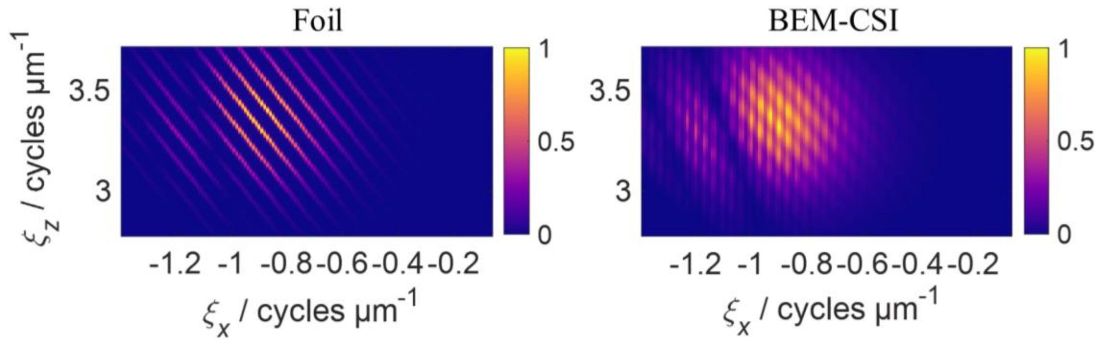


**Figure 5.11.** Magnitude of the CSI fringe spectrum for a sinusoidal surface (PV of 1.4 µm, surface wavelength of 14.8 µm) tilted at 30° , for an NA of 0.4, for the foil model (left) and the BEM-CSI model (right), where Cartesian blurring with insufficient blurring parameters has been used for the BEM-CSI model, degrading the underlying diffraction orders. The Cartesian blurring parameters used were sufficient in the untilted case.

It is possible that the blurring associated with the illumination sampling density should strictly be in the direction of $\boldsymbol{\xi} = \mathbf{k}_\mathrm{s} - \mathbf{k}_\mathrm{i}$, rather than in the direction of $\mathbf{k}_\mathrm{s}$, as both $\mathbf{k}_\mathrm{s}$ and $\mathbf{k}_\mathrm{i}$ scale together with the choice of $k_0$ (i.e. $\boldsymbol{\xi} = k_0(\hat{\mathbf{s}}_\mathrm{s} - \hat{\mathbf{s}}_\mathrm{i})$); however, such a blurring mode has not yet been implemented. The radial blurring in terms of $\mathbf{k}_\mathrm{s}$ nonetheless appears to be a sufficient substitute to blurring along $\boldsymbol{\xi}$, and benefits from always being orthogonal to the tangential blurring of $\mathbf{k}_\mathrm{s}$ (associated with the observation sampling density).

The scatter most affected by a change between blurring in $\mathbf{k}_\mathrm{s}$ or $\boldsymbol{\xi}$ is specular scatter from large incident angles, found at the bottom of each monochromatic distribution as shown in Figure 5.9c). However, in these regions the blurring in $\mathbf{k}_\mathrm{s}$ is almost exactly that needed for blurring associated with the incident angle sampling density chosen, i.e., the different $\mathbf{k}_\mathrm{i}$ considered. This is not explicitly implemented in any blurring mode as it is for now not obvious how to obtain an expression for the spacing between sets of coordinates for $\tilde{O}(\boldsymbol{\xi})$ for two different angles of $\mathbf{k}_\mathrm{i}$, or suitably combine the need to blur for three parameters (spectrum, observation angle, and incident angle sampling) together. In contrast, the regions associated with backscatter, shown in Figure 5.10b), are where the largest "gaps" between samples appear and are where the radial blurring is most required. In these regions, the direction of $\boldsymbol{\xi}$ and $\mathbf{k}_\mathrm{s}$ are parallel or almost parallel, such that radial blurring along $\mathbf{k}_\mathrm{s}$ is equivalent to blurring in the direction of $\boldsymbol{\xi}$. Nevertheless, for any choice of blurring mode, an increase of sampling parameters (and computation time) can be used to mitigate the effects of the specific blurring mode chosen, so this aspect remains a relatively minor issue.

Note that scatter locations for even just monochromatic illumination can at times appear to form lines, visible in Figure 5.9b), where each line if extended would intercept $\boldsymbol{\xi} = \mathbf{0}$. However, this is just a consequence of the arbitrary choice of sampling made, which occurs only when the incidence angular spacing is a multiple of the observation angular spacing, or partially occurs when the simplest ratio between the two contain integers smaller than the number of angular samples made.

Also note that the symbol $k$ is used instead of $\xi$ for the spatial frequency of the fringes from this point onwards in this thesis, as using $k$ for spatial frequencies is a much more common notation, and because taking care to distinguish between the spatial frequencies of the wave and of the fringes is unnecessary when not comparing the two.

## 5.4 Methods and materials

To verify the BEM-CSI model, the results from the model are compared with those from experimental measurements. A range of prismatic surfaces were measured using a Zygo Nexview™ NX2 CSI instrument, see Table 3.1. Results for similar surfaces from a linear model of CSI can be seen in [74]. In each case, a 10 μm scan along the optical axis ($z$-axis) was performed using a 50× objective lens, which has a NA of 0.55 (acceptance angle of ~33°), a Sparrow criteria optical resolution of 0.52 μm, a field of view (FOV) of (0.174 × 0.174) mm when using the 1.0× zoom lens, and from the 1000 × 1000 pixel FOV, a spatial sampling of 0.174 μm per pixel. Here the circular illumination aperture fills the whole NA of the lens; i.e. the system's illumination NA is equal to the NA of the objective lens. This is confirmed by the experimentally measured 3D surface transfer function of the same instrument configuration seen in [159]. Due to the design of the objective lens, the polarisation of illumination incident on the surface is nominally circular, with a small radial component resulting from the high NA of the objective lens. The signal data measured and recorded by the instrument, i.e., the intensity measured at each pixel for each scan position, is exported as a 3D array of integers. The spatial-frequency domain ($k$-space) fringe data is then obtained through use of the 3D Fourier transform, and a band-pass filter (BPF) applied to isolate the high spatial frequency fringe components. A subsequent inverse Fourier transform of the filtered signal provides the real-space experimental fringe data without low spatial frequency components.

**Table 5.1** Surfaces measured and modelled for this paper

| **Surface type** | **Specific surface measured** | **Nominal parameters** |
|---|---|---|
| Optical flat | NPL AFL | Measured areal root-mean-square roughness *Sq*: 1.4 nm (Levelling by least-squares mean plane subtraction; S-filter with a nesting index of 0.8 μm; L-filter with a nesting index of 80 μm) |
| Sinusoidal grating | Rubert 543E | Peak-valley amplitude: 0.12 μm<br>Surface wavelength: 2.5 μm |
| Sinusoidal grating | Rubert 528E | Peak-valley amplitude: 1.5 μm<br>Surface wavelength: 50 μm |
| Step height with sharp edge | NPL ACG-2.1 XP01 | Step height: 2.1 μm |
| Vee-groove | N/A (only modelled) | Vee-groove dihedral angle: 70°<br>Depth: 10 μm |

The BEM-CSI model is provided with the corresponding curves that specify the real surfaces, e.g. a sinusoid for a sinusoidal grating and a horizontal line for an optical flat. Each surface in Table 3.1, with the exception of the vee-groove, has a length of 170 μm along the lateral direction, i.e. $x$-direction, matching the FOV of the experiment, and the surface geometry was sampled with a spacing of 0.099 μm.

For modelling with the BEM-CSI model, it was assumed that the light is incident upon a perfect conductor and can be treated as linear TE polarisation illumination. The spectral density as a function of wavenumber is modelled as a Gaussian distribution with a mean of 1.72 μm$^{-1}$, and FWHM of 0.24 μm$^{-1}$ (corresponding to a mean of 0.58 μm and a FWHM of 0.08 μm) and approximately matching the corresponding parameters of the instrument. The real-space fringe signal $O(\mathbf{r})$ is determined at coordinates with lateral and axial spacing that match that of the real instrument's signal data, i.e. using a lateral spacing of 0.174 μm and an axial spacing of 0.071 μm, with 1000 lateral points and 205 axial points. This corresponds to a $k$-space grid spacing of 0.0058 μm$^{-1}$ and 0.0673 μm$^{-1}$ for the lateral and axial directions respectively. The spectrum is sampled 15 times over three standard deviations of the total spectrum (i.e. from 1.42 μm$^{-1}$ to 2.03 μm$^{-1}$), and the incident angles sampled 18 times over the angles within the acceptance angle for the NA. Over the same range of angles, 1113 observation angles are chosen, at which the far-field scatter is calculated.

Under these conditions, the CSI signal simulation took around 45 minutes for each surface on a PC with Intel® Xeon® E5-1620 v4 @ 3.50 GHz CPU and 64 GB RAM.

However, for these surfaces, a reduction to 9 incident angles halves this time with very little effect on the generated fringes. Additionally, it is expected that more computationally efficient approaches, e.g., parallelisation, would reduce this time considerably.

These comparisons are intended to be qualitative, not quantitative, due to the limitations of the BEM-based CSI model in matching the 3D nature of the experimental measurement, e.g., the circular aperture of the instrument. Due to the commercial nature of the system, adjusting this aperture to a slit was not possible. Therefore, to allow for qualitative comparison this difference is mitigated through the measurement of grating or prismatic surfaces, due to their strong scattering characteristics into the plane in which BEM is limited to.

Note that the definition used for spatial frequency $k_x$ (along the $x$-axis), as seen in Figure 5.13 and all subsequent $k$-space figures, is not the angular frequency definition, but the linear frequency definition (an unscaled reciprocal of space). This is done as the grating pitch can more easily be connected to the $k$-space diffraction patterns produced.

## 5.5 Results

### 5.5.1 Optical flat

First the experimental results when measuring an optical flat are compared with results from the model, as seen in Figure 5.12 and Figure 5.13. Qualitative agreement is achieved, showing that the model generates fringes that match the experimental results. The coherence envelope of the fringes slightly differs between the experimental results and those from the CSI model, which is expected due to the 2D limitation of the BEM modelling, and because the instrument’s source spectrum is not exactly Gaussian. Differences in spectral distribution causing the coherence envelope to differ are shown in Fig. 4 of [74], where a linear 3D CSI model based on the KA and CSI experimental measurement data are compared. It is well-known that a narrower spectrum will lead to a broader coherence envelope.

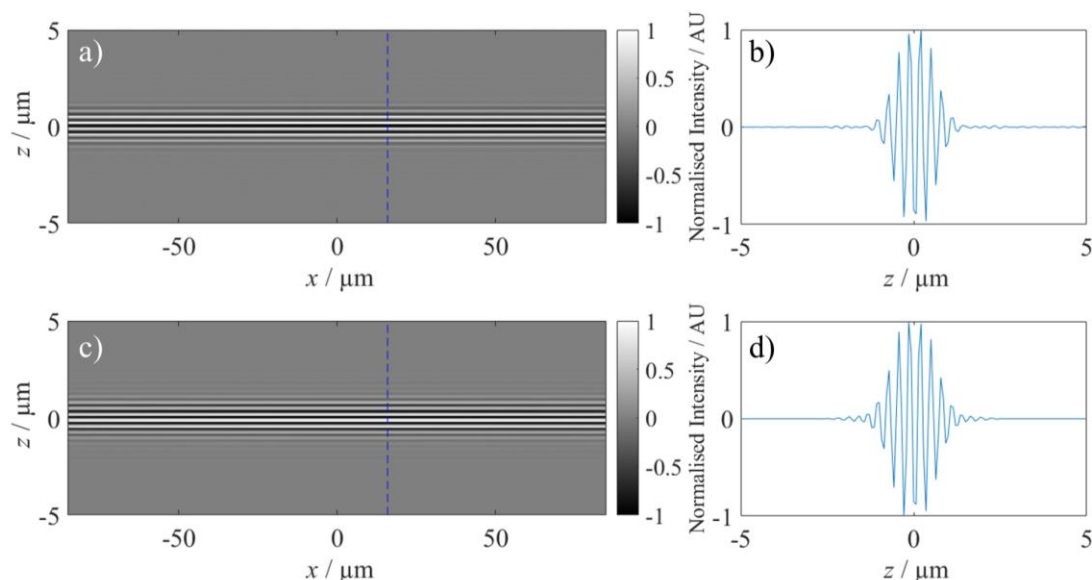


**Figure 5.12.** Cross-sectional CSI signal of an optical flat, a) experimental result after BPF filtering, c) corresponding simulation of fringe, where along the blue dotted lines the profiles b) and d) have been taken from measurement and simulation respectively. The fringe intensity has been normalised to lie within ±1 in each case.

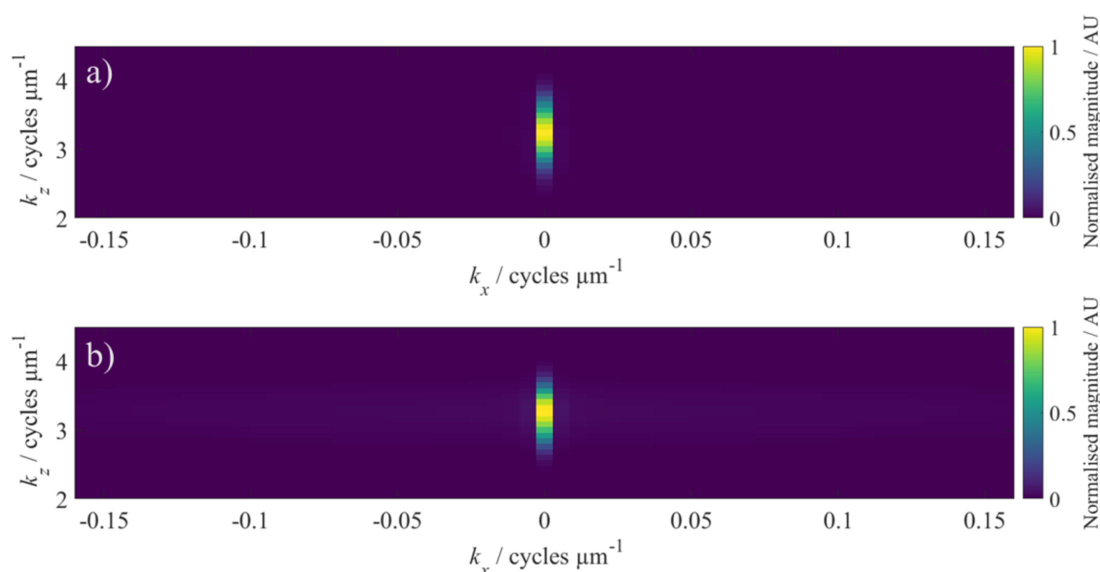


**Figure 5.13.** Cross section of the magnitude of the $k$-space CSI signal from measurement of an optical flat, a) experimental result and b) corresponding simulation. The $k$-space signal magnitude has been normalised to +1 in each case.

## 5.5.2 Sinusoidal gratings

In Figure 5.14 and Figure 5.15, a high spatial frequency, low amplitude sinusoidal grating is used, as specified in Table 3.1. As expected from elementary Fourier optics [182,192,245], the diffraction orders produced are spaced relatively far apart due to the surface wavelength of 2.54 µm. Qualitative agreement between experiment and

simulation is again seen, with the signals in both the real space and *k*-space appearing to match. However, the amplitudes of the higher diffraction orders, relative to the zeroth-order, are weaker in the experimental measurement. This is partly because the current BEM algorithm only considers in-plane illumination, but in the experiment, the zeroth-order will have a few contributions from off-axis illumination that increase its magnitude, i.e., this effect can be considered as the difference between measuring a grating using a spherical lens and a cylindrical lens. In addition, this effect is partially caused by the imperfect transfer function of the instrument due to optical aberration and apodization due to the reference mirror in its Mirau objective [144,159].

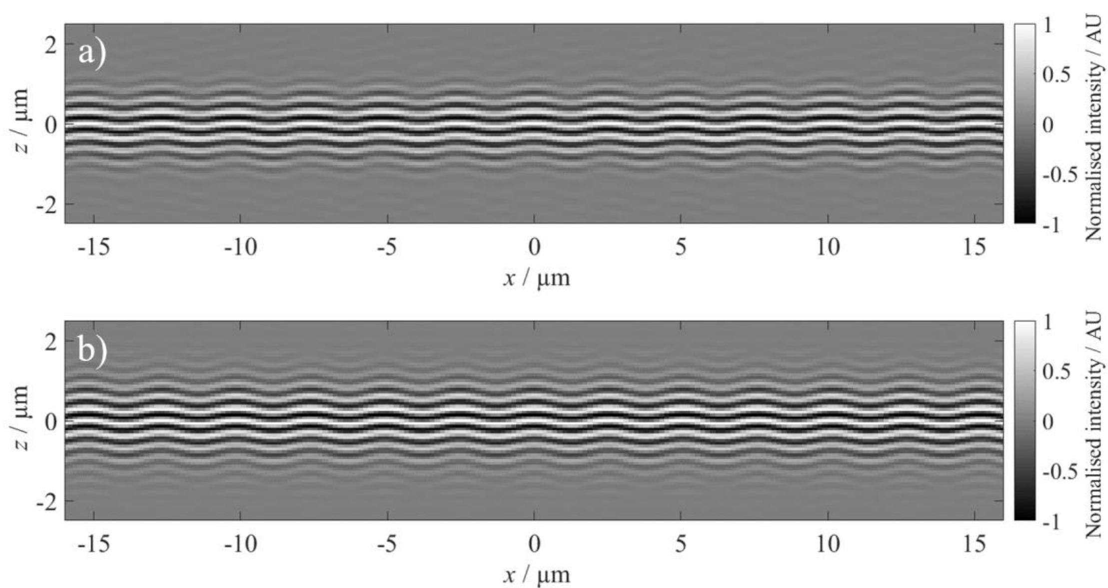


**Figure 5.14.** Cross-sectional CSI signal of a sinusoidal grating Rubert 543E, a) experimental result and b) corresponding simulation. Note that the fringes were measured a) and generated b) over the same FOV as in Figure 5.12, but the display window has been shrunk for better visual comparison.

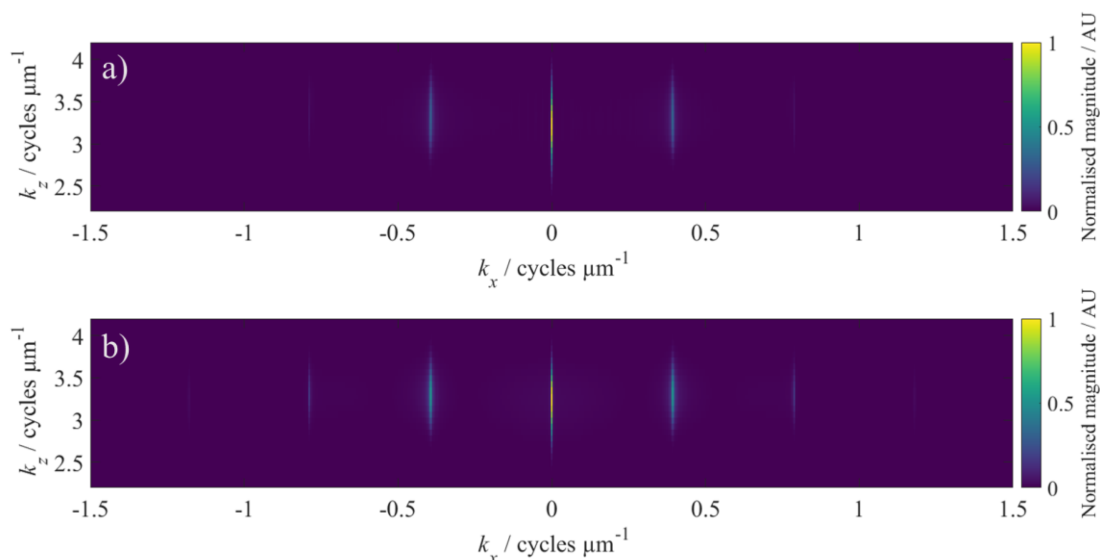


**Figure 5.15.** Cross section of the magnitude of the *k*-space CSI signal from a sinusoidal grating Rubert 543E, a) experimental result and b) corresponding simulation.

In Figure 5.16 and Figure 5.17, comparison is made using a sinusoidal grating with higher amplitude and longer wavelength, as specified in Table 3.1. The surface wavelength of 50 µm causes the resulting pattern in *k*-space to be closer together, and the increased amplitude gives the more complex pattern seen here. Qualitative agreement is again seen for both the real and *k*-space fringe data.

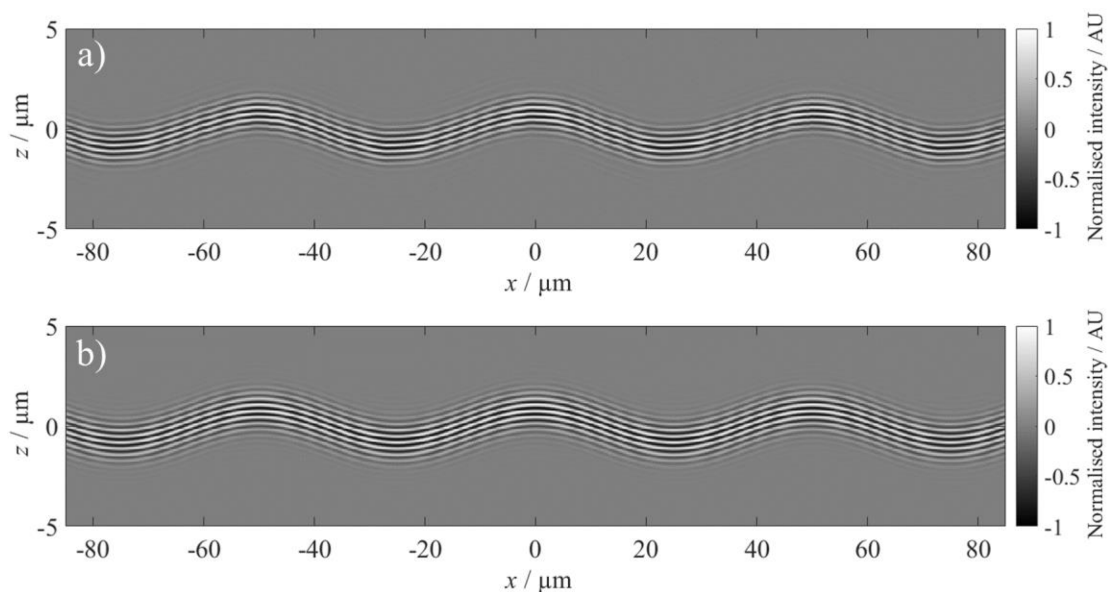


**Figure 5.16.** Cross-sectional CSI signal of a sinusoidal grating Rubert 528E, a) experimental result and b) corresponding simulation.

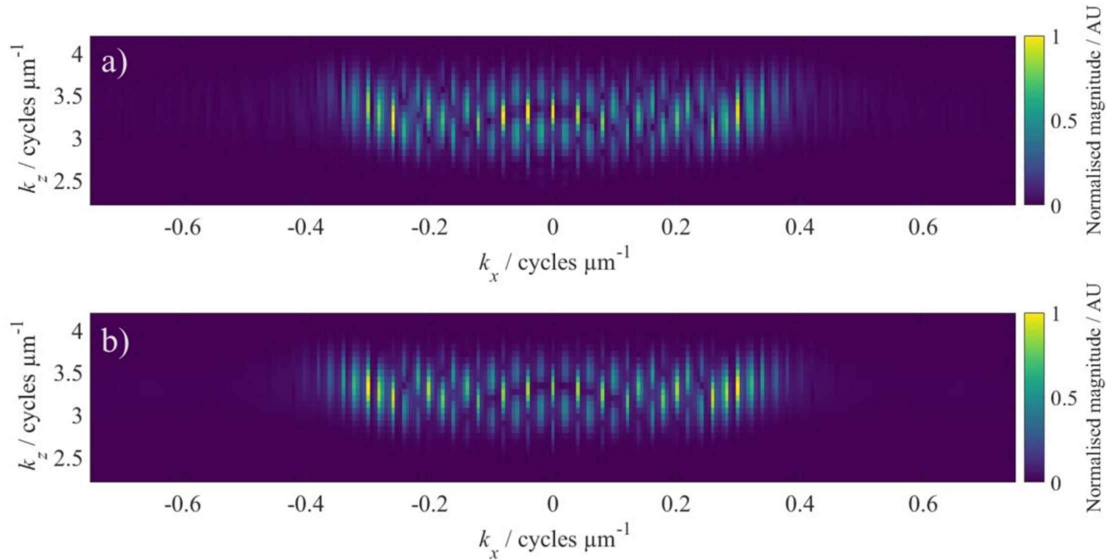


**Figure 5.17.** Cross section of the magnitude of the *k*-space CSI signal from a sinusoidal grating Rubert 528E, a) experimental result and b) corresponding simulation.

### 5.5.3 Step height

The final comparison between the model and experiment uses a step height, as shown in Figure 5.18 and Figure 5.19, and as specified in Table 3.1. The experimental results and the modelled results in Figure 5.18 a) and b) respectively differ around the step itself. This discrepancy likely occurs due to the inherent difference between the CSI model, which is restricted to surfaces that only scatter within the plane of incidence, and a real 3D measurement; this can in part be seen through examination of the fringes after filtering of the out-of-plane *k*-space signal in Figure 5.18 c).

This filter was a simple binary mask where only a central slice of the three-dimensional Fourier transform of the signal data was taken, and the rest discarded. The data was then inverse Fourier transformed, the real part taken, and the central slice displayed as the fringe data. This filter does not work exactly as a physical slit aperture (located at the back focal plane of the objective lens) but can nonetheless remove the out-of-plane scatter of the in-plane illumination, as well as part of the scatter of the out-of-plane illumination. Therefore, the filter should moderately improve the comparison.

Polarisation effects introduced by the instrument's optical elements, and in particular the Mirau interferometric objective [280], are not considered in this CSI model, which could also contribute to this difference. In addition to these effects, the tilted fringes near the corner and the vertical wall of the modelled step height are probably caused by

the double reflection between the two orthogonal surfaces, which are likely less pronounced in the experiment because the texture of the vertical wall is higher compared to the smooth surface assumed in the simulation. This discrepancy could be investigated in future work with a full 3D BEM-based CSI model.

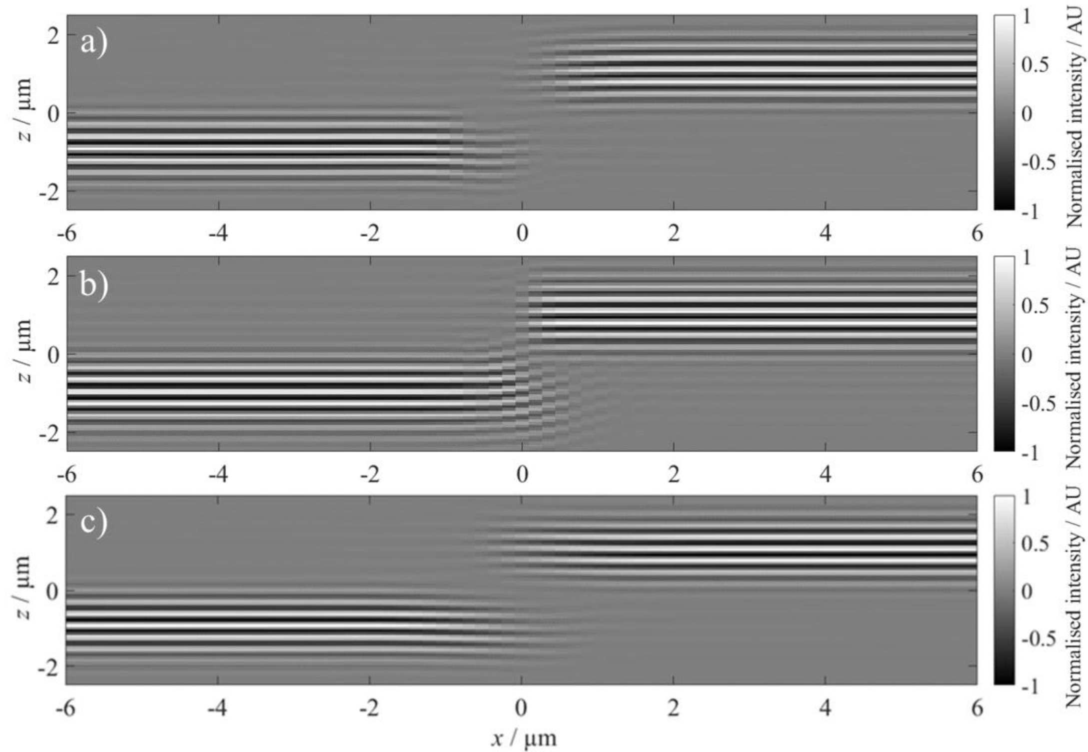


**Figure 5.18.** Cross-sectional CSI signal of a step height obtained from cross grating sample NPL ACG-2.1 XP01, a) experimental result, b) corresponding simulation for a step height, assuming a step inclination of 90°, and c) experimental result after removal of the out-of-plane *k*-space signal.

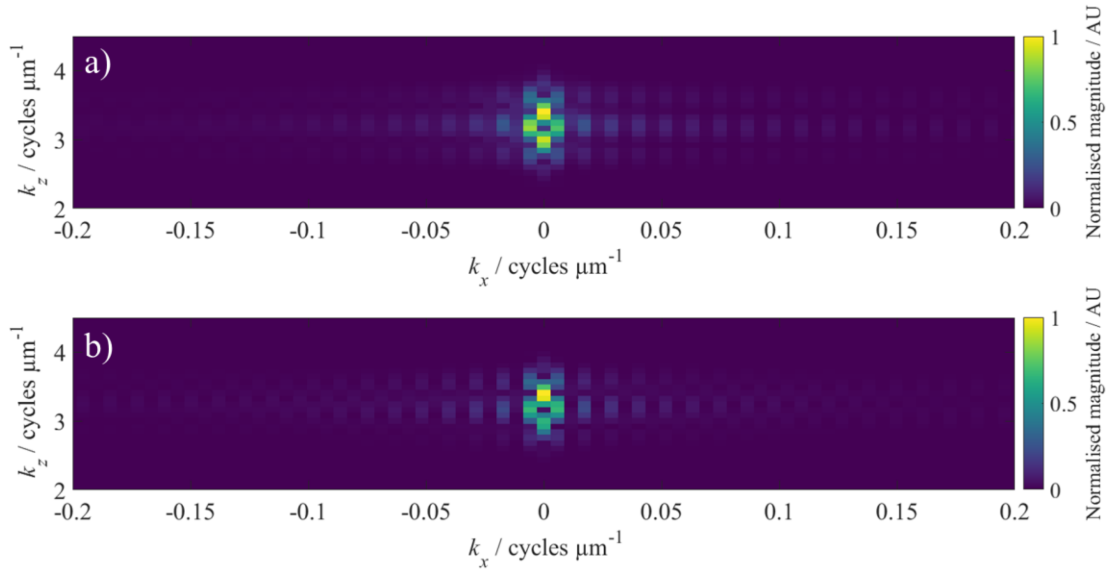


**Figure 5.19.** Cross section of the magnitude of the *k*-space CSI signal from a step height found on the cross grating sample, a) experimental result, b) corresponding simulation for a step height.

### 5.5.4 Vee-groove

In addition to comparisons to experimental measurements, in Figure 5.20 the model's results of a 10 μm deep vee-groove with 70° dihedral angle are presented, where the sampling in wavenumber and incident angle has been increased. The inverted "v" fringe pattern seen at the pit of the vee-groove is understood to be virtual images of the two vee-groove walls, generated by multiple reflection [175,178]; and the relationship (described in [178]) which relates the dihedral angle of the multiple reflection image to the vee-groove dihedral angle appears to be satisfied here. The result also visually matches that found elsewhere [49]. This result, therefore, presents evidence that the model can account for multiple scattering.

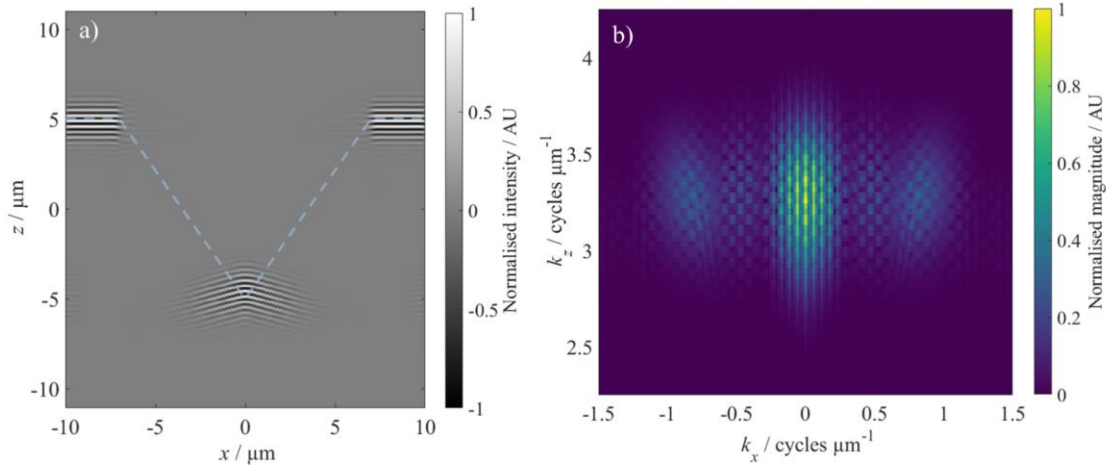


**Figure 5.20.** a) Simulated CSI signal in real space for a vee-groove as described in Table 3.1. Note that the blue dashed line denotes the geometry of the vee-groove modelled. b) The magnitude of the *k*-space CSI signal.

## 5.6 Conclusion and discussion

The BEM-CSI model was verified through comparison with experimental CSI measurements of various surfaces, including two sinusoidal gratings and an optical flat, showing agreement. Comparison with a step height showed some agreement, though some discrepancies were also present. Verification of the model's capability to predict multiple scattering was performed through comparison of results of modelling a vee-groove to results seen in the literature, with agreement again seen. Such a model will eventually provide opportunities to accurately measure complex surfaces, e.g., through iterative improvement of surface topography through the minimisation of the differences between measured and modelled CSI images, or to improve accuracy by using the model to evaluate uncertainty.

One of the primary limitations of the model that limits the comparison between the model and experimental measurement is the 2D nature of the model, compared to the 3D nature of the experimental measurement. The use of a cylindrical objective lens could have brought the experiment closer to the model, but this substitution was not possible, and the usual spherical objective lens was used instead. While a BPF can remove off-axis fringe spectrum data prior to comparison, it cannot prevent the surface from being illuminated by off-axis illumination in the first place; the 2D BEM model can only account for in-plane illumination. While measuring grating surfaces mitigates the effect of this on the comparison made, it is inevitable that some differences are still present.

The use of a 3D optical scattering model would alternatively enable closer agreement with the experimental measurement while avoiding the need to only measure grating surfaces, however such a model was not readily available initially, and the use of a 3D scattering model presents numerous additional challenges in the development of the CSI model. Even were these theoretical and programming issues resolved, the computational demands and associated hardware requirements of a 3D scattering model present a significant practical problem. For example, the 3s boundary source method (3sBSM) model is similar to the BEM scattering model in its approach to modelling scatter, and is implemented in MATLAB by the same authors [220]. However, for an adequately sampled 20 × 20 µm surface (434 × 434 points) illuminated by monochromatic illumination from a single direction, the 3sBSM model requires the use of a high-performance computer, requiring approximately 420 GB of RAM and taking 45 minutes to calculate the far-field scatter. In contrast, for a 20 µm wide surface, the BEM model obtains surface field values and far-field scatter in less than 1 second on a desktop PC, requiring under 0.1 GB of RAM. Producing CSI signal data from a scattering model not only requires running the scattering model multiple times (on the order of ~1000 times), but also increases RAM requirements, as the complex scattered field values must be stored in 3D arrays to preserve their locations in *k*-space.

Ideally the capability of the BEM-CSI model to accurately predict multiple scattering would have been verified experimentally, while in this chapter the vee-groove modelling results are only compared against results in the literature. It was however not possible to obtain a vee-groove to measure, and it was also difficult to obtain an alternative surface that produced scattering that is distinctly multiple scattering from a specific section of the surface. Such a surface would also have to be prismatic and simple with mostly smooth surfaces; it is likely a vee-groove is the most suitable candidate for this. The ability to model the response of a vee-groove by modelling geometrically the multiple reflections that occur is beneficial in confirming any result obtained [175]. It was also better to confirm the validity of the model through comparison to surfaces which can be readily modelled using other methods and that produce intuitive fringe spectra. This does however mean that the sinusoidal surfaces modelled are those that the foil model (see Chapter 3) can also model accurately; the opportunity to explore the region where the foil model begins to fail to accurately predict scatter is therefore missed.

Some discrepancies seen are attributed to a difference between the modelled illumination spectral density and that used in the instrument. The modelled spectral density is in general suitable for predicting the spectral density's effects on the CSI signal obtained, as shown in Figure 2.8. However, in future work including Chapter 6, the spectrum used was obtained from a measurement of instrument's illumination spectral density, indirectly obtained from the signal data of a low-NA measurement of an optical flat. Other discrepancies can be attributed to the fact that polarisation effects introduced by the instrument's optical elements are not considered in this CSI model, and that the illumination of the instrument is treated as TE polarised illumination. The effect of approximating the effects of polarisation is lower for lower NAs, but as resolving high spatial frequency details of surfaces requires larger NAs, a compromise had to be made when choosing an objective NA to measure with here.

## 5.7 Summary

In this chapter, a rigorous model of CSI based on BEM was presented. The model's theory was derived and its implementation details for interpolation in spatial frequency space discussed. The model is based on a BEM model which accounts for multiple scattering effects, and therefore the BEM-CSI model is a promising approach for generating fringes for arbitrarily complex surfaces. Evidence of the model's validity was provided by comparison to experimental measurements from a commercial CSI instrument for several surfaces, giving qualitative agreement. Modelling of a vee-groove was also performed to provide evidence towards the model's capability to account for multiple scattering. This model is used further in Chapter 6.

# Chapter 6: Measurement beyond the specular reflection limit with CSI

In Chapter 5, the theory and implementation of the BEM-CSI model was presented, showing that the model can predict fringes caused by multiple scattering, and demonstrating qualitative agreement with experimental coherence scanning interferometry (CSI) measurement results of sinusoidal gratings. In this chapter, the capability of optical surface topography measurement methods for measurement of steep and tilted surfaces through modelling using BEM-CSI is investigated. Of particular interest is the effect on the interference signal and measured topography when tilting the measured object at angles larger than the specular reflection limit (SRL) of the instrument, determined by the instrument's numerical aperture (NA). The results presented illustrate the capabilities, limitations, and modelling methods for interferometers to measure beyond the SRL.

The work in this chapter is a modified version of that published in [52] (journal paper), and also includes the preliminary results presented earlier at the SPIE: Photonics Europe 2020 conference [225].

## 6.1 Introduction

As discussed in sections 1.1 and 2.2, interferometry for surface topography measurement is used across many industries that rely on quality control of parts, ranging from machined automotive components to additively manufactured parts [37,104,105]. In recent years, technological enhancements to measurement sensitivity have extended CSI measurement capabilities to parts having surface slope angles that exceed the specular acceptance angle, defined for incoherent microscope illumination by $\theta_{NA} = \sin^{-1} A_n$, where $A_n$ is the variable for the NA of the objective. This capability is attributed to capturing the weakly-reflected light scattered at high scattering angles [35,36]. Reference [225] details the current state of the art and potential of high slope measurement with optical instruments, with further information detailed in section 2.6. This new practical capability poses a theoretical challenge for researchers in an applications area where the need is clear: instrument users need to

know under what circumstances measurement results for steeply-sloped surfaces are meaningful and have a quantifiable uncertainty. The answer to these questions will be highly dependent on the specific part type and measurement configuration, hence the need for appropriate physical models.

First, the capability of a CSI instrument to capture surface information beyond the SRL was preliminarily investigated through measurement of both a roughened flat and a blazed grating, considering both the form and texture components of the surface topography produced. In comparison to reference measurements, such as CSI measurements of the surface while untilted and from an atomic force microscopy (AFM) instrument, problems seen with the surface texture obtained from measurements as a surface is tilted are discussed. Using only a simple monochromatic surface scattering boundary element method (BEM) model, some intuition towards the effect of tilting a blazed grating is provided, in lieu of the full BEM-CSI model.

Next, the use of the BEM-CSI model [51] on the same blazed diffraction grating oriented at several tilt angles is demonstrated, as an informative example case. This object was specifically chosen for further study to represent several aspects of the steep-slope problem, including re-entrant features, a mixture of brightly-reflecting and weakly-scattering surface areas, and a known periodic structure [225]. The BEM-CSI model was chosen as it accounts for multiple scattering and other characteristics of complex surface topography and can use a point cloud representation of the part surface—an essential capability when dealing with re-entrant features. Prior publications involving this CSI model include [50,51]. Using the model, several characteristics of measurements of a chosen blazed grating are predicted, by gradually increasing the tilt angle until the mean plane of the grating exceeds the SRL determined by the NA of the objective. These results are also verified experimentally. Together these results confirm the capability of CSI for measuring steeply-sloped surfaces while clarifying the limitations of the results, leading to greater confidence when using CSI to measure surfaces with complex geometries.

# 6.2 Materials and methods

## 6.2.1 CSI instrument

A commercial CSI instrument[9] with specifications outlined in Table 6.1 was used for the experimental measurements. A detailed description of the working principle of CSI can be found in section 2.3 and elsewhere [84,105,110]. The optical process of a CSI instrument can also approximately be described using a three-dimensional (3D) surface transfer function, as given in section 3.2; more information on this "foil model" approach can be found elsewhere [74,119,159,185,247]. A CSI instrument first acquires 3D fringe data from a surface by taking images over a scan along the optical axis. To this fringe data, a surface reconstruction algorithm is applied, typically taken along the history of each pixel, to calculate the surface topography by using the coherence envelope and/or fringe phase information.

**Table 6.1.** Instrument specification

| Magnification | 20× | 50× |
|---|---|---|
| NA | 0.40 | 0.55 |
| Acceptance half-angle from $\arcsin(\mathrm{NA})$ | 23.6° | 33.4° |
| Field of view (using 1.0× zoom lens) | (0.43 × 0.43) mm | (0.17 × 0.17) mm |
| Optical resolution (Sparrow criterion) | 0.71 µm | 0.52 µm |
| Spatial sampling | 0.43 µm/pixel | 0.17 µm/pixel |
| Illumination central wavelength | ~0.56 µm | |
| Illumination full width at half maximum (FWHM) | ~0.11 µm | |
| Axial scanning step | 0.071 µm | |

## 6.2.2 Test samples

### Roughened flat

The first surface measured was a randomly roughened metal flat, with an *Sq,* areal root-mean-square roughness parameter, of 237 nm evaluated over six regions with standard

[9] Zygo Nexview™ NX2

deviation of 17 nm. This surface was measured using the 20× lens as specified in Table 6.1. The surface parameters stated here and in section 6.3.1 are calculated from the surface texture, obtained from the measured topography from the following procedure: Gaussian S-filter with a nesting index of 2.5 µm; levelling by rotation of least-squares mean plane; and Gaussian L-filter with a nesting index of 250 µm.

## Blazed grating

The second surface measured was a blazed grating (Thorlabs GR13-0305 visible ruled reflective diffraction grating) with a groove spatial frequency of 300 lines per millimetre. The grating substrate is made of soda lime glass, with an aluminium reflective coating. Using a measurement of the sample with an AFM instrument in tapping mode, the grating was found to have a pitch of approximately 3.4 µm, and a peak-to-valley height (PV) of approximately 0.2 µm, as shown in Figure 6.1; these parameters are used for modelling the grating. The AFM instrument used a tip with a maximum radius of 12 nm, obtaining topography over a (10 × 10) µm region with sample spacing of 26.1 nm, and with a Z sensor noise level of around 30 pm root-mean-square.

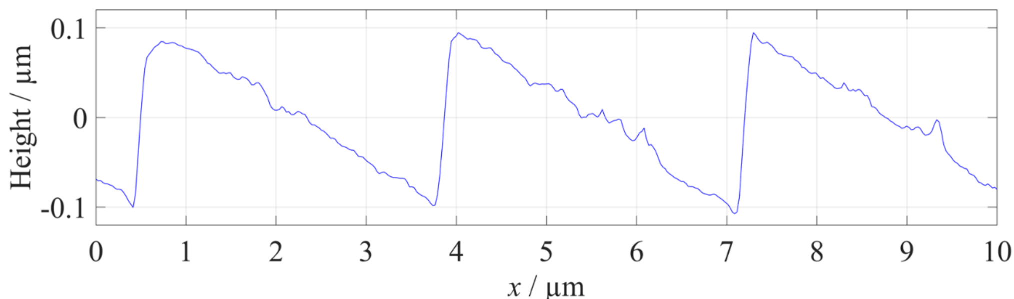


**Figure 6.1.** The profile of the GR13-0305 blazed grating as measured by an AFM instrument.

A periodic grating was chosen for measurement for several reasons. Such surfaces with a single characteristic spatial frequency can be considered as representing one of the many spatial frequency components of a more complex surface. The far-field scatter/diffraction pattern of a grating can be accurately modelled with a variety of methods, and locations of scatter can be predicted analytically. Experimental measurement of a sample at different tilt angles is made much easier with a grating due to the similarity of the surface across the sample, allowing for tilted measurements to be taken from different regions of the sample, rather than requiring finding or creating

fiducials visible at any surface tilt angle. The prismatic nature of such surfaces means that for light incident perpendicular to the grooves, the scatter outside the plane of incidence is negligible. This feature allows the use of a two-dimensional (2D) surface scattering model to simulate the far-field scatter pattern without significant loss of accuracy. Here, this 2D model corresponds to an 3D optical system with a slit pupil such that the observation can only be carried out within the plane of incidence, and the illumination is equally limited.

A blazed grating was specifically considered in this work as the asymmetric profile produces asymmetrically distributed scatter patterns. This asymmetry allows inspection of the differences in the fringes and topography formed that occur when the surface is tilted, for example, by a constant amount but in each direction. As the scatter is asymmetric, it is expected that more scatter, and therefore more energy, would be lost in one of the two cases. Understanding results produced from such a surface is a valuable step towards obtaining and understanding more general results.

## 6.2.3 Experimental methods

### Roughened flat

The roughened flat is measured with the 20× lens (Table 6.1) while tilted by 30°, to examine the effect on the surface topography information obtained when the collection of the specular scatter is prevented, here for an effectively randomly rough surface. It is expected that useful topography information can still be obtained from both the surface form (determined by the tilt) and the surface texture.

### Blazed grating

The blazed grating is measured with the 50× lens (Table 6.1) at different tilt angles, in one of two cases shown in Figure 6.2; note that at 0° tilt angle, the L and R cases are mirror images of each other. In this way, the L and R cases indirectly represent a rotation of the grating in both the positive and negative directions.

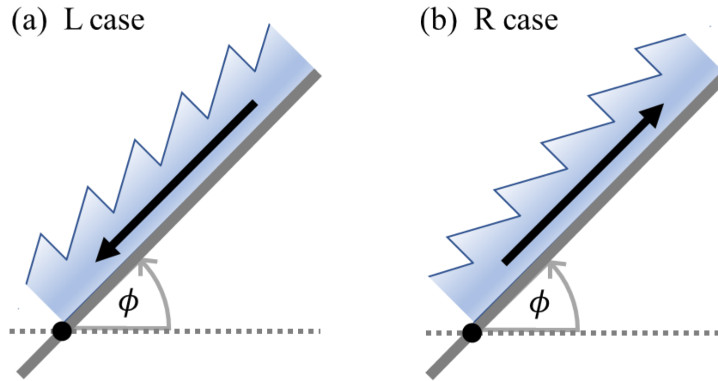


**Figure 6.2.** Diagram presenting the two measurement cases used for measurement of the blazed grating while tilted at angle $\phi$, where the black arrow denotes the blaze direction of the grating. (a) L case: the sample is tilted at an angle $\phi$ with downward facing blaze, (b) R case: the grating is tilted at an angle $\phi$ with upward facing blaze.

First, the grating is measured when untilted, and when tilted at 45° in both the L and R cases, and the topography obtained, inspected, and compared.

Following these preliminary results, the grating is then measured in the L and R cases at tilt angles between 0° to 50° in increments of 10°, with the fringes (signal data) inspected and compared. Estimated topography is then obtained for the tilt angles that are beyond the objective lens's acceptance half-angle. The fringe data obtained by the instrument is stored as a 3D numerical array. By using a 3D Fourier transform, the fringe spectrum in the spatial frequency domain ($k$-space) is obtained. The high spatial frequency fringe components that are of interest and contribute to surface reconstruction are isolated before display through application of a band-pass filter (BPF) as described elsewhere [247].

Note that the surface homogeneity of the grating was confirmed to allow comparison of measurements from different regions as though they were taken from the same region. Repeat measurements at specific tilts were taken to confirm that the results obtained at that tilt were independent of the measurement location.

## 6.2.4 Modelling methods

### Monochromatic modelling

Blazed gratings produce an asymmetric distribution of scatter. Consequently, under the Abbe theory of imaging, measurements of the gratings taken at the same absolute tilt

but in each direction are expected to produce different topography results. To quantify a blazed grating's scatter distribution, the BEM scattering model, described in section 4.1 and 4.2, was first used. This 2D BEM model was used to simulate the scattering by a blazed grating at different tilt angles when illuminated by a monochromatic plane wave at normal incidence. Intensity values are obtained from both s- and p-polarised illumination, and the mean of the two taken, to represent the result of unpolarised illumination. As previously stated, the model is limited to modelling of surfaces of homogenous refractive index with surfaces fully described by surface boundaries that lie on the plane of incidence ($x$-$z$ plane).

### BEM-CSI modelling

To better model the measurement process, the rigorous BEM-CSI model described in detail in Chapter 5 is used to simulate measurements of the blazed grating at different tilt angles (described in section 6.2.3) by the CSI instrument (described in section 6.2.1), using the 50× lens (described in Table 6.1). For illustrative purposes, the modelling process is illustrated in Figure 6.3, using a blazed grating surface as input. To summarise: in this model, the incident broadband illumination is decomposed into a combination of monochromatic Gaussian beams that illuminate the surface at specific incident angles. For each choice of illumination wavelength and incident angle, scatter is obtained using an algorithm based on a BEM for surface scattering [261], and the results of this are combined. Following a basic aberration-free imaging process via back propagation of the scatter, while accounting for the limited NA, a CSI fringe image can be synthesised [51,185]. See sections 2.5 and 5.2 for the mathematical theory used.

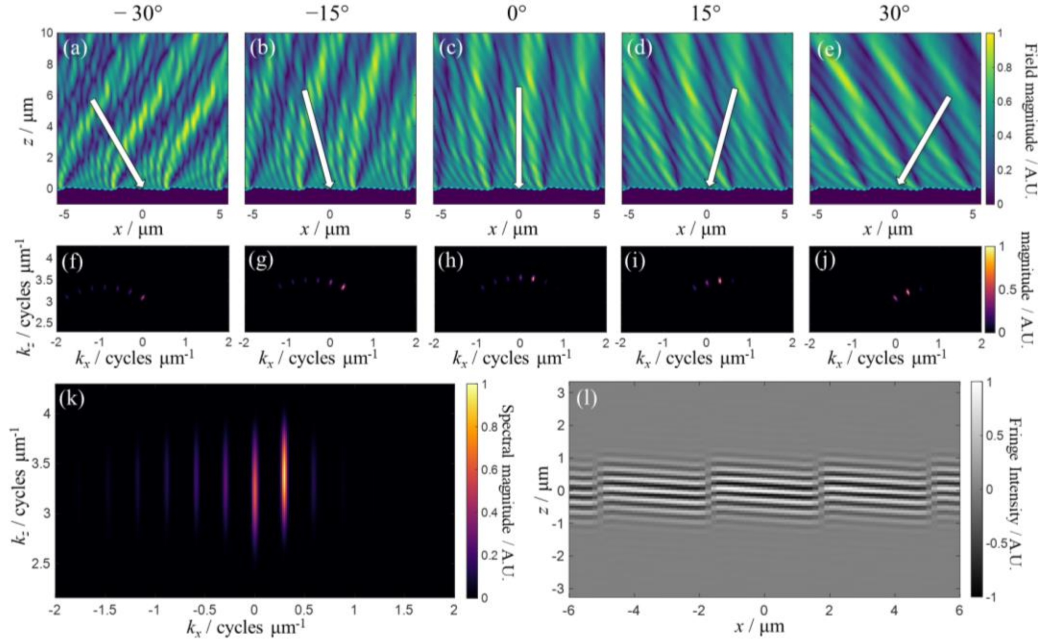


**Figure 6.3.** CSI fringe generation based on a BEM scattering model. (a-e) Scattered field due to monochromatic illumination at different angles, with the incident direction denoted with a white arrow; (f-j) the magnitude of the far-field scatter in *k*-space for the corresponding incident angles used in (a-e). (k) The combination of *k*-space results given in (f-j) but from multiple angles and multiple wavelengths, weighted by the spectral density used, considered the fringe spectrum. (l) The modelled fringes obtained from the real part of the inverse Fourier transform of the fringe spectrum (k).

This 2D model is limited to consider surface profiles and their scatter in the plane of incidence (*x*-*z* plane), corresponding to an instrument with a slit pupil. However, the experimental measurement uses an instrument with a circular pupil and illuminates the surface with a right circular cone of illumination. Therefore, to allow for qualitative comparison with experiment, this limitation of the BEM-CSI model is mitigated through the measurement of gratings or prismatic surfaces, due to their strong scattering characteristics into the plane into which BEM is limited. As the CSI instrument in the experiment uses circularly polarised illumination with a small radial component also present due to the objective lens' high NA, both s-polarisation and p-polarisation illuminations are considered using the BEM model. The modelling results of the two linear polarisations are displayed separately.

The blazed grating profile described in section 6.2.2 is chosen for modelling, considered in both the L and R cases, and across the various tilt angles as described in section 6.2.3. The modelled profile, shown in Figure 6.4, combines the surface texture measured by an AFM instrument along the longer facet (given in Figure 6.1) with an ideal smooth

blazed grating profile. Relative to the axis along which the pitch and surface width is measured ($x$-axis), the longer and shorter facets are inclined at 3.6° and 48.0°, respectively.

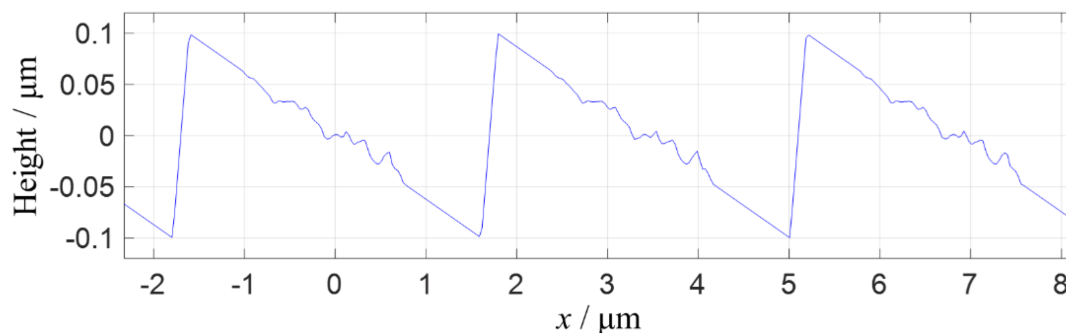


**Figure 6.4.** Geometry of the profile used for modelling, where the central region of each longer facet has had surface texture added digitally, with the texture obtained from an AFM measurement. Note that the data aspect ratio of the axes is adjusted for easier display.

## 6.3 Results and analysis

### 6.3.1 Roughened flat topography

Despite the 23.6° acceptance angle of the 20× objective lens used, in Figure 6.5(a) and (d) the instrument is shown capable of obtaining topography from the measurement of the 30° tilted roughened flat, providing form data with surface inclination agreeing closely with the chosen tilt. Similar results on CSI instrument capability are given in [35,36]. Clearly, even the loss of the specular component of the scatter does not prevent useful topography information from being obtained, and that this topography information must originate from the non-specular scatter captured.

Presented in Figure 6.5(b) is the surface texture information obtained from the surface while tilted, as per the approach outlined in section 6.2.2. Measurements of this tilted surface from six different locations provide a $Sq$ of 246 nm with a standard deviation of 34 nm, which is similar to that obtained at 0° tilt (237 ± 17 nm, detailed in section 6.2.2), and this similarity is shown in Figure 6.5 between plots (b) and (c). However, comparison of the surface topography from the same location while at different tilts is difficult as it is a random surface, and therefore it cannot be concluded from this result alone whether or not the surface texture has been accurately measured. To investigate how the loss of scatter affects the measured surface texture, measurement of a grating which contains periodic and well-defined surface structure is needed.

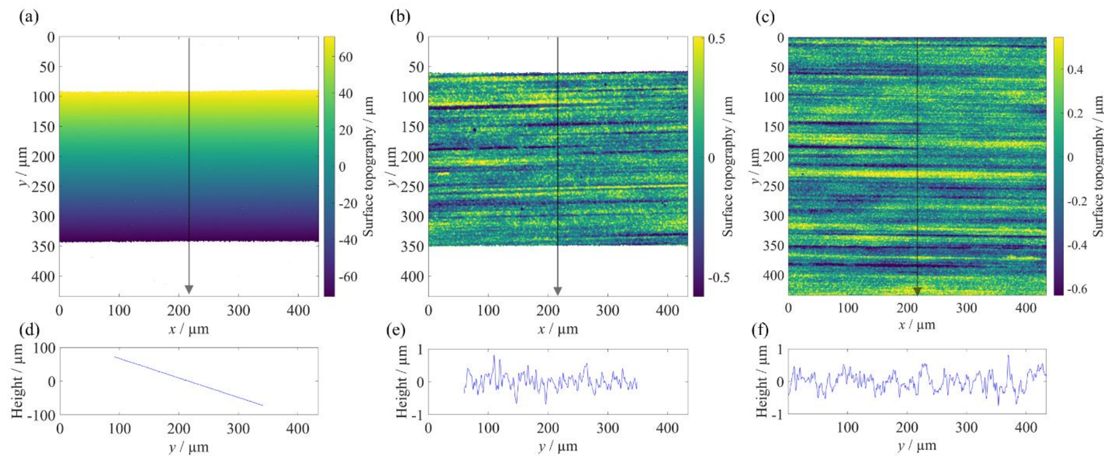


**Figure 6.5.** Topography results from a 20× lens of the roughened flat (a,b,d,e) when tilted at 30°, and (c, f) when untilted. Shown is the (a) raw topography obtained when the surface was tilted, (b) the topography after levelling with the least-squares best fit plane, and (c) the raw topography obtained when the surface was untilted. Plots (d-f) are the north-south profiles taken from plots (a-c) respectively, as marked by the black arrows.

## 6.3.2 Blazed grating topography

Shown in Figure 6.6 are the topography results from the measurement of the blazed grating using the 50× lens corresponding to the L case at 0° (L0), the L case at 45° (L45), and the R case at 45° (R45), as defined in Figure 6.2.

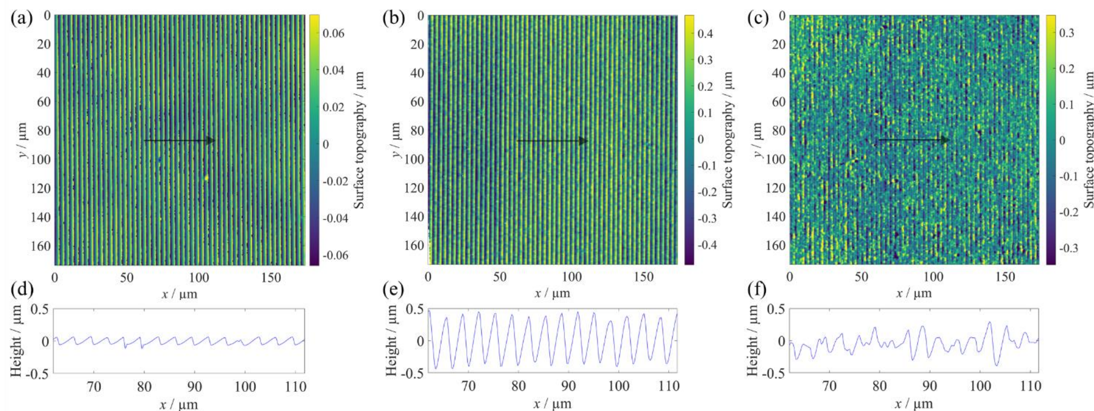


**Figure 6.6.** Topography results after plane form removal from a CSI measurement of a GR13-0305 blazed grating with tilting arrangements of (a) L0, (b) L45, and (c) R45, using a 50× lens; corresponding profiles are shown below in plots (d-f). These profiles are taken along and in the direction of the lines marked by the black arrows.

These results show that the texture information obtained from the blazed grating is influenced significantly by tilting, and the tilting direction chosen. From the 0° results

shown in Figure 6.6(a), the grating's blazed profile is shown, however, the PV heights across the profile are approximately 0.12 µm, below the 0.2 µm PV height measured by the AFM instrument. This reduction in height is expected and occurs due to the spatial frequency transfer characteristics of the CSI instrument [74,88,142,281], with a transmission magnitude at 0.3 $\mu m^{-1}$ of approximately 70% [159]. Further reductions to the transmittance are expected as the instrument will have had some reference mirror defocus present while the measurements were taken [119].

Despite being measurements of the same surface and at the same absolute tilt, the results from case L45 and case R45 differ significantly; the topography from case L45 retains the overall blazed structure, while case R45 provides significantly less visible structure. This difference occurs due to the asymmetry of scatter from the grating. The simulated far-field scattering/diffraction of an ideal blazed grating with geometry matching that of the GR13-0305 under normally incident monochromatic plane wave illumination of wavelength 580 nm (the central wavelength of the CSI system) is shown in Figure 6.7. Clearly, more scattered power is collected within the aperture and a high SNR is achieved for the L45 case (Figure 6.7(b)) compared to the R45 case (Figure 6.7(c)).

Although the measurement results in the L45 case retain a blazed grating structure with the correct pitch, the PV height of the blazed structure is approximately 0.82 µm, around four times larger than the value from the AFM measurement. Clearly, the CSI measurement of the L0 case (0° tilt) provides a result that is much closer to the reference measurement. This result is consistent with the scattering modelling in Figure 6.7(a) where more diffraction orders are captured at a high SNR within the NA limit.

However, from these results it is not possible to entirely understand why the measured grating's PV height and surface height variation are amplified in cases L45 and R45. It is possible that to explain this, a rigorous fully 3D CSI model that considers polychromatic incoherent illumination is required, an extension of the 2D rigorous CSI model [50]. Such a model could be based on the recently reported boundary source method surface scattering model [220].

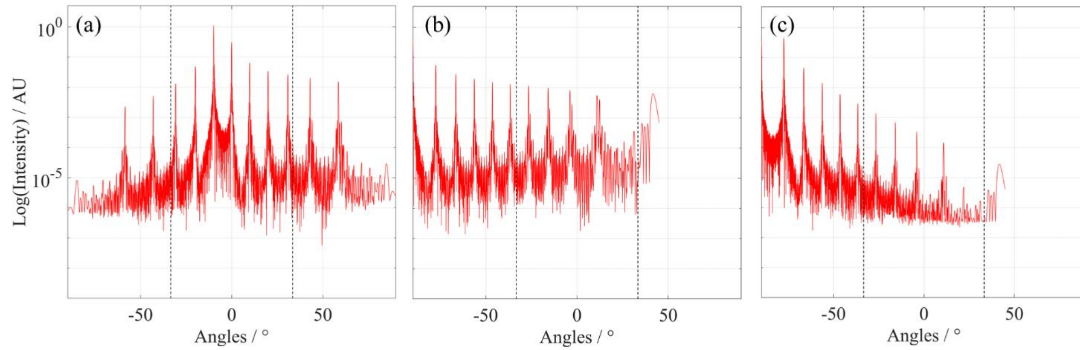


**Figure 6.7.** Modelling results for scattered intensity from the blazed grating shown in Figure 6.6, for the mean intensity obtained from both s- and p-polarised monochromatic illumination of wavelength 580 nm, with tilting arrangement (a) L0, (b) L45, and (c) R45. The region between the dashed black lines denotes the ±33.4° acceptance cone for the 50× lens (0.55 NA).

### 6.3.3 Fringe generation

The blazed grating in both the L case and the R case are tilted at a range of angles, as previously described in section 6.2, and fringes obtained as a result, displayed in Figure 6.8 and Figure 6.9. On average, less energy is captured as surface tilt angle is increased [225], with the R case losing more energy compared to the L case as a function of increasing surface tilt angle. To optimise the signal-to-noise ratio for each tilt angle in the experimental case, the illumination light level of the CSI instrument was adjusted for each measurement. Consequently, meaningful comparison between the maximum absolute fringe intensities at different tilt angles is difficult. Therefore, the experimental data has been normalised so that the maximum fringe intensity in each plot is unity. Conversely, as the illumination in the model remains constant, the modelled fringes at all tilt angles can be normalised by the same factor, chosen so that the maximum fringe intensity from the 0° tilt angle case is unity. The scale covered by the greyscale colourmap in each plot shrinks to ensure fringes remain visible, visually obscuring the overall reduction in fringe contrast with increasing tilt angle but emphasising the relative variation in fringe contrast at each tilt angle.

Modelled results using s-polarised and p-polarised illumination are shown in both Figure 6.8 and Figure 6.9. The results from both polarisation states provide similar qualitative agreement with the experimental result. Visually, the p-polarisation result provides a slightly better agreement. However, due to limited time, a detailed

investigation and discussion regarding the effects of polarisation is omitted here and is left for future work. For the L case (Figure 6.8), fringes along the longer facets fade out as the surface tilt angle increases, whereas fringe packets, reminiscent of a point spread function (PSF) eventually appear at the sharp-edged shorter facets. A PSF obtained using the Foil model is visually compared with the fringes from this facet in Figure 6.10, and a PSF obtained from experimental characterisation of the CSI instrument can be seen in both Figure 3.6, and in Figure 3 of [159]. At 50° tilt angle, these short facets, shorter than half the central wavelength, act as discrete surface points and produce fringes that appear as a tilted train of PSFs. In the R case, shown in Figure 6.9, a similar effect is seen; as tilt angle increases, the fringe contrast reduces for the long facets, and PSF-like fringes form for the short facets. However, at 40° and 50°, fringes form along the longer facets due to the profile's surface texture.

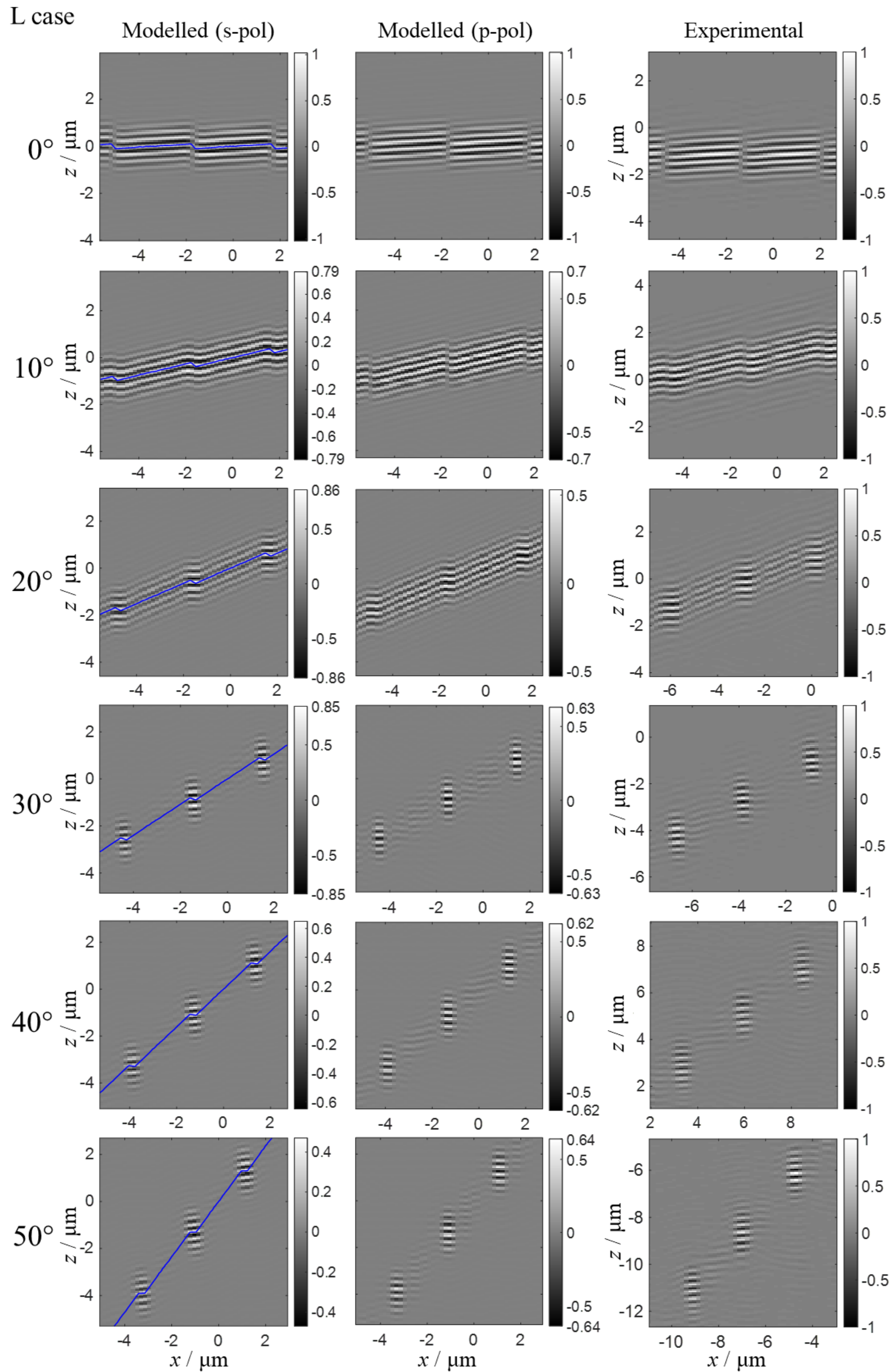


**Figure 6.8.** Modelled (left and middle column) and experimental (right column) fringes of the L case blazed grating at different tilts, where modelled fringes are produced from s-polarisation (left) and p-polarisation (middle) illumination. The solid blue line represents the surface profile used in the model. The grayscale variation represents variation in intensity, with arbitrary units used as described in section 6.3.3.

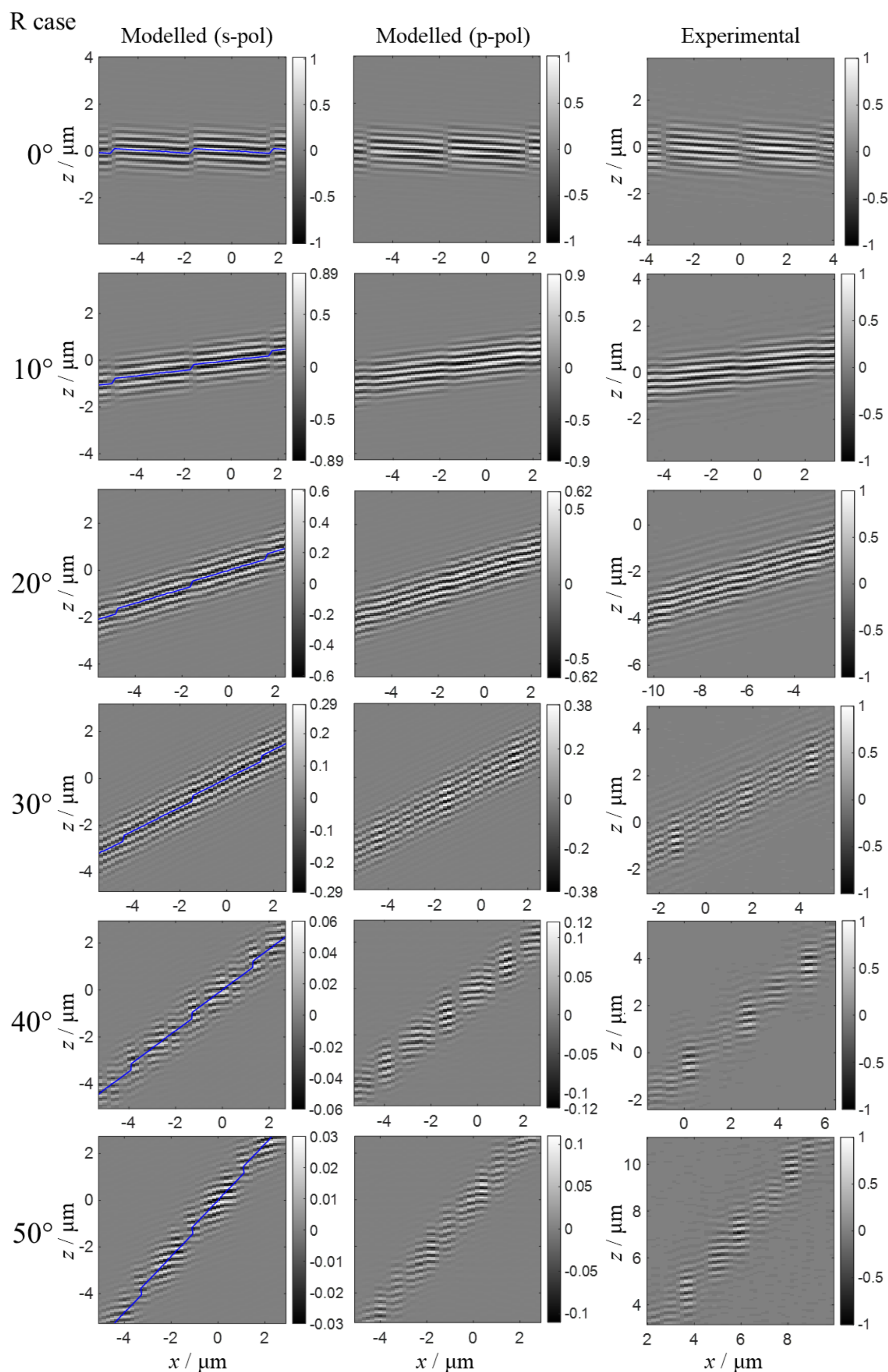


**Figure 6.9.** Modelled (left and middle column) and experimental (right column) fringes of the R case blazed grating at different tilts, where modelled fringes are produced from s-polarisation (left) and p-polarisation (middle) illumination. The solid blue line represents the surface profile used in the model. The grayscale variation represents variation in intensity, with arbitrary units used as described in section 6.3.3.

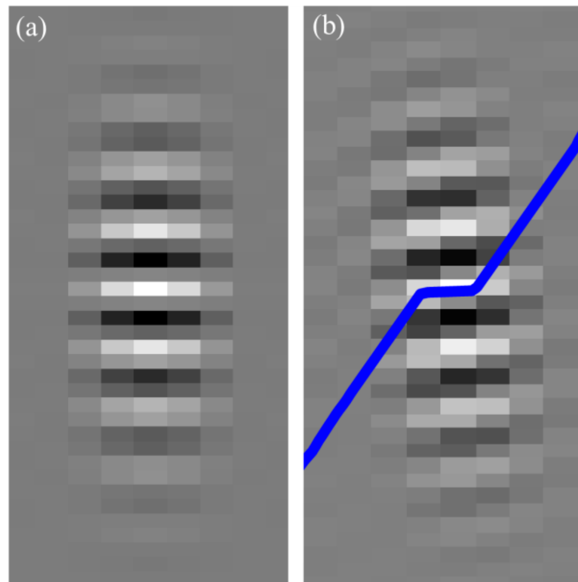


**Figure 6.10.** Visual comparison of (a) the PSF obtained from the Foil model associated with an ideal CSI instrument, and (b) modelled fringes from the BEM-CSI model near to the shorter facet for the L case blazed grating tilted at 50° , as seen in the bottom left of Figure 6.8.

Both the L and R modelling results at 50° tilt angle have reduced fringe contrast from the long surface facets. The long facet has a slope of 54° and 46° for the L50° and R50° case respectively, both easily exceeding the arcsine of the NA of the instrument (33.4°). Under the Huygens-Fresnel principle, this phenomenon can be understood as each point along the longer facets acting as a point source, and interfering with each other, such that specular reflection dominates the scatter, causing the majority of the scatter to be lost, and that which is visible appears to be produced by the fine (nano-scale) surface texture.

Both the L50° and R50° results also produce PSF-like fringes around the shorter facet. The shorter facets, being only 0.27 µm long, can be considered points of discontinuity on an optical scale for a central illumination wavelength of 0.56 µm. In the L50° case, the shorter facets can be considered as strong under-resolved point sources when illuminated from above, as the shorter facets are almost parallel with the horizontal. In the R50° case, the sharp edge at the junction of the shorter and the longer facets may diffract light back towards the lens. This type of surface discontinuity also produces similar PSF-like fringes. While scatter from high spatial frequency surface texture along this shorter facet will contribute to this, the BEM-CSI model has PSF-like fringes appear even for gratings with perfectly smooth facets. From the modelling results, it

appears that scatter from high spatial frequency surface texture along the longer facets will also generate fringes at large surface tilt angles.

From these modelled and experimental results at higher surface tilt angles, the train of PSF-like patterns obtained clearly allows for the tilt angle of the surface to be acquired, i.e., in this case, allowing for the surface topography to be obtained. For rough surfaces, and where phase information may be less reliable, it is good practice in CSI to rely only on the fringe envelope to provide a surface estimate [110]. As the periodicity of the surface is also obtained from these patterns, it can be concluded that at least some high spatial frequency surface texture can be captured when the surface is tilted beyond the acceptance angle, and even when all facets have inclination greater than the acceptance angle. As fringe data can be recorded even when all facets have an inclination greater than the acceptance angle, it should be possible to retrieve surface topography with a certain degree of accuracy. However, meaningful discussion on the effect of tilt angle on the obtainable surface topography requires consideration of the height estimation process.

### 6.3.4 Fringe analysis

Typical surface reconstruction methods rely on evaluating the height at each lateral position, by considering at each camera pixel the interferogram formed along the optical axis over the scanning process. The axial profiles from the modelled profile L50° and R50° case, shown in Figure 6.11, and the experimental case, shown in Figure 6.12, are investigated.

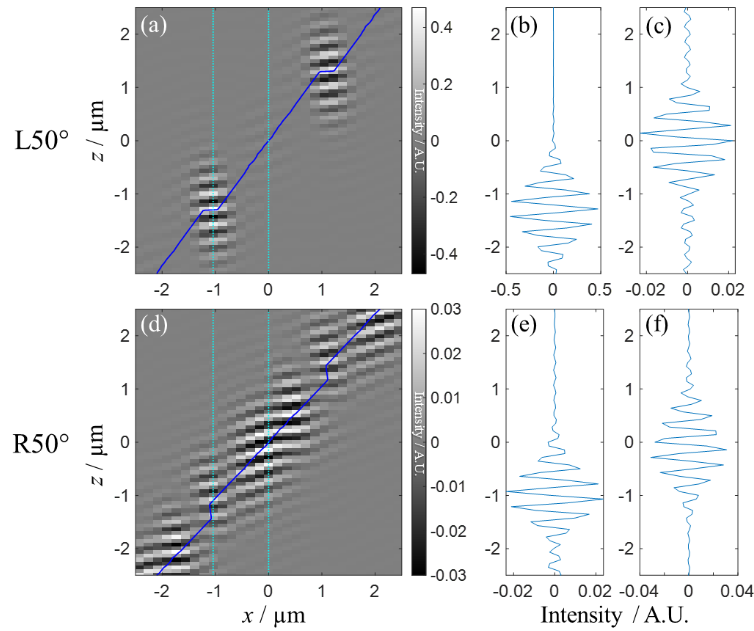


**Figure 6.11.** Modelled fringes from the modelled blazed grating profile tilted at 50° under s-polarisation illumination in the (a-c) L case, and (d-f) the R case. The solid blue line in (a) and (d) represents the surface topography used in the model, while the two dotted cyan lines are the lines along which fringe profiles are obtained. The $x = -1$ µm and $x = 0$ µm profiles are shown in (b,e) and (c,f) respectively. Note the change in intensity range across all plots.

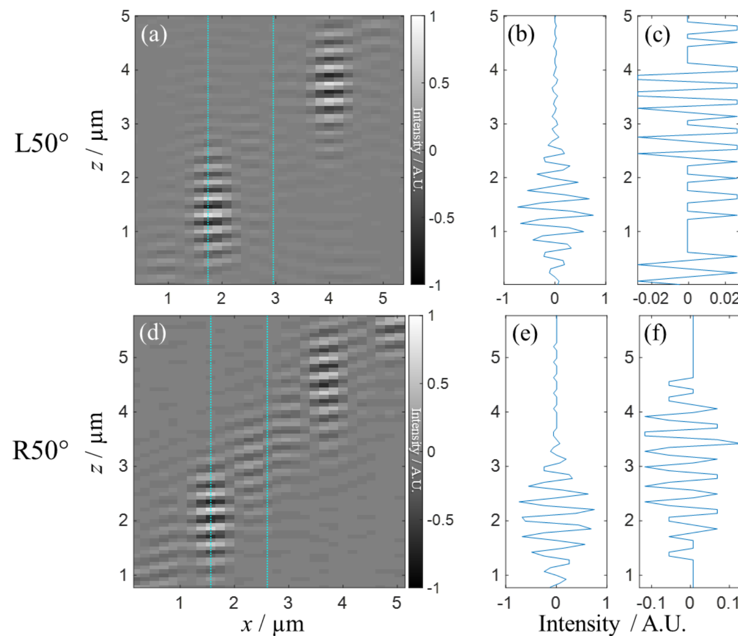


**Figure 6.12.** Experimental fringes from the blazed grating tilted at 50° in the (a-c) L case, and (d-f) the R case. The two dotted cyan lines seen in (a) and (d) are the lines along which fringe profiles are obtained. The left and right profiles are shown in (b,e) and (c,f) respectively. Note the change in intensity range in (c) and (f).

The differences seen between the modelled and experimental fringes, which are larger in the R case, can be attributed to noise present in the experimental measurement, due to the low proportion of scattered light captured from the surface. The differences are also likely due to imperfections in the grating, compared to that used in the model, and the inability of the model to fully imitate the actual measurement process (the slit aperture configuration of the model).

The topography obtained from the experimental measurement of the blazed grating tilted at 50° in the L and R cases can be seen in Figure 6.13, with results very similar to that of the grating at 45° tilt shown previously in Figure 5(b,e) of [225] and in Figure 6.6. These results use only the coherence profile and do not depend on the phase data present in the fringes.

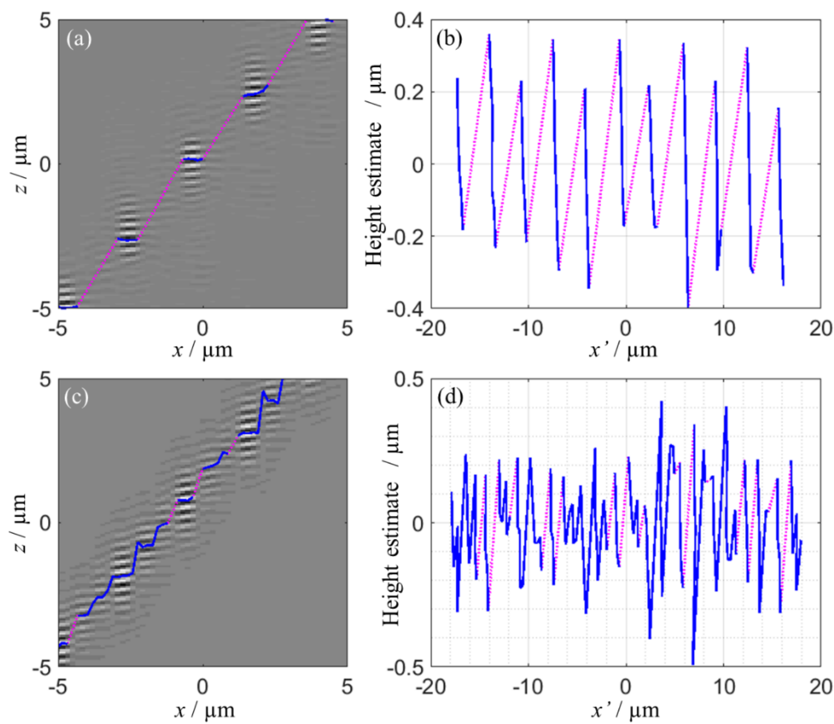


**Figure 6.13.** Topography estimate (coherence profile) obtained from the experimental measurement of the blazed grating tilted at 50° in (a,b) the L case, and (c,d) the R case. The topography with confidence above a set threshold is denoted with the blue solid line, and in regions where height data falls below this threshold a dotted magenta line instead connects with straight lines the regions of confident height data. In (a,c) the topography estimate is displayed on top of the corresponding band-passed fringes, and in (b,d) the topography is rotated 50° to remove the form (levelled).

The original geometry of the blazed grating can be seen in Figure 6.13 to mostly be lost. In the L case, this occurs because the shorter facet's width (≈ 0.27 μm) is small enough that the PSF's width exceeds it, for the illumination used. Therefore, the PSF-fringes provide a false "facet width" dependent primarily on the confidence threshold of the height algorithm; this limitation would occur for any diffraction limited optical system with similar NA and illumination. Depending on the algorithm and confidence threshold chosen, height information may be reported along the magenta lines in Figure 6.13(b) through the assumption that the regions of confidence are likely joined by a surface close to a straight line, despite the lack of useful fringe data. This is the cause of the height results reported in Figure 5(b,e) of [225] and in Figure 6.6. In the R case, the high spatial frequency micro- and nano-scale surface texture is the source of a significant proportion of the captured scatter, and combined with the low signal-to-noise ratio, and a similar PSF issue, the blazed grating surface structure is almost lost.

## 6.4 Conclusion and discussion

Surface measurement based on optical imaging relies on using an objective lens to collect diffracted or scattered light from the surface of an object. A mirror-like flat surface cannot be measured if the surface is tilted at an angle greater than the SRL given by the NA because the dominant specular reflected light cannot be collected by the objective lens. To measure a surface tilted beyond the SRL of the objective lens, the surface must contain structures that cause light to be scattered backwards and collected by the lens. The complex scattering amplitude is then holographically recorded through the 3D interferometric imaging process to generate the 3D fringe data [185] from which surface topography is reconstructed.

Through BEM-CSI modelling and experimental results, it has been demonstrated that even when the mean plane of the blazed grating is tilted beyond the NA limit, fringes with the shape of CSI point spread function can be generated due to diffraction and scattering by surface structures such as the sharp edges, local facets smaller or comparable to the optical scale, fine surface textures, and other surface irregularities. Therefore, despite the loss of specular scatter due to surface tilt, with sufficient micro/nano-scale surface structures, it is possible to obtain useful surface information from the non-specular, backward scattered light.

One specific limitation of the work is that the blazed grating chosen contains features that are small relative to the mean wavelength of illumination, and thus small relative to the PSF width. This is illustrated in Figure 6.14, where for the 50× lens the lateral spatial sampling and the axial scanning step spacing are shown as dashed gridlines, alongside the sparrow criterion and modelled PSF. As the grating is tilted, the shorter facets and longer facets are sampled differently due to the rectangular "voxels", which contain the captured intensity information, aligning differently with the facets at different tilt angles. While the sampling processes are naturally very different between the lateral and axial directions, treating the surface as being "sampled" by these rectangular voxels is useful in understanding the fringe results obtained. To some degree, this "dilution" of the surface across the rectangular voxels is a cause of the differing topography results at each tilt angle, for the L and R cases. However, it is unclear whether this also extends to surfaces with larger amplitudes or those comprised of different spatial frequencies; more investigation across a wider range of surfaces is required. Note that this limitation is similar to the "interferometric slope effect" discussed elsewhere [232].

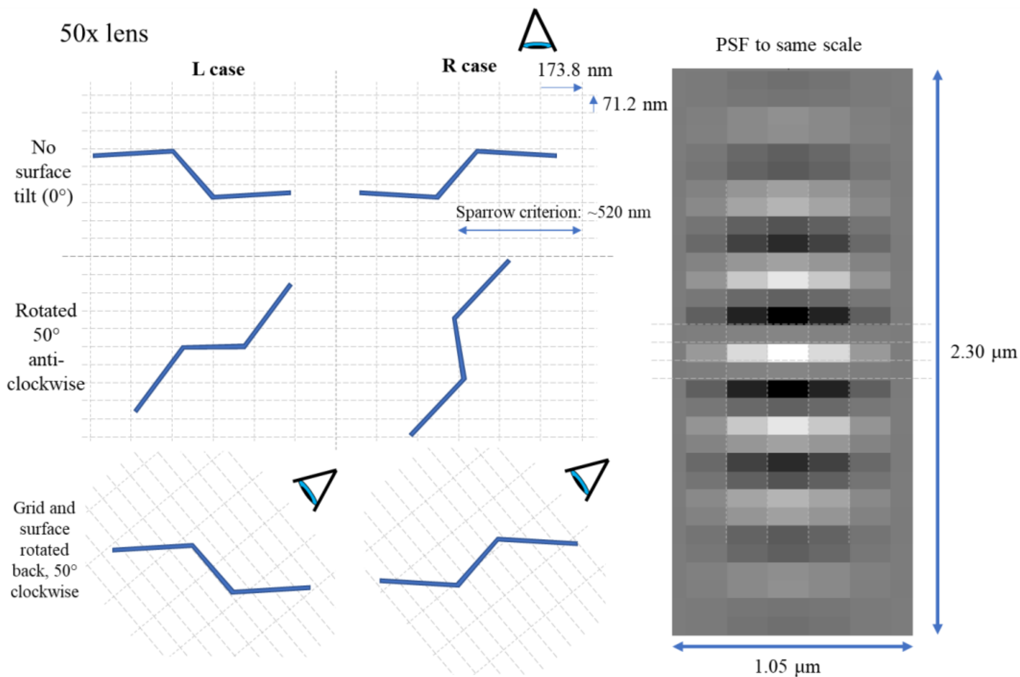


**Figure 6.14.** Diagram of the relative sizes of the blazed grating shorter facet and the instrument sampling spacing for different measurement conditions, alongside a PSF of the instrument to scale. Parameters used are listed in Table 6.1. Note that the lateral resolution for this objective lens, represented in this figure by the sparrow criterion ($0.5\ \lambda/A_n$), is determined by the optical resolution, as here the optical information collected is sufficiently sampled by the imaging sensor. The PSF shown is generated using the Foil model, obtained by inverse Fourier transform of a modelled 3D transfer function of a distortion-free instrument.

However, limitations in the BEM-CSI model's capabilities also restrict what virtual experiments can be performed with confidence, and these limitations are likely the cause of some of the discrepancies still seen for the blazed grating between the modelled and experimental results. As previously noted in section 4.1, section 5.1, and earlier in this chapter; the model is 2D and can only consider 2D surfaces with both the illumination and scatter similarly limited to the same 2D plane. This limitation is mitigated by only considering prismatic surfaces for modelling. The model is also limited to a choice of orthogonal linear polarisations, and therefore cannot properly replicate the CSI instrument's circular polarised illumination; both the lens and imaging process is also considerably simplified compared to reality.

Although the size of relevant surface features being comparable to the central illumination wavelength allows faster modelling of the surface (compared to surfaces with larger/wider features), such surfaces require large magnification lenses to resolve the small features, typically also accompanied by larger NAs. While this somewhat

increases modelling time due to the larger range of illumination and observation angles considered, the primary disadvantage is that fringes obtained from such larger NA objective lenses have a greater dependence on the polarisation of light (and its interaction with the surface chosen) due to the wider range of incident illumination angles used. When polarisation cannot be handled fully in a model, the use of a larger NA can increase the differences seen between the model and experiment.

In the future, a more developed model, perhaps based on the 3D boundary source method optical scattering model [220], could be used to investigate a wider range of surfaces and better define the domain within which the conclusions presented here also remain accurate.

## 6.5 Summary

In this chapter, an experimentally-verified BEM-CSI model was used to investigate several characteristics of measurements of a blazed diffraction grating, by gradually increasing the tilt angle until some areas exceed the specular reflection limit determined by the numerical aperture of the objective. At high tilt angles, it was found that the sharp edges with undercuts still provide strong signals, and appear as plateaus in the topography data, with a width corresponding to the width of the point spread function of the instrument. Consistent with current practical guidance when using CSI instruments for very high slope angles, it was also found that useful phase information is lost and that the optimum results are obtained using coherence-based data evaluation methods. Finally, it was confirmed that in many surface areas, there is sufficient fine-scale surface texture to provide useful overall form information from the non-specular scattered light.

# Chapter 7: Conclusions and future work

In this chapter the conclusions of the thesis are summarised and compared to the aims and objectives of the work as given in section 1.2, contributions to the field are explicitly noted, and the areas for future work are described. The contributions to science during the PhD consist of the key results, findings, and outputs produced and are listed as part of the summary of conclusions.

## 7.1 Thesis summary

### 7.1.1 Aims and objectives

The problem tackled by the thesis, the industrial and academic motive to tackle it, the aims and objectives selected to investigate and address the problem, and the novelty of the chosen approach, were presented in Chapter 1. The aims were:

1) To advance methods that enable extending the range of surface slopes that can be reliably measured by optical surface topography measurement
2) To investigate the reliability of the current capability

This was to be done primarily through the development and use of instrument models, and with a focus on coherence scanning interferometry (CSI). The objectives were to:

1) Characterise and capture how an instrument responds to surface spatial frequencies, allowing for topography error on surface slopes caused by lens aberration to be mitigated
2) Develop and verify a CSI model that can accurately generate fringes for complex surfaces, which may contain slopes beyond the specular reflection slope limit, including accounting for any multiple scattering present
3) Demonstrate and improve understanding on the effect of surface slope on CSI fringes and topography, including slopes beyond the specular reflection slope limit

These objectives were addressed in the subsequent chapters: Chapter 3 addresses objective 1, Chapter 4 and Chapter 5 address objective 2, while Chapter 6 addresses objective 3.

### 7.1.2 Contribution to the field

In Chapter 2, the relevant state of the art was discussed, and the accompanying background presented. This includes an overview on metrology, surface topography metrology, and on CSI instrument principles and capability. A review of CSI models in the literature was given, and the scalar scatter theory relevant in subsequent chapters derived. The state of the art on the capability of optical surface topography measurement methods for measurement of steep and tilted surfaces was reviewed, with a focus on CSI measurement and the effect on the measured topography when tilting the measured object at angles larger than the numerical aperture (NA) slope limit (a.k.a. the specular reflection slope limit) of the instrument. This work represents a contribution to the field in the form of a summary review.

In Chapter 3, an approximate CSI model based on the Kirchhoff approximation (KA) was introduced, in which the instrument response of a CSI instrument can be described by a three-dimensional (3D) surface transfer function (STF). The 3D STF is an informative metric for quantitatively evaluating and comparing the performance of an optical surface measuring instrument in the linear regime, including the instrument's response to various slope angles and spatial frequencies. Real optical 3D imaging instruments always exhibit some degree of aberration, which in a CSI instrument can cause various topography errors and other slope- and spatial frequency-dependent errors in the height data; the effects of aberration are seen in an experimentally obtained STF as non-zero phase. In Chapter 3, an instrument's STF was obtained through measurement of microspheres and an inverse filter (IF) generated from the STF. The filter provides error correction at a fundamental level by modifying the raw 3D fringe data prior to surface reconstruction and any post-processing. From measurements of freeform surfaces, the topographies obtained from before and after compensation by an IF were compared both to each other and to measurements of the surfaces by a traceable contact stylus instrument, demonstrating a reduction in topography errors due to the IF.

The first contribution of this work is the experimental verification of the underlying approximate CSI model that allows for the response of an instrument to be characterised by a 3D STF. The second contribution is the demonstration and experimental verification of a novel surface topography error correction method for CSI that compensates for the effect of lens aberration through filtering signal data prior to

surface reconstruction and any post-processing. These contributions included the following publications [119,144,159,244], and was performed in collaboration with Dr Rong Su.

In Chapter 4, a rigorous two-dimensional (2D) model of electromagnetic surface scatter was presented and verified, based on a boundary element method (BEM) established by Simonsen [261]. The theory of the model was outlined, where the model is expected to be able to accurately predict scattering from any surface. To verify the model, scattering data from the BEM model was compared to scattering data from various analytical models for different surfaces with good agreement, including comparison with an exact analytical solution of a cylindrical surface via the Mie scattering solution to Maxwell's equations. The model was experimentally verified by comparison of the simulated far-field scatter with measurements from a laser scatterometer for a sinusoidal grating. These comparisons provided evidence that verify the accuracy of the BEM model, and in the case of the Mie solution, provided evidence of its capability to accurately predict scatter from complex surfaces and for surfaces with high curvature and slopes, including those surfaces that linear models cannot accurately model. The BEM model was also compared against a KA-based method for the sinusoid grating geometry measured experimentally, providing further agreement, and for a range of different sinusoidal grating geometries, showing that disagreement occurs for geometries where multiple scattering is expected to occur under geometrical optics.

The contributions of this work are the experimental verification of the BEM optical scattering model and the verification of the model's capabilities to accurately model more complex surfaces with high curvature and slopes. These contributions included the following conference presentation [209].

In Chapter 5, a rigorous model of CSI based on the previous chapter's BEM optical scattering model was presented and verified, capable of accurately modelling the CSI signal for complex surfaces which contain steep surfaces and can produce multiple scattering. The CSI model's theory was presented, derived from scalar scattering theory, and implementation details, including interpolation in spatial frequency space onto discrete coordinates, were also discussed. The model produces CSI fringes by correctly combining in spatial frequency space the far-field scatter produced by the BEM model for a range of illumination wavelengths and incident angles, accounting

for imaging through backpropagation to a reconstructed scattered field. Evidence of the CSI model's validity was provided by comparison with experimental measurements from a commercial CSI instrument for several surfaces, giving qualitative agreement. CSI model fringe data for a vee-groove surface geometry was produced and compared to results in the literature to demonstrate the model's capability to account for multiple scattering and scatter from steep surfaces.

The contributions of this work are the development and verification of a CSI model based on a BEM optical scatter method, believed to be the first published rigorous CSI model based on BEM. This included demonstrating evidence of the CSI model's capability to predict multiple scattering. These contributions included the following publications [50,51].

In Chapter 6, the capability of optical surface topography measurement methods for measurement of steep and tilted surfaces was investigated. Of particular interest was the effect on the interference signal and measured topography when tilting the measured object at angles larger than the specular reflection limit, determined by the NA of the instrument. The results presented illustrate the capabilities, limitations, and modelling methods for interferometers to measure beyond the specular reflection limit. The experimentally-verified BEM-CSI model given in Chapter 5 was used to investigate several characteristics of measurements of a blazed diffraction grating, by gradually increasing the tilt angle until some areas exceeded the specular reflection limit determined by the NA of the objective. At high tilt angles, it was found that the sharp edges with undercuts still provide strong signals, and appear as plateaus in the topography data, with a width corresponding to the width of the point spread function of the instrument. Consistent with current practical guidance when using CSI instruments for very high slope angles, it was also found that useful phase information is lost and that the optimum results are obtained using coherence-based data evaluation methods. It was confirmed that in many surface areas, there is sufficient fine-scale surface texture to provide useful overall form information from the non-specular scattered light.

The first contribution is the specific demonstration of the effect of surface tilt on the CSI signal measured for a blazed grating, tilted at a range of angles that include those that exceed the specular reflection limit. This includes presenting the differences

between fringes produced by a blazed grating with the same tilt angle but different blaze direction. The second contribution is the specific result demonstrating the effect of surface tilt at specific tilt angles that exceed the specular reflection limit on the topography obtained. This result, alongside the CSI fringes obtained, provide an explanation to previously published erroneous CSI measurement results [225]. This result also shows that even when the mean plane of the blazed grating is tilted beyond the specular reflection limit, fringes with the shape of CSI point spread function can be generated due to diffraction and scattering by surface structures such as the sharp edges, local facets smaller or comparable to the optical scale, fine surface textures, and other surface irregularities. The third contribution is the general result that despite the loss of specular scatter due to surface tilt, it is possible to obtain useful surface information from the non-specular backward scattered light. The fourth contribution is the demonstration that fringe results for the tilted blazed grating can be accurately generated using a rigorous CSI model, even when the model is limited to 2D. This suggests that similar investigations for any arbitrary surface could also be performed and provide useful results, with the benefit that the virtual surface "measured" is known exactly. These contributions included the following publications [52,225].

## 7.2 Areas for future work

Areas for future work can be generally placed into one of two sections. The first section covers specific improvements or alternative approaches for each chapter that would further or improve the work presented, such as those recognised in hindsight. The second section covers novel future work that could be undertaken to develop this area of research further, including methods built upon the work presented in this thesis.

### 7.2.1 Specific improvements

Specific improvements to the work presented in Chapter 3 are limited, as issues previously present in earlier publications about the work were addressed in preparation to producing [159]. This included ensuring the most suitable window filtering parameters are chosen in the generation of the 3D STF and improving the accuracy of the alignment between the virtual foil and the measured fringes of the microsphere. One area of specific improvement would be to consider more locations in the instrument's field of view (FOV) at which to measure the microsphere, with locations varying in

both lateral directions, to characterise the degree to which shift-invariance does not strictly hold along both lateral axes.

One improvement to the work presented in Chapter 4 would be for the scatterometry measurement to be made with a smaller aperture and much smaller angular steps, with both the angular steps and the collection aperture kept fixed throughout the entire measurement process. While agreement was found between the BEM model and the measured data, a relatively wide convolution kernel was used to account for the aperture width, which could be reduced if a smaller aperture was used. In addition, avoiding the experimental method errors discussed in section 4.4.2 would increase confidence in the verification of the model by experiment. Another improvement would be to additionally perform verification of the BEM model through comparison with an existing rigorous optical scattering model that has already been verified, for both the experimental surface and for surfaces where multiple scattering is expected.

In Chapter 5, the results from the CSI model developed partly depend on the methods of sampling and interpolation chosen, seen clearly when the Cartesian blurring was found to be insufficient for tilted surfaces, and polar blurring was introduced for the modelling presented in Chapter 6. While both modes have been shown to be effective and produce results that match experiment, the development of a method of blurring that accounted for all three ranges sampled would be valuable in producing accurate results even at the very minimum samples provided. This would also motivate the development of automatically obtaining the minimum number of samples required, perhaps through an iterative process, saving computation time. In addition, verification of the CSI model by taking measurements of a surface that produces multiple scattering (such as a vee-groove) and comparing to the model would better support the claim that the model accounts for multiple scattering and steep surfaces. Verification through comparison with other rigorous CSI models that have been developed since publishing the BEM-CSI model [50], such as [183,188], could also provide evidence to support the BEM-CSI model's validity. Further testing against step height surfaces may also be valuable, but the surface texture of the vertical step facet would need to be accurately measured first and use of a 3D scattering model may still be necessary.

Specific improvements for the work presented in Chapter 6 include controlling the illumination light level used in the experimental case. If the light level could be fixed

throughout all the measurements without negatively impacting the measurement quality, then the loss of scatter captured by the instrument could be quantitively assessed in the experimental case and compared to that predicted by the CSI model. With a variable light level, not even relative quantitative comparison between experimental fringes from different tilts can be made. If the light level must be changed to compensate for the reduction in captured scatter as surface tilt is increased, then with appropriate characterisation of the relationship between light level and fringe intensity acquired, the amplitude of each set of measured fringes could be adjusted to values equivalent to that obtained from a constant light level, and a quantitative comparison performed. Another improvement would be to measure a taller blazed grating at different tilts, so that PSF-like fringes that form over the shorter facets of the tilted grating can be associated specifically with either the sharp edges of the grating or the relatively flat shorter facet. A taller grating would also mitigate the effect of the spatial sampling shown in Figure 6.14.

As the blazed grating generally produces regions of well-defined scatter along lines in spatial frequency space, the sensitivity of the measured fringes to tilting can vary significantly at different angles. For example, at certain surface tilts, a small change in surface tilt can cause an entire diffraction order to no longer be captured; in other areas a much weaker effect would be seen. It would therefore be valuable to measure the grating at surface tilts before and after each of these key tilting locations to show the non-linear impact of surface tilt on fringe visibility. Using the CSI model, it would also be possible to obtain fringes for many surface tilts and to correlate how the values of the fringe spectrum at certain surface tilts are related to the fringes obtained, providing an improved understanding. The same approach could be applied to the change in the topographies obtained. Finally, if a similar blazed grating with minimal nano-scale surface texture was available, then the experimental results in the R-case at large tilts (shown in Figure 6.9) could be compared to equivalent measurements of the smoother grating, to ascertain with confidence which fringes are associated with which part of the grating in the experimental results.

### 7.2.2 Novel future work

As already discussed, from the work presented in Chapter 3 the instrument is shown to not strictly be shift-invariant, and 3D STFs are obtained from three regions to enable

effective topography correction over the entire measurement FOV. One area of future work could be the investigation of the degree to which this shift invariance holds for different lenses of the same instrument and for different instruments, parameterising the anisotropy of this variation. A greater understanding about the relationship between the different measurement configurations and the degree to which they are shift invariant could further define domains of validity for the foil model. For a specific measurement configuration, it could also allow for the minimum adequate number of 3D STFs required for effective topography correction to be determined. Another direction of future work is making use of the detailed transfer characteristics provided in an instrument's 3D STF to provide a more comprehensive comparison between optical measuring instruments for measurements in the linear regime, in contrast to just comparing single parameters such as lateral resolution. While this naturally allows for comparison between different instruments of the same model or between the same kind of instrument made by different manufacturers, a similar method could be developed to allow for comparison of a 3D STF from a CSI instrument with STFs obtained from other optical topography measurement technologies, such as focus variation.

Regarding Chapter 3's foil model, which underpins the IF work, there is value in establishing the regions of validity of the model compared to other models. This could be done though comparison to simpler, more well-established linear models to confirm the added value of the foil model, and against rigorous models to confirm the boundaries of validity where care must be taken. Some specific comparisons with a simpler linear model have already been done in [182,246]. Developing the instrument model further into a virtual instrument for measurement uncertainty evaluation, the value of which is given in Chapter 1, is another area of future work; progress towards this has already been made in [186].

The BEM optical scattering model verified in Chapter 4 can be used in more than just a CSI model. One direction of future work is to develop a rigorous model of another instrument technology, such as focus variation, using similar theory to that described in Chapter 5. However, the BEM model is useful on its own for the purpose of producing accurate virtual scatterometry data for rough surfaces, and has already been used for training deep learning methods for on-machine surface defect detection [226–228]. For this work, the quantity of scattering data and the size of the surfaces required

prevents practical use of a 3D rigorous model, whereas the 2D BEM model remains viable.

In Chapter 5, the CSI model developed is verified against a range of experimental CSI measurements, and a vee-groove surface geometry is also used in the model. As previously mentioned, the theory developed is not only limited to CSI, and alternative rigorous instrument models using the BEM scattering model could be produced. The CSI model accounts for the imaging process in an idealised way, without considering the instrument's optics beyond the NA. Therefore, to develop an accurate virtual instrument model for evaluating measurement uncertainty, more complex imaging methods are required, such as those that account for the separate components of the optical system. Alternatively, the CSI model could be combined with a part of the foil model (from Chapter 3). As an experimental characterisation of an instrument provides detailed information on its imaging process, the 3D STF obtained could be combined with the BEM-CSI model to provide more accurate CSI fringe data for a specific instrument. If computational challenges could be overcome (as given in section 5.6), the same CSI modelling theory could be used with a 3D optical surface scattering model, such as the 3s boundary source method [220]. In experimental comparisons, the issues between the 3D measurement and 2D model would no longer be present, and modelling of non-prismatic surfaces such as a randomly rough surface would become possible.

In Chapter 6, a blazed grating was measured at various tilts, and at certain tilts the topography was also obtained and compared. The stated conclusions are primarily associated with the specific grating measured, and further development of this work would be to confirm the effectiveness of the model for a wider variety of complex surfaces, through further experimental comparison. This could begin with modelling and measuring high amplitude sinusoidal surfaces that have non-negligible multiple-scatter, to improve understanding of the (non-specular) instrument response to steep surfaces. The use of a low objective NA and measuring relatively low spatial frequency surfaces would reduce the effect of polarisation effects in the instrument, reducing differences between the instrument and the model associated with approximating the polarisation of the illumination. A low NA also requires only small surface tilts to reach the specular reflection limit. Another area of future work is to investigate through modelling the effects of lateral chromatic aberration (i.e., lateral colour) and dispersion

effects on the CSI fringes and topography produced by an instrument, including the effect on tilted surface sections. This area of work has some developments published in [153,174], which are briefly discussed in section 2.3.5. Similarly, through modelling the effect of the surface topography on the spectral composition of the fringes produced can be investigated, especially for tilted surfaces. Some existing work in this area can be seen in [172,187], which are also discussed briefly in section 2.3.5.

Beyond further experimental verification of various challenging surfaces, the CSI model could be used to obtain the CSI fringes and topography for surfaces that would be impractical to manufacture or measure, i.e., the model expands the domain of surfaces for which CSI fringes can be accurately predicted. Through modelling, results could be obtained about the capabilities of a measurement method such as CSI for carefully constructed virtual surfaces, providing a more general understanding of image formation for steep and complex surfaces. Of industrial interest is to improve the understanding of the instrument response for surfaces that cannot currently be measured or are challenging to measure, to assist in understanding why they cannot be measured or are challenging and over what surface and measurement configurations they remain a challenge. This includes measurement of very rough additive manufactured surfaces, surfaces with optically unresolved surface features, high-aspect ratio surfaces such as deep holes (discussed in section 2.6.1), and surfaces with high slopes and sharp edges (as seen with the blazed grating) [36]. Producing a case study directed specifically at modelling and measuring parts of industrial interest and improving understanding of their response is an area of scientific and commercial interest.

Eventually, a rigorous CSI model could be used to improve the quality of topography data obtained from measurements of parts with surfaces that produce non-negligible amounts of non-specular scatter. This could be done though height estimation methods that rely on the model and an iterative process that changes a virtual surface until differences in the virtual and measured fringes are minimised [49].

# References


[1] Bruzzone A A G, Costa H L, Lonardo P M and Lucca D A 2008 Advances in engineered surfaces for functional performance *CIRP Ann.* **57** 750–69 10.1016/j.cirp.2008.09.003

[2] Malshe A, Rajurkar K, Samant A, Hansen H N, Bapat S and Jiang W 2013 Bio-inspired functional surfaces for advanced applications *CIRP Ann.* **62** 607–28 10.1016/j.cirp.2013.05.008

[3] Costa H and Hutchings I 2015 Some innovative surface texturing techniques for tribological purposes *Proc. Inst. Mech. Eng. J: J. Eng. Tribol.* **229** 429–48 10.1177/1350650114539936

[4] Bruzzone A A G and Costa H L 2013 Functional characterization of structured surfaces for tribological applications *Procedia CIRP* **12** 456–61 10.1016/j.procir.2013.09.078

[5] Gachot C, Rosenkranz A, Hsu S M and Costa H L 2017 A critical assessment of surface texturing for friction and wear improvement *Wear* **372–373** 21–41 10.1016/j.wear.2016.11.020

[6] Hutchings I and Shipway P 2017 *Tribology: Friction and Wear of Engineering Materials* 2nd ed. (Kidlington, Oxford, UK: Butterworth-Heinemann) 10.1016/B978-0-08-100910-9.09983-9

[7] Ramsden J J, Allen D M, Stephenson D J, Alcock J R, Peggs G N, Fuller G D and Goch G 2007 The design and manufacture of biomedical surfaces *CIRP Ann.* **56** 687–711 10.1016/j.cirp.2007.10.001

[8] Kokubo T, Matsushita T, Takadama H and Kizuki T 2009 Development of bioactive materials based on surface chemistry *J. Eur. Ceram. Soc.* **29** 1267–74 10.1016/j.jeurceramsoc.2008.08.004

[9] Pugliese G, Tavares S M O, Ciulli E and Ferreira L A 2008 Rough contacts between actual engineering surfaces: Part II. Contact mechanics *Wear* **264** 1116–28 10.1016/j.wear.2007.08.027

[10] Yu H, Wang X and Zhou F 2010 Geometric Shape Effects of Surface Texture on the Generation of Hydrodynamic Pressure Between Conformal Contacting Surfaces *Tribol. Lett.* **37** 123–30 10.1007/s11249-009-9497-4

[11] Enomoto T and Sugihara T 2010 Improving anti-adhesive properties of cutting tool surfaces by nano-/micro-textures *CIRP Ann.* **59** 597–600 10.1016/j.cirp.2010.03.130

[12] Enomoto T, Sugihara T, Yukinaga S, Hirose K and Satake U 2012 Highly wear-resistant cutting tools with textured surfaces in steel cutting *CIRP Ann.* **61** 571–4 10.1016/j.cirp.2012.03.123

[13] Bewilogua K, Bräuer G, Dietz A, Gäbler J, Goch G, Karpuschewski B and Szyszka B 2009 Surface technology for automotive engineering *CIRP Ann.* **58** 608–27 10.1016/j.cirp.2009.09.001

[14] Chatterjee S, Murallidharan J S, Agrawal A and Bhardwaj R 2021 Designing antiviral surfaces to suppress the spread of COVID-19 *Phys. Fluids* **33** 052101 10.1063/5.0049404

[15] Fang F Z, Zhang X D, Weckenmann A, Zhang G X and Evans C 2013 Manufacturing and measurement of freeform optics *CIRP Ann.* **62** 823–46 10.1016/j.cirp.2013.05.003

[16] Echouchene F, Belmabrouk H, Le Penven L and Buffat M 2011 Numerical simulation of wall roughness effects in cavitating flow *Int. J. Heat Fluid Flow* **32** 1068–75 10.1016/j.ijheatfluidflow.2011.05.010

[17] Kretzer J P, Jakubowitz E, Sonntag R, Hofmann K, Heisel C and Thomsen M 2010 Effect of joint laxity on polyethylene wear in total knee replacement *J. Biomech.* **43** 1092–6 10.1016/j.jbiomech.2009.12.016

[18] Leach R K 2014 *Fundamental Principles of Engineering Nanometrology* 2nd ed. (Amsterdam, NL: William Andrew Publishing (Elsevier))

[19] Leach R K 2011 *Optical Measurement of Surface Topography* 1st ed. (Berlin, Heidelberg: Springer Berlin Heidelberg) 10.1007/978-3-642-12012-1

[20] Leach R K 2014 Surface topography measurement instrumentation *Fundamental Principles of Engineering Nanometrology* 2nd ed. Micro and Nano Technologies (Oxford, UK: William Andrew Publishing (Elsevier)) pp 133–204 10.1016/B978-1-4557-7753-2.00006-2

[21] de Groot P 2017 The meaning and measure of vertical resolution in optical surface topography measurement *Appl. Sci.* **7** 54 10.3390/app7010054

[22] Abbe E 1881 VII.—On the estimation of aperture in the microscope. *J. R. Microsc. Soc.* **1** 388–423 10.1111/j.1365-2818.1881.tb05909.x

[23] Masters B R 2006 Abbe theory of image formation and diffraction of light in transmitted light microscopes *Confocal Microscopy and Multiphoton Excitation Microscopy: The Genesis of Live Cell Imaging* (Bellingham, WA, US: SPIE Press) pp 37–49

[24] Marinello F, Bariani P, Carmignato S, Savio E, De Chiffre L and Bossard M 2007 Increase of maximum detectable slope with optical profilers: theory and applicative examples *Proceedings of the 7th euspen International Conference* International Conference of the European Society for Precision Engineering and Nanotechnology (Bremen, DE)

[25] Jiang X, Gao F and Mateboer A 2010 An approach of assessment for ultra-precision v-groove structured surfaces *Proceedings of the euspen International Conference* International Conference of the European Society for Precision Engineering and Nanotechnology (Delft, NL: euspen) pp 512–6

[26] Colonna de Lega X, Dresel T, Liesener J, Fay M F, Gilfoy N, Delldonna K and de Groot P 2017 Optical form and relational metrology of aspheric micro optics *Proc. 32nd Annual Meeting ASPE vol 67* ASPE Annual Meeting (Charlotte, NC, US: American Society for Precision Engineering) pp 20–3

[27] de Groot P J 2019 A review of selected topics in interferometric optical metrology *Rep. Prog. Phys.* **82** 056101 10.1088/1361-6633/ab092d

[28] Ren F, Wang Z, Qian J, Liang Y, Dang S, Cai Y, Bianco P R, Yao B and Lei M 2019 Multi-view object topography measurement with optical sectioning structured illumination microscopy *Appl. Opt.* **58** 6288 10.1364/AO.58.006288

[29] Conroy M, Burton R, Yu Y and Kumagi T 2015 Recent advances in non-contact metrology, high speed measurement, steep slope measurement and correlation with stylus data *Proceedings of Malaysian International Tribology Conference 2015* Malaysian International Tribology Conference 2015 (MITC2015) (Penang, MY) pp 314–5

[30] Zhang T, Gao F and Jiang X 2017 Surface topography acquisition method for double-sided near-right-angle structured surfaces based on dual-probe wavelength scanning interferometry *Opt. Express* **25** 24148–56 10.1364/OE.25.024148

[31] Zhang T, Gao F, Martin H and Jiang X 2019 A method for inspecting near-right-angle V-groove surfaces based on dual-probe wavelength scanning interferometry *Int. J. Adv. Manuf. Technol.* **104** 1–7 10.1007/s00170-018-2331-0

[32] Leach R K, de Groot P and Haitjema H 2018 Infidelity and the calibration of surface topography measuring instruments *Proc. 33rd Annual Meeting ASPE* ASPE Annual Meeting (Las Vegas, NV, US: American Society for Precision Engineering)

[33] Danzl R and Helmli F 2006 Three-dimensional reconstruction of surfaces with steep slopes using an optical measurement system based on a colour focus sensor *Proceedings of the 6th euspen International Conference* International Conference of the European Society for Precision Engineering and Nanotechnology (Baden bei Wien, AT)

[34] Zangl K, Danzl R, Helmli F and Prantl M 2018 Highly accurate optical µCMM for measurement of micro holes *Procedia CIRP* **75** 397–402 10.1016/j.procir.2018.05.098

[35] Fay M F, Colonna de Lega X and de Groot P 2014 Measuring high-slope and super-smooth optics with high-dynamic-range coherence scanning interferometry *Proc. Classical Optics 2014* Optical Fabrication and Testing 2014 (Kohala Coast, HI, US: Optical Society of America) p OW1B.3 10.1364/OFT.2014.OW1B.3

[36] Fay M F, Colonna de Lega X and Schmidt M 2014 Measuring high-slope parts using coherence scanning interferometry *Proc. 29th Annual Meeting ASPE* ASPE Annual Meeting (Boston, MA, US: American Society for Precision Engineering)

[37] Gomez C, Su R, Thompson A, DiSciacca J, Lawes S and Leach R K 2017 Optimization of surface measurement for metal additive manufacturing using coherence scanning interferometry *Opt. Eng.* **56** 111714 10.1117/1.OE.56.11.111714

[38] Hiersemenzel F, Petzing J N, Leach R K, Helmli F and Singh J 2012 Areal texture and angle measurements of tilted surfaces using focus variation methods *3rd International Conference on Surface Metrology* International Conference on Surface Metrology (Annecy, FR) p 5

[39] Petzing J, Coupland J M and Leach R K 2010 *The measurement of rough surface topography using coherence scanning interferometry* (National Physical Laboratory)

[40] Haitjema H 2016 Measurement uncertainty ed The International Academy for Produ, L Laperrière and G Reinhart *CIRP Encyclopedia of Production Engineering* 1–5 10.1007/978-3-642-35950-7_6599-3

[41] Leach R K, Giusca C L, Haitjema H, Evans C and Jiang X 2015 Calibration and verification of areal surface texture measuring instruments *CIRP Ann.* **64** 797–813 10.1016/j.cirp.2015.05.010

[42] de Groot P J 2014 Progress in the specification of optical instruments for the measurement of surface form and texture *Proc. SPIE vol 9110* Dimensional Optical Metrology and Inspection for Practical Applications III (Baltimore, MD, US: SPIE) pp 131–42 10.1117/12.2054435

[43] de Groot P J and Fitzgerald D 2017 Measurement, certification and use of step-height calibration specimens in optical metrology *Proc. SPIE vol 10329* Optical Measurement Systems for Industrial Inspection X (Munich, DE: SPIE) pp 328–36 10.1117/12.2269800

[44] ISO/TC 213 2019 ISO 25178-600:2019 - Geometrical product specifications (GPS) — Surface texture: Areal — Part 600: Metrological characteristics for areal topography measuring methods

[45] Leach R K, Haitjema H, Su R and Thompson A 2020 Metrological characteristics for the calibration of surface topography measuring instruments: a review *Meas. Sci. Technol.* **32** 032001 10.1088/1361-6501/abb54f

[46] ISO/TC 213 2021 [Under Development] ISO 25178-700 - Geometrical product specifications (GPS) — Surface texture: Areal — Part 700: Calibration, adjustment and verification of areal topography measuring instruments

[47] Wübbeler G, Marschall M, Kniel K, Heißelmann D, Härtig F and Elster C 2022 GUM-Compliant Uncertainty Evaluation Using Virtual Experiments *Metrology* **2** 114–27 10.3390/metrology2010008

[48] Haitjema H 2018 Measurement uncertainty *Basics of Precision Engineering* 1st ed. (Boca Raton, FL, US: CRC Press) pp 413–48 10.1201/9781351204118-9

[49] Coupland J M and Lobera J 2010 Measurement of steep surfaces using white light interferometry *Strain* **46** 69–78 10.1111/j.1475-1305.2008.00595.x

[50] Thomas M, Su R, Nikolaev N, Coupland J M and Leach R K 2019 Modelling of coherence scanning interferometry for complex surfaces based on a boundary element method *Proc. SPIE vol 11057* Modeling Aspects in Optical Metrology VII (Munich, DE: SPIE) p 1105713 10.1117/12.2526015

[51] Thomas M, Su R, Nikolaev N, Coupland J M and Leach R K 2020 Modeling of interference microscopy beyond the linear regime *Opt. Eng.* **59** 034110 10.1117/1.OE.59.3.034110

[52] Thomas M, Su R, de Groot P J, Coupland J M and Leach R K 2021 Surface measuring coherence scanning interferometry beyond the specular reflection limit *Opt. Express* **29** 36121–31 10.1364/OE.435715

[53] Savio E, De Chiffre L, Carmignato S and Meinertz J 2016 Economic benefits of metrology in manufacturing *CIRP Ann.* **65** 495–8 10.1016/j.cirp.2016.04.020

[54] Stephenson A G, LaPiana L S, Mulville D R, Rutledge P J, Bauer F H, Folta D, Dukeman G A, Sackheim R and Norvig P 1999 *Mars Climate Orbiter Mishap Investigation Board Phase I Report* (Washington, D.C., US: NASA)

[55] Bureau International des Poids et Mesures (BIPM) 2019 The International System of Units (SI)

[56] Leach R K 2014 Some basics of measurement *Fundamental Principles of Engineering Nanometrology* 2nd ed. Micro and Nano Technologies (Oxford, UK: William Andrew Publishing (Elsevier)) pp 7–39 10.1016/B978-1-4557-7753-2.00002-5

[57] JCGM/WG 2 2012 JCGM 200:2012 - International vocabulary of metrology – Basic and general concepts and associated terms (VIM)

[58] Bell S 2001 *The Beginner's Guide to Uncertainty of Measurement* 2nd ed. (Teddington, UK: National Physical Laboratory)

[59] Possolo A and Meija J 2020 *Measurement Uncertainty: A Reintroduction* (Montevideo, UY: Sistema Interamericano de Metrologia (SIM) [Inter American Metrology System])

[60] Felkel E 2013 Scanning White-Light Interferometry Fingerprints the Polishing Process *Photonics Spectra* **47** 48–51

[61] Thomas T R 2014 Roughness and function *Surf. Topogr.: Metrol. Prop.* **2** 014001 10.1088/2051-672X/2/1/014001

[62] Bhushan B 2013 *Principles and Applications of Tribology* 2nd ed. (John Wiley & Sons, Ltd) 10.1002/9781118403020

[63] ISO/TC 213 2010 ISO 25178-6:2010 - Geometrical product specifications (GPS) — Surface texture: Areal — Part 6: Classification of methods for measuring surface texture

[64] Bhushan B, Wyant J C and Koliopoulos C L 1985 Measurement of surface topography of magnetic tapes by Mirau interferometry *Appl. Opt.* **24** 1489–97 10.1364/AO.24.001489

[65] Scott P 2002 Recent developments in the measurement of aspheric surfaces by contact stylus instrumentation *Proc. SPIE vol 4927* Optical Design and Testing (Shanghai, CN: SPIE) pp 199–207 10.1117/12.464331

[66] Le Bosse J C, Hansali G, Lopez J and Dumas J C 1999 Characterisation of surface roughness by laser light scattering: diffusely scattered intensity measurement *Wear* **224** 236–44 10.1016/S0043-1648(98)00333-0

[67] Miura K and Nose A 2011 Point autofocus instruments *Optical Measurement of Surface Topography* 1st ed. ed R K Leach (Berlin, Heidelberg: Springer Berlin Heidelberg) pp 107–29 10.1007/978-3-642-12012-1_6

[68] Blateyron F 2011 Chromatic confocal microscopy *Optical Measurement of Surface Topography* 1st ed. ed R K Leach (Berlin, Heidelberg: Springer Berlin Heidelberg) pp 71–106 10.1007/978-3-642-12012-1_5

[69] Helmli F 2011 Focus variation instruments *Optical Measurement of Surface Topography* 1st ed. ed R K Leach (Berlin, Heidelberg: Springer Berlin Heidelberg) pp 131–66 10.1007/978-3-642-12012-1_7

[70] Repitsch C, Zangl K, Helmli F and Danzl R 2020 Focus variation *Advances in Optical Surface Texture Metrology* IOP Series in Emerging Technologies in Optics and Photonics (Bristol, UK: IOP Publishing) pp 3–1 to 3–30

[71] Artigas R 2011 Imaging confocal microscopy *Optical Measurement of Surface Topography* 1st ed. ed R K Leach (Berlin, Heidelberg: Springer Berlin Heidelberg) pp 237–86 10.1007/978-3-642-12012-1_11

[72] de Groot P 2011 Phase shifting interferometry *Optical Measurement of Surface Topography* 1st ed. ed R K Leach (Berlin, Heidelberg: Springer Berlin Heidelberg) pp 167–86 10.1007/978-3-642-12012-1_8

[73] Bruning J H, Herriott D R, Gallagher J E, Rosenfeld D P, White A D and Brangaccio D J 1974 Digital Wavefront Measuring Interferometer for Testing Optical Surfaces and Lenses *Appl. Opt.* **13** 2693–703 10.1364/AO.13.002693

[74] Su R, Wang Y, Coupland J M and Leach R K 2017 On tilt and curvature dependent errors and the calibration of coherence scanning interferometry *Opt. Express* **25** 3297–310 10.1364/OE.25.003297

[75] Thamizhmanii S, Saparudin S and Hasan S 2007 Analyses of surface roughness by turning process using Taguchi method *J. Achiev. Mater. Manuf. Eng.* **20** 503–6

[76] Whitehouse D J 1982 The parameter rash — is there a cure? *Wear* **83** 75–8 10.1016/0043-1648(82)90341-6

[77] Leach R K and Groot P de 2015 The standards rash – is there a cure? *Int. J. Metrol. Qual. Eng.* **6** 101 10.1051/ijmqe/2015001

[78] ISO/TC 213 1997 ISO 4287:1997 - Geometrical Product Specifications (GPS) — Surface texture: Profile method — Terms, definitions and surface texture parameters

[79] ISO/TC 213 2012 ISO 25178-2:2012 - Geometrical product specifications (GPS) — Surface texture: Areal — Part 2: Terms, definitions and surface texture parameters

[80] Bennett J M and Mattsson L 1999 *Introduction to Surface Roughness and Scattering* 2nd ed. (Washington, D.C., US: Optical Society of America)

[81] Leach R K 2014 Surface topography characterisation *Fundamental Principles of Engineering Nanometrology* 2nd ed. Micro and Nano Technologies (Oxford, UK: William Andrew Publishing (Elsevier)) pp 241–94 10.1016/B978-1-4557-7753-2.00008-6

[82] Leach R K 2013 *Characterisation of Areal Surface Texture* 1st ed. (Springer Berlin Heidelberg)

[83] ISO/TC 213 2013 ISO 25178-604:2013 - Geometrical product specifications (GPS) — Surface texture: Areal — Part 604: Nominal characteristics of non-contact (coherence scanning interferometry) instruments

[84] de Groot P 2011 Coherence scanning interferometry *Optical Measurement of Surface Topography* 1st ed. ed R K Leach (Berlin, Heidelberg: Springer Berlin Heidelberg) pp 187–208 10.1007/978-3-642-12012-1_9

[85] Larkin K G 1996 Efficient nonlinear algorithm for envelope detection in white light interferometry *J. Opt. Soc. Am. A* **13** 832–43 10.1364/JOSAA.13.000832

[86] Wyant J C 2002 White light interferometry *Proc. SPIE vol 4737* Holography: A Tribute to Yuri Denisyuk and Emmett Leith (Orlando, FL, US: SPIE) pp 98–107 10.1117/12.474947

[87] de Groot P, Colonna de Lega X, Kramer J and Turzhitsky M 2002 Determination of fringe order in white-light interference microscopy *Appl. Opt.* **41** 4571–8 10.1364/AO.41.004571

[88] Coupland J M and Lobera J 2008 Holography, tomography and 3D microscopy as linear filtering operations *Meas. Sci. Technol.* **19** 074012 10.1088/0957-0233/19/7/074012

[89] de Groot P J and Deck L 1995 Surface profiling by analysis of white-light interferograms in the spatial frequency domain *J. Mod. Opt.* **42** 389–401 10.1080/09500349514550341

[90] de Groot P J, Deck L L, Su R and Osten W 2022 Contributions of holography to the advancement of interferometric measurements of surface topography *Light: Adv. Manuf.* **3** 1–20 10.37188/lam.2022.007

[91] Hooke R 1665 Observ. IX. Of the colours observable in muscovy glass, and other thin bodies *Micrographia: Some Physiological Descriptions of Minute Bodies Made by Magnifying Glasses with Observations and Inquiries Thereupon* (London, UK: Royal Society) pp 47–67

[92] Newton I 1672 A Letter of Mr. Isaac Newton … containing his New Theory about Light and Colors *Philos. Trans.* **6** 3075–87

[93] Hooke R 1757 Considerations upon Mr. Newton's discourse on light and colours - Robert Hooke's critique of Newton's theory of light and colors (delivered 1672) *The History of the Royal Society of London for Improving of Natural Knowledge [...] as a Supplement to The Philosophical Transactions* vol 3, ed T Birch (Strand, London, UK: Andrew Millar) pp 10–5

[94] Michelson A A 1893 Light-Waves and their Application to Metrology *Nature* **49** 56–60 10.1038/049056a0

[95] Flournoy P A, McClure R W and Wyntjes G 1972 White-Light Interferometric Thickness Gauge *Appl. Opt.* **11** 1907–15 10.1364/AO.11.001907

[96] Mirau A H 1952 Interferometer US Patent Office US2612074 A (Issued September 30, 1952)

[97] Lee B S and Strand T C 1990 Profilometry with a coherence scanning microscope *Appl. Opt.* **29** 3784–8 10.1364/AO.29.003784

[98] Dresel T, Häusler G and Venzke H 1992 Three-dimensional sensing of rough surfaces by coherence radar *Appl. Opt.* **31** 919–25 10.1364/AO.31.000919

[99] Caber P J 1993 Interferometric profiler for rough surfaces *Appl. Opt.* **32** 3438–41 10.1364/AO.32.003438

[100] McCallum J 2017 Memory Prices 1957+ http://www.jcmit.net/memoryprice.htm

[101] de Groot P and Colonna de Lega X 2004 Signal modeling for low-coherence height-scanning interference microscopy *Appl. Opt.* **43** 4821–30 10.1364/AO.43.004821

[102] Colonna de Lega X, Fay M F, Kruse R, Grigg D, Darwin M, Knowles M, Barnak J and Wu M 2009 Interference microscopy for semiconductor back end patterning metrology *AIP Conf. Proc.* **1173** 359–63 10.1063/1.3251251

[103] Maniscalco B, Kaminski P M, Conroy M, Mansfield D, Yu Y, Bass K, Claudio G and Walls J M 2011 Metrology of silicon photovoltaic cells using Coherence Correlation Interferometry *Proc. 2011 37th IEEE Photovoltaic Specialists Conference* 37th IEEE Photovoltaic Specialists Conference (PVSC 37) (Seattle, WA, US: IEEE) pp 003370–4 10.1109/PVSC.2011.6186670

[104] Sachs R and Stanzel F 2014 Interference microscopy for clean air – How optical metrology is improving quality control of fuel injection systems *Fringe 2013: 7th International Workshop on Advanced Optical Imaging and Metrology* ed W Osten (Heidelberg New York Dordrecht London: Springer) pp 535–8 10.1007/978-3-642-36359-7_96

[105] Su R 2020 Coherence scanning interferometry *Advances in Optical Surface Texture Metrology* IOP Series in Emerging Technologies in Optics and Photonics (Bristol, UK: IOP Publishing) pp 2–1 to 2–27

[106] Born M and Wolf E 1999 *Principles of Optics: Electromagnetic Theory of Propagation, Interference and Diffraction of Light* 7th ed. (Cambridge, UK: Cambridge University Press)

[107] Born M and Wolf E 1999 Elements of the theory of interference and interferometers *Principles of Optics: Electromagnetic Theory of Propagation, Interference and Diffraction of Light* 7th ed. (Cambridge, UK: Cambridge University Press) pp 286–411

[108] Born M and Wolf E 1999 Interference and diffraction with partially coherent light *Principles of Optics: Electromagnetic Theory of Propagation, Interference and Diffraction of Light* 7th ed. (Cambridge, UK: Cambridge University Press) pp 554–632

[109] Goodman J W 2015 *Statistical Optics* 2nd ed. (Hoboken, NJ, US: John Wiley & Sons, Inc.)

[110] de Groot P 2015 Principles of interference microscopy for the measurement of surface topography *Adv. Opt. Photon.* **7** 1–65 10.1364/AOP.7.000001

[111] Born M and Wolf E 1999 Image-forming instruments *Principles of Optics: Electromagnetic Theory of Propagation, Interference and Diffraction of Light* 7th ed. (Cambridge, UK: Cambridge University Press) pp 261–85

[112] Murphy D B and Davidson M W 2012 *Fundamentals of Light Microscopy and Electronic Imaging* 2nd ed. (Hoboken, NJ, US: John Wiley & Sons)

[113] Zygo Corporation 2014 *NewView 8300 specification sheet SS-0100*

[114] Zygo Corporation 2018 *Nexview NX2 specification sheet*

[115] Linnik V P 1933 Ein apparat für mikroskopisch-interferometrische untersuchungen reflektierender objekte (mikrointerferometer) [An apparatus for microscopic-interferometric investigation of reflective objects] *Dokl. Akad. Nauk SSSR (Proc. USSR Acad. Sci.)* 18–23

[116] de Groot P and Biegen J F 2015 A new class of wide-field objectives for 3D interference microscopy *Proc. SPIE vol 9525* Optical Micro- and Nanometrology IV (Brussels, BE: SPIE) p 95250N 10.1117/12.2183628

[117] de Groot P and Biegen J F 2016 Interference microscope objectives for wide-field areal surface topography measurements *Opt. Eng.* **55** 074110 10.1117/1.OE.55.7.074110

[118] Chakmakjian S, Biegen J F and de Groot P J 1996 Simultaneous focus and coherence scanning in interference microscopy *Technical Digest of International Workshop on Interferometry* International Workshop on Interferometry (Riken, JP) pp 171–3

[119] Su R, Thomas M, Leach R K and Coupland J M 2018 Effects of defocus on the transfer function of coherence scanning interferometry *Opt. Lett.* **43** 82–5 10.1364/OL.43.000082

[120] Beverage J L, Colonna de Lega X and Fay M F 2014 Interferometric microscope with true color imaging *Proc. SPIE vol 9203* Interferometry XVII: Techniques and Analysis (San Diego, CA, US: SPIE) pp 216–25 10.1117/12.2063264

[121] Colonna de Lega X 2015 Surface topography interferometer with surface color World Intellectual Property Organization WO2014126778A3 (Issued January 15, 2015)

[122] Roth J and de Groot P J 1997 Wide-field scanning white light interferometry of rough surfaces *Proc. ASPE Spring Topical Meeting vol 15* ASPE Spring Topical Meeting on Advances in Surface Metrology (Annapolis, MD, US: American Society for Precision Engineering)

[123] Colonna de Lega X and de Groot P 2012 Lateral resolution and instrument transfer function as criteria for selecting surface metrology instruments *Proc. Imaging and Applied Optics Technical Papers* Optical Fabrication and Testing 2012 (Monterey, CA, US: Optical Society of America) p OTu1D.4 10.1364/OFT.2012.OTu1D.4

[124] Goodman J W 2017 Frequency analysis of optical imaging systems *Introduction to Fourier Optics* 4th ed. (New York: W. H. Freeman) pp 185–230

[125] Pawley J B 2006 Points, pixels, and gray levels: digitizing image data *Handbook of Biology Confocal Microscopy* 3rd ed. (New York: Springer Science+Business Media, LLC) pp 59–79

[126] Leach R K, Sims-Waterhouse D, Medeossi F, Savio E, Carmignato S and Su R 2018 Fusion of photogrammetry and coherence scanning interferometry data for all-optical coordinate measurement *CIRP Ann.* **67** 599–602 10.1016/j.cirp.2018.04.043

[127] Marinello F, Bariani P, De Chiffre L and Hansen H N 2007 Development and analysis of a software tool for stitching three-dimensional surface topography data sets *Meas. Sci. Technol.* **18** 1404–12 10.1088/0957-0233/18/5/028

[128] de Groot P and Deck L 1993 Three-dimensional imaging by sub-Nyquist sampling of white-light interferograms *Opt. Lett.* **18** 1462–4 10.1364/OL.18.001462

[129] Proakis J G and Manolakis D G 2006 Sampling and reconstruction of signals *Digital Signal Processing* (Upper Saddle River, NJ, US: Pearson) pp 384–448

[130] Giusca C L and Leach R K 2013 *Calibration of the metrological characteristics of coherence scanning interferometers (CSI) and phase shifting interferometers (PSI)* (National Physical Laboratory)

[131] Eifler M, Hering J, Seewig J, Leach R K, Freymann G von, Hu X and Dai G 2020 Comparison of material measures for areal surface topography measuring instrument calibration *Surf. Topogr.: Metrol. Prop.* **8** 025019 10.1088/2051-672X/ab92ae

[132] de Groot P J and Beverage J 2015 Calibration of the amplification coefficient in interference microscopy by means of a wavelength standard *Proc. SPIE vol 9526* Modeling Aspects in Optical Metrology V (Munich, DE: SPIE) pp 239–49 10.1117/12.2184975

[133] Fitzgerald D and de Groot P 2019 Long-term stability of the wavelength method of height scale calibration for interference microscopy *Proc. SPIE vol 11102* Applied Optical Metrology III (San Diego, CA, US: SPIE) p 111020K 10.1117/12.2528155

[134] Ekberg P and Mattsson L 2018 Traceable X , Y self-calibration at single nm level of an optical microscope used for coherence scanning interferometry *Meas. Sci. Technol.* **29** 035005 10.1088/1361-6501/aaa39d

[135] Gomez C, Su R, de Groot P and Leach R K 2020 Noise reduction in coherence scanning interferometry for surface topography measurement *Nanomanufacturing Metrol.* **3** 68–76 10.1007/s41871-020-00057-4

[136] Schmit J and Olszak A G 2002 Challenges in white-light phase-shifting interferometry *Proc. SPIE vol 4777* Interferometry XI: Techniques and Analysis (Seattle, WA, US: SPIE) pp 118–28 10.1117/12.472211

[137] Kiselev I, Kiselev E I, Drexel M and Hauptmannl M 2018 Precision of evaluation methods in white light interferometry. Correlogram correlation method *Measurement* **123** 125–8 10.1016/j.measurement.2018.03.060

[138] Chim S S C and Kino G S 1990 Correlation microscope *Opt. Lett.* **15** 579–81 10.1364/OL.15.000579

[139] Chim S S C and Kino G S 1991 Phase measurements using the Mirau correlation microscope *Appl. Opt.* **30** 2197–201 10.1364/AO.30.002197

[140] Bankhead A D and McDonnell I 2008 Surface profiling apparatus US7385707 B2 (Issued June 10, 2008)

[141] Beckmann P and Spizzichino A 1963 *The Scattering of Electromagnetic Waves from Rough Surfaces* 1st ed., vol 4 (Oxford; London; New York; Paris: Pergamon Press)

[142] de Groot P and Colonna de Lega X 2006 Interpreting interferometric height measurements using the instrument transfer function *Fringe 2005: 5th International Workshop on Automatic Processing of Fringe Patterns* ed W

Osten (Berlin Heidelberg New York: Springer) pp 30–7 10.1007/3-540-29303-5_3

[143] Deck L L and de Groot P J 2017 Using the instrument transfer function to evaluate Fizeau interferometer performance *Proc. Optical Design and Fabrication 2017 (Freeform, IODC, OFT)* Optical Fabrication and Testing 2017 (Denver, CO, US: Optical Society of America) p OM2B.7 10.1364/OFT.2017.OM2B.7

[144] Su R, Thomas M, de Groot P, Coupland J M and Leach R K 2018 Determination of the lateral resolution of an interference microscope using a micro-scale sphere *Proc. 33rd Annual Meeting ASPE* ASPE Annual Meeting (Las Vegas, NV, US: American Society for Precision Engineering) pp 225–9

[145] de Groot P J and Colonna de Lega X 2020 Fourier optics modelling of instrument response for interference microscopy *Proc. SPIE vol 11490* Interferometry XX (Online only: SPIE) p 114900T 10.1117/12.2569391

[146] de Groot P J 2021 The instrument transfer function for optical measurements of surface topography *J. Phys. Photonics* **3** 024004 10.1088/2515-7647/abe3da

[147] Zangl K, Danzl R, Muraus U, Helmli F and Prantl M 2019 Vertical focus probing for high-precision optical dimensional metrology *Proc. 14th International Symposium on Measurement Technology and Intelligent Instruments* ISMTII2019 (Niigata, JP)

[148] Hecht E 2017 More on geometrical optics *Optics* 5th ed. (Harlow, England: Pearson) pp 255–89

[149] Henning A, Giusca C, Forbes A, Smith I, Leach R K, Coupland J M and Mandal R 2013 Correction for lateral distortion in coherence scanning interferometry *CIRP Ann.* **62** 547–50 10.1016/j.cirp.2013.03.026

[150] Ekberg P, Su R and Leach R K 2017 High-precision lateral distortion measurement and correction in coherence scanning interferometry using an arbitrary surface *Opt. Express* **25** 18703–12 10.1364/OE.25.018703

[151] Pförtner A and Schwider J 2001 Dispersion error in white-light Linnik interferometers and its implications for evaluation procedures *Appl. Opt.* **40** 6223–8 10.1364/AO.40.006223

[152] Pavliček P and Soubusta J 2004 Measurement of the influence of dispersion on white-light interferometry *Appl. Opt.* **43** 766–70 10.1364/AO.43.000766

[153] Lehmann P 2010 Vertical scanning white-light interference microscopy on curved microstructures *Opt. Lett.* **35** 1768–70 10.1364/OL.35.001768

[154] Deck L L 2007 High precision interferometer for measuring mid-spatial frequency departure in free form optics *Proc. SPIE vol 10316* Optifab 2007: Technical Digest (Rochester, NY, US: SPIE) pp 77–80 10.1117/12.719404

[155] Baer G, Schindler J, Pruss C, Siepmann J and Osten W 2014 Calibration of a non-null test interferometer for the measurement of aspheres and free-form surfaces *Opt. Express* **22** 31200–11 10.1364/OE.22.031200

[156] Hovis C, Shahinian H and Evans C 2019 Observations on the effect of retrace error in scanning white light interferometry of smooth optical surfaces *Proc. Optical Design and Fabrication 2019 (Freeform, OFT)* Optical Fabrication and

Testing 2019 (Washington, D.C., US: Optical Society of America) p OM4A.2 10.1364/OFT.2019.OM4A.2

[157] Shahinian H, Shahinian H, Hovis C D and Evans C J 2021 Effect of retrace error on stitching coherent scanning interferometry measurements of freeform optics *Opt. Express* **29** 28562–73 10.1364/OE.433435

[158] Mikš A and Novák J 2019 Point spread function of an optical system with defocus and spherical aberration—analytical formulas *Appl. Opt.* **58** 5823–9 10.1364/AO.58.005823

[159] Su R, Thomas M, Liu M, Drs J, Bellouard Y, Pruss C, Coupland J M and Leach R K 2020 Lens aberration compensation in interference microscopy *Opt. Lasers Eng.* **128** 106015 10.1016/j.optlaseng.2020.106015

[160] Leach R K, Brown L, Jiang X, Blunt R, Conroy M and Mauger D 2008 *Guide to the measurement of smooth surface topography using coherence scanning interferometry* (National Physical Laboratory)

[161] de Groot P J 2009 Compensation of systematic effects in low coherence interferometry United States US7522288B2 (Issued April 21, 2009)

[162] Pavliček P and Hýbl O 2012 White-light interferometry on rough surfaces—measurement uncertainty caused by noise *Appl. Opt.* **51** 465–73 10.1364/AO.51.000465

[163] Liu M, Cheung C F, Ren M and Cheng C-H 2015 Estimation of measurement uncertainty caused by surface gradient for a white light interferometer *Appl. Opt.* **54** 8670–7 10.1364/AO.54.008670

[164] Gao F, Leach R K, Petzing J and Coupland J M 2007 Surface measurement errors using commercial scanning white light interferometers *Meas. Sci. Technol.* **19** 015303 10.1088/0957-0233/19/1/015303

[165] Harasaki A and Wyant J C 2000 Fringe modulation skewing effect in white-light vertical scanning interferometry *Appl. Opt.* **39** 2101–6 10.1364/AO.39.002101

[166] Harasaki A, Schmit J and Wyant J C 2000 Improved vertical-scanning interferometry *Appl. Opt.* **39** 2107–15 10.1364/AO.39.002107

[167] Lehmann P, Xie W and Niehues J 2012 Transfer characteristics of rectangular phase gratings in interference microscopy *Opt. Lett.* **37** 758–60 10.1364/OL.37.000758

[168] Xie W, Lehmann P, Niehues J and Tereschenko S 2016 Signal modeling in low coherence interference microscopy on example of rectangular grating *Opt. Express* **24** 14283–300 10.1364/OE.24.014283

[169] Xie W, Hagemeier S, Woidt C, Hillmer H and Lehmann P 2016 Influences of edges and steep slopes in 3D interference and confocal microscopy *Proc. SPIE vol 9890* Optical Micro- and Nanometrology VI (Brussels, BE: SPIE) p 98900X 10.1117/12.2228307

[170] Pahl T, Hagemeier S, Hüser L, Xie W and Lehmann P 2020 Two-dimensional modelling of systematic surface height deviations in optical interference microscopy based on rigorous near field calculation *J. Mod. Opt.* **67** 963–73 10.1080/09500340.2020.1801871

[171] Harasaki A and Schmit J 2002 Bat-wing attenuation in white-light interferometry US6493093 B2 (Issued December 10, 2002)

[172] Lehmann P, Tereschenko S, Allendorf B, Hagemeier S and Hüser L 2019 Spectral composition of low-coherence interferograms at high numerical apertures *J. Eur. Opt. Soc.-Rapid Publ.* **15** 5 10.1186/s41476-019-0101-8

[173] Xie W 2017 *Transfer characteristics of white light interferometers and confocal microscopes* Doctoral Thesis (Kassel, Hesse, DE: University of Kassel)

[174] Lehmann P, Kühnhold P and Xie W 2014 Reduction of chromatic aberration influences in vertical scanning white-light interferometry *Meas. Sci. Technol.* **25** 065203 10.1088/0957-0233/25/6/065203

[175] Gao F, Coupland J M and Petzing J 2006 V-groove measurement with white light interferometry *Proc. Photon06* Photon06 (Manchester, UK)

[176] Lobera J, Gao F, Petzing J, Coupland J M and Leach R K 2008 Limitations and innovations in scanning white light interferometry *Proceedings of the euspen International Conference* International Conference of the European Society for Precision Engineering and Nanotechnology (Zurich, CH) pp 287–91

[177] Kaplonek W and Lukianowicz C 2012 Coherence correlation interferometry in surface topography measurements *Recent Interferometry Applications in Topography and Astronomy* pp 1–26

[178] Fang F, Zeng Z, Zhang X and Jiang L 2016 Measurement of micro-V-groove dihedral using white light interferometry *Opt. Commun.* **359** 297–303 10.1016/j.optcom.2015.09.101

[179] Bischoff J, Pahl T, Lehmann P and Manske E 2020 Model-based dimensional optical metrology *Proc. SPIE vol 11352* Optics and Photonics for Advanced Dimensional Metrology (Online only: SPIE) p 113520P 10.1117/12.2554517

[180] de Groot P J and Colonna de Lega X 2004 Signal modeling for modern interference microscopes *Proc. SPIE vol 5457* Optical Metrology in Production Engineering (Strasbourg, FR: SPIE) pp 26–34 10.1117/12.546226

[181] Roy M, Cooper I, Moore P, Sheppard C J R and Hariharan P 2005 White-light interference microscopy: effects of multiple reflections within a surface film *Opt. Express* **13** 164–70 10.1364/OPEX.13.000164

[182] de Groot P J, Colonna de Lega X, Su R, Coupland J M and Leach R K 2021 Modeling of coherence scanning interferometry using classical Fourier optics *Opt. Eng.* **60** 104106 10.1117/1.OE.60.10.104106

[183] Pahl T, Hagemeier S, Künne M, Danzglock C, Reinhold N, Schulze R, Siebert M and Lehmann P 2021 Vectorial 3D modeling of coherence scanning interferometry *Proc. SPIE vol 11783* Modeling Aspects in Optical Metrology VIII (Online only: SPIE) p 117830G 10.1117/12.2592617

[184] Coupland J M, Mandal R, Palodhi K and Leach R K 2013 Coherence scanning interferometry: linear theory of surface measurement *Appl. Opt.* **52** 3662–70 10.1364/AO.52.003662

[185] Su R, Coupland J M, Sheppard C J R and Leach R K 2021 Scattering and three-dimensional imaging in surface topography measuring interference microscopy *J. Opt. Soc. Am. A* **38** A27–42 10.1364/JOSAA.411929

[186] Su R and Leach R K 2021 Physics-based virtual coherence scanning interferometer for surface measurement *Light: Adv. Manuf.* **2** 1–16 10.37188/lam.2021.009

[187] Lehmann P, Künne M and Pahl T 2021 Analysis of interference microscopy in the spatial frequency domain *J. Phys.: Photonics* **3** 014006 10.1088/2515-7647/abda15

[188] Pahl T, Hagemeier S, Künne M, Yang D and Lehmann P 2020 3D modeling of coherence scanning interferometry on 2D surfaces using FEM *Opt. Express* **28** 39807–26 10.1364/OE.411167

[189] de Groot P, Colonna de Lega X, Liesener J and Darwin M 2008 Metrology of optically-unresolved features using interferometric surface profiling and RCWA modeling *Opt. Express* **16** 3970–5 10.1364/OE.16.003970

[190] Sheppard C J R and Larkin K G 1995 Effect of numerical aperture on interference fringe spacing *Appl. Opt.* **34** 4731–4 10.1364/AO.34.004731

[191] Xie W, Lehmann P and Niehues J 2012 Lateral resolution and transfer characteristics of vertical scanning white-light interferometers *Appl. Opt.* **51** 1795–803 10.1364/AO.51.001795

[192] Goodman J W 2017 *Introduction to Fourier Optics* 4th ed. (New York: W. H. Freeman)

[193] Gao S, Felgner A, Hüser D and Koenders L 2019 Characterization of the topography fidelity of 3D optical microscopy *Proc. SPIE vol 11057* Modeling Aspects in Optical Metrology VII (Munich, DE: SPIE) p 110570G 10.1117/12.2526032

[194] Debye P 1909 Das verhalten von lichtwellen in der nähe eines brennpunktes oder einer brennlinie [The behavior of light waves near a focal point or a focal line] *Ann. Phys. (Berl.)* **335** 755–76 10.1002/andp.19093351406

[195] Sheppard C J R 2013 Cylindrical lenses - focusing and imaging: a review *Appl. Opt.* **52** 538–45 10.1364/AO.52.000538

[196] Born M and Wolf E 1999 Elements of the theory of diffraction *Principles of Optics: Electromagnetic Theory of Propagation, Interference and Diffraction of Light* 7th ed. (Cambridge, UK: Cambridge University Press) pp 412–516

[197] Richards B and Wolf E 1959 Electromagnetic diffraction in optical systems, II. Structure of the image field in an aplanatic system *Proc. Royal Soc. A* **253** 358–79 10.1098/rspa.1959.0200

[198] Wirgin A 1983 Scattering from sinusoidal gratings: an evaluation of the Kirchhoff approximation *J. Opt. Soc. Am.* **73** 1028–41 10.1364/JOSA.73.001028

[199] Harvey J, Krywonos A and Vernold C L 2007 Modified Beckmann-Kirchhoff scattering model for rough surfaces with large incident and scattering angles *Opt. Eng.* **46** 078002 10.1117/1.2752180

[200] Lehmann P, Hagemeier S and Pahl T 2021 Three-dimensional transfer functions of interference microscopes *Metrology* **1** 122–41 10.3390/metrology1020009

[201] Foreman M R, Giusca C L, Coupland J M, Török P and Leach R K 2013 Determination of the transfer function for optical surface topography measuring

instruments—a review *Meas. Sci. Technol.* **24** 052001 10.1088/0957-0233/24/5/052001

[202] Berman D H and Perkins J S 1985 The Kirchhoff approximation and first-order perturbation theory for rough surface scattering *J. Acoust. Soc. Am.* **78** 1045–51 10.1121/1.393022

[203] Ishimaru A and Chen J S 1990 Scattering from very rough surfaces based on the modified second-order Kirchhoff approximation with angular and propagation shadowing *J. Acoust. Soc. Am.* **88** 1877–83 10.1121/1.400210

[204] Voronovich A G 1994 Kirchhoff-tangent plane approximation *Wave Scattering from Rough Surfaces* Springer Series on Wave Phenomena (Springer, Berlin, Heidelberg) pp 109–45 10.1007/978-3-642-97544-8_5

[205] Bruce N C 2008 Single-scatter vector-wave scattering from surfaces with infinite slopes using the Kirchhoff approximation *J. Opt. Soc. Am. A* **25** 2011–7 10.1364/JOSAA.25.002011

[206] Bruce N C 2011 Vector-electromagnetic scattering from metal surfaces using the infinite-slope Kirchhoff approximation *Proc. SPIE vol 8011* 22nd Congress of the International Commission for Optics: Light for the Development of the World (Puebla, MX: SPIE) p 80115T 10.1117/12.901259

[207] Shi F, Choi W, Lowe M J S, Skelton E A and Craster R V 2015 The validity of Kirchhoff theory for scattering of elastic waves from rough surfaces *Proc. R. Soc. Lond. A* **471** 20140977 10.1098/rspa.2014.0977

[208] Beckmann P 1963 The general Kirchhoff solution for scattering from rough surfaces *The Scattering of Electromagnetic Waves from Rough Surfaces* 1st ed. International series of monographs on electromagnetic waves vol 4 (Oxford; London; New York; Paris: Pergamon Press) pp 17–33

[209] Thomas M, Leach R K, Nikolaev N, Widjanarko T, Senin N, Aryan H and Coupland J M 2018 Verification of a rigorous 2D model of rough surface scattering *Proc. European Optical Society Biennial Meeting (EOSAM) 2018* European Optical Society Biennial Meeting (EOSAM) 2018 (Delft, NL: European Optical Society (EOS)) pp 311–2

[210] Brekhovskikh L M 1952 Difrakcya voln na nerovnoj poverhnosti: 1, Obschaya teoriya [The diffraction of waves by a rough surface: part 1, general theory] *Zh. Eksp. Teor. Fiz* **23** 275–88

[211] Ogilvy J A 1991 Kirchhoff theory *Theory of Wave Scattering From Random Rough Surfaces,* (Bristol, England ; Philadelphia: IOP Publishing) pp 73–117

[212] Bondeson A, Rylander T and Ingelström P 2005 *Computational Electromagnetics* (New York, US: Springer)

[213] Sheng X-Q and Song W 2012 *Essentials of Computational Electromagnetics* 1st ed. (Singapore: Wiley-IEEE Press)

[214] de Groot P, Colonna de Lega X and Liesener J 2009 Model-based white light interference microscopy for metrology of transparent film stacks and optically-unresolved structures *Fringe 2009: 6th International Workshop on Advanced Optical Metrology* (Heidelberg Dordrecht London New York: Springer) pp 1–8 10.1007/978-3-642-03051-2_40

[215] Coupland J M and Nikolaev N 2020 Surface scattering and the 3D transfer characteristics of optical profilers *Proc. SPIE vol 11352* Optics and Photonics for Advanced Dimensional Metrology (Virtual event: SPIE) p 113520K 10.1117/12.2556878

[216] Künne M, Pahl T and Lehmann P 2021 Spatial-frequency domain representation of interferogram formation in coherence scanning interferometry *Proc. SPIE vol 11782* Optical Measurement Systems for Industrial Inspection XII (Online only: SPIE) p 117820T 10.1117/12.2593347

[217] Totzeck M and Tiziani H J 1997 Interference microscopy of sub-λ structures: A rigorous computation method and measurements *Opt. Commun.* **136** 61–74 10.1016/S0030-4018(96)00677-3

[218] Totzeck M, Jacobsen H and Tiziani H J 2000 Edge localization of subwavelength structures by use of polarization interferometry and extreme-value criteria *Appl. Opt.* **39** 6295–305 10.1364/AO.39.006295

[219] Totzeck M 2001 Numerical simulation of high-NA quantitative polarization microscopy and corresponding near-fields *Optik* **112** 399–406 10.1078/0030-4026-00085

[220] Coupland J M and Nikolaev N I 2019 A new approach to vector scattering: the 3s boundary source method *Opt. Express* **27** 30380–95 10.1364/OE.27.030380

[221] Tavrov A, Schmit J, Kerwien N, Osten W and Tiziani H 2005 Diffraction-induced coherence levels *Appl. Opt.* **44** 2202–12 10.1364/AO.44.002202

[222] Netgen/NGSolve https://ngsolve.org/

[223] UNIGIT - Home https://www.unigit.net/

[224] High-Performance Photonic Simulation Software https://www-origin.lumerical.com/

[225] Thomas M, Su R, de Groot P J and Leach R K 2020 Optical topography measurement of steeply-sloped surfaces beyond the specular numerical aperture limit *Proc. SPIE vol 11352* Optics and Photonics for Advanced Dimensional Metrology (Virtual event: SPIE) p 1135207 10.1117/12.2554568

[226] Liu M and Leach R K 2019 Defect detection for structured surfaces via light scattering and machine learning *Proc. 14th International Symposium on Measurement Technology and Intelligent Instruments* ISMTII2019 (Niigata, JP)

[227] Liu M, Senin N, Su R and Leach R K 2020 Cascaded machine learning model for reconstruction of surface topography from light scattering *Proc. SPIE vol 11352* Optics and Photonics for Advanced Dimensional Metrology (Online only: SPIE) pp 174–82 10.1117/12.2555035

[228] Liu M, Cheung C F, Senin N, Senin N, Wang S, Su R and Leach R K 2020 On-machine surface defect detection using light scattering and deep learning *J. Opt. Soc. Am. A* **37** B53–9 10.1364/JOSAA.394102

[229] Born M and Wolf E 1999 Scattering from inhomogeneous media *Principles of Optics: Electromagnetic Theory of Propagation, Interference and Diffraction of Light* 7th ed. (Cambridge, UK: Cambridge University Press) pp 695–734

[230] Goodman J W 2017 Foundations of scalar diffraction theory *Introduction to Fourier Optics* 4th ed. (New York: W. H. Freeman) pp 43–74

[231] Zhou K C, Qian R, Dhalla A-H, Farsiu S, Farsiu S, Izatt J A and Izatt J A 2021 Unified k-space theory of optical coherence tomography *Adv. Opt. Photon.* **13** 462–514 10.1364/AOP.417102

[232] Lehmann P, Tereschenko S and Xie W 2016 Fundamental aspects of resolution and precision in vertical scanning white-light interferometry *Surf. Topogr.: Metrol. Prop.* **4** 024004 10.1088/2051-672X/4/2/024004

[233] Behrends G, Stöbener D and Fischer A 2020 Lateral scanning white-light interferometry on rotating objects *Surf. Topogr.: Metrol. Prop.* **8** 035006 10.1088/2051-672X/aba484

[234] Wang J, Leach R K and Jiang X 2015 Review of the mathematical foundations of data fusion techniques in surface metrology *Surf. Topogr.: Metrol. Prop.* **3** 023001 10.1088/2051-672X/3/2/023001

[235] Li L, Liu J, Liu Y, Liu C, Zhang H, You X, Gu K, Wang Y and Tan J 2018 A promising solution to the limits of microscopes for smooth surfaces: fluorophore-aided scattering microscopy. *Nanoscale* **10** 9484–8 10.1039/c8nr00731d

[236] Zangl K, Danzl R, Urlep D and Helmli F 2021 Optical 3D measurement of cooling holes in gas turbine and aircraft engines *Proc. 14th International Conference and Exhibition on Laser Metrology, Coordinate Measuring Machine and Machine Tool Performance (LAMDAMAP 2021)* LAMDAMAP 2021 (Södertälje, SE (virtual))

[237] Leach R K, de Groot P and Haitjema H 2018 Surface slope limits in the measurement of areal surface topography *CIRP Winter Meetings* CIRP Winter Meetings (Paris, FR)

[238] Colonna de Lega X and de Groot P 2005 Optical topography measurement of patterned wafers *AIP Conf. Proc.* **788** 432–6 10.1063/1.2062999

[239] Sheridan J T and Sheppard C J R 1993 Coherent imaging of periodic thick fine isolated structures *J. Opt. Soc. Am. A* **10** 614–32 10.1364/JOSAA.10.000614

[240] Sheridan J T and Sheppard C J R 1994 Modelling of images of square-wave gratings and isolated edges using rigorous diffraction theory *Opt. Commun.* **105** 367–78 10.1016/0030-4018(94)90411-1

[241] Sheridan J T and Sheppard C J R 1993 Diffraction by striated muscle fibres: Application to image modelling *Bioimaging* **1** 214–27 10.1002/1361-6374(199312)1:4<214::AID-BIO4>3.0.CO;2-T

[242] Sheridan J T and Körner T O 1995 Imaging periodic surface relief structures *J. Microsc.* **177** 95–107 10.1111/j.1365-2818.1995.tb03539.x

[243] Körner T O, Sheridan J T and Schwider J 1995 Interferometric resolution examined by means of electromagnetic theory *J. Opt. Soc. Am. A* **12** 752–60 10.1364/JOSAA.12.000752

[244] Su R, Thomas M, Liu M, Coupland J M and Leach R K 2019 High-accuracy surface measurement through modelling of the surface transfer function in interference microscopy *Proc. SPIE vol 11102* Applied Optical Metrology III (San Diego, CA, US: SPIE) p 1110205 10.1117/12.2528911

[245] de Groot P J and Colonna de Lega X 2020 Fourier optics modeling of interference microscopes *J. Opt. Soc. Am. A* **37** B1–10 10.1364/JOSAA.390746

[246] de Groot P J, Colonna de Lega X, Su R, Coupland J M and Leach R K 2021 Fourier optics modelling of coherence scanning interferometers *Proc. SPIE vol 11817* Applied Optical Metrology IV (San Diego, CA, US: SPIE) p 118170M 10.1117/12.2595668

[247] Mandal R, Coupland J M, Leach R K and Mansfield D 2014 Coherence scanning interferometry: measurement and correction of three-dimensional transfer and point-spread characteristics *Appl. Opt.* **53** 1554–63 10.1364/AO.53.001554

[248] Su R, Coupland J M, Wang Y and Leach R K 2017 Tolerance on sphere radius for the calibration of the transfer function of coherence scanning interferometry *Proc. SPIE vol 10329* Optical Measurement Systems for Industrial Inspection X (Munich, DE: SPIE) p 103290L 10.1117/12.2272041

[249] Sheppard C J R and Aguilar F 1999 Fresnel coefficients for weak reflection, and the scattering potential for three-dimensional imaging *Opt. Commun.* **162** 182–6 10.1016/S0030-4018(99)00084-X

[250] Mandal R 2014 *Calibration and adjustment of coherence scanning interferometry* Doctoral Thesis (Loughborough, UK: Loughborough University)

[251] Bellouard Y, Said A, Dugan M and Bado P 2004 Fabrication of high-aspect ratio, micro-fluidic channels and tunnels using femtosecond laser pulses and chemical etching *Opt. Express* **12** 2120–9 10.1364/OPEX.12.002120

[252] Drs J, Kishi T and Bellouard Y 2015 Laser-assisted morphing of complex three dimensional objects *Opt. Express* **23** 17355–66 10.1364/OE.23.017355

[253] Newton L, Senin N, Gomez C, Danzl R, Helmli F, Blunt L and Leach R K 2019 Areal topography measurement of metal additive surfaces using focus variation microscopy *Addit. Manuf.* **25** 365–89 10.1016/j.addma.2018.11.013

[254] Giusca C L, Leach R K, Helary F, Gutauskas T and Nimishakavi L 2012 Calibration of the scales of areal surface topography-measuring instruments: part 1. Measurement noise and residual flatness *Meas. Sci. Technol.* **23** 035008 10.1088/0957-0233/23/3/035008

[255] Liu M Y, Cheung C F, Feng X, Wang C J and Cao Z C 2020 Any-degrees-of-freedom (anyDOF) registration for the characterization of freeform surfaces *Precis. Eng.* **62** 170–80 10.1016/j.precisioneng.2019.12.003

[256] McCutchen C W 1964 Generalized aperture and the three-dimensional diffraction image *J. Opt. Soc. Am.* **54** 240–4 10.1364/JOSA.54.000240

[257] Gu M 2000 *Advanced Optical Imaging Theory* vol 75 (Berlin, Heidelberg: Springer) 10.1007/978-3-540-48471-4

[258] Leach R K and Haitjema H 2010 Bandwidth characteristics and comparisons of surface texture measuring instruments *Meas. Sci. Technol.* **21** 032001 10.1088/0957-0233/21/3/032001

[259] Leach R K and Haitjema H 2010 Corrigendum: Bandwidth characteristics and comparisons of surface texture measuring instruments *Meas. Sci. Technol.* **21** 079801 10.1088/0957-0233/21/7/079801

[260] Nikolaev N, Petzing J and Coupland J M 2016 Focus variation microscope: linear theory and surface tilt sensitivity *Appl. Opt.* **55** 3555–65 10.1364/AO.55.003555

[261] Simonsen I 2010 Optics of surface disordered systems. A random walk through rough surface scattering phenomena *Eur. Phys. J. Spec. Top.* **181** 1–103 10.1140/epjst/e2010-01221-4

[262] Maradudin A A, Michel T, McGurn A R and Méndez E R 1990 Enhanced backscattering of light from a random grating *Ann. Phys. (N. Y.)* **203** 255–307 10.1016/0003-4916(90)90172-K

[263] Born M and Wolf E 1999 Electromagnetic potentials and polarization *Principles of Optics: Electromagnetic Theory of Propagation, Interference and Diffraction of Light* 7th ed. (Cambridge, UK: Cambridge University Press) pp 75–115 10.1016/B978-0-08-026482-0.50009-8

[264] Sein J J 1970 A note on the Ewald-Oseen extinction theorem *Opt. Commun.* **2** 170–2 10.1016/0030-4018(70)90008-8

[265] Dialetis D 1978 Equivalence of the Ewald-Oseen extinction theorem as a nonlocal boundary-value problem with Maxwell's equations and boundary conditions *J. Opt. Soc. Am.* **68** 602–10 10.1364/JOSA.68.000602

[266] Sommerfeld A 1912 Die Greensche Funktion der Schwingungslgleichung [The Green's function of the oscillation equation] *Jahresber. Dtsch. Math.-Ver.* **21** 309–52

[267] Goldstein M and Thaler R M 1958 Bessel functions for large arguments *Math. Tables Other Aids Comput.* **12** 18–26 10.2307/2002123

[268] Mie G 1908 Beiträge zur Optik trüber Medien, speziell kolloidaler Metallösungen [Contributions to the optics of cloudy media, especially colloidal metal solutions] *Ann. Phys. (Berl.)* **330** 377–445 10.1002/andp.19083300302

[269] Wriedt T 2012 Mie theory: A review *The Mie Theory: Basics and Applications* Springer Series in Optical Sciences ed W Hergert and T Wriedt (Berlin, Heidelberg: Springer) pp 53–71 10.1007/978-3-642-28738-1_2

[270] Cheever D R, Cad F M, Klicker K A and Stover J C 1987 Design Review Of A Unique Complete Angle Scatter Instrument (CASI) *Proc. SPIE vol 0818* Current Developments in Optical Engineering II (San Diego, CA, US: SPIE) pp 13–21 10.1117/12.978542

[271] Stover J C 2017 CASI technical specifications

[272] Stover J C 2012 *Optical Scattering: Measurement and Analysis* 3rd ed. (Bellingham, WA, US: SPIE Press) 10.1117/3.975276

[273] Leach R K, Bointon P, Feng X, Lawes S, Piano S, Senin N, Sims-Waterhouse D, Stavroulakis P, Su R, Syam W and Thomas M 2018 Information-rich manufacturing metrology International Precision Assembly Conference (Chamonix, FR)

[274] Su R and Leach R K 2021 Virtual coherence scanning interferometer for surface measurement *Proc. SPIE vol 11782* Optical Measurement Systems for Industrial Inspection XII (Online only: SPIE) p 117820L 10.1117/12.2592255

[275] Lehmann P, Xie W, Allendorf B and Tereschenko S 2018 Coherence scanning and phase imaging optical interference microscopy at the lateral resolution limit *Opt. Express* **26** 7376–89 10.1364/OE.26.007376

[276] Coupland J M 2014 Linear theory of optical surface measuring instruments *Fringe 2013: 7th International Workshop on Advanced Optical Imaging and Metrology* 1st ed. (Heidelberg New York Dordrecht London: Springer) pp 63–70 10.1007/978-3-642-36359-7_8

[277] Voelz D G 2011 *Computational Fourier Optics: A MATLAB® Tutorial* (Bellingham, WA, US: SPIE Press) 10.1117/3.858456

[278] Iizuka K 2019 Optical signal processing *Engineering Optics* 4th ed. (New York, US: Springer-Verlag) pp 277–334 10.1007/978-3-319-69251-7

[279] Park I 2021 *Towards the measurement of surfaces on a large scale: synthetic aperture interferometry* Ph.D. (Loughborough, UK: Loughborough University) 10.26174/thesis.lboro.14976984.v1

[280] Palodhi K 2013 *Absolute surface topography measurement with polarisation sensitive coherence scanning interferometry* Doctoral Thesis (Loughborough, UK: Loughborough University)

[281] Church E L, Dainty C, Gale D M and Takacs P Z 1992 Comparison of optical and mechanical measurements of surface finish *Proc. SPIE vol 1531* Advanced Optical Manufacturing and Testing II (San Diego, CA, US: SPIE) pp 234–50 10.1117/12.134865

# List of Publications

A list of publications by the author are given here in one place for ease of reference.

**Journal papers**

- Thomas M, Su R, de Groot P J, Coupland J M and Leach R K 2021 Surface measuring coherence scanning interferometry beyond the specular reflection limit *Opt. Express* **29** 36121–31 10.1364/OE.435715
- Su R, Thomas M, Liu M, Drs J, Bellouard Y, Pruss C, Coupland J M and Leach R K 2020 Lens aberration compensation in interference microscopy *Opt. Lasers Eng.* **128** 106015 10.1016/j.optlaseng.2020.106015
- Thomas M, Su R, Nikolaev N, Coupland J M and Leach R K 2020 Modeling of interference microscopy beyond the linear regime *Opt. Eng.* **59** 034110 10.1117/1.OE.59.3.034110
- Su R, Thomas M, Leach R K and Coupland J M 2018 Effects of defocus on the transfer function of coherence scanning interferometry *Opt. Lett.* **43** 82–5 10.1364/OL.43.000082

**Conference papers/presentations**

- Thomas M, Su R, de Groot P J and Leach R K 2020 Optical topography measurement of steeply-sloped surfaces beyond the specular numerical aperture limit *Proc. SPIE vol 11352* Optics and Photonics for Advanced Dimensional Metrology (Virtual event: SPIE) p 1135207 10.1117/12.2554568
- Su R, Thomas M, Liu M, Coupland J M and Leach R K 2019 High-accuracy surface measurement through modelling of the surface transfer function in interference microscopy *Proc. SPIE vol 11102* Applied Optical Metrology III (San Diego, CA, US: SPIE) p 1110205 10.1117/12.2528911
- Thomas M, Su R, Nikolaev N, Coupland J M and Leach R K 2019 Modelling of coherence scanning interferometry for complex surfaces based on a boundary element method *Proc. SPIE vol 11057* Modeling Aspects in Optical Metrology VII (Munich, DE: SPIE) p 1105713 10.1117/12.2526015

- Su R, Thomas M, de Groot P, Coupland J M and Leach R K 2018 Determination of the lateral resolution of an interference microscope using a micro-scale sphere *Proc. 33rd Annual Meeting ASPE* ASPE Annual Meeting (Las Vegas, NV, US: American Society for Precision Engineering) pp 225–9
- Thomas M, Leach R K, Nikolaev N, Widjanarko T, Senin N, Aryan H and Coupland J M 2018 Verification of a rigorous 2D model of rough surface scattering *Proc. European Optical Society Biennial Meeting (EOSAM) 2018* European Optical Society Biennial Meeting (EOSAM) 2018 (Delft, NL: European Optical Society (EOS)) pp 311–2
- Leach R K, Bointon P, Feng X, Lawes S, Piano S, Senin N, Sims-Waterhouse D, Stavroulakis P, Su R, Syam W and Thomas M 2018 Information-rich manufacturing metrology International Precision Assembly Conference (Chamonix, FR)

# Appendix A: Foil model inverse filtering graphical user interface

A pre-existing code base had already been developed that was capable of loading signal data from the commercial CSI instrument, cropping the data to chosen parameters, saving the cropped data, applying certain filtering operations to clean the data, simulate a spherical foil from a given sphere diameter, calculate the transfer function and use this to produce an inverse filter to apply to further measurements. The flow chart for this work can be seen in Figure A.1.

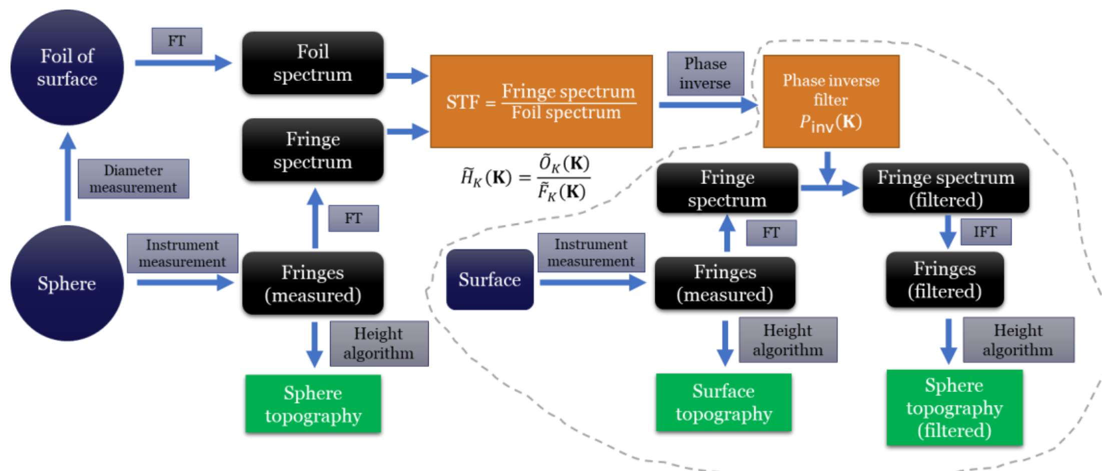


**Figure A.1**. Flow chart for the method to produce the surface transfer function (STF) and associated inverse filter via measurement of a microsphere and generation of the foil model of the surface, and (circled by the dashed line) the application of the inverse filter to measured fringe data. FT and IFT denote the Fourier transform and inverse Fourier transform respectively. Details such as real and foil sphere alignment are omitted.

However, the use of this code was limited heavily by its linear structure, with all operations following each other in series from start to finish. A lack of user interface made changing parameters slower and made the current choice of parameters harder to see. To allow this code to easily measure the STF and apply the inverse filter to other measurements, a graphical user interface (GUI) was made, and the underlying code heavily restructured to allow for the GUI code wrapping. The core objectives were:

- Easy changing of parameters while preserving default/unchanged parameters

- Quick and easy testing of different spheres, especially for quickly changing the selection of which file(s) to load using a selection dialog
- Allow for adding of additional features, such as distortion correction, & automation
- Rework overall structure of code into more modular components for flexibility, to allow for testing of independent components independently
- Optimise code to reduce redundant function calls, structural issues, packaging of arguments
- As part of quick and easy testing of spheres, wrap the data format converter command line program provided by the instrument manufacturer with a GUI
- Fix any bugs present

Work was performed to complete these objectives including the development of a GUI to, shown in Figure A.2. In addition to successfully meeting the previously stated objectives, some additional features not present in the original code base were added. This includes:

- Data converter GUI wrapper makes further changes to file format beyond the command line program's conversion, using HDF5-based version 7.3 MAT-files for data arrays, allowing for fast preview of slices of data
- Approximate auto-centring of fringes via finding peak intensity
- Lateral repositioning of the cropping centre
- Independent cropping and saving of data
- Filter windowing lateral and axial size adjustment
- Independently generate and save BPF mask, using relevant GUI values
- Coarse automatic spatial co-alignment between generated foil model and measured fringe data
- Finetune repositioning of foil shell, iterative adjustment, or pre-set values
- Distortion correction of optical elements can be loaded from a file
- Generation and saving of inverse filter via averaging of saved STFs
- Application of saved inverse filter to other measurements
- Utility functions (open explorer, close all figures, disabling of unticked features)

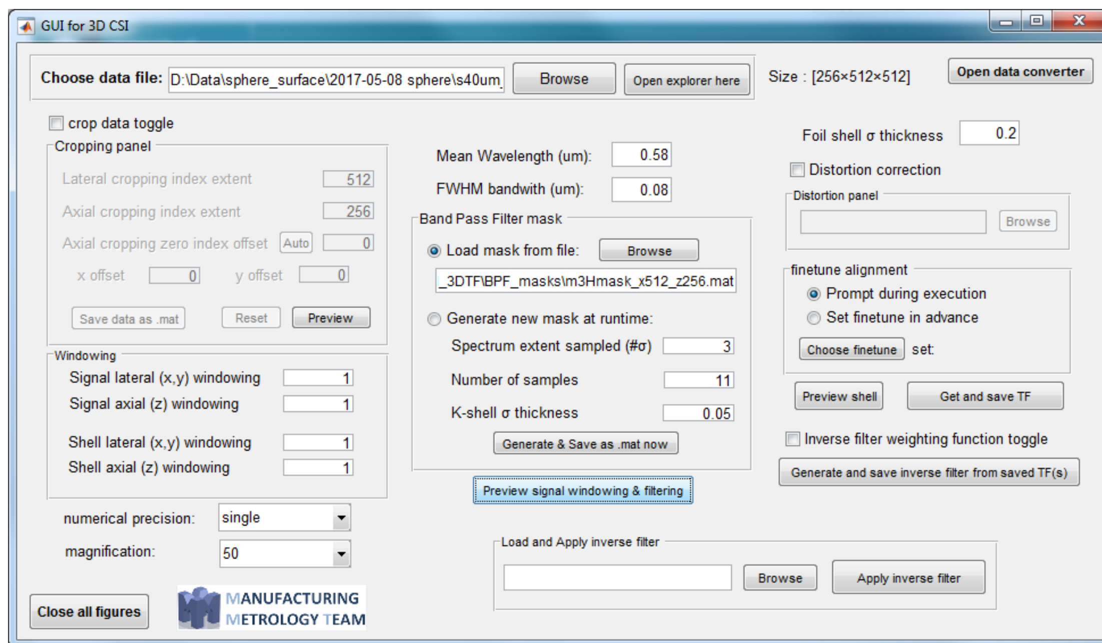


**Figure A.2**. Screenshot of the GUI for the loading, filtering and analysing of fringe data, to obtain STFs via method displayed in Figure A.1.

Of particular benefit is the ability to:

- Independently generate and save the band pass filter (BPF) mask for a chosen instrument configuration
- Crop, filter and save the fringe data; preview the foil shell for the current settings
- Get and save the STF from a single measurement
- Average a set of saved STFs to calculate and save an inverse filter; and load and apply this filter to any other measurement

Some example outputs for the fringe data after Gaussian filtering and its associated k-space form after bandpass filtering are displayed in Figure A.3 and Figure A.4 respectively.

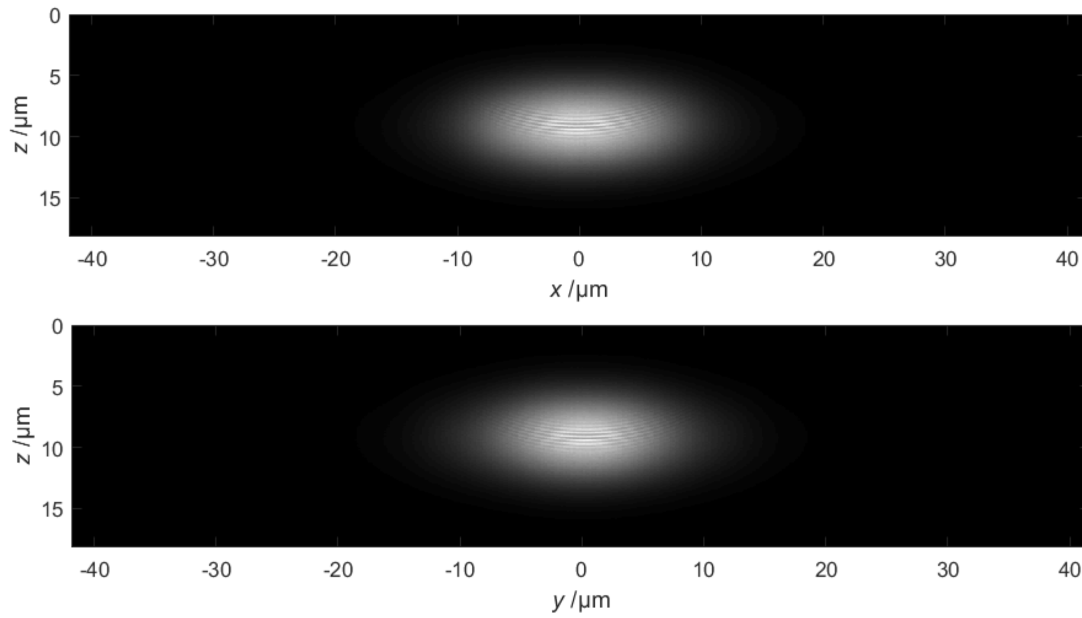


**Figure A.3.** Fringe data of a measurement of a microsphere, after Gaussian spatial filtering

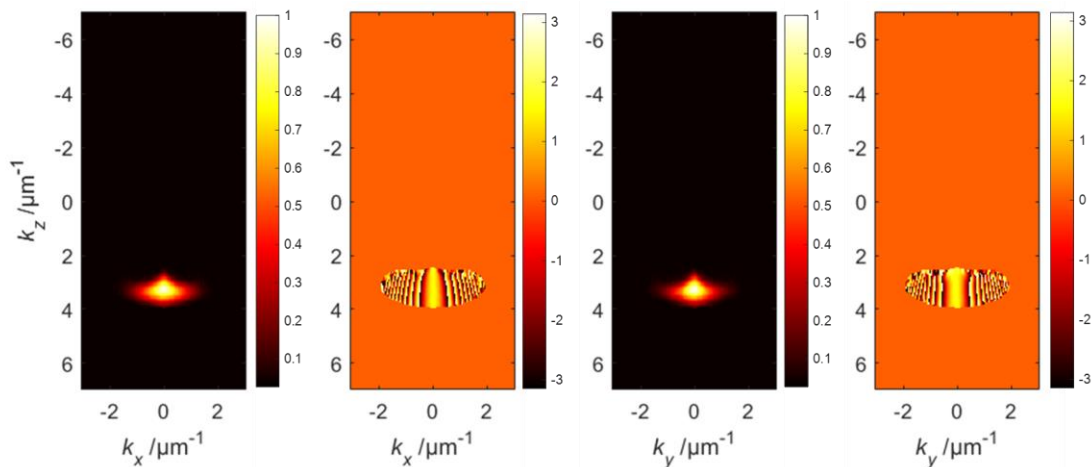


**Figure A.4.** The associated k-space form of Figure A.3, after a BPF mask has been applied to the relevant section. Note the absolute parts and phase angle parts are displayed across two perpendicular planes both aligned with the optical axis.

This work was developed further outside of the PhD project by the author of this thesis, working on an EPSRC IAA project "Calibration and correction of optical topography measuring technology" as a research associate.

# Appendix B: Summation identities for complex numbers

As given in Eq. (5-1) and Eq. (5-2), the expression for the fringe component of the intensity is $2\Re\{E_m(\mathbf{r})E_r(\mathbf{r})^*\}$, equally expressed as $E_m(\mathbf{r})E_r(\mathbf{r})^* + E_m(\mathbf{r})^*E_r(\mathbf{r})$, where $\Re\{\cdot\}$ denotes taking the real part of a complex number. Taking the real part of the complex $O(\mathbf{r})$ to obtain the imaged fringes is implicitly implied in [88,184] and explicitly included in [185] for their equivalent expressions for Eq. (5-2). However, the choice in either case to handle the complex $O(\mathbf{r})$ rather than the real $I(\mathbf{r}) = 2\Re\{O(\mathbf{r})\}$ is made as the intensity obtained from multiple illumination wavevectors can be expressed as a function of a linear sum of the complex fringe terms, to be shown in this appendix. For a superposition of intensity values, where each intensity value is a result of illumination by a specific incident illumination wavevector $\mathbf{k}_\mathrm{i}$, the total intensity is given by

$$\begin{aligned} I_{\mathrm{total}}(\mathbf{r}) &= \sum_{\mathrm{i}} I^{(\mathrm{i})}(\mathbf{r}) = \sum_{\mathrm{i}} 2\Re\{O^{(\mathrm{i})}(\mathbf{r})\} \\ &= \sum_{\mathrm{i}} \left[O^{(\mathrm{i})}(\mathbf{r}) + O^{(\mathrm{i})}(\mathbf{r})^*\right] \end{aligned} \tag{7-1}$$

and the Fourier transform of this gives

$$\begin{aligned} \tilde{I}_{\mathrm{total}}(\mathbf{k}) &= \sum_{\mathrm{i}} \tilde{O}^{(\mathrm{i})}(\mathbf{k}) + \sum_{\mathrm{i}} \tilde{O}^{(\mathrm{i})}(-\mathbf{k})^* \\ &= \tilde{O}_{\text{k-total}}(\mathbf{k}) + \tilde{O}_{\text{k-total}}(-\mathbf{k})^*, \end{aligned} \tag{7-2}$$

where $\tilde{O}_{\text{k-total}}(\mathbf{k})$ has been defined as the summation of $\tilde{O}^{(\mathrm{i})}(\mathbf{k})$, and consequently the summation of $\tilde{O}^{(\mathrm{i})}(-\mathbf{k})^*$ is given by $\tilde{O}_{\text{k-total}}(-\mathbf{k})^*$. As the fringes $I_{\mathrm{total}}(\mathbf{r})$ are real, redundant information is unsurprisingly obtained from $\tilde{I}_{\mathrm{total}}(\mathbf{k})$ in $k$-space, i.e., knowledge of all $\tilde{O}^{(\mathrm{i})}(\mathbf{k})$ alone is enough to obtain $\tilde{I}_{\mathrm{total}}(\mathbf{k})$, as a corresponding $\tilde{O}^{(\mathrm{i})}(-\mathbf{k})^*$ can always be generated for each $\tilde{O}^{(\mathrm{i})}(\mathbf{k})$ found. However, this redundancy can alternatively be better expressed by considering the inverse Fourier transform of Eq. (7-2), where

$$I_{\text{total}}(\mathbf{r}) = \mathcal{F}^{-1}\{\tilde{I}_{\text{total}}(\mathbf{k})\} = O_{\text{k-total}}(\mathbf{r}) + O_{\text{k-total}}(\mathbf{r})^* \\ = 2\Re\{O_{\text{k-total}}(\mathbf{r})\}, \tag{7-3}$$

where $O_{\text{k-total}}(\mathbf{r})$ has been defined by

$$O_{\text{k-total}}(\mathbf{r}) = \mathcal{F}^{-1}\{\tilde{O}_{\text{k-total}}(\mathbf{k})\}, \tag{7-4}$$

which can be equally expressed as

$$O_{\text{k-total}}(\mathbf{r})^* = \mathcal{F}^{-1}\{\tilde{O}_{\text{k-total}}(-\mathbf{k})^*\}. \tag{7-5}$$

Eq. (7-4) shows that only $2\Re\{O_{\text{k-total}}(\mathbf{r})\}$ is needed to calculate $I_{\text{total}}(\mathbf{r})$, and as such only $\tilde{O}_{\text{k-total}}(\mathbf{k})$ must be found and $\tilde{O}_{\text{k-total}}(-\mathbf{k})^*$ does not need to be considered.

Combining Eq. (7-3) and Eq. (7-4) for an explicit expression of $\tilde{O}_{\text{k-total}}(\mathbf{k})$ gives

$$I_{\text{total}}(\mathbf{r}) = \sum_{\text{i}} 2\Re\{O^{(\text{i})}(\mathbf{r})\} = 2\Re\{O_{\text{k-total}}(\mathbf{r})\} \\ = 2\Re\left\{\mathcal{F}^{-1}\left\{\sum_{\text{i}} \tilde{O}^{(\text{i})}(\mathbf{k})\right\}\right\}. \tag{7-6}$$

This expression gives the approach taken by the BEM-CSI model to calculate fringes from a summation of fringe field values in *k*-space. Note that using the linearity of the Fourier transform, $O_{\text{k-total}}(\mathbf{r})$ can also be related to $O^{(\text{i})}(\mathbf{r})$ directly by

$$O_{\text{k-total}}(\mathbf{r}) = \mathcal{F}^{-1}\left\{\sum_{\text{i}} \tilde{O}^{(\text{i})}(\mathbf{k})\right\} = \mathcal{F}^{-1}\left\{\sum_{\text{i}} \mathcal{F}\left\{O^{(\text{i})}(\mathbf{r})\right\}\right\} \\ = \mathcal{F}^{-1}\left\{\mathcal{F}\left\{\sum_{\text{i}} O^{(\text{i})}(\mathbf{r})\right\}\right\} = \sum_{\text{i}} O^{(\text{i})}(\mathbf{r}) \equiv O_{\text{total}}(\mathbf{r}). \tag{7-7}$$

This should not come as a surprise, as from Eq. (7-1) and Eq. (7-3) there is $I_{\text{total}}(\mathbf{r}) = \sum_{\text{i}} 2\Re\{O^{(\text{i})}(\mathbf{r})\}$ and $I_{\text{total}}(\mathbf{r}) = 2\Re\{O_{\text{k-total}}(\mathbf{r})\}$ respectively; combining these two and using the identity $\sum_{\text{i}} \Re\{Q(\mathbf{r})\} = \Re\{\sum_{\text{i}} Q(\mathbf{r})\}$ for complex valued $Q(\mathbf{r})$ also gives Eq. (7-7).